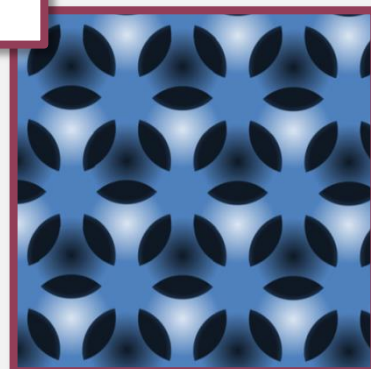
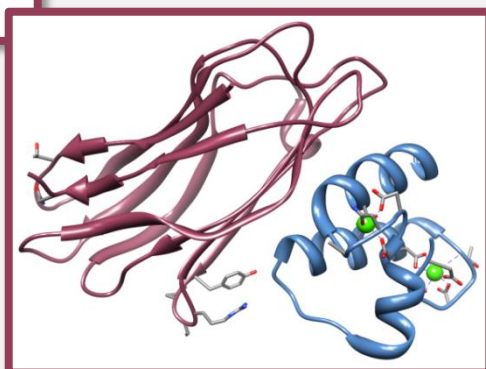
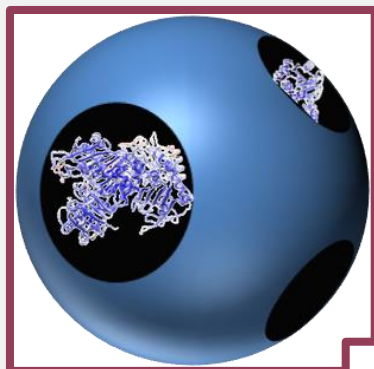


Dorothee Irmgard Fried



DESIGNED ENZYME-INORGANIC HYBRID MATERIALS FOR APPLICATIONS IN BIOCATALYSIS

Dissertation

zur Erlangung des Grades

Doktor der Naturwissenschaften (Dr. rer. nat.)

im Department Chemie der Universität Hamburg

Januar 2014

Die vorliegende Arbeit wurde im Zeitraum von Januar 2010 bis Januar 2014 in der Arbeitsgruppe von Prof. Dr. Michael Fröba am Institut für Anorganische und Angewandte Chemie im Fachbereich Chemie der Universität Hamburg angefertigt.

1. Gutachter: Prof. Dr. Michael Fröba

2. Gutachter: Prof. Dr. Sascha Rohn

Tag der Disputation: 17.01.2014

Erklärung über frühere Promotionsversuche

Hiermit erkläre ich, dass vorher keine weiteren Promotionsversuche unternommen wurden. Die vorliegende Dissertationsschrift habe ich an keiner anderen Stelle in gleicher oder ähnlicher Form zur Promotion vorgelegt.

Hamburg, den 02.12.2013

Dorothee I. Fried

Eidesstattliche Erklärung

Hiermit versichere ich an Eides statt, dass ich die vorliegende Dissertation selbständig angefertigt habe und keine anderen als die von mir angegebenen Quellen und Hilfsmittel verwandt habe.

Hamburg, den 02.12.2013

Dorothee I. Fried

DANKSAGUNG

Die Erstellung dieser Arbeit wäre ohne die Hilfe einiger Personen nicht möglich gewesen, denen ich an dieser Stelle danken möchte:

Prof. Dr. M. Fröba für die Betreuung dieser Arbeit. Ich danke Ihnen nicht nur für die spannende Themenstellung meiner Arbeit, sondern auch für das Vertrauen, dass Sie mir damit entgegengebracht haben, die biochemische Ausrichtung meiner Arbeit als „Pionier“ in der Arbeitsgruppe zu bearbeiten. Insbesondere in den letzten Monaten der Doktorarbeit hat mir Ihre Unterstützung besonders geholfen, mich auf das Wesentliche zu fokussieren.

Prof. Dr. Sascha Rohn für die Erstellung des Zweitgutachtens.

Dr. Felix Brieler für die Korrekturen und die Zusammenarbeit beim Schreiben und der graphischen Gestaltung des Reviews.

Allen, die an der Analytik meiner Proben mitgewirkt haben: Uta, Sandra, Conny, Isabelle, Tamás und Christopher aus dem AK Fröba sowie Maria Trusch, Christian Klinke, Renate Walter, Günter Koch und Andreas Meyer.

Uta und Sandra für die kompetente Einarbeitung in die Physisorption und die gute Zusammenarbeit im Physisorptionsteam, einschließlich Christopher.

Dem ganzen Arbeitskreis für die schönen Jahre. Insbesondere Sebastian Kraas, der sich meiner als „Neuling“ an der Uni angenommen hat und mit Michael 1 und 2 sowie Kristin eine perfekte Bürobesezung für mich war. Katharina Peikert als sehr geschätzte Laborpartnerin und der Küchenfraktion für Ablenkung und leckeres Essen.

Michael Dreifke für seine Arbeit als Praktikant und Diplomand sowie für die Verstärkung der Bio-Gruppe.

Meinen Praktikanten, die mich die letzten vier Jahre begleitet haben und sehr gute Arbeit geleistet haben.

Dr. Matthias Thommes für die Beantwortung vieler Fragen rund um das Thema Physisorption im Allgemeinen und Wasserdampfsorption im Speziellen.

Nicht nur das Verfassen dieser Arbeit, sondern vielmehr der jahrelange Weg dorthin von der Schule über das Studium bis heute, wurde von zahlreichen Menschen begleitet bei denen ich mich bedanken möchte. Auch wenn oder gerade weil Ihr nicht direkt an dieser Arbeit mitgewirkt habt, ist Eure Unterstützung doch umso wichtiger für mich gewesen! Dafür danke ich:

Meinen Eltern. Ihr habt mich immer unterstützt und durch die schweren Zeiten in der Schule, dem Studium und der Doktorarbeit begleitet. Immer, wenn ich in den letzten Jahren zu Hause war, haben mir die Distanz zur Arbeit und eure Anwesenheit geholfen, die Anstrengung und den Stress hinter mir zu lassen.

Meiner Schwester dafür, dass du dein Leben anders gestaltetest als ich und mir dadurch auch noch eine andere Sicht auf die Dinge ermöglichst.

Ralf, für deine Geduld und Unterstützung.

Meinen Freunden insbesondere Helga Koch.

Milli.

*„Einen Lehrer gibt es, der ist vortrefflich,
wenn wir ihn verstehen;
es ist die Natur.“*

Heinrich von Kleist

(1777-1811)

TABLE OF CONTENTS

TABLE OF CONTENTS.....	IX
0 LIST OF ABBREVIATIONS	XIII
1 INTRODUCTION	1
1.1 ENZYMES	3
1.1.1 GLUCOSE-6-PHOSPHATE DEHYDROGENASE (G6PDH) FROM <i>L. MESENTEROIDES</i>	5
1.1.2 CELLULOSOME OF <i>CLOSTRIDIUM THERMOCELLUM</i>	8
1.2 IMMOBILIZATION OF ENZYMES ONTO SOLID SUPPORTS.....	12
1.3 ENZYME-INORGANIC HYBRID MATERIALS	16
1.3.1 INORGANIC POROUS MATERIALS FOR ENZYME IMMOBILIZATION	16
1.3.1.1 Synthesis and functionalization of porous materials	16
1.3.1.2 Immobilization of enzymes in porous silicas.....	25
1.3.1.3 Immobilization of enzymes in periodic mesoporous organosilicas (PMOs)	34
1.3.1.4 Immobilization of enzymes in porous carbons	36
1.3.2 MAGNETIC IRON OXIDE PARTICLES FOR ENZYME IMMOBILIZATION	38
1.3.2.1 Magnetic iron oxide particles.....	38
1.3.2.2 Synthesis and functionalization of magnetic iron oxide particles.....	43
1.3.2.3 Immobilization of enzymes onto magnetic iron oxide composite materials	47
1.3.3 ENZYME-INORGANIC HYBRID MATERIALS FOR APPLICATIONS IN BIOCATALYSIS	50
1.3.3.1 Green chemistry.....	50
1.3.3.2 Enzyme cascades and cofactor regeneration.....	53
2 CHARACTERIZATION TECHNIQUES	58
2.1 POWDER X-RAY DIFFRACTION (PXRD)	58
2.2 CHARACTERIZATION OF POROSITY	59
2.2.1 VOLUMETRIC NITROGEN PHYSISORPTION.....	60
2.2.2 GRAVIMETRIC WATER VAPOR SORPTION	63
2.2.3 MERCURY POROSIMETRY.....	66
2.3 LIGHT SCATTERING TECHNIQUES	70
2.3.1 DYNAMIC LIGHT SCATTERING (DLS)	71
2.3.2 ZETA POTENTIAL MEASUREMENTS.....	73
2.4 ULTRAVIOLET-VISIBLE SPECTROSCOPY (UV-Vis)	78

TABLE OF CONTENTS

2.5	ELECTRON MICROSCOPY	79
2.6	THERMAL ANALYSIS (TG/DTA/MS)	80
2.7	INFRARED (IR) SPECTROSCOPY	81
2.8	MATRIX ASSISTED LASER DESORPTION/IONIZATION-TIME OF FLIGHT MASS SPECTROMETRY (MALDI-TOF)	82
2.9	MAGNETOMETRY	82
3	<u>MOTIVATION</u>	84
4	<u>TAILORING POROUS MATERIALS FOR G6PDH IMMOBILIZATION</u>	86
4.1	INTRODUCTION	86
4.2	RESULTS AND DISCUSSION	89
4.2.1	CHARACTERIZATION OF NANOPOROUS SUPPORTS	89
4.2.1.1	Siliceous mesostructured cellular foams (MCF)	89
4.2.1.2	Organosilane functionalized MCF	99
4.2.1.3	PMOs with alkyl-amine bridged precursors	111
4.2.1.4	Hierarchical porous carbon	116
4.2.2	IMMOBILIZATION OF G6PDH WITHIN NANOPOROUS SUPPORTS	121
4.2.3	INFLUENCE OF THE TYPE OF AMINE-MODIFICATION ON THE IMMOBILIZATION OF G6PDH	144
4.2.3.1	Maximum uptake capacity of MCF-C ₃ -NH ₂	144
4.2.3.2	Michaelis-Menten kinetics of MCF-C ₃ -NH ₂	147
4.2.3.3	Effect of spacer length and hydrophobicity	148
4.2.3.4	Effect of type (primary, secondary, tertiary) and site of amine moities	165
4.2.4	CONVERSION OF GLUCOSE-6-PHOSPHATE TO RIBULOSE-5-PHOSPHATE BY G6PDH AND 6PGDH	181
4.3	EXPERIMENTAL SECTION	186
4.3.1	CHARACTERIZATION TECHNIQUES - INSTRUMENTAL DETAILS	186
4.3.2	SYNTHESIS AND FUNCTIONALIZATION OF NANOPOROUS SUPPORTS	189
4.3.2.1	Synthesis of mesostructured cellular foams (MCF)	189
4.3.2.2	Functionalization of MCF	189
4.3.2.3	Synthesis and oxidation of hierarchical porous carbons	194
4.3.3	IMMOBILIZATION OF G6PDH ONTO NANOPOROUS SUPPORTS	195
4.3.4	BIOCHEMICAL CHARACTERIZATION	195
4.4	SECTION SUMMARY AND CONCLUSION	200
5	<u>ASSEMBLY OF AN ARTIFICIAL CELLULOSOME ON MAGNETIC INORGANIC PARTICLES</u>	207
5.1	INTRODUCTION	207
5.2	RESULTS AND DISCUSSION	209

5.2.1	CHARACTERIZATION OF SILICA (STÖBER) NANOPARTICLES AS A MODEL SYSTEM	209
5.2.2	ASSEMBLY OF THE CELLULOSOME ONTO SILICA NANOPARTICLES	216
5.2.2.1	Covalent immobilization of cohesin-CBM onto silica particles by an active ester approach.....	216
5.2.2.2	Covalent immobilization of cohesin-CBM onto silica particles by click-chemistry	219
5.2.2.3	Recombination of cohesin and dockerin.....	223
5.2.3	CHARACTERIZATION OF PURE AND COATED MAGNETITE PARTICLES AS POSSIBLE SUPPORT MATERIAL FOR THE ASSEMBLY OF A CELLULOSOME.....	225
5.2.3.1	Characterization of Fe ₃ O ₄ and Fe ₃ O ₄ @SiO ₂ particles	225
5.2.3.2	Modification of the shell thickness	233
5.3	EXPERIMENTAL SECTION.....	239
5.3.1	CHARACTERIZATION TECHNIQUES – INSTRUMENTAL DETAILS.....	239
5.3.2	SYNTHESIS AND FUNCTIONALIZATION OF INORGANIC PARTICLES	240
5.3.3	BIOCONJUGATION AND ASSEMBLY OF CELLULOSOME COMPONENTS ONTO SILICA PARTICLES	244
5.4	SECTION SUMMARY AND CONCLUSION	246
6	<u>GENERAL CONCLUSION AND OUTLOOK</u>	<u>249</u>
7	<u>ZUSAMMENFASSUNG</u>	<u>253</u>
8	<u>BIBLIOGRAPHY</u>	<u>257</u>
9	<u>APPENDIX</u>	<u>271</u>
9.1	SUPPLEMENTARY INFORMATION FOR CHAPTER 4.....	271
9.1.1	CALCULATION OF ACTIVITY FOR G6PDH	271
9.1.2	CALCULATION OF THE FUNCTIONALIZATION DENSITY FOR MCF SAMPLES	271
9.1.3	CHANGE OF PH DURING GENERATION OF NADPH.....	271
9.1.4	BROMOCRESOL GREEN STAINING	272
9.1.5	MICHAELIS-MENTEN KINETICS	273
9.1.6	ARGON PHYSISORPTION ISOTHERMS.....	277
9.1.7	CELLULASE ACTIVITY ASSAY.....	278
9.2	CHEMICALS CATEGORIZED ACCORDING TO GHS	279
10	<u>PUBLICATIONS AND PRESENTATIONS</u>	<u>286</u>

0 LIST OF ABBREVIATIONS

3D	3-dimensional
6PG	6-Phosphogluconate
a	Lattice constant
ADH	Alcohol dehydrogenase
APTES	3-Aminopropyltriethoxysilane
Asp	Aspartate
BET	<i>Brunauer-Emmet-Teller</i>
BSA	Bovine serum albumin
BSE	Backscattered electron
CALB	<i>Candida antarctica</i> Lipase B
CBM	Cellulose binding module
cel	Cellulase
CKT	Carbon materials from KIT-5
CLCT	Cooperative liquid crystal templating
CLEA	Cross-linked enzyme aggregate
CMC	Critical micelle concentration
CMK	Carbon Mesostructured by <i>Korea Advanced Institute of Science and Technology</i>
cyt C	Cytochrome C
d ₁₀₀	Diffraction plane (100) spacing
D _{p, ads/des}	Pore diameter determined from adsorption or desorption branch
DAAO	D-amino acid oxidase
DLS	Dynamic light scattering
DLVO	Derjaguin, Landau, Verwey, Overbeek
DTA	Differential thermal analysis
DSC	Differential scanning calorimetry
EC	Enzyme commission
EDC	N-(3-Dimethylaminopropyl)-N-ethylcarbodiimide-hydrochloride

EISA	Evaporation-induced self-assembly
FA	Formaldehyde
FcMeOH	Ferrocene methanol
FDH	Formate dehydrogenase
FDU	<i>Fudan University</i>
FFR	Fast field reversal
G6P	Glucose-6-phosphate
G6PDH	Glucose-6-phosphate dehydrogenase
GatDH	Galactitol dehydrogenase
GOx	Glucose oxidase
h_{hex}	Wall thickness
HI	Hydrophobic interactions
His	Histidine
HRP	Horseradish peroxidase
IR	Infrared
IUPAC	<i>International Union of Pure and Applied Chemistry</i>
KIT	<i>Korea Advance Institute of Science and Technology</i>
LDH	Lactate dehydrogenase
LDV	Laser Doppler velocimetry
lys	Lysozyme
MALDI	Matrix-assisted laser desorption/ionisation
MCF	Mesostructured cellular siliceous foams
MCF-C	Mesocellular carbon foams
MCM	<i>Mobil composition of matter</i>
MS	Mass spectrometry
myo	Myoglobin
NAD ⁺ /NADH	Nicotinamide adenine dinucleotide
NADP ⁺ /NADPH	Nicotinamide adenine dinucleotide phosphate
NHS	N-hydroxysuccinimide
NMR	Nuclear magnetic resonance
OPH	Organophosphorus hydrolase
PAH	Polyaromatic hydrocarbons

PEG	Polyethylene glycol
PdI	Polydispersity index
pI	Isoelectric point
PSD	Pore size distribution
PMO	Periodic mesoporous organosilica
PXRD	Powder X-ray diffraction
S_{BET}	Surface area determined according to the BET theory
SAXS	Small-angle X-ray scattering
SBA	<i>University of California Santa Barbara</i>
SDA	Structure directing agent
SE	Secondary electron
SEM	Scanning electron microscopy
SFR	Slow field reversal
TA	Thermal analysis
TEM	Transmission electron microscopy
TEOS	Tetraethylorthosilicate
TG	Thermogravimetry
TLCT	True liquid crystal templating
TMB	Trimethylbenzene
TOF	Time of flight
TPD	Temperature programmed desorption
UV-Vis	Ultraviolet-visible
V_p	Pore volume
VSM	Vibrating sample magnetometry
XPS	X-ray photoelectron spectroscopy
XRD	X-ray diffraction

1 INTRODUCTION¹

In 2005 Linqiu Cao published a report based on the key question: “Immobilized enzymes: science or art?”.^[1] He answered this question clearly and emphasized that the use of immobilized enzymes can overcome many problems of enzymes in solution, like their instability at certain conditions and their difficult recovery. The immobilization of enzymes on supports that are perfectly tailored according to the particular enzyme could replace the need for extensive enzyme engineering. Those designed enzyme-hybrid materials cover a wide range of materials but the focus in the last years laid especially on nanoporous and nanostructured magnetic materials and their combination with enzymes as catalytic unit. Both inorganic-enzyme hybrid materials have their special charm and have addressed many of today’s important environmental needs like the generation of biofuels or the application of *Green Chemistry* in industry as will be discussed later on.

Since the first publication on the topic of protein immobilization in ordered mesoporous materials from Balkus and Diaz in 1996 many researchers tried to optimize the immobilization of proteins in these materials.^[2] In the following years the uptake of proteins like cytochrome C (cyt C) and lysozyme (lys) by mesoporous silicas was systematically investigated. These model proteins were ideally suited for studies concerning the uptake of proteins by mesoporous materials due to their small size and low costs. Optimization of these model systems was the first step to achieve efficient biocatalysis in nanoporous materials with large enzymes in the future. With increasing protein size it became more and more important to introduce porous materials with large pores and different pore connectivities.^[3] Today, materials with macropores and hierarchical pore systems are used in enzyme immobilization. Besides porosity, surface modification drew the attention of the researchers due to the effect of the surface properties on the adsorption capacity and performance of the respective biocatalyst. Each material has different functional groups and therefore varying forces apply during the uptake. Many of the disadvantages (leaching, low stabilization) of adsorptive

¹ Parts of this introduction have been published in a review titled “Designing Inorganic Porous Materials for Enzyme Adsorption and Applications in Biocatalysis” (D.I. Fried, F.J.Brieler and M. Fröba) and are reprinted with permission from Wiley-VCH.^[301]

immobilization can be overcome by adsorption in specifically designed porous materials and their high surface areas offer the possibility of high loadings. One of the recent trends in biocatalysis with porous materials was the combination of magnetic particles with nanoporous materials to sum up the unique properties of both materials.

However, magnetic materials especially iron oxide composite particles, either functionalized or as core-shell particles, have drawn the attention of many researchers even without the combination with porous materials.^[4-6] Medical applications of iron oxide particles are intensively investigated since their magnetism offers the possibility to direct them by an external magnetic field. Therefore applications in targeted drug-delivery, magnetic resonance tomography or as contrast agents are highly favorable. Narrow particle size distributions, high magnetization and a small size of the particles is mandatory for medical applications. In the last years biocatalysis and protein separation with magnetic iron-oxide particles has become more and more popular due to an easy recovery procedure by an applied external magnetic field. The low synthesis costs and the high environmental compatibility are additional benefits thinking of biocatalysis with iron oxide composites as supports for enzymes.

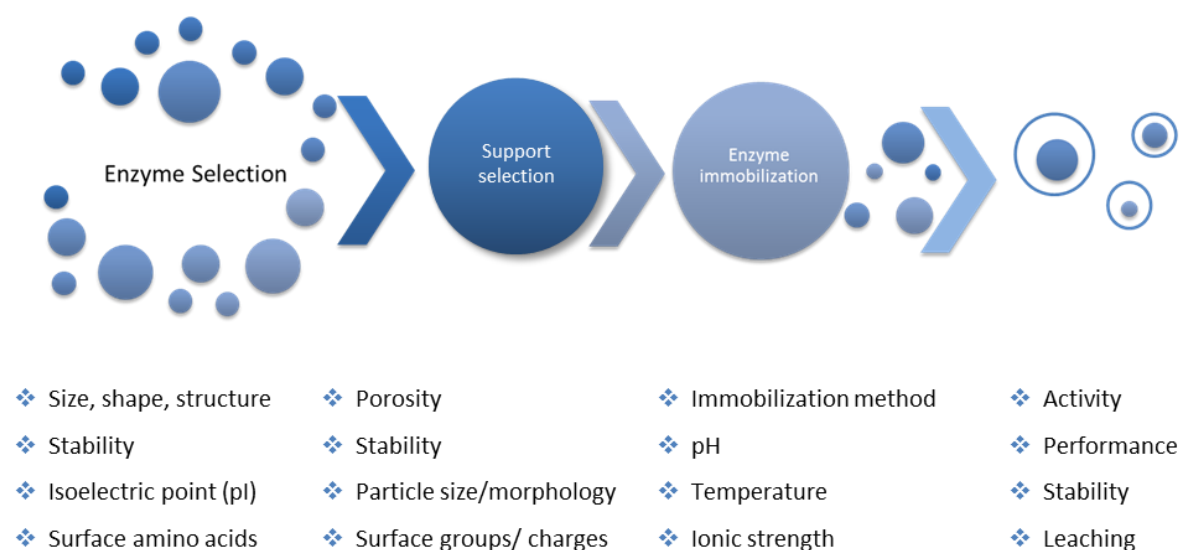


Figure 1.1: Pathway and major characteristics for the immobilization of proteins onto solid supports starting with the selection of enzyme and support, the immobilization procedure and ending with the performance of the biocatalyst.^[7]

In Figure 1.1 a general overview of the parameters that have an influence on the immobilization process is given. Systematical investigations of the adsorption process

are usually started with one specific material the researchers want to analyze and then an appropriate protein is chosen. However, in biocatalysis the materials are tailored, according to the parameters addressed in Figure 1.1, to ideally fit a support to the enzyme. Hence, systematical investigations are always the preliminary step prior to applications in biocatalysis. It has become more and more common for materials chemists not only to look into the material properties but to include the characteristics of the proteins. Crystal structures of many enzymes exist and a variety of information can be accessed from the structure and the amino acid sequence. Electrostatic and hydrophobic mappings of the protein surface are crucial to understand the interactions between support and enzyme. If no crystal structure can be found in the databases the isoelectric point (pI) can give a hint on the applying forces. Additionally, the accurate enzyme size can be extracted from the crystal structure. All in all the combination of highly functional enzymes and specifically designed materials including a deeper knowledge of the immobilization process is mandatory to achieve efficient biocatalysts.

1.1 ENZYMES

Enzymes are fascinating biocatalysts that are usually proteins (except ribozymes) which are built of a sequence of only 20 different naturally occurring amino acids. However, their high catalytic efficiency and substrate specificity is not mainly affected by the primary structure (amino acid sequence) but by their three dimensional (3D) structure. The tertiary structure of a protein develops during a complex folding process of the amino acid chain which creates a defined ordered protein structure. Protein folding is governed by intermolecular forces, mainly hydrophobic forces and hydrogen bonds that are generated between the protein backbone and the amino acid residues. This effect leads to mostly hydrophobic parts in the inner part of an enzyme and hydrophilic parts on the outer surface. Enzymes exhibit compact but still flexible structures that exhibit usually a “cleft” called the active site. This cleft consists of hydrophobic residues as well as hydrophilic sites which participate in the catalytic process. The binding of the substrate in the active site is a highly specific process that was once named key-lock principle because of the perfect match between active site and substrate.^[8] It has to be

mentioned that enzyme and substrate are flexible parts and thus conformational changes during the binding process sometimes take place in the protein structure. In some enzymatic reactions a cofactor, that can be a small organic molecule or a metal ion, is required. The cofactor is associated either tightly with the protein structure (prosthetic group) or binds only for the one catalytic step (coenzyme) and is released afterwards. But how does an enzyme catalyze a specific process?

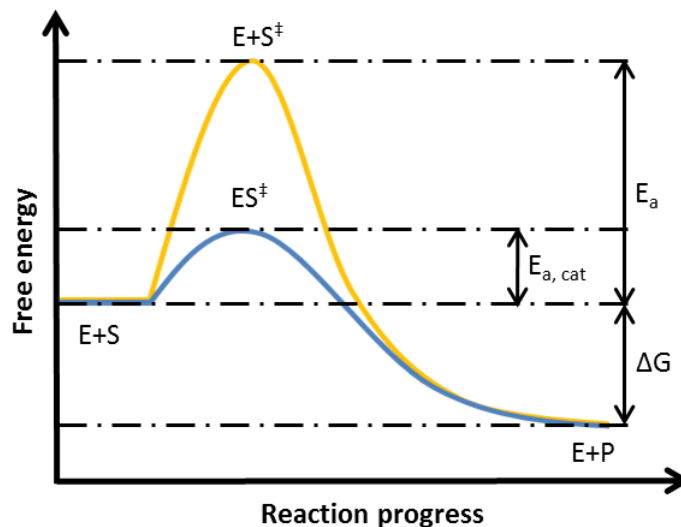


Figure 1.2: Simplified catalysis procedure depicting the change of the free energy during the conversion of a substrate (S) to a product (P) catalyzed by an enzyme (E) (blue curve) and noncatalyzed (yellow curve). The reduction of the activation energy (E_a) proceeds via an enzyme-substrate transition state (ES^\ddagger). However usually enzymatic catalysis involve more than one transition state.

Enzymes work like a chemical catalysts by reducing the activation energy. The amino acid residues in the active site stabilize the transition state of the reaction by formation of an enzyme-substrate complex and catalyze the conversion of substrate to product (Figure 1.2). Since enzymes can catalyze several reaction types the International Union of Biochemistry defined six different Enzyme Commission (EC) numbers (Table 1.1).^[9]

Table 1.1: EC classification of enzymes by their catalytic reactions.^[9]

Class	Catalytic reaction
1 Oxidoreductases	Redox reactions (oxidation/reduction)
2 Transferases	Transfer of organic groups
3 Hydrolases	Hydrolysis
4 Lyases	Addition/removal of organic groups; formation double bond
5 Isomerases	Isomerization
6 Ligases	Bond creation between 2 substrates under ATP hydrolysis

1.1.1 GLUCOSE-6-PHOSPHATE DEHYDROGENASE (G6PDH) FROM *L. MESENEROIDES*

G6PDH is an oxidoreductase (EC 1.1.1.49) that regulates in most organisms the pentose phosphate way catalyzing the catabolic reaction of glucose and generating NADPH. Besides the generation of important five-carbon sugars as building blocks for nucleotides, ATP and other biomolecules, the oxidative part of the pentose phosphate pathway is an important supplier of NADPH for the cell. NADPH is further used for reductive biosynthesis of *e.g.* cholesterol and fatty acids and most important for the protection of the cell against oxidative damage by reduction of glutathione. In humans the lack of G6PDH (G6PDH deficiency syndrome) caused by mutations on the X-chromosome results in oxidative damage of the red blood cells and finally to hemolysis. In research G6PDH is widely used as a cofactor regenerator in cascade reactions.^[10–12] In *Leuconostoc mesenteroides* there is one important difference to other G6PDHs since this enzyme can use either NADP⁺ or NAD⁺ for its catalytic reactions depending on the organism's demands. Since this enzyme lacks a glycolytic pathway generated NADPH is used for reductive biosynthesis whereas the formation of NADH is linked to fermentation processes.^[13] This different catalysis behavior is also reflected in the catalytic mechanism as will be explained later on.

In the following chapter at first, the 3D structure of G6PDH from *L. mesenteroides* is explained in order to provide a deeper insight into its catalytic behavior.^[14] G6PDH is a dimer built up from two nearly identical monomeric units (homodimer) that are rotated by 178.6°. The monomer consists of 485 amino acids and is 55 kDa large. One difference in the amino acid composition of the monomers leads to a slight conformational change between both monomers: The configuration of Pro 49 is *cis* in subunit a and *trans* in b but in contrast to all other amino acids where the *trans* conformation is preferred in proline due to its cyclization both are low-energy states. As can be seen from the crystal structure in Figure 1.3 the monomeric units (Figure 1.3b) are highly dense structures whereas the dimer is expanded leading to 11.2 nm as largest dimension. The monomers consist of one large mainly antiparallel β -sheet (9 strands), some isolated strands (6) and 17 α -helices connected by several loops. The interface between the enzymes is built up from parts of the antiparallel sheets and some loops to increase the contact area between both. The dimers stick together mainly by hydrophobic interactions (200) and

some salt bridges (20) between charged residues. Besides 610 water molecules three phosphate ions connected to histidine (His) residues are part of the substrate association process.

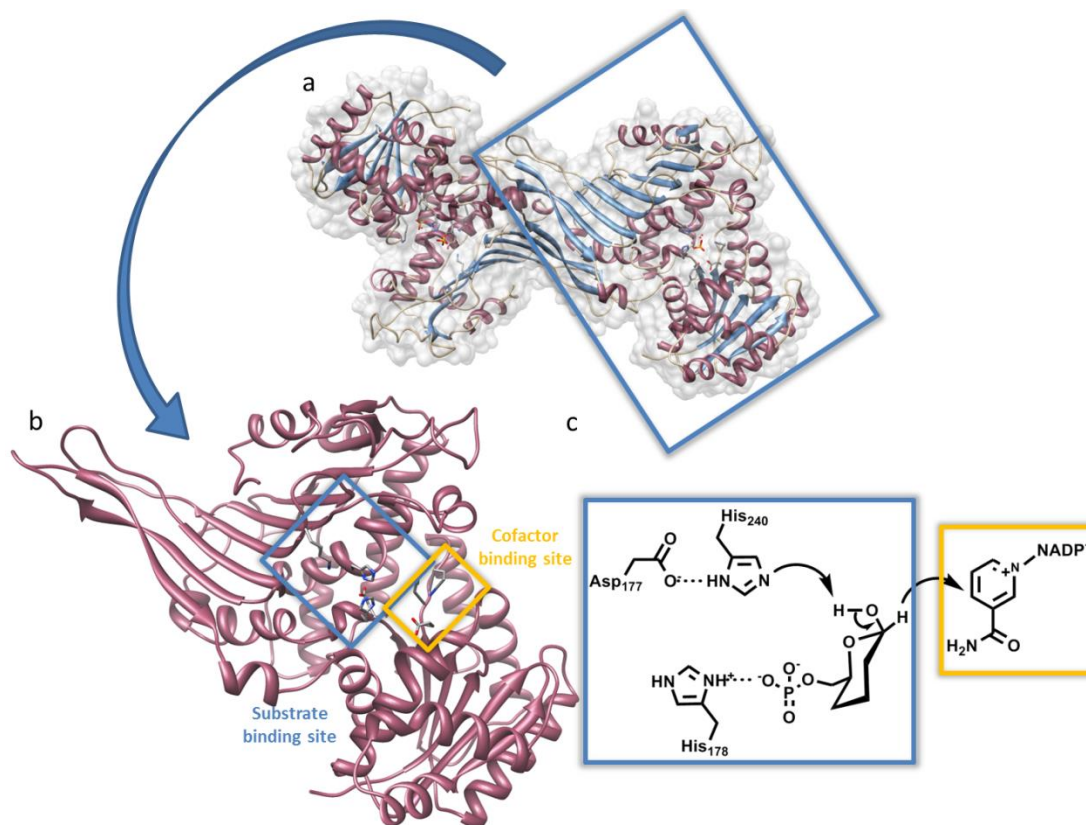
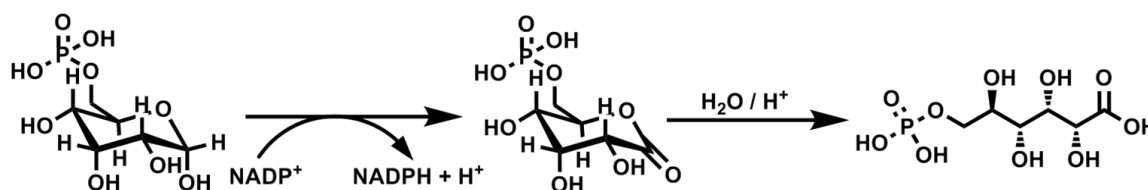


Figure 1.3: Crystal structure (PDB ID code: 1dpg) and mechanism of G6PDH.² The homodimer consists of a combination of helices (blackberry), single strands (blue) and two large antiparallel sheets that built up the contact area of the monomers. The surface is shown in light grey (a). Each monomer contains a substrate and a cofactor binding site whereas only one at a time is active (b). The ordered sequential catalytic mechanism (c) starts with the attachment of NADP^+ in the binding site, then the G6P is bound and positioned by His-178 while a hydride ion is bound by NADP^+ . Simultaneously, His-240 polarized by Asp-177 (catalytic dyad) abstracts a proton from the hydroxyl group and the product is released.

Looking now deeper into the enzymes catalysis the location of cofactor binding and active site are mandatory.^[15–17] The active site is located in a pocket near the domain boundary (Figure 1.3b, blue square) next to bound phosphate residues and contains a conserved 8-residue peptide that was supposed to be the key to the catalytic activity of G6PDH. The coenzyme binding site (Figure 1.3b yellow square) is built up from a

² All molecular graphics and analyses in this thesis were performed with the UCSF Chimera package. Chimera is developed by the Resource for Biocomputing, Visualization, and Informatics at the University of California, San Francisco (supported by NIGMS P41-GM103311).^[302]

dinucleotide binding fold found in many NADP^+ and NAD^+ dependent enzymes. This binding fold consist of a $\beta\alpha\beta\alpha\beta$ unit with an additional β strand to form a cleft were the cofactor can associate. Since most of the residues in the cleft are hydrophobic the interactions between the cofactor and the binding site is supposed to be built of hydrogen bonds. Although two nearly identical monomers exist only one is active assuming that the dimeric form is due to stabilization of the enzyme.^[14]



Scheme 1.1: Catalytic oxidation of glucose-6-phosphate to 6-phosphoglucono- δ -lactone by G6PDH and hydrolysis of the lactone to 6-phosphogluconate.

G6PDH catalyzes the oxidation of glucose-6-phosphate (G6P) to 6-phosphoglucono- δ -lactone by simultaneous reduction of NADP^+ to NADPH (Scheme 1.1). Afterwards the lactone is irreversibly hydrolyzed to 6-phosphogluconate (6PG). The mechanism of the catalytic process was though extensively investigated not solved completely but the major steps have been accessed.^[15,16] Some differences occur in the mechanism whether using NAD^+ or NADP^+ . While the reaction mechanism for NAD^+ follows a more random release and binding of substrate and cofactor, NADPH leads to an ordered sequential mechanism. Mutations of three major amino acids in the active sites shed light and led to the following proposed mechanism (Figure 1.3): The first step of this mechanism is the binding of NADP^+ then G6P is bound and positioned by positively charged His-178.^[15] Afterwards a hydride ion from C1 of the G6P is abstracted by NADP^+ and His-240 abstracts a proton from the OH group. Aspartate (Asp-177) is associated to the His-240 (catalytic dyad) but some confusions exist whether it stabilizes the His or polarizes it to enhance its basicity.^[16] In the end the product is released prior to NADPH .

1.1.2 CELLULOSOME OF *CLOSTRIDIUM THERMOCELLUM*

Since the energy demands are continuously increasing and will be even more in the future, the search of alternatives to fossil fuels has been accelerated in the last decade. Since cellulose is a highly abundant carbon source it is an obvious alternative. However, the structure of lignocellulose (Figure 1.4) is highly complex and rigid. Enzymatic hydrolysis is one solution to deconstruction of plant walls but there is no single enzyme that can fulfill this challenge. Anaerobic organisms have invented highly facile protein complexes for the degradation of crystalline cellulose called cellulosomes that self-organize on bacterial or fungal cells, attach to plant cell walls and deconstruct them.^[18-21]

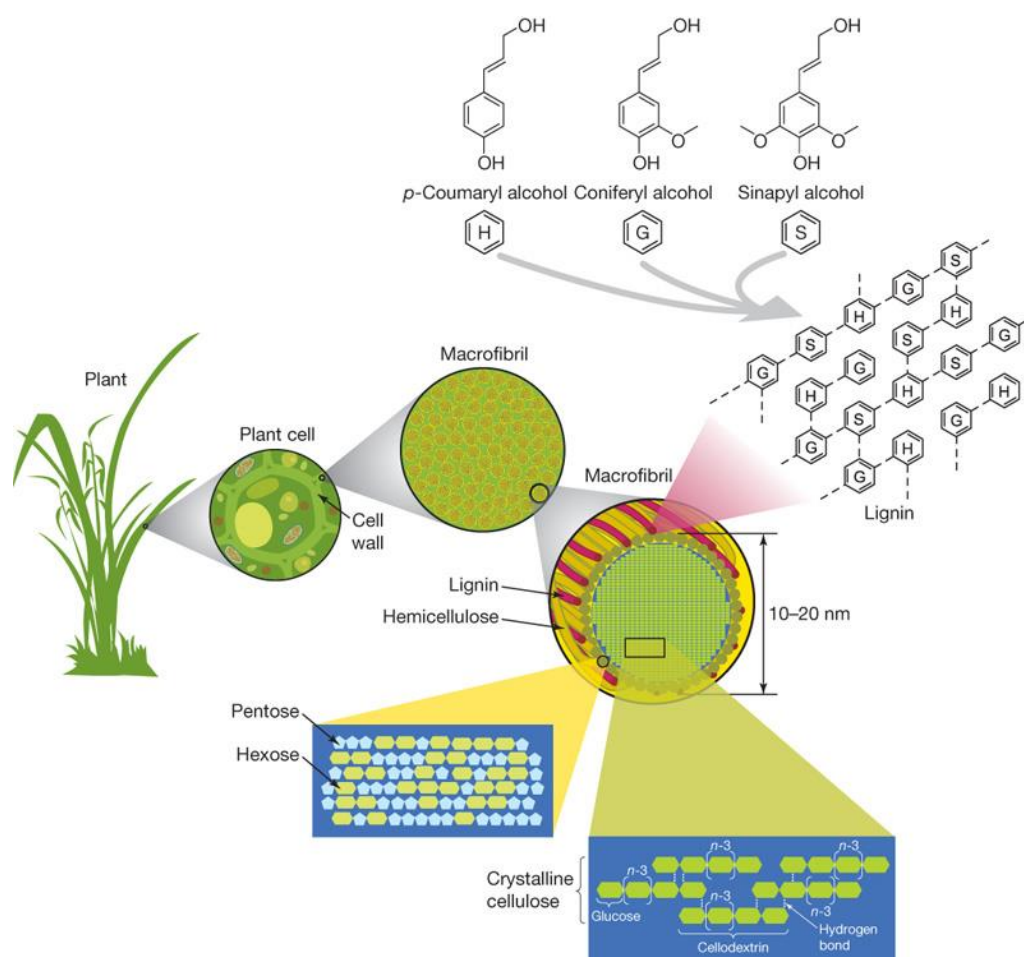


Figure 1.4: Lignocellulose is the major building block of plant cell walls. Macrofibrills composed of lignin, hemicellulose and cellulose are the structure element of plant cells. In contrast to hemicellulose and cellulose that are built from carbohydrates, the structural units of lignin are phenolic compounds. Hemicellulose is much more inhomogeneous compared to cellulose since it consists of several five- and six-membered carbohydrates while cellulose is a linear polymer of D-glucose. Reprinted with permission from Nature Publishing Group.^[22]

Despite its simple chemical composition the structure of crystalline cellulose is highly complex.^[18] D-glucose molecules are linked to each other in linear chains of up to 10000 molecules by 1,4-glycosidic bonds where each second glucose molecules is tilted by 180°. Multiple hydrogen bonds between the chains and in the chain itself lead to strongly bound ordered microfibrils that are insoluble in aqueous media. The insolubility makes a mediator between hydrolytic enzymes and cellulose mandatory. Cellulosomes are highly complex and versatile multienzyme machines that consist not only of catalytic active enzymes but also of protein molecules that take part in structuring of those complex molecules and mediating between cellulose and the enzymes.^[18,20,23] The so-called protein scaffold for the enzymes has several advantages: First, enzymes are placed in the right directions in very high concentrations; second, the proximity to the substrate minimizes diffusion losses and makes this process highly efficient. The correct ratio of all components is always maintained and the optimal spacing between the enzymatic units is established. Last, the affinity of the enzymatic subunits to the cellulose is enhanced.^[18] Since the fascination of cellulosomes is based on their structure and assembling process most of this chapter is dedicated to its assembly and architecture.

Since natural cellulosomes can consist of multiple of each components their size range from 2-6.5 MDa and the diameter can easily reach 100 nm.^[24] Today, smaller cellulosomes called “Designer Cellulosomes” are often built up from only a few of those components using them as a sort of “molecular Lego” (Figure 1.5).^[25] The positioning on the cellulose is performed by small proteins called cellulose-binding module (CBM). The CBM-IIIa of *Clostridium thermocellum* is shown in Figure 1.6a. The flat binding area (red circle) of the CBM consists of several aromatic residues that provide a hydrophobic surface for high cellulose affinity. Some charged amino acid residues are responsible for the position of binding by building up hydrogen bonds to the cellulose hydroxyl groups. Two anchor amino acid residues are associated to the substrate by H-bonds that are supposed to disrupt the cellulose structure by breaking H-bonds hence destabilizing the cellulose surface.^[26]

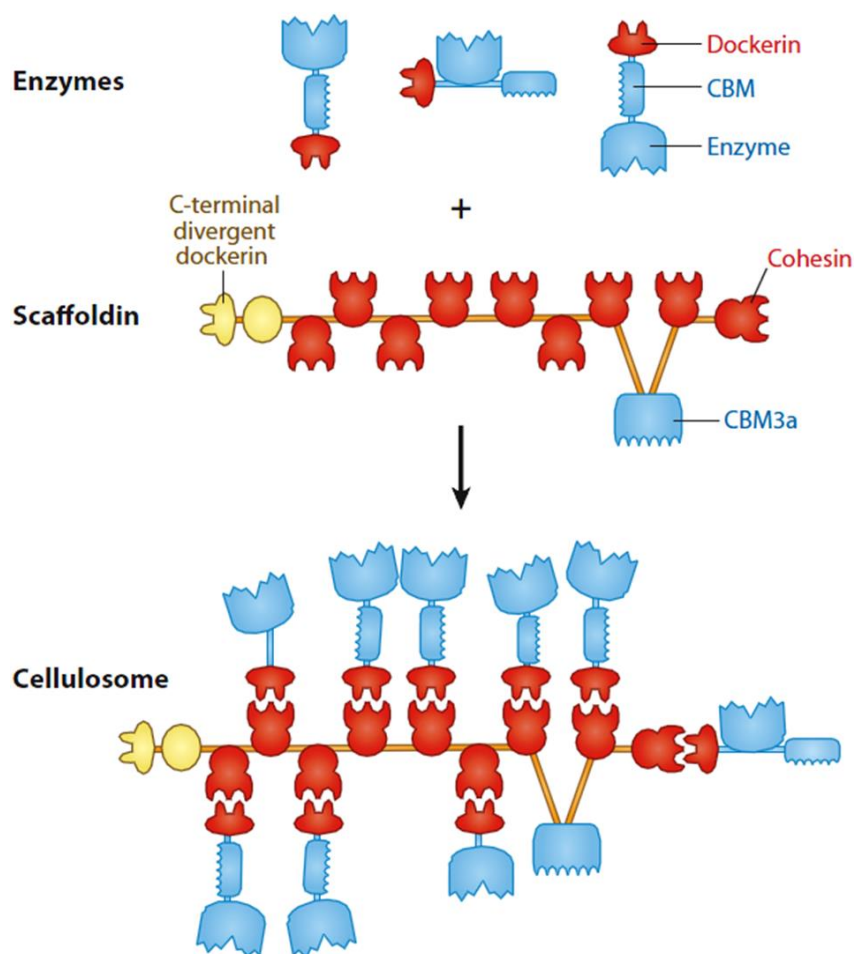


Figure 1.5: Schematic illustration the cellulosome assembly. The scaffoldin is built from cellulose-binding modules (CBM), cohesins and a dockerin that is responsible for the connection to a bacterial cell. The respective catalytic domains are connected to the scaffoldin by cohesin-dockerin interactions. Reprinted with permission.^[27]

The assembly of the enzymes to the CBM and thus the cellulose is mediated by two protein units: cohesin and dockerin often described as plug and socket (Figure 1.6b). The cohesin (socket) is directly linked to the CBM whereas the dockerin (socket) is bound to the enzymes. The binding of cohesin and dockerin is a highly selective process governed by very high binding affinities. The dissociation constant ($K_d = 10^{-11} \text{M}^{-1}$) is one of the highest reported affinity interactions between biomolecules.^[28] The rupture force was recently investigated by single-molecule-force spectroscopy and was found to be up to 120 pN. The dissociation was caused by dissociation of one of the Ca^{2+} ions that led to distortion of the dockerin structure.^[24] The strong affinity between both proteins is mainly due to multiple hydrophobic interactions (101) and hydrogen bonds (9). The structure of the cohesin-dockerin complex is shown in Figure 1.6b. Interestingly, cohesin

is able to bind to dockerin in two different conformations (dual-binding mode) resulting in more conformational space for the enzymatic subunits assembled on the scaffoldin. The Ca^{2+} ions in the dockerin unit stabilize the dockerin structure and lead to a correct folding. During the assembly process a conformational change in dockerin is observed whereas the cohesin unit is rigid.^[28]

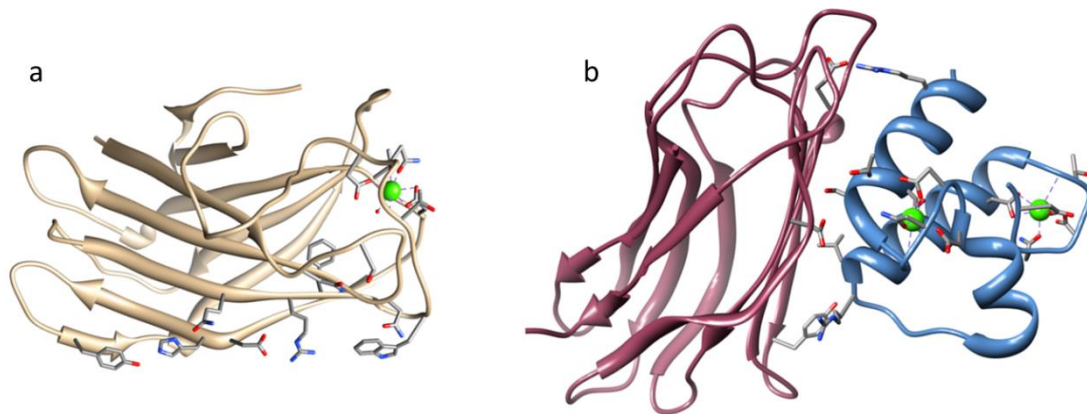


Figure 1.6: Building blocks of the *Clostridium thermocellum* cellulosome. Carbohydrate binding module (PDB ID code: 1nbc) with respective residues responsible for the interactions with crystalline cellulose (a). The CBM consists of two antiparallel β -sheets in which the interacting residues are located in the larger sheet. The Ca^{2+} ions are depicted in green with their coordination sphere pentagonal-bipyramidal in the CBM and octahedral in dockerin (b). The cohesin-dockerin assembly is shown in (b). The structure of the cohesin (blackberry) is mainly built up from an 9-stranded β -barrel with jelly-roll topology with an aromatic core. The dockerin (blue) consist of three helices with loops stabilized by the Ca^{2+} ions. The most important amino acids responsible for cohesin-dockerin interactions are depicted at the interface of cohesin and dockerin.

The last components of the cellulosome are the enzymatic subunits that can be a diversity of cellulolytic enzymes. They are assembled by the connected dockerin unit that binds to a corresponding cohesin.

1.2 IMMOBILIZATION OF ENZYMES ONTO SOLID SUPPORTS

Easy separation of catalyst and reaction mixture, modification of catalytic properties, catalyst reuse or continuous use and prevention of protein contamination are only some advantages of protein immobilization.^[29] Probably the most important benefit is the increased long-term stability of enzymes due to the rigidification of their 3D structure. The binding sites of the protein to the carrier fix the enzyme in a defined direction and the resulting decreased mobility of the protein increases the stability under extreme conditions (solvent, thermal, pH) and reduces unfolding.^[30–32] Multipoint immobilization is usually preferred especially with multimeric enzymes since subunit dissociation occurs as the first step of deactivation prior to unfolding.^[33] Many important proteins in industry are multimers (e.g. aldolases, dehydrogenases) and need special focus on their stabilization. If only a few of the subunits are immobilized the unbound subunits can dissociate and the enzyme loses its catalytic function. Strong electrostatic and covalent multipoint interactions between enzyme and support surface are preferred in relation to the stability of the 3D structure but can also result in enzyme distortion and “spreading”.^[34] In that case unfolding and hence deactivation of the protein occurs in order to maximize the contact points between protein and surface.

Porous carriers have additional benefits for protein immobilization. The concave curvature of the pore increases the contact surface and therefore the binding sites with globular protein structures compared to flat surfaces.^[35] Leaching is reduced in porous materials due to diffusion restrictions of the proteins out of the pore system. The spatial separation inside the pores prevents the proteins from deactivation by fouling, distortion by gas bubbles, autolysis and aggregation. But the immobilization of enzymes in porous materials can have difficulties as well. Deactivation can occur due to diffusion restrictions (pore-plugging) or shielding of the active site.^[30,32,36]

Three main approaches of enzyme immobilization exist: covalent binding, adsorption and encapsulation. Figure 1.7 depicts an overview of the different approaches and the corresponding interactions between carrier and enzyme. Encapsulation can diminish leaching by introduction of physical barriers. It is separated in three approaches: Microencapsulation and channel entrapment are performed postsynthetically the entrapment of enzymes in gels is performed in-situ during the material synthesis.

Another possibility is cross-linking of the proteins inside the pores. The cross-linked enzyme aggregates (CLEAs) are usually too large to leach out of the pore system. All encapsulation procedures are usually not performed under optimal enzymatic conditions and can therefore cause damage in the 3D structure. Additionally encapsulation might plug the pores and restrict the diffusion of products, substrates or cofactors during enzymatic catalysis.^[37]

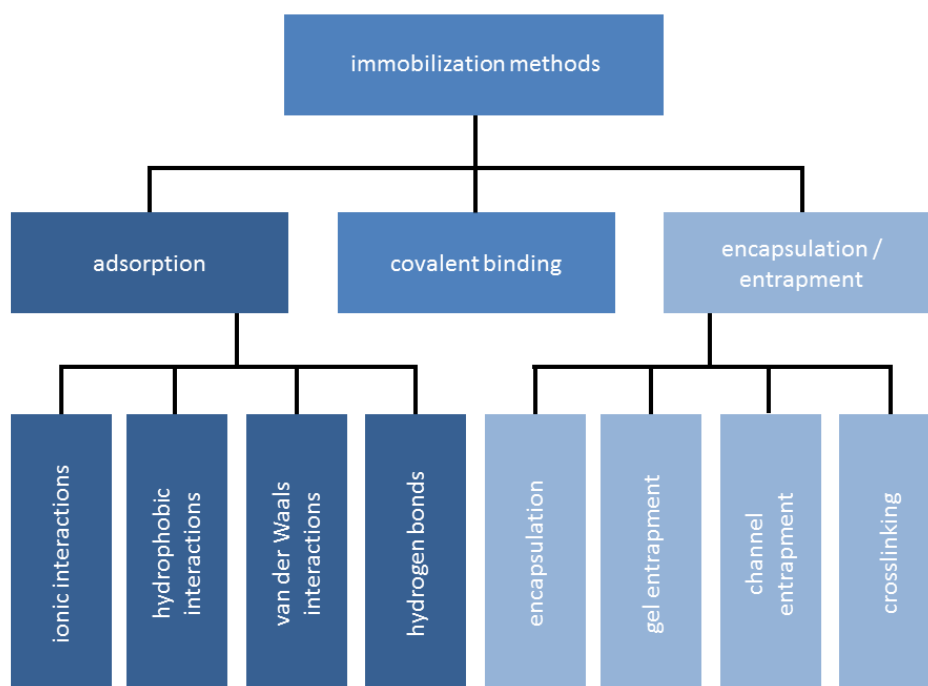


Figure 1.7: Methods and respective interactions for the immobilization of enzymes onto solid supports with covalent binding, adsorption and encapsulation/entrapment as main techniques. Figure reprinted with permission from Wiley-VCH.^[7]

The covalent attachment of proteins results in strong bonds ($200\text{--}400\text{ kJmol}^{-1}$) between protein and support and therefore stabilizes them against harsh conditions by rigidification. Depending on the type of covalent immobilization this method can be site-directed.^[31,32] Chemical or genetic modifications of proteins can be used to introduce singular functional groups for covalent site-specific immobilization.^[38] This allows on one hand control of the protein orientation and therefore of the orientation of the active site but on the other hand single-point immobilization does not significantly stabilize the protein. Multipoint covalent immobilization is known to stabilize enzymes but is usually not site-directed. All these parameters make covalent binding a key method for the

design of biocatalysts for industrial applications since stabilization of enzymes is mandatory for applications in reactors. Especially non-porous materials benefit of covalent binding since pores and high surface area that can prevent leaching are lacking. However, covalent immobilization includes several steps (activation of the support, covalent binding, blocking of reactive groups) which makes this technique expensive and time-consuming. Furthermore, harsh conditions and chemical modification of the protein due to covalent binding reduce the activity of enzymes after the covalent immobilization.^[31,32,37]

These disadvantages can be compensated using simple adsorption which is a cost-efficient, simple and fast route to immobilize enzymes on different carriers. It is performed by bringing carrier and protein in contact with each other and is a reversible process. Reversibility of the immobilization opens up the possibility to remove inactive enzymes and reuse costly carriers. The change of pH and salt concentrations strongly affect the electrostatic protein-support interactions and can lead to desorption of the protein.^[3,31] Adsorption is usually an effect of simple van der Waals forces. However, electrostatic interactions and hydrophobic forces as well as hydrogen bonding are usually included in the term of enzyme adsorption. This is not only caused by the fact that these forces only attach and not covalently bind the enzymes to the support but also due to the combination of various forces in the immobilization process. Owing to the diversity of functional groups in proteins, caused by the presence of various amino acids and carbohydrates, the differentiation of the forces is very difficult and the binding is not site-specific.

Van der Waals forces are present in every system but too weak to sufficiently immobilize an enzyme. The resulting biocatalysts are prone to leaching and the effect of stabilization is low. Hydrophobic interactions of polymers with hydrophobic surfaces result from entropic effects during the physical attachment process between the protein and the support. The entropic effect arises from the release of water molecules from the protein and the support surface. Hydrogen bonding can be performed with polar amino acids and predominantly carbohydrates that are naturally attached to the enzyme surface. Ionic interactions occur between charged amino acid residues and oppositely charged functional groups on the support. The electrostatic interaction between the proteins itself has to be taken into account. Ionic forces ($< 50 \text{ kJmol}^{-1}$) are the strongest

of these non-covalent interactions followed by hydrophobic interactions ($< 40 \text{ kJmol}^{-1}$), hydrogen bonds (ca. 20 kJmol^{-1}) and van der Waals forces ($< 5 \text{ kJmol}^{-1}$). Since many functional groups interact in this system, adsorption links the protein not only on one point to the support but on several points stabilizing the protein.

1.3 ENZYME-INORGANIC HYBRID MATERIALS

1.3.1 INORGANIC POROUS MATERIALS FOR ENZYME IMMOBILIZATION

1.3.1.1 Synthesis and functionalization of porous materials

Today the synthesis of inorganic porous materials is mainly based on template-assisted routes, namely exo- (hard-) and endo- (soft-) templating (Figure 1.8).

Table 1.2: Characteristics of porous materials used for protein immobilization.

Material	Structure	Pore geometry	Pore size / nm	$S_{\text{BET}} / \text{m}^2\text{g}^{-1}$	Template	Precursor
Mesoporous silicas ^[39]						
MCM-41 ^[40]	p6mm	2D channels	2-4	800-1000	Alkylammonium salts	TEOS, TMOS
MCM-48 ^[41]	la3d	3D channels	2-4	1000-1200	Alkylammonium salts	TEOS, TMOS
SBA-15 ^[42]	p6mm	2D channels	6-12	600-900	Block-copolymer (P123) ^[a]	TEOS, TMOS
SBA-16 ^[43]	Immm	3D spherical	5-8, 3-4	700-1000	Block-copolymer (F127) ^[b]	TEOS, TMOS
KIT-6 ^[44]	la3d	3D channels	6-12	500-1000	Block-copolymer (P123) ^[a] , butanol	TEOS, TMOS
FDU-1 ^[45]	Fm3m	3D spherical	9-15 4-9	ca. 700	Block-copolymer (B50-6600) ^[c] , TMB	TEOS, TMOS
FDU-12 ^[46]	Fm3m	3D spherical	20-24 5-12	300-700	Block-copolymer (F127) ^[b]	TEOS, TMOS
MCF ^[43]	Foam	3D ink-bottle	20-40 9-20	400-1000	Block-copolymer (P123) ^[a] , TMB	TEOS, TMOS
PMOs ^[47]	See Silica	2D, 3D	2-50	500-1000	Ionic and nonionic SDAs	Bisilylated precursors
Mesoporous carbons ^[48]						
CMK-3 ^[49]	Hexagonal		3-5	800-1500	SBA-15	Sucrose
CKT ^[50]	Cubic		4-6	450-1350	KIT-5	Sucrose
FDU-15 ^[51]	p6mm	2D channels	4	450-1050	Block-copolymer (F127) ^[b]	Phenol/FA
MCF-C ^[52]	Foam	3D ink-bottle	27, 11	650	MCF	Phenol/FA, Sucrose
Macroporous silicas ^[53]						
Macroporous silicas ^[53]	Cubic or hexagonal	3D spherical	0.1-5 μm	-	Spheres (PMMA, PS)	TEOS, TMOS
Macroporous carbons ^[53]	Cubic or hexagonal	3D spherical	0.1-5 μm	-	Spheres (PMMA, PS, silica)	Phenol/FA, Sucrose
S_{BET} = BET surface area; [a] P123: PEO ₂₀ PPO ₇₀ PEO ₂₀ [b] F127: PEO ₁₀₆ PPO ₇₀ PEO ₁₀₆ [c] PEO ₃₉ PBO ₄₇ PEO ₃₉						

Depending on the templates the pore size can range between molecular and macroscopic levels.^[54] The general process of both routes is discussed in this chapter, whilst the details for each group of materials are shown in Table 1.2.

Soft-templating

In the endo- or so-called soft-templating approach (Figure 1.9) a template that can be either a molecular, a supramolecular (e.g. micelle) or a macroscopic template (e.g. polymer spheres) is included during the formation of the solid.^[54] After the removal of the template by liquid extraction or calcination (thermal decomposition) the pore system of the material is created.

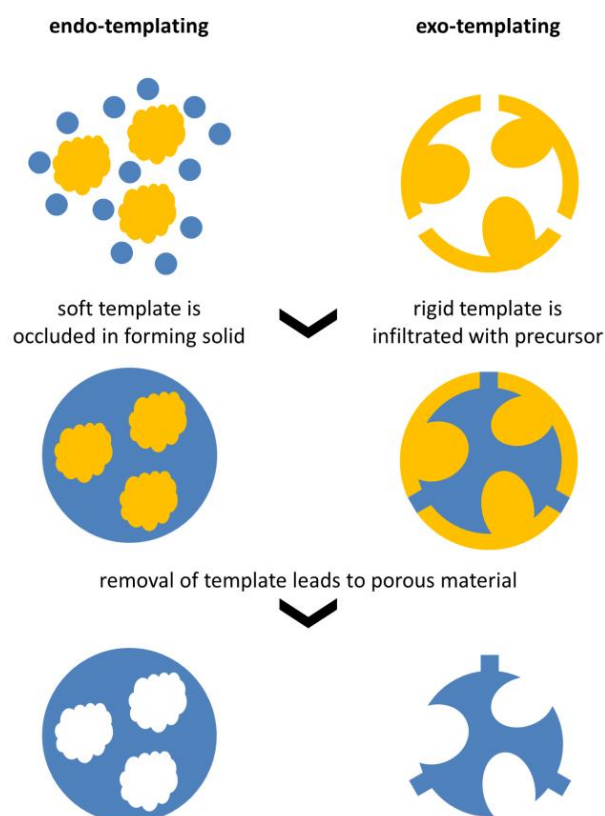


Figure 1.8: Schematic description of endo- and exo-templating approach for the preparation of porous solids made of a template (orange) and a precursor (blue). During the endo-templating approach a porous structure develops from a soft template whereas the hard-templating approach utilizes an already porous matrix that is replicated. Reproduced from^[54].

Most of the mesoporous silica materials are prepared by soft-templating with ordered micelle aggregates that assemble to liquid crystals.^[39,47] Two different liquid crystal templating mechanisms exist (Figure 1.9): True liquid crystal templating (TLCT) occurs when the concentration of the structure directing agent (SDA) exceeds the critical micelle concentration (CMC). Thus a liquid crystal is obtained at given conditions prior to the addition of the inorganic precursor.^[55] In contrast the formation of micelles is induced at lower SDA concentrations in the cooperative-liquid crystal templating (CLCT) mechanism. The micelle formation is initiated here by the addition of the precursor and a liquid crystal template is formed.^[56]

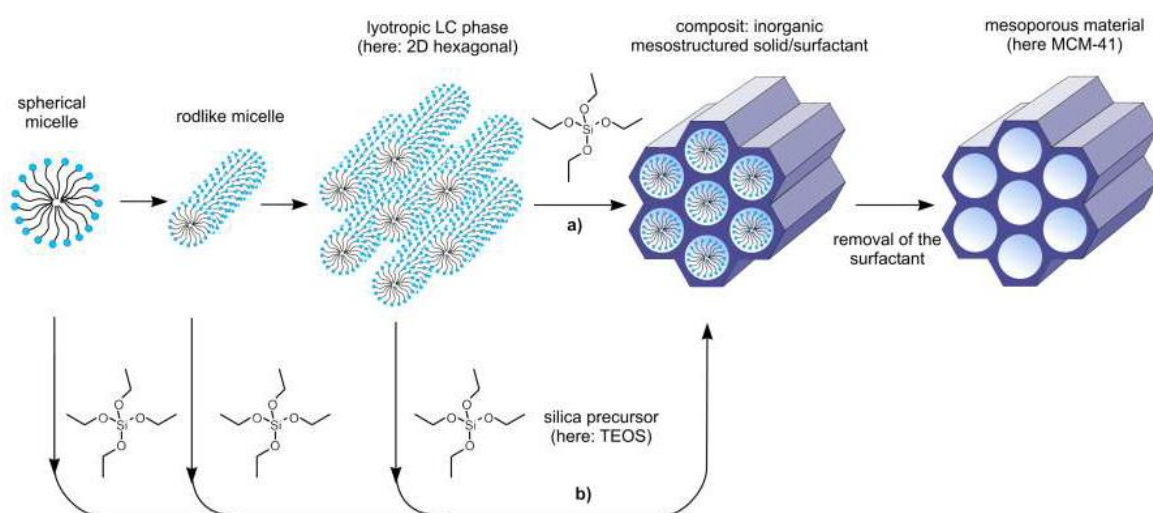


Figure 1.9: Soft-templating mechanisms for the synthesis of mesoporous silica (here: MCM-41). In the true-liquid crystal templating route (a) a lyotropic crystal phase is developed prior to the addition of an inorganic precursor (here: TEOS) whereas for surfactant concentrations lower than the CMC a cooperative assembly (b) of the inorganic precursor together with the surfactant is observed. The surfactant is removed from the composite material by extraction of calcination. With permission from Wiley-VCH.^[47]

The first mesoporous silicas (M41S series) were reported in 1992 by Mobil Oil Company using cationic surfactants that assembled to different micelle structures which served as supramolecular templates for the different mesoporous materials.^[40] Owing to the small pore sizes (about 4 nm) different structure-directing agents (SDAs) were introduced into the synthesis procedures in the following years. With non-ionic surfactants (e.g. block-copolymers) and pore swelling agents (e.g. mesitylene (TMB)) it is now possible to synthesize mesoporous materials with pore sizes up to 50 nm. Depending on the type and concentration of the SDA as well as the reaction conditions it

exist a variety of micelle structures and hence types of mesoporous materials (Figure 1.12). The materials used for protein immobilization and their important characteristics are summarized in Table 1.2.

Although this synthesis approach was first reported for mesoporous silica the synthesis of PMOs and porous carbons follow similar mechanisms.^[39,47,48,57–59] The difference in the synthesis of mesoporous carbons is based on the induction mechanism for the micelle formation. In the so-called evaporation-induced self-assembly (EISA) process the concentration of the SDA is lower than the CMC but during the slow evaporation of the solvent (water, EtOH) the CMC is reached and a liquid crystal is formed.^[60]

Mesostructured siliceous cellular foam

MCFs are synthesized via microemulsion templating from a stable emulsion of water, oil (TMB) and surfactant (P123).^[43,61–63] In an aging process the spherical micelles aggregate together with TEOS (droplet-packing effect) and after hydrothermal treatment and calcination a highly porous (up to 85% porosity) silica is obtained. The 3D porous network consists of spherical pores, templated by the micelles, and smaller connecting windows that arise from the contact area between the micelles.

Since the synthesis conditions are equivalent to those from hexagonal SBA-15, except the use of TMB, special focus was laid on the investigation of the formation mechanism and the corresponding changes in the pore network. Lettow et al. observed that at an oil-to-polymer ratio of 0.2-0.3 resulted in a sudden increase in the pore size proven by nitrogen physisorption but no change in the mesoscopic order was evident by SAXS. A further increase of the oil-to-polymer ratio led to a phase transformation from hexagonal to monodisperse sphere model. The authors assumed that a transformation phase was formed between an oil-to-polymer ration of 0.2-0.3 that consisted of a noded rod structure (Figure 1.10).^[62]

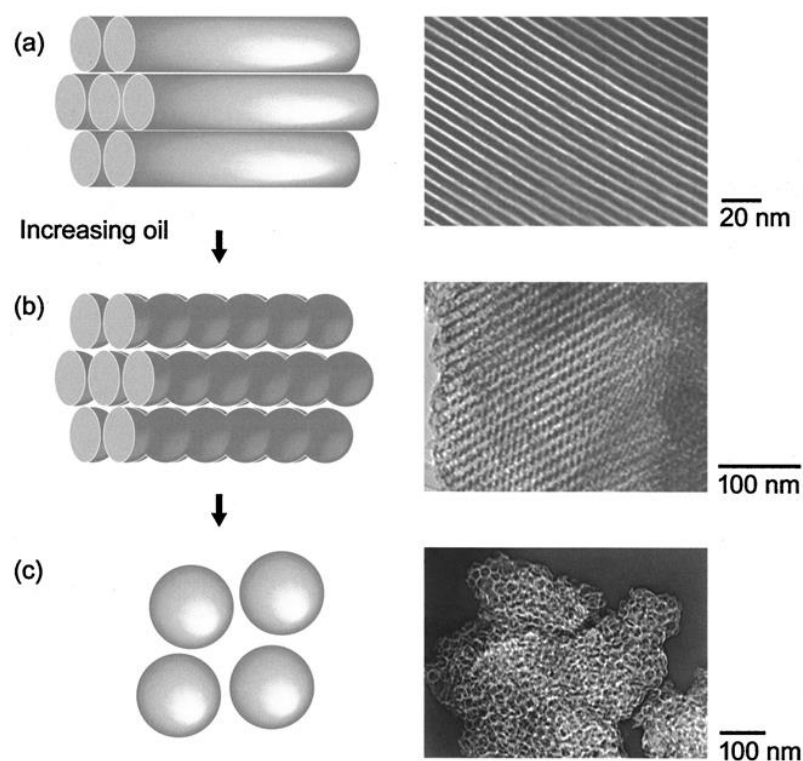


Figure 1.10: Schematic illustration and TEM images of the morphological transition of SBA-15 to MCF . By simply adding TMB to the reaction mixture of SBA-15 a microemulsion can be prepared and MCF is obtained. The linear pore channels of SBA-15 (a) undergo with the addition of TMB (oil) a structural change and transform into noded linear channels (b) that are further transformed under addition of TMB to the spherical pores (c) of MCF. The oil-to-polymer ratio is 0.0 (a), 0.2 (b) and 0.5 (c). Reproduced with permission from ACS.^[62]

The reason for the interesting transition of a pure hexagonal material to a material with spherical pores only triggered by TMB addition was explained with the packing parameter P (Equation 1).^[62]

$$P = \frac{a_T}{a_H} \quad (1)$$

a_T = cross-sectional area of hydrophobic group

a_H = cross-sectional area of hydrophilic head group

Hydration and entropic effects play a major role using amphiphilic block-copolymers that are built from hydrophilic PEO segments and hydrophobic PPO segments which are less soluble. In water those surfactants are completely hydrated most likely in their PEO

segment where each hydrogen bond is assembled by three water molecules and each PEO segment additionally by 19-25 water molecules whereas the PPO segments are less hydrated.^[64,65] Their strong hydration is accompanied by a large cross-sectional area; hence a small packing parameter and a high curvature, and thus spherical micelles are formed (Figure 1.11). Under SBA-15 synthesis conditions in highly acidic solution with chloride ions present, the curvature is reduced due to three major facts. First, chloride ions are known to decrease the solubility of the PEO segments, ethanol from the hydrolysis of TEOS induces a swelling of PEO and PPO segments and the highly acidic medium reduces the hydration of the PEO segment. After addition of oil a swelling of the less polar component is observed but little amount of TMB does not change the structure. After the PPO segment is completely filled with TMB further addition of TMB results in the formation of an oil core and a transformation to spherical micelles. Although the curvature is not significantly changed a decrease of surface-to-volume ratio and hence a reduction of the amount of polymer needed per oil triggers the transformation in a micelle.

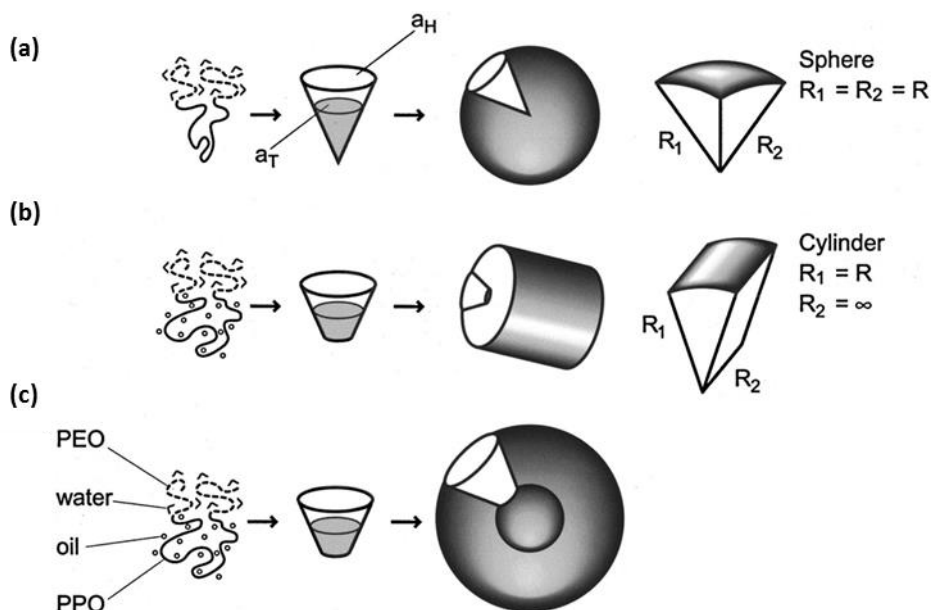


Figure 1.11: The solvation of the surfactant has a major effect on the shape of the micelles since it induces the transformation of channel-like to spherical micelles. In aqueous solution without any additives the micelles of SBA-15 are spherical (a). The presence of HCl dehydrates the polymer and ethanol as well as the oil solvates the hydrophobic part. Both aspects lead to cylindrical micelles with less curvature (b). Further addition of oil induces the formation of an oil core and thus a spherical micelle to reduce the amount of polymer per oil. Reproduced with permission from ACS.^[62]

Another major aspect during the synthesis of MCF is the enlargement of the window size that is of major importance thinking of the immobilization of large enzymes. Usually, ammonium fluoride is used for the enlargement of the windows.^[63] NH_4F is known as a catalyst and a mineralizer used in the sol-gel process.^[66] In small amounts it does not contribute to structural changes but it can enhance the condensation process of the silica species. It is known that it promotes the reversible hydrolysis and condensation reaction of the silica. Thus the dissolution of the silica wall in MCFs is favored at the windows and hence the erosion occurs primarily at the windows.

Hard-templating

The hard-templating approach starts with an exotemplate (e.g. mesoporous silicas, polymer spheres) whose pores are filled with a precursor solution.^[48,53,57,59] Depending on the materials, carbonization for carbons or calcination for oxidic materials is necessary prior to the removal of the exotemplate by thermal decomposition or extraction. The obtained negative replica of the template can either be mesoporous or in the case of microsphere templating methods macroporous. Various mesoporous carbons can be synthesized with mesoporous silica as a hard-template. Templating with highly ordered polymer or silica spheres (opals) results in 3D macroporous structures that are called inverse opals.^[53] The combination of sphere- and soft-templating is a well-established procedure to get hierarchical meso-/macroporous materials. In this approach additionally to the macroporous structure created by sphere-templating, mesopores are introduced in the walls of the opal structure by soft-templating.

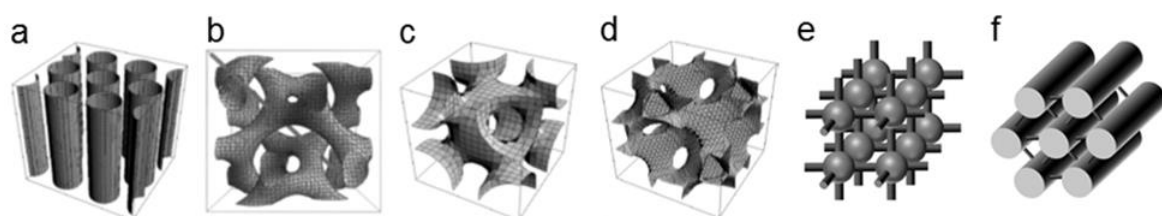


Figure 1.12: Structures of mesoporous materials that have been used for enzyme immobilization with channel pore geometry: $p6mm$ (a), $Ia3d$ (b), with cage-like pore geometry: $Im3m$ (c), $Fm3m$ (d) and carbon nanocage (e), CMK-3 replicated from a (f). a-d reproduced with permission from ^[67].

Functionalization

In contrast to the similarities in the formation mechanisms of the discussed porous materials the functionalization of their surfaces is quite different. Whereas carbons have an inert surface, silicas exhibit reactive silanol groups on their surface. Generally carbons need activation performed by oxidative treatment (nitric acid, ammonium peroxodisulfate). This approach is not very selective and various oxygen-containing functional groups are created (Figure 1.13c). Postsynthetic modification (grafting) is the most widely used functionalization method for oxidic materials like silica (Figure 1.13a).^[47] In this approach the hydroxyl groups on the surface of the material are condensed with organotrialkoxy- or organotrichlorosilanes. The modification reduces the porosity of the material but the order of the structure is maintained. Sometimes this approach leads to the enrichment of the silanes in the pore entrances and therefore to pore blocking and thus restrictions in diffusion.

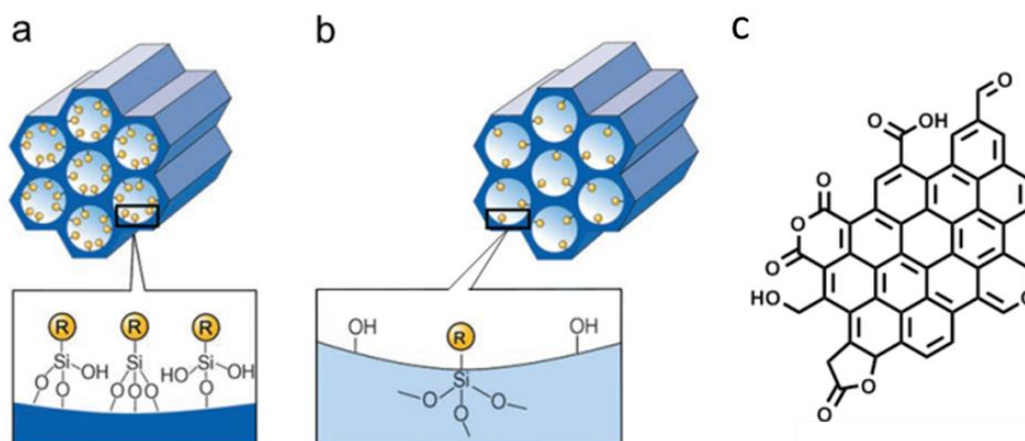


Figure 1.13: Functionalization approaches for porous materials: Postsynthetic grafting leads to organic residues extended into the pore system (a) similar to the co-condensation approach (b). Oxidation of porous carbons leads to various oxygen containing functional groups on the surface of the material (c). Reproduced with permission from ^[47].

A second approach for the functionalization of silicas is the co-condensation (Figure 1.13b) of organosilanes with the silica precursor. The organic groups are hence more homogeneously distributed over the silica surface and the theoretical functionalization density can be higher than with the postsynthetic approach. Major drawbacks are the different condensation rate of the precursors as well as the possible influence of the

functional groups on the formation of micelles that lead to lower order of the porous silica. Due to the thermal instability of the organic molecules, the removal of the template is usually done by extraction.^[47] Since a variety of silanes exist these approaches offer the possibility to synthesize materials with various functional groups.

Periodic mesoporous organosilica

A special case of functionalized mesoporous silicas are periodic mesoporous organosilicas (PMOs, Figure 1.13) that are synthesized with organic-bridged silica precursors $((R'O)_3Si-R-Si(OR')_3)$.^[47] The organic functionalities of PMOs are located within the mesopore walls and do not necessarily extend in the middle of the pore compared to grafted or co-condensed mesoporous silicas. Since the organic functionality is incorporated in the middle of the precursor homogeneous distribution and dense packing of the organic groups in the pore walls are observed (Figure 1.14).

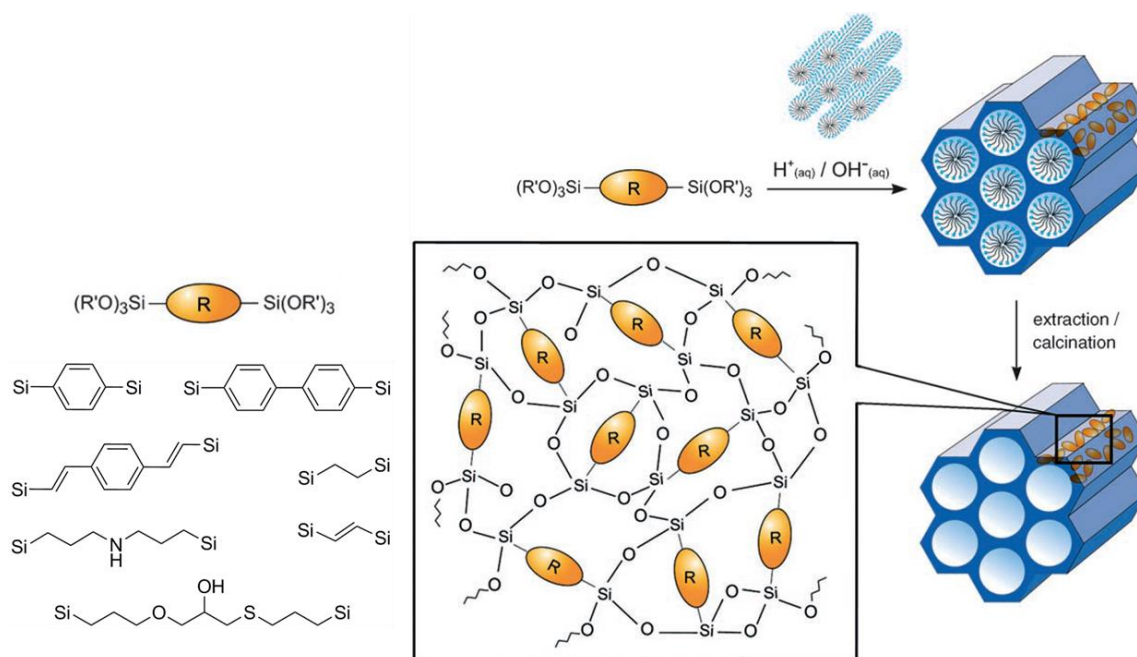


Figure 1.14: Schematic description of the synthesis of PMOs without crystal-like arrangement in the pore walls and precursors of PMOs used for enzyme immobilization. The synthesis route for PMOs is similar to pure silicas except of the bridged precursor. The precursor assembles and condenses around micelles that are extracted due to the thermal instability of the organic-inorganic network to obtain the porous material in the last step. The long alkyl-chain precursor (bottom left) was co-condensed with TEOS and is hence not a “real” PMO. Adapted with permission from Wiley-VCH.^[47]

Additionally to the periodicity of the pore network some PMOs have a crystal-like arrangement of the organic bridges in the walls.^[68] Simple PMO precursors that are mainly rigid and symmetric are suitable for the synthesis of PMOs with crystal-like walls since the rotation in these precursors is hindered. The organic bridge leads to a distinct hydrophobicity of the PMOs.

The variety of organic functional groups in PMOs can be further increased with the application of a second precursor. Similar to the co-condensation approach it is necessary to take the condensation behavior of both precursors into account. The second precursor can be either a bridged bisilylated compound to yield “pure” PMOs or a terminal alkoxy silane. Postsynthetic grafting is another possibility for the functionalization of PMOs.

1.3.1.2 Immobilization of enzymes in porous silicas

Influence of the particle size and morphology on the adsorption of proteins

The effect of the morphology and the size of porous silica particles for the adsorption process of proteins are often ignored although these are important parameters in particular, if different types of silicas are compared. The morphology of a particle has a strong influence on the external surface area and hence on the length of the diffusion path. Particles with an irregular shape and a rough surface exhibit a higher external surface area than a smooth surface.^[69] Both size and morphology are key parameters for the rate of adsorption and the protein loading capacity of the materials (Figure 1.15). For example, pore blocking can be strongly reduced with materials with small particles since their pore channels are shorter and thus the diffusion into the pores proceeds over smaller distances. Additionally, a high external surface area and a small particle size allow proteins to access the particles from many different pore entrances thus leading to high and fast protein loading.

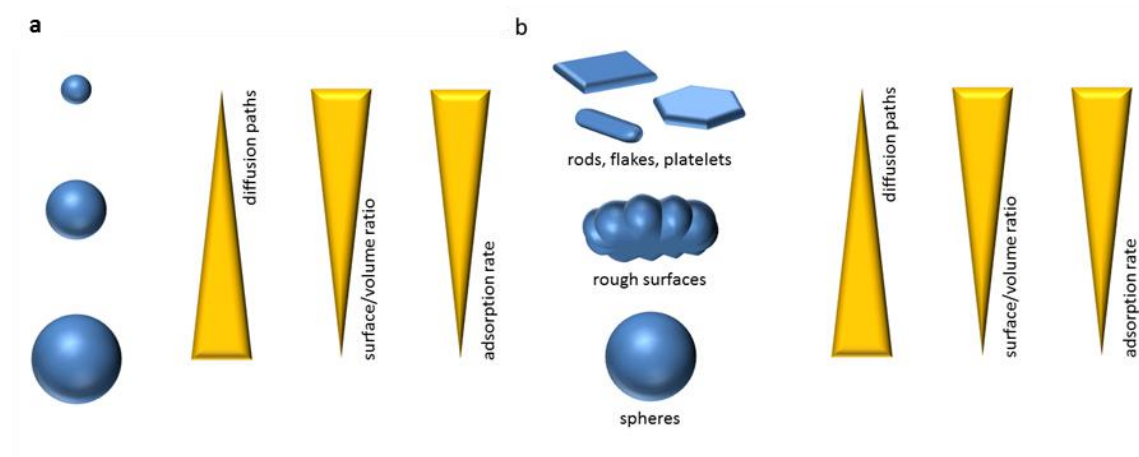


Figure 1.15: Influence of the particle size (a) and the morphology (b) on the adsorption of proteins. An increase in the particle size results in longer diffusion paths and hence a decrease in the adsorption rate whereas rough and thin particles decrease diffusion paths and enhance the adsorption. Figure reprinted with permission from Wiley-VCH.^[7]

In the last years there have been several systematic studies on the influence of the particle morphology on the adsorption properties (Figure 1.15b). Most of the researchers used lys as a model protein but the conditions of the immobilization varied.^[69–71] Therefore a direct comparison is difficult but the effects derived from the morphology are quite similar. Various morphologies of silicas have been analyzed by Liu et al.^[69] They reported that the highest and fastest uptake of protein was observed with a rugged hollow silica. Shan et al. compared sphere-like silica (1 μm) with flake-like silica for RNase adsorption.^[72] The adsorption in flake-like silica was very fast due to the easy diffusion caused by the small thickness of the flakes (200 nm). The same effect was observed for SBA-15 platelets in cyt C adsorption experiments. Additionally a very high adsorption capacity (35 $\mu\text{mol g}^{-1}$) was achieved.^[73] In 2009 the effect of the particle morphology on lipase activity was investigated.^[74] The researchers compared rod-like and vesicle-like silica. The rod-like material with channel pore geometry exhibited, as expected, a higher and faster uptake of protein. Interestingly, the stability, reusability and activity were increased for the vesicle-like silica with lamellar pores. The authors assigned this effect to the stabilizing convex curvature of the pores that increases the number of contacts with the protein and the larger pore size.

Influence of pore size and geometry on the adsorption of proteins

The efficiency of protein adsorption, selectivity and stability, the reduction of leaching and diffusion limitations are only a few parameters that are affected by the pore size and the pore geometry of the support. The investigation of the effect of the pore dimensions on these topics started very early with the first publication in the field of protein immobilization in mesoporous silica from Balkus and Diaz in 1996.^[2] They showed that only several proteins could access the pores of MCM-41 (4.0 nm). Cyt C, papain and trypsin were able to adsorb in the pore system due to their size being smaller than the pore size of MCM-41. Horseradish peroxidase (HRP, 4.6 nm) was too large and immobilized only on the external surface. This size exclusion effect was reproduced several times for different systems.^[75,76] Usually, mesoporous silicas with different pore diameters in combination with one protein are investigated. Several important facts were derived from these studies:

First, obviously the enzyme size has to be smaller compared to the pore size. Second, the loading is usually higher with larger pores.^[75,77-79] Third, the stabilization effect on the protein occurs only when the pore is not much larger than the protein itself.^[80,81] Additionally, leaching occurs easier if the enzyme is not tightly fitted into the pore. If the protein loading exceeds a limit, which depends on the protein, pore size and geometry, pore blocking and diffusion limitation occur. Up to now, the largest protein immobilized in mesoporous silicas is the photosystem II, which is 756 kDa and about 20 nm large. This work was done by T. Noji in SBA-15 with 15 nm and 23 nm pores.^[77] The highest protein loading (15 mg g⁻¹) was achieved in SBA-15 with 23 nm. The position of the protein in the particles was determined by confocal fluorescence microscopy where the homogeneously distributed fluorescence in SBA-15 with 23 nm pores indicated that the protein was able to diffuse inside whereas the 15 nm pores were too small. The protein loadings that can be obtained in mesoporous materials with smaller proteins can easily exceed 100 mg g⁻¹ and go up to 800 mg g⁻¹.^[77]

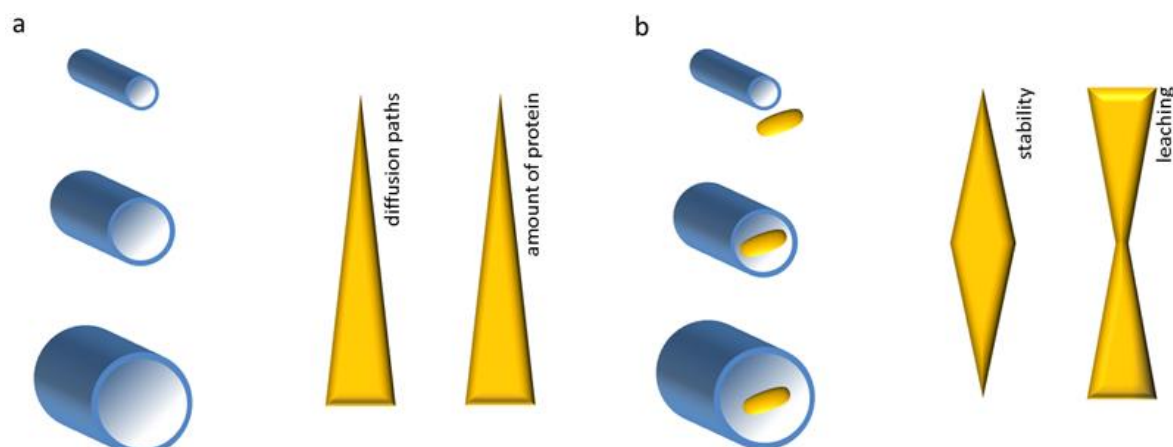


Figure 1.16: Influence of the pore size on the adsorption of proteins (a). Pore-size matching (b). Large pore diameter in general enhance the diffusion as well as the amount of protein that is adsorbed but if a certain diameter is exceeded leaching is observed. The stability is usually enhanced with enzymes fitted tightly to the pores. Figure reprinted with permission from Wiley-VCH.^[7]

The adsorption of proteins correlates not only with the pore size but also with the geometry of the pore system (Figure 1.17). The systematic investigation of the immobilization process started with MCM-41 in 1996, as mentioned above. Afterwards also MCM-48 and SBA-15 have been used for enzyme immobilization.^[81–83] Several cubic systems have been developed in the following years with different pore geometries and larger pore sizes. The benefits of cubic structures are on one hand their 3D connectivity on the other cage-like structures with smaller pore entrances diminish leaching. Occasionally, even the larger pores of SBA-, KIT- and FDU-type materials are too small for particular enzymes. Therefore less ordered materials like mesoporous cellular siliceous foams (MCF) have been utilized. Additionally, there is an upward trend to macroporous and hierarchical materials to achieve high protein loadings and less internal diffusion limitation.^[84–88] Most of the reports are systematical investigations with model proteins (e.g. BSA, lys) and do not contain any information on enzymatic activities.

Macroporous materials are often used if a good flow and diffusion through the pores is necessary.^[85,88] Guo et al. compared the proteolysis of mouse liver extract by trypsin immobilized on SBA-15 and macroporous silica.^[85] The extraction efficiency was higher with trypsin immobilized in the macroporous silica and the enrichment of the liver extract inside the pores enhanced the digestion speed compared to trypsin in solution. This study also revealed that high loadings can inhibit protein activity by enzyme

crowding and diffusion limitation. Diffusion can be further enhanced by introduction of bimodal porosity.^[84,86,87] Hierarchical meso-macroporous materials can accommodate enzymes in one pore and the diffusion of the substrate can be done in another pore.^[84,87] Sun et al. showed that a size-selective protein separation is possible by carefully tuning the entrance size to the macropores of a hierarchical silica monolith.^[86]

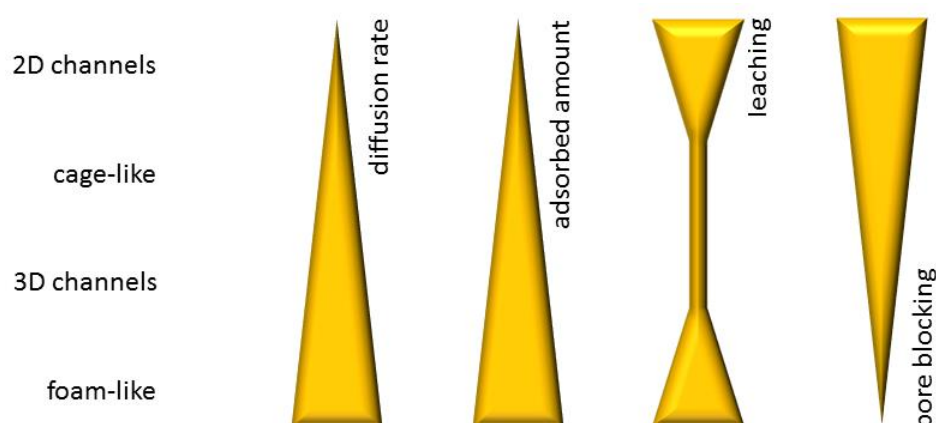


Figure 1.17: Influence of the pore geometry on the adsorption of proteins. The rate of enzyme diffusion into the pore system as well as the amount of adsorbed enzyme increases with increased connectivity of the pore network and with the pore size while pore blocking is reduced. Leaching however is reduced in 3D pore networks with smaller pores. Figure reprinted with permission from Wiley-VCH.^[7]

Sang et al. proposed and experimentally validated a geometrical pore filling model for mesoporous materials.^[89] They demonstrated that the immobilization of the globular model proteins lys, myoglobin (myo) and BSA at their isoelectric points (pIs) was correlated to the pore volume and size of SBA-15 and CMK-3. At the pI the net charge of the protein is zero and therefore less repulsion between the proteins and hence dense packing of proteins occurs. The quantification of densely packed proteins was performed by this group which was able to develop a model that specifies the proportionality of the pore volume to the amount of adsorbed protein.

The first report on large-mesopore cubic silica with Ia3d structure was published by Vinu et al.^[78] They reported the adsorption of lys near its pI on KIT-6 with different pore sizes. A Langmuir-type adsorption was observed and the highest adsorption capacity was achieved with KIT-6 with the largest pore size (12 nm). The maximum adsorption capacity for lys was $55 \mu\text{mol g}^{-1}$ which exceeds the uptake capacity for lys on hexagonal

materials. With this study it was proven that a 3D pore system can enhance the uptake due to less pore plugging and diffusion limitation. The adsorption in cage-like porous materials can improve the resistance against leaching due to the existence of small entrances to larger pores.^[60,90–98] Additionally, the inner diameter of spherical pores in cubic structures is usually larger compared to channel-like pore systems and is able to host large enzymes. The group of Lu used FDU-12-type materials with very large pores and entrances that were suitable for cellulase (cel) adsorption.^[90,91] The cel system usually contains a mixture of enzymes with different sizes and pIs. By tuning the entrance size the cel was able to enter the large pore. A systematic study on the adsorption of lipase B from *Candida Antarctica* (CALB) with a size of 3x4x5 nm was performed on a variety of materials. In this study it was clearly demonstrated how pore size and geometry affect leaching and uptake. The pores of MCM-41 were not large enough to host CALB whereas KIT-6, SBA-15, SBA-16 and FDU-12 adsorbed the enzyme. Channel-like pore systems (SBA-15, KIT-6) exhibited faster adsorption compared to FDU-12 and SBA-16 owing to less pore plugging in 3D systems. No diffusional restrictions occurred in channel-like pore systems with pore sizes twice as big as the protein size. The slow adsorption in FDU-12 and SBA-16 was caused by the small pore entrances where the enzyme needed to orient itself to access the pore. Due to the high connectivity in 3D systems (KIT-6) several exit barriers exist the protein needs to overcome and leaching is minimized compared to SBA-15. The larger pores of FDU-12 allowed faster leaching compared to SBA-16.^[67]

Recently, the immobilization of proteins in MCF was performed by several groups.^[82,85,92,93,95–97,99–105] MCFs have large spherical pores with smaller windows to host large enzymes or in some cases enzyme aggregates. The CLEAs are produced by enzyme cross-linking with glutardialdehyde after adsorption inside the large spherical pores.^[101] This approach diminishes leaching and leads to an enhanced stability of the densely packed enzymes.

Support and enzyme interactions during the adsorption of proteins

Different interactions between the protein surface and the silica surface can occur during the adsorption process.^[31,36] Modifications of the materials surface, variation of

the pH and salt concentration have a great influence on the kind of the interactions. Van der Waals forces, hydrogen bonds, hydrophobic and ionic interactions can be observed. Ionic forces are the strongest non-covalent interactions and do not only occur between support and protein but also between the protein molecules. The repulsion among the biomolecules is minimized when the pH is near pI. The pI assigns the pH where no net charge is present on the protein surface and therefore the repulsion of the proteins to each other is minimized and a dense packing of biomolecules can be achieved.^[3,89] Nevertheless, there are still charged groups on the protein that can interact with each other and with the surface but the adsorption process is now dominated by hydrogen bonds, hydrophobic interactions and van der Waals forces (Figure 1.18).

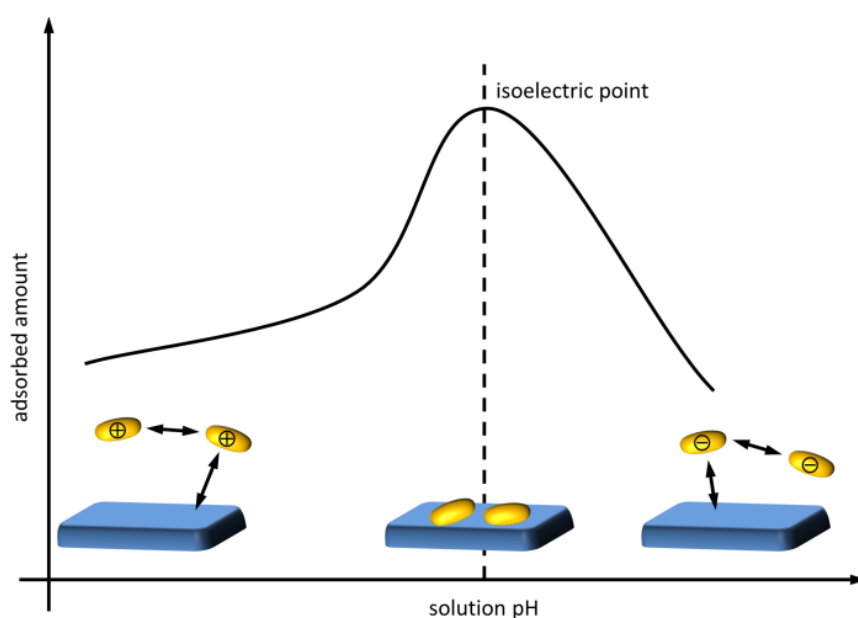


Figure 1.18: Influence of the pH on the interactions and the adsorbed amount during immobilization: The amount equally charged protein molecules repel each other when immobilizing at a pH that is different from the pI of the protein thus reducing a tight packing of proteins and hence the adsorbed amount. The highest adsorbed amount is usually observed at the pI of the protein. Reproduced from ^[113].

The pI of proteins can be determined experimentally or by using computer programs that calculate the pI from the amino acid sequence. Accessing images of the electrostatic protein surface can help to gain information on possible interactions.^[99,106–109] Lei et al. discussed the effect of orientation of organophosphorus hydrolase (OPH) and glucose oxidase (GOx) in MCF on the basis of the protein crystal structure in detail.^[110] They used electrostatic interactions to immobilize both proteins in carboxylic acid- and amine-

modified MCF. By means of the charge distribution on the protein surface they were able to discuss the orientation of the electrostatic binding and the loss in activity observed for GOx when the enzyme was adsorbed sideways on the wall so that the access to the active side was blocked.

As discussed before, a dense packing at the pI can be favorable but sometimes leads to reduced activity due to crowding and diffusion limitations. One main disadvantage with this procedure is that the pI is usually not the optimum pH for the catalytic reactions of the respective enzyme. Changes in the pH after immobilization can lead to repulsion either between the proteins or the protein molecule and the pore wall and thus to leaching.^[111] Depending on the protein it is sometimes more reasonable to keep the pH constant and match the charge between protein and support for optimum attraction. Best conditions for electrostatic immobilizations occur if the pI of the material is lower and the pI of the protein higher than the pH during immobilization (or vice versa).^[99,107] Thus the net charges of both components are opposite and an attractive force is present.

Not only information on the protein surface is important but information on the surface of the support. Zeta potential titrations have been widely used to determine pI and the net charge of various materials at a certain pH.^[98,112,113] The role of the charge of enzyme and support material on biocatalysis was investigated by Feller et al. on nonporous materials.^[112] They demonstrated that a high electrostatic interaction is important for an effective adsorption but can also hinder the enzymatic activity if the motion of the protein is completely frozen. One of the first publications that investigated the role of the zeta potential of mesoporous supports to the adsorption of proteins was published in 2002 by the group of Magner.^[107] They showed that a careful matching of the pI of the protein and the opposite charge of the support is crucial for efficient immobilization. The model proteins (cyt C, BSA, myo, subtilisin, chymotrypsin, trypsin, HRP, GOx, pepsin) have different pIs. The adsorption of cyt C on a cyanopropyl modified surface was investigated in detail. The highest loading of cyt C (pI 10.6) was observed at pH 6.5 indicating that the positively charged protein is attracted by the negatively charged silica.

The walls of mesoporous silicas can be either made more hydrophobic or hydrophilic by functionalization. Most of the proteins have a hydrophilic surface and are

immobilized more efficiently on hydrophilic silicas.^[90,91,96,98,104,107,110,114,115] But there are some enzymes like lipases that are activated by a hydrophobic environment.^[67,93,94,102,105,116,117] Hartono et al. discussed the effect of FDU-12 functionalization with various silanes on the uptake and activity of a cel mixture in detail.^[90] The pI of cel is 4.8 and hence a much higher uptake for amine-modified FDU-12 was observed than for thiol-, vinyl-, phenyl-modified and pure silicas. However, the high uptake was accompanied by a drastic loss in activity. The authors assumed and proved that a covalent bonding between amines and carboxylic acids on the protein surface occurred using XPS. They proposed that the creation of amide bonds induced conformational changes in the protein structure and therefore caused deactivation. It has to be mentioned here, that the equilibrium of amide bond formation is strongly shifted to the side of the hydrolysis and a lot of energy is required. The immobilization of carbonic anhydrase on SBA-15 with different amine-densities showed an activation on the support with the largest amine density.^[114]

A direct proof of the forces that apply during the adsorption of proteins is not easily made but flow microcalorimetry was recently used to investigate the energetics of the adsorption of lys on aminopropyl-modified MCF.^[96] The authors showed that the main driving forces for the adsorption were electrostatic interactions. These interactions got weaker with increasing salt concentration (sodium acetate and sulfate), indicated by a decreasing peak in the thermogram. The ions in the solution thus compensated the charges of the support and the protein and therefore the electrostatic forces between both were reduced.

In the last years the immobilization of lipases has drawn the attention of many researchers due to their high industrial importance. Lipases are hydrolytic enzymes that have defined hydrophobic areas on their surface. Therefore their immobilization is predominantly performed on hydrophobic materials.^[67,93,94,102,105,116,117] On hydrophobic surfaces they do not only show high immobilization yields but also increased activity. This phenomenon is called “interfacial activation” and is correlated to the lid that closes the active site of the lipase. The effect was discussed for porous materials but never proven. Jin et al. tried to resolve the problem using time-resolved fluorescence spectroscopy. They correlated the fluorescence lifetime of tryptophan with the mechanism of the activation.^[102] One of the tryptophan side chains of lipase from

Pseudomonas cepacia was located near the lid. When the lid opened the tryptophan residue was exposed to water the fluorescence lifetime decreased. This was only observed for materials with hydrophobic residues indicating that they activated the lid to open.

1.3.1.3 Immobilization of enzymes in periodic mesoporous organosilicas (PMOs)

The first immobilization of proteins in PMOs was reported in 2005 by Hudson et al.^[118] All general trends that have already been observed for mesoporous silicas can be transferred to the adsorption of proteins in PMOs. Thus the reports on pore size and morphology variation in PMOs for the immobilization process are only touched by some articles and not discussed extensively.^[119–124] However, the major advantages of PMOs are their hydrophobic surface (Figure 1.19) and the high and homogeneously distributed functionalization density. The first PMOs synthesized in 1999 were ethane-, ethylene- and later phenylene-bridged systems.^[68,125–127] Due to the extensively investigated synthesis conditions those are the most used PMO materials for enzyme adsorption experiments.^[119,120,122–124,128–137] In the beginning these materials were synthesized with small cationic template molecules. Therefore the small pore sizes limited the immobilization of larger enzymes. The first ethane-bridged PMO with block copolymers as template was synthesized to obtain larger pores and hence adsorb larger enzymes.^[138] The hydrophobic property of PMOs has been found to be especially attractive for lipase immobilization.^[124,135,137] The immobilization of lipase from *Thermomyces lanuginosus* in large pore PMOs with cage-like pores was discussed in detail by Zhou et al.^[124,137] They observed hyperactivation (500 %) of the lipase adsorbed on an ethane-bridged PMO but the largest uptake on a benzene-bridged PMO.

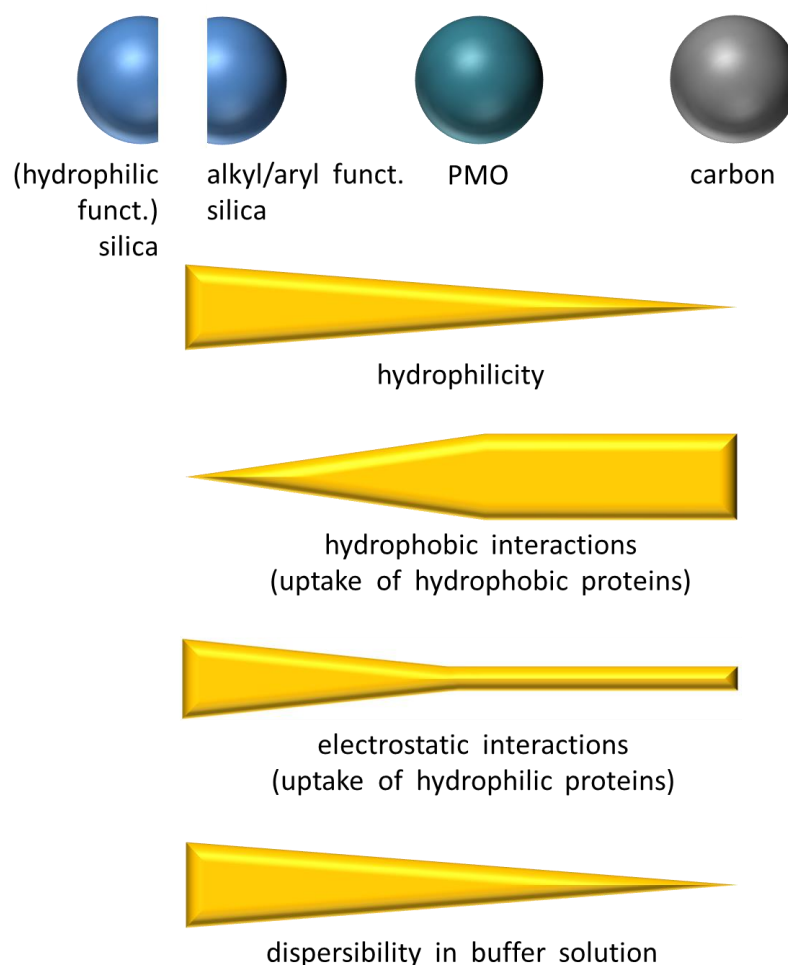


Figure 1.19: Characteristics of porous materials for the immobilization of proteins: The dispersibility in aqueous solvents is directly coupled to the hydrophilicity that is reduced starting with porous silica ending with nonoxidized hydrophobic carbons. While the interactions in silicas are mainly of electrostatic nature, hydrophobic interactions are favored in PMOs and carbons. Figure reprinted with permission from Wiley-VCH.^[7]

Some groups tried to make the PMOs more hydrophilic, either by co-condensation with monosilylated organosilanes, by introduction of hydrophilic bisilylated precursors or by postsynthetic modification.^[118,121,128,130,136,139] They attempted to make the PMO materials accessible for more hydrophilic proteins but most of these publications reported lower adsorption capacities than for the respective enzymes immobilized on mesoporous silicas.

Many applications of PMOs are in the field of peptide enrichment and separation.^[120,132,133,140] Some recently published results show effective enrichment of phosphopeptides in PMOs.^[141] The introduction of phosphonic acid residues in an ethane-bridged PMO by co-condensation was performed in metal affinity

chromatography. The phosphonic acid residues were complexated with zirconia and iron ions to separate phosphopeptides from an aqueous phase by coordination. The size-exclusion effect was shown to be an effective tool in separating proteins from protein extracts. Qian et al. synthesized ethane PMO spheres with 3 nm pores and used them in the enrichment of the E7 peptide from BSA or lys.^[120] They chose a PMO over silica because of its good dispersibility in organic solvents.

PMOs were not only used for separation and enrichment purposes but for refolding of denatured proteins. Wang et al. showed that it is possible to refold lys from a solution with high concentration of denaturants. The adsorption inside the pores minimized the agglomeration and irreversible damage of the protein.^[133] After the enrichment of the denatured lys in the hydrophobic pores of an ethane-bridged PMO the release was triggered with polyethylene glycol (PEG). PEG is able to form strong H-bonds with the silanol groups of the PMO and therefore displaced the protein efficiently. After the release the protein was able to refold in an oxidative environment. This publication shows on one hand the reversibility of the adsorption process and on the other hand the effective refolding (80 %) of proteins.

These reports show that PMOs have a great potential for hydrophobic protein immobilization and separation purposes. The characteristics of PMOs, and therefore the interactions between protein and material, can be tuned in detail by introduction of different organic moieties. The design of the PMOs can be performed more precise compared to their mesoporous silica analogues but the precursor synthesis makes the fabrication of these materials more complicated and limits the application of PMOs as mainly hydrophobic supports (Figure 1.19). Only a few reports have been published on the synthesis of PMOs with charged quaternary amine precursors but these materials have not yet been used for protein immobilization experiments.^[142]

1.3.1.4 Immobilization of enzymes in porous carbons

Mesoporous carbons have been rarely used for enzyme adsorption experiments due to their strong hydrophobicity.^[50,143–163] The hydrophobicity of carbons can be analyzed for example by water adsorption or contact angle measurements.^[162] As-synthesized carbon materials usually have a surface covered with non-polar residues and are therefore

hardly dispersible in aqueous solvents (Figure 1.19). The immobilization is usually directed by hydrophobic forces due to the lack of charged groups. But nevertheless there have been reports that prove the successful adsorption of proteins on mesoporous carbons. The first publication about the immobilization of biomolecules in CMK-3 was written by Vinu et al. who studied CMK-3 and CKT as supports with cyt C and lys as model proteins.^[50,158–161] The systematic studies showed that the carbon materials behaved similar to mesoporous silicas when the adsorption is governed by hydrophobic forces. The maximum of adsorbed protein was reached near the pI and large pore volumes and sizes led to high adsorption capacities. The steep rise of the fitted Langmuir isotherms indicated strong hydrophobic attraction. A higher water stability of the mesoporous carbons compared to the mesoporous silicas was reported.^[158]

Oxidation is a widely used method to make carbon surfaces more hydrophilic and hence more accessible for biomolecules.^[146,161,163] Since the oxidation of carbon surfaces leads to several functional groups (Figure 1.13d) the interactions between proteins and the materials can be diverse. Therefore a detailed analysis of the carbon surface is required. Traditionally, IR spectroscopy, temperature programmed desorption (TPD) or X-ray photon spectroscopy (XPS) are used. Recently, TPD was used not only for the surface analysis of a porous carbon but for the quantification of adsorbed protein.^[151,163] With TPD/MS it was possible to correlate the H₂S liberation to the amount of sulfur in the respective protein. The authors were able to provide a calibration curve for BSA and cyt C and determine the amount of the respective protein in an unknown sample. The amount of protein accessed with the traditional methods (quantification in the supernatant) was in accordance with the amount determined by TPD/MS. Additionally, information on the nature of the interactions and the conformational changes after the immobilization have been gained from the TPD/MS profiles. The authors compared the combustion of the free protein with the immobilized one and found different peak profiles. In the case for BSA a second peak indicated the presence of weakly and strongly bound protein molecules. The TPD profiles for cyt C showed a slight shift to higher temperatures. The authors assigned this effect to conformational changes in the enzyme structure.

Since the pore size of most mesoporous carbons was limited due to the template used many proteins were not able to access the pores of the systems. The synthesis of

carbons with larger pores was a major breakthrough to adsorb enzymes with large molecular mass.^[145,153–157,163] GOx for example has a molecular weight of 160 kDa and its pI at pH 4.6. Due to its low pI the immobilization in mesoporous silicas was often inhibited by repulsive forces.^[155] The synthesis of foam-like carbons (MCF-C) was one possibility to immobilize this large protein efficiently.^[154–156] MCF-C materials have spherical pores with large pore entrances and substrate diffusion pores (4.6 nm) between the main pores. Hybrid materials of GOx in combination with porous carbons have been used as glucose biosensors.^[155,157] The unique combination of conductive carbon and assembled proteins made the electron transfer reaction of the protein and therefore the sensing more efficient due to small electron transfer paths from enzyme to enzyme or enzyme to carbon. But the limitation of the pore size is not necessarily a drawback. This effect can be used for size-selective enrichment or separation.^[153,162] Qin et al. prepared a device for protein analysis from blood serum. Mesoporous carbons were able to extract more proteins than mesoporous silicas due to their hydrophobicity. From a sample of 20 μL it was possible to identify 3400 different proteins after enrichment in mesoporous carbon.^[162]

1.3.2 MAGNETIC IRON OXIDE PARTICLES FOR ENZYME IMMOBILIZATION

1.3.2.1 Magnetic iron oxide particles

Iron oxide nano- or microparticles have been widely used in the last years since their magnetic behavior is attractive for many applications.^[164–166] The most common iron oxides are magnetite (Fe_3O_4), maghemite ($\gamma\text{-Fe}_2\text{O}_3$) and hematite ($\alpha\text{-Fe}_2\text{O}_3$) that are found as minerals in rocks and soils. All three types of iron oxides can be transformed into each other (Figure 1.20). Since hematite is the most stable modification it is usually the end product. All crystal structures of iron oxides are built from two polyhedrons that are linked via edges, corners or faces: mostly FeO_6 octahedrons and less common FeO_4 tetrahedrons. Since the O^{2-} ion ($r = 0.14 \text{ pm}$) is the larger ion it builds a closest packed structure of ions with the smaller iron ions ($r(\text{Fe}^{2+}) = 0.082$; $r(\text{Fe}^{3+}) = 0.065$) in the interstices.^[167]

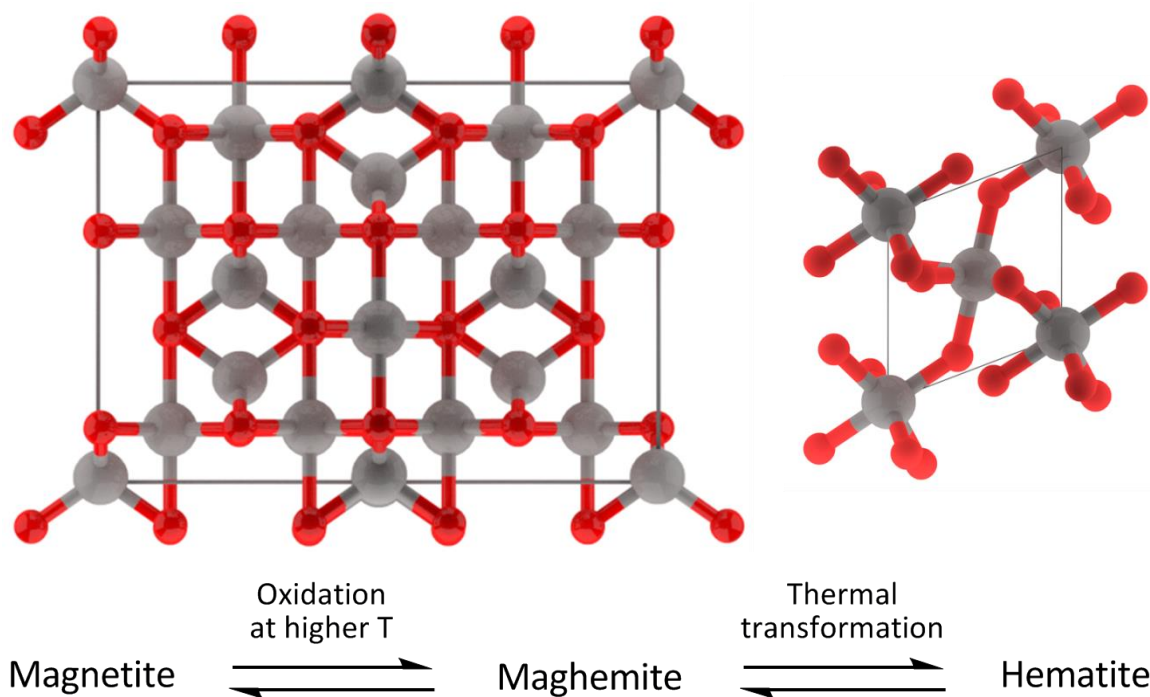


Figure 1.20: Unit cell of magnetite/maghemite (left) and hematite (right). Whereas the coordination of the iron ions is strictly octahedral in the tetragonal structure of hematite. The inverse spinel structure of maghemite and magnetite shows octahedral and tetrahedral coordination. Magnetite can be easily oxidized to maghemite which can be transformed to hematite by thermal treatment.

The magnetism of iron oxides is probably the most appealing property of those materials. Besides the common weak diamagnetism, that all materials exhibit, iron oxides show paramagnetic properties due to their unpaired electron spins. Without an applied magnetic field the spins in paramagnetic materials are statistically distributed and have no net magnetization (Figure 1.21). After an external magnetic field is applied the spins are partially aligned and a net magnetization is observed.

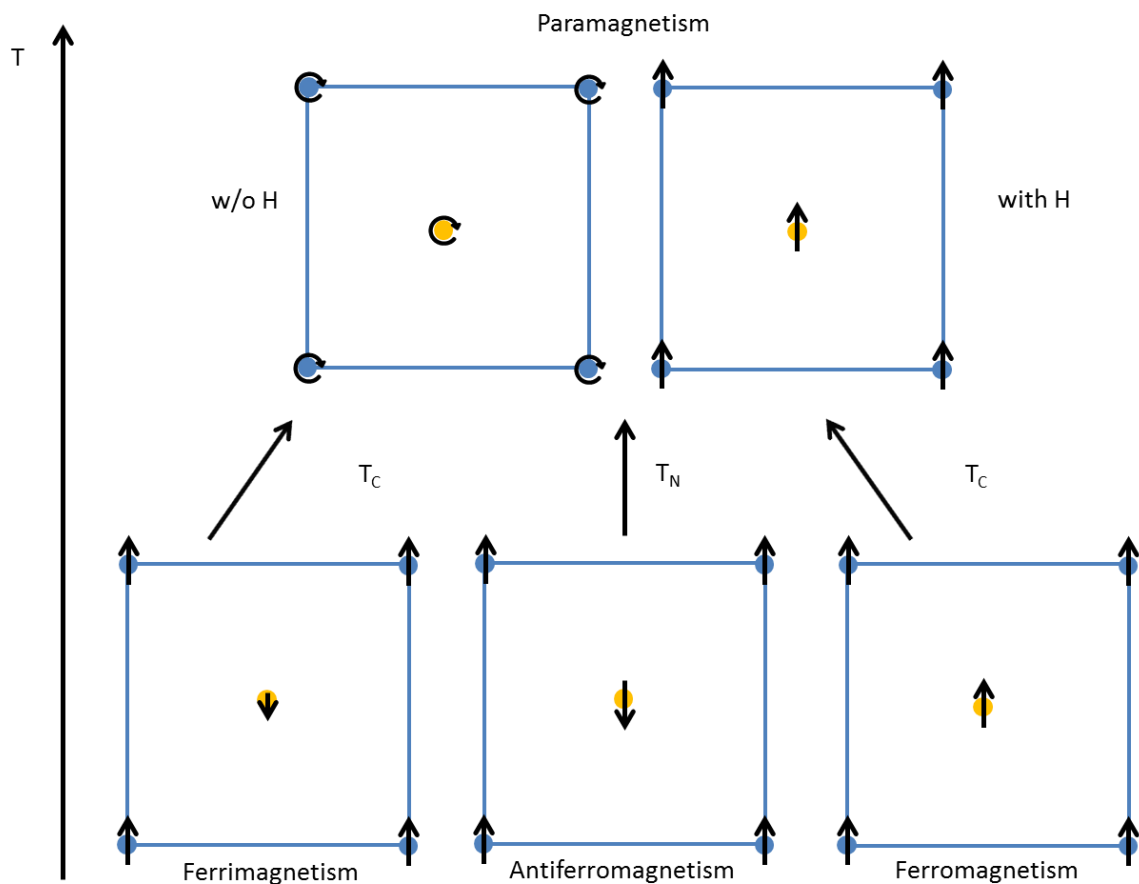


Figure 1.21: Cooperative magnetism of paramagnetic materials. Above the critical temperatures the cooperative behavior gets lost and the spins will align only when a magnetic field (H) is applied. Ferromagnetic materials have parallel aligned spins whereas the spins in ferrimagnetic and antiferromagnetic materials are antiparallel. In ferrimagnetic materials a net magnetization is observed due to the different size of the magnetization vector.

In iron oxides additionally some cooperative mechanisms (Figure 1.21) apply. Cooperative mechanisms lead to magnetic domains where the spins are aligned in one direction (*“Weißsche Bezirke”*) even without an applied magnetic field. The domains are aligned to each other after applying an external magnetic field. Ferromagnetic behavior occurs when all spins are aligned in the direction of the external field. A net magnetization is observed whereas in antiferromagnetic materials no net magnetization is present. Two kinds of spins are aligned parallel and antiparallel to the applied field. Since both spins have the same value no net magnetization is observed. The antiparallel alignment of spins is also present in ferrimagnetic materials but the value of the spins is unequal and a net magnetization can be measured. Usually, the respective type of magnetization is influenced by the temperature since thermal movement of the spins is

opposed to the order of the magnetization. At some point the cooperative magnetization of the material is lost and the materials become simply paramagnetic. For ferro- and ferrimagnetic materials this temperature is called Curie temperature (T_C) and for materials with antiferromagnetic properties Neel temperature (T_N).

Table 1.3: Data of magnetite, maghemite and hematite.^[167]

	Magnetite	Maghemite	Hematite
Formula	Fe_3O_4	$\gamma\text{-Fe}_2\text{O}_3$	$\alpha\text{-Fe}_2\text{O}_3$
Type of magnetism	Ferrimagnetism	Ferrimagnetism	Ferromagnetism or antiferromagnetism (weak)
T_C/T_N / K	850	820-986 ^a	955
Crystallographic system	Cubic	Cubic	Hexagonal
Space group	Fd3m	P4 ₃ 32	R3c
Unit cell dimensions	a = 0.8396	a = 0.8347	a = 0.5034, b = 1.3752
Structural type	Inverse spinel	Defect spinel	Corundum

a: The T_C for maghemite is not exactly determinable since a thermal transition leads to hematite.

Superparamagnetism is another phenomenon often related to magnetic iron oxide nanoparticles especially magnetite particles. Magnetic anisotropy leads to the alignment of the spin orientation parallel to the applied field. It requires certain activation energy to change the direction into an antiparallel one. In very small particles (< 20 nm) where the thermal energy of the particles is larger than the mentioned activation energy for the switching of the spins the spin direction is fluctuating and no net magnetization is observed until a magnetic field is applied.

Magnetite (Fe_3O_4)

Magnetite is probably the most interesting of the iron oxides in structure and magnetic behavior since it consist of iron ions in two valence states ($\text{Fe}^{2+}/\text{Fe}^{3+}$). It crystalizes in the inverse spinel structure (AB_2O_4) where the oxygen anions built a cubic face-centered closest packing. The interstitial sites with tetrahedral geometry (A-sites) are occupied to 1/3 with smaller Fe^{3+} ions and the octahedral B-sites to 2/3 with both Fe^{3+} and Fe^{2+} . Tetrahedra as well as edge-sharing octahedra form layers along the [111] direction. Both polyhedra are linked by corners to each other.^[167]

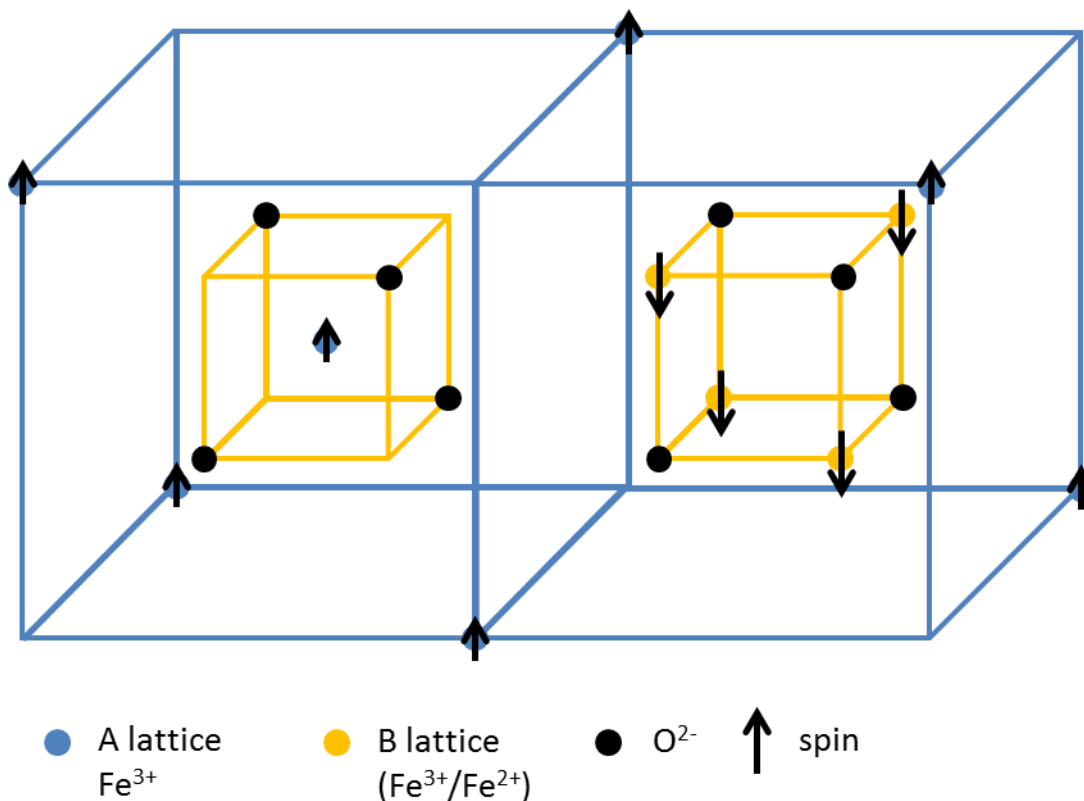
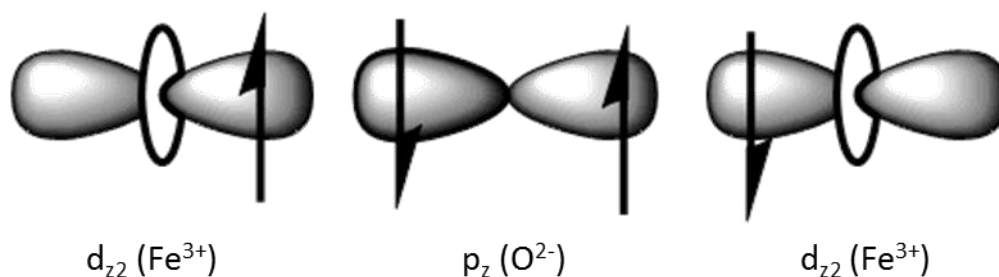


Figure 1.22: A- and B-lattice of magnetite. The spins in each sublattice are aligned parallel whereas the spins of the sublattices are antiparallel.

Below its Curie temperature ($T = 850 \text{ K}$) magnetite is ferrimagnetic. The two interpenetrating sublattices of the A and B-site cations (Figure 1.22) are responsible for this phenomenon. The spins of the cations on A- and B-sites are aligned antiparallel and their magnitudes are unequal. The net magnetization is obtained along the $[111]$ direction.



Scheme 1.2: Coupling of the iron species in magnetite via superexchange. The coupling of the unpaired spins in the d-orbital of Fe³⁺ proceeds over the fully occupied p_z orbital of O²⁻ to the d-orbital of the adjacent Fe³⁺.

The coupling of the iron species to each other proceeds by a so-called superexchange (electrostatic exchange interaction) mechanism. The p_z -orbital of the connecting oxygen ion is able to interact with the unpaired electrons from the iron cations in the d_{z^2} -orbital (Scheme 1.2). The magnetic exchange interaction is mainly dependent on the bond length and angle. When the species are aligned linear the transfer and hence the antiferromagnetic coupling is stronger. The bond angle in magnetite is 127° for the $\text{Fe}_A\text{-O-Fe}_B$ connection.^[167]

1.3.2.2 Synthesis and functionalization of magnetic iron oxide particles

Synthesis

A variety of synthesis procedures (gas and liquid state) for iron oxide nanoparticles was investigated over the last decades: thermal decomposition, co-precipitation, hydrothermal synthesis, microemulsion or inverse micelle methods, sonochemical synthesis and chemical vapor deposition are just a few of them.^[164–166,168] All synthesized particles differ in size, morphology, surface chemistry, polydispersity, crystallinity and many parameters more. Depending on the kind of application one has to choose which method yields iron oxide particles in quality and amount suitable for one's purpose. The four main synthesis approaches are addressed here shortly (Table 1.4).

Table 1.4: Comparison of the main procedures for the synthesis of iron oxide particles. Reprinted and modified with permission of Wiley-VCH.^[164]

Synthetic method	Synthesis	T / °C	Time	Solvent	Size distribution	Shape control	Yield
Co-precipitation	Simple, ambient cond.	20-90	min	water	Medium-broad	Not good	High, scalable
Thermal decomposition	Complicated, inert atmos.	100-320	h-d	Organic	Narrow	Very good	High, scalable
Microemulsion	Complicated, ambient cond.	20-50	h	Organic	Medium	Good	Low
Hydrothermal synthesis	Simple, high pressure	130-250	h-d	Polar	Narrow	Very good	Medium

The co-precipitation method was one of the first approaches to synthesize magnetic iron oxide particles. With this fast and inexpensive method a high amount of product

can be obtained. In general for the synthesis of magnetite a stoichiometric mixture (2:1) of Fe(II) and Fe(III) salts in water under basic conditions leads to flocculation of magnetite that is further oxidized under air to maghemite.^[165] The synthesis in aqueous environment results in the formation of a hydroxylated particle surface that makes the particles prone to aggregation but also accessible for further functionalization and dispersible in water. Whereas the crystallinity of the particles is low the magnetization can be relatively high (30-80 emu g⁻¹, bulk: 100 emu g⁻¹).^[166] Since the kinetic control of particle growth is difficult to accomplish (strict separation of nucleation and growth) a broader particle size distribution is obtained that can be sharpened using stabilizers.

One method to obtain high quality nanoparticles is the thermal decomposition of organometallic precursors (e.g. acetylacetonates, carbonyls) in high boiling organic solvents. At a certain temperature the loss of the organic ligand leads to the formation of small seeds that grow further usually at a higher temperature to separate nucleation and growth of the particles. The use of stabilizing surfactants (e.g. oleylamine, oleic acid) strictly limits the growth and leads to a narrow particle size distribution and the high temperatures produce crystalline nanoparticles. A variety of morphologies and sizes can be obtained varying the concentration and nature of solvent and reagents. However, a major drawback of these particles is their hydrophobicity.

The use of microemulsions or inverse micelles is another possibility to restrict the size of the iron oxide particles since the surfactants assembled at the oil-water interface enhance the stabilization of the droplets. In these restricted droplets the synthesis of the iron oxide takes place and the growth is stopped by the surfactant.

The differences of reactant and product solubility play a major role in the hydrothermal synthesis of iron oxides. High pressure and high temperatures lead to crystalline particles with high saturation magnetization. In general besides the iron salts components (stabilizer, surfactants) with high boiling points are used.

Functionalization

The surface modification of magnetic particles is not only necessary for the introduction of functionality but also for stabilization. The existence of singly, doubly or triply coordinated as well as germinal surface hydroxyl groups offer the possibility of a variety

of chemical modifications but also promote particle agglomeration. The surface of iron oxide particles has due to the amphoteric character of the hydroxyl groups an amphoteric character (pI 6.8).^[167] The use of stabilizing molecules or polymers can prevent the agglomeration as well as the chemical degradation of those particles. Stable particle dispersions can be obtained when attractive and repulsive forces are carefully balanced. Despite the attractive van der Waals forces a dipolar magnetic component is introduced in iron oxide nanoparticle systems. Steric and electrostatic repulsion counter the attractive forces.^[165,166]

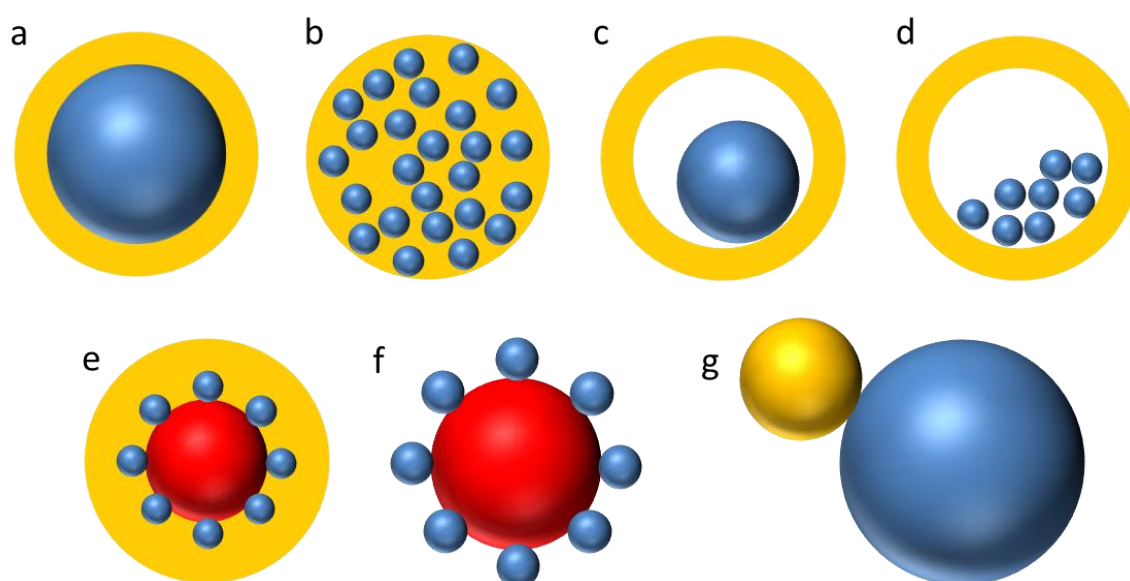


Figure 1.23: Different types of iron oxide core-shell particles. The iron oxide component (blue) is incorporated in a shell that can be an inorganic or organic component (yellow). In some cases the iron oxide is immobilized onto a carrier (red; e,f). Typical core-shell particles consist of a shell that is directly coated onto one or more cores (a,b) whereas a cavity separates core and shell in yolk-shell particles (c,d). A carrier for the iron oxide particles is sometimes used when the affinity of the iron oxide and the shell component is low (e,f). The dumbbell structure (g) is not strictly a core-shell structure but is sometimes obtained when a low affinity of core and shell is present. The shell separates from the core and builds nanoparticles that are deposited onto the iron oxide. Multiple shells can be synthesized for most structure types (a-e).

Organic or inorganic small molecules and polymers are used for the modification of the particles building a variety of core-shell-type structures (Figure 1.23) consisting of a magnetic core and an isolating protective shell. Dealing with the particle stabilization by small molecules, like salts, the term of “shell” is somehow exaggerated. Sulfate, phosphate and carboxylates are known to provide a sufficient electrostatic stabilization especially in polar solvents by simple complexation of the iron oxide surface oxygen

atoms. “Real” core-shell structures can be obtained with organic polymers, metals and inorganic components. The simplest model is a shell of defined thickness directly coated onto one or more magnetic cores (a,b). Yolk-shell particles (c,d) are another subclass that is characterized by a void between a loose core and the shell. Some types of core-shell structures use a matrix to immobilize magnetic particles (e-f).^[166]

Surfactants are frequently used during or after the synthesis in both aqueous and organic solvents. The surfactants not only offer steric and electrostatic stabilization but also a barrier for the particle growth. Silanization is another straight forward method to obtain stable and highly functional materials. The silanes are postsynthetically grafted onto the surface hydroxyl groups of the iron oxide core.

Organic polymers can be either attached covalently or adsorptively onto magnetic particles. A facile method to obtain highly uniform shells is the atom transfer radical polymerization to build up synthetic polymers but also natural polymers like dextran or alginate are popular due to their biocompatibility. The polymer shell provides sufficient protection against aggregation and can be helpful to disperse the nanoparticles in aqueous solution but its structure is not dense enough to chemically protect the surface. Another disadvantage is the loss in saturation magnetization that is usually obtained with thicker shells.

Chemical protection as well as catalytic applications are reasons to coat the particle with precious metals. The most common metal is gold due to its low chemical reactivity and the known thiol-functionalization for biomolecule immobilization. The nanoseed method is one approach to yield highly uniform iron oxide@Au particles and is explained in the next chapter.

The most common coating component is probably silica. The Stöber synthesis, the sol-gel approach and aerosol pyrolysis are used to precisely control the thickness of the layer. Silica enhances the biocompatibility, hydrophilicity, chemical stability and the electrostatic repulsion and hence the dispersibility of the particles. The easy functionalization and the introduction of porosity are additional benefits. All in all, the modification of magnetic nanoparticles with other materials is mandatory to enhance most important the chemical stability and the dispersibility of the nanoparticles.

1.3.2.3 Immobilization of enzymes onto magnetic iron oxide composite materials

Not only the stability of iron oxides is a reason for the synthesis of magnetic iron oxide composites but also the use in biomolecule immobilization demands a modification of the iron oxides. A direct combination of enzymes and iron oxides can lead to a loss of enzyme activity by iron complexation of the enzymes or reactions at cysteine sites.^[5] One possibility for the creation of magnetic biohybrids is however the utilization of pure or silanized iron oxides.^[169–174] Other methods start with porous carbons or silicas followed by entrapment or binding of iron oxide nanoparticles.^[147,149,175–180] Coating of magnetic particles with a non-magnetic shell creates highly versatile core-shell particles.^[181–191] These composite materials all have become very popular in the last years, due to the easy recovering of the biocatalysts. One focus in this chapter is laid on core-shell particles that combine the benefits of an inorganic shell (e.g. easy functionalization) with the magnetism of the iron oxide core. The second focus is on the combination of porous materials with magnetic iron oxides.

One of the first publications on the immobilization of magnetite nanoparticles inside of mesoporous silicas in 2005 described the adsorption of chymotrypsin and magnetic nanoparticles inside MCF. After the adsorption the enzymes were cross-linked with glutaraldehyde. The enzyme aggregates encapsulated the nanoparticles and thus diminished leaching of protein and particles. The obtained biocatalyst exhibited very high stability and good recoverability.^[192] Magnetic core-shell particles composed from an iron oxide core and a silica shell (iron oxide@SiO₂) are not limited to one possible assembly method. Multiple shells and the introduction of porosity enlarge this concept. Lipase immobilization was recently performed on Fe₃O₄@SiO₂ particles consisting either of a single nonporous shell or two shells (Fe₃O₄@SiO₂@porous-SiO₂). The pore diameter of the outer silica shell was varied. The loading of lipase was directly correlated to the surface area. The lowest lipase loading and surface area was observed for Fe₃O₄@SiO₂ and the highest for the particles with two shells and smaller pores. The porosity reduced the substrate accessibility compared to the nonporous system.^[193]

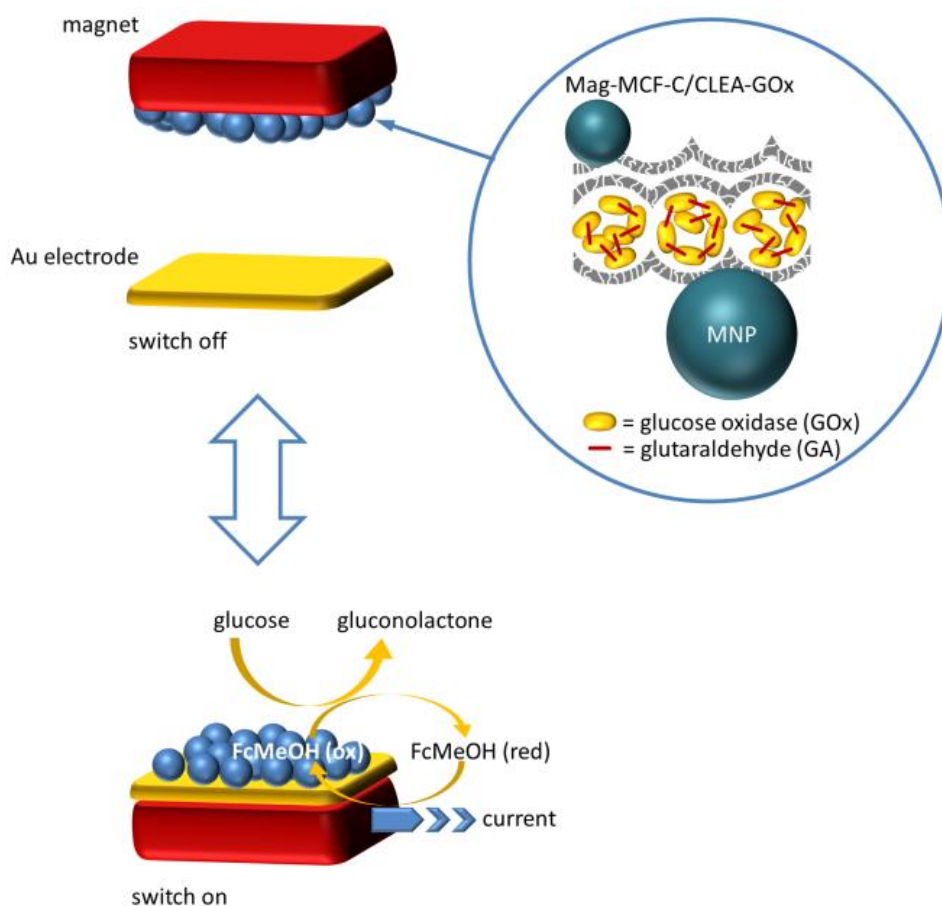


Figure 1.24: Magnetic MCF-C-GOx composite applied as a biosensor for the detection of glucose. The sensor is switch on when the magnet is brought in contact with the gold electrode and the magnetic composite is pulled towards the electrode. GOx, that is crosslinked in the channels of the MCF-C, oxidizes glucose to gluconolactone and the electrons are transported via ferrocene methanol (FcMeOH) as an electron mediator to the electrode and an anodic current is developed. Reproduced with permission from Wiley-VCH.^[177]

Porous carbons have, besides their porosity, the ability to conduct electrical current. This combination makes them ideal candidates for the preparation of biosensors in combination with redoxactive enzymes. The conductivity of the carbon materials can improve the electron transport and therefore the catalytic performance. The addition of a magnetic component makes these composites even more appealing.^[175,177,194] Lee et al. built a device that was composed of a MCF-C, cross-linked GOx and iron oxide particles (Figure 1.24).^[177] This sensor was able to be switched on and off using a magnet. If the magnet was brought in contact with an Au electrode, the carbon composite was pulled towards the electrode and an electric current was employed. The catalytic oxidation of glucose to gluconolactone was performed by GOx and supplied the current that was transferred by the electric conductive carbon.

In most publications on the topic of magnetic composite materials the possible influence of the iron oxide particles on the catalytic performance of the reactions is not considered. However, Kim et al. reported peroxidase-like behavior of the magnetite particles.^[175] The authors incorporated magnetic nanoparticles inside MCF-C and entrapped the particles and GOx by cross-linking. During the oxidation of glucose, hydrogen peroxide is released and the authors observed the effective conversion of the peroxide to water. This decomposition of hydrogen peroxide was proven to be a result of the catalytic reaction by the magnetite particles. This additional reaction increased the sensitivity of the biosensor significantly.

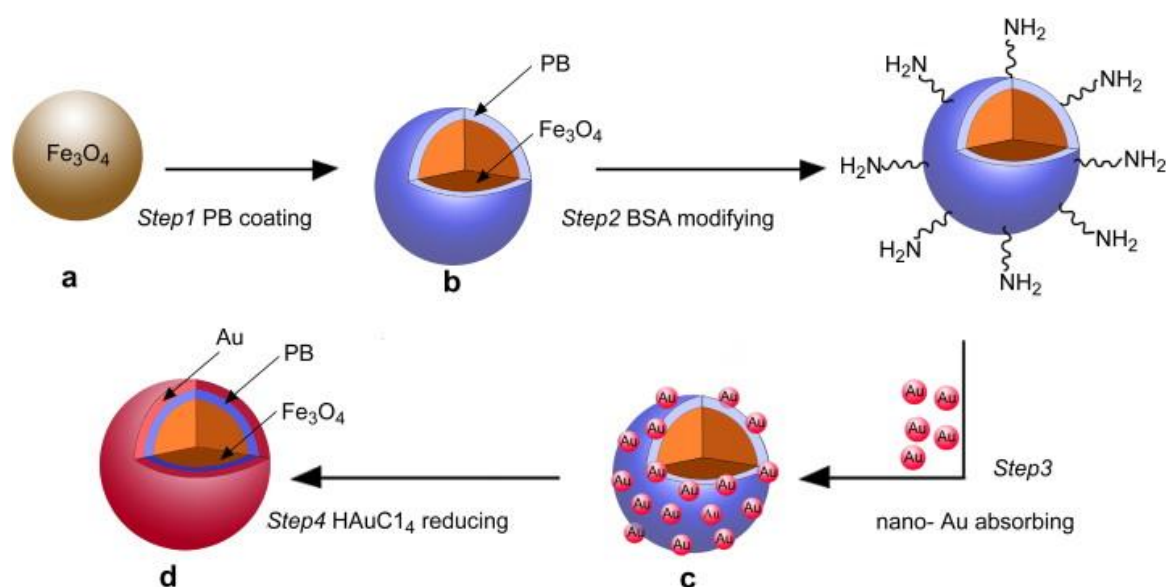


Figure 1.25: Schematic illustration of the synthesis of a complex immunosensor made of coated magnetite particles. A Prussian blue shell was synthesized to enhance the redoxactivity in the first step. The PB shell was further functionalized to allow gold nanoparticles to assemble on the surface. In the last step the gold nanoparticles were reduced with citrate to give another shell. Figure reproduced with permission from Elsevier.^[190]

A highly complex core-shell system (Figure 1.25) was prepared for immunosensing of a model antibody.^[190] The antibody was conjugated to particles consisting of a magnetite core and two shells. A Prussian blue shell was incorporated for enhanced redoxactivity and its peroxidase like behavior (reduction of hydrogen peroxide). The last shell was composed of gold to enhance the electron transport. On the surface of the particle two enzymes namely HRP and GOD were immobilized to amplify the signal

coming from the recombination of antigen and antibody. The antibody was immobilized on the surface of the particle and the antigen on a gold electrode. The combination of all components led to an amplification of the signal of the immunosensor so that it was possible to detect even concentrations pgmL^{-1} of the antibody.

1.3.3 ENZYME-INORGANIC HYBRID MATERIALS FOR APPLICATIONS IN BIOCATALYSIS

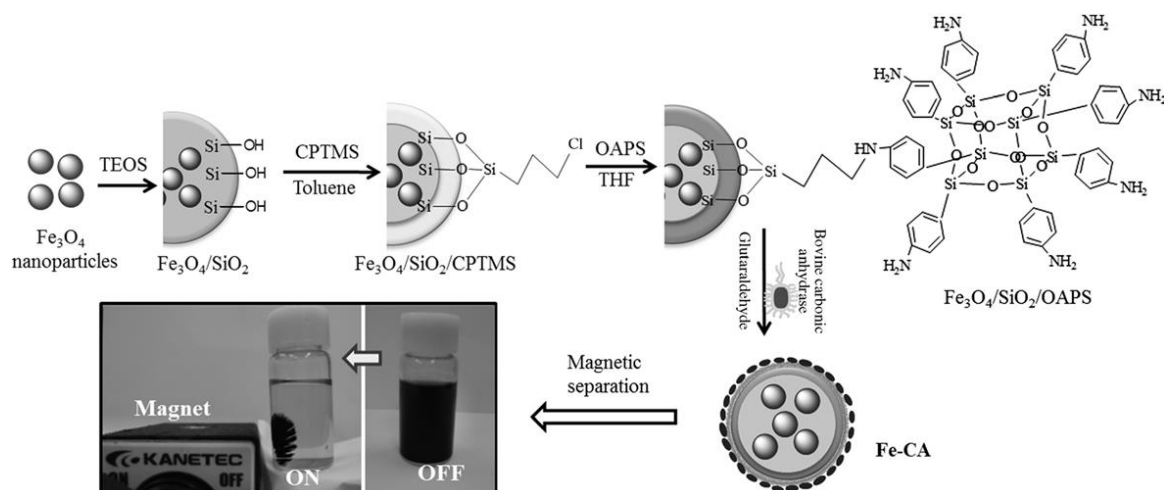
1.3.3.1 Green chemistry

Roger A. Sheldon, one of the pioneers in green chemical processes design, defined *Green chemistry* as follows: "Green chemistry efficiently utilizes (preferably renewable) raw materials, eliminates waste and avoids the use of toxic and/or hazardous reagents and solvents in the manufacture and application of chemical products."^[195] In general a process that fulfills these criteria is not only environmentally attractive but also economically supported by the reduction of waste and energy in the production process. In order to obtain green chemical products natural renewable sources like cellulose or starch are used as reagents for the synthesis of green products. The main problem for example with cellulose is the complex extraction from lignocellulosic feedstocks by thermochemical or hydrolysis approaches.^[196,197] However, in the large pool of enzymes there are several that catalyze the hydrolysis of lignocelluloses and further the depolymerization of cellulose (glucanases, glucosidases, cellobiohydrolases and many more). The advantage of enzymes in green chemistry in general are their mild reaction conditions, their high activity, their biodegradability as well as their high selectivity that leads to pure products and reduces the application of protecting groups and activating reagents. Some of these remarkable approaches have also been performed with immobilized enzymes in designed inorganic hybrid materials. Special focus is laid here on porous materials as well as the application of magnetic iron oxide composite materials.

The catalytic behavior of lipases for biodiesel production is one topic that has been discussed lately.^[173,174,198–200] Salis et al. reported the conversion of sunflower oil into biodiesel using a lipase from *Pseudomonas fluorescens*.^[200] The immobilization of this enzyme on SBA-15 was performed covalently as well as adsorptively. The authors observed the common deactivation after covalent bonding as well as the low cycle

stability of the adsorptively immobilized enzyme. The effect of crowding inside the pores was reported since a loading larger than 180 mg g^{-1} caused deactivation by diffusion limitation. The conversion of sunflower oil in a solvent-free process into the respective esters was completed in less than 7 h indicating the construction of an effective biocatalyst.^[200] A similar performance of lipase from *Thermomyces lanuginosa* conjugated onto magnetite nanoparticles was observed by Xie et al.^[174] After successful transesterification (90 %) of soybean oil the particles were magnetically separated from the reaction mixture and could be reused for 5 cycles.^[174] Another interesting approach was recently reported for *Aspergillus niger* lipase where the concept of CLEAS was transferred onto magnetic iron oxide particles covered with crosslinked lipase aggregates. The corresponding heterogeneous biocatalyst was applied in the synthesis of glycerol carbonate that can be synthesized via carbonylation of glycerol produced during the biodiesel production. Hence, it is a product that fulfills the *Green Chemistry* approach and offers the opportunity to be utilized as a *Green solvent* or a precursor for *Green polymers*.^[172]

The hydrolysis of biomass is a key issue in environment friendly chemistry that addresses the use of enzymes for the production of building blocks in organic synthesis of fine chemicals.^[84,92,115,181,183,201–204] Recently, Bernal et al. reported the efficient immobilization of β -galactosidase (gal) from *Kluyveromyces lactis* on a new hierarchical silica.^[84] The large enzyme (14 nm, 220-240 kDa) was immobilized inside the mesopores in order to guarantee an efficient diffusion of the substrate through the pore system. The performance of gal in hydrolysis of lactose was monitored over a period of several hours and remained constant. Starch hydrolysis was performed with immobilized α -amylase on polydopamine coated magnetic chitin particles. The biocatalyst exhibited no significant loss in activity after immobilization and due to the higher thermal stability of the enzyme it was possible to carry out efficient starch hydrolysis at $30 \text{ }^\circ\text{C}$.^[183]



Scheme 1.3: Synthesis of a magnetic composite for carbonic anhydrase immobilization. Multiple iron oxide nanoparticles are embedded in a silica shell that is further functionalized with 3-chloropropyltrimethoxysilane (CPTMS) to bind OAPS on the surface. In the last step CA is immobilized with glutaraldehyde. The magnetic separation is shown in the inset picture. Reprinted with permission from Wiley-VCH.^[184]

The reduction of greenhouse gases has been a major concern in the last decade. The degradation of toxic or harmful products is not included in the conventional green chemistry since green chemistry is based on the avoidance of harmful byproducts during the process. However, it is still an important procedure to protect the environment and thus mentioned here. The enzymatic sequestration of CO₂ using carbonic anhydrases (CA) emerged as a key issue in biocatalysis with porous materials in the last two years.^[114,205,206] CAs catalyze the conversion of CO₂ to bicarbonate. In a solution with Ca²⁺ the bicarbonate precipitates as CaCO₃ and the CO₂ is captured. The instability of the enzyme is the major problem in this process. Vinoba et al. successfully stabilized the enzyme in amine-functionalized SBA-15 with 75 % retention of activity after 40 cycles.^[114] The conversion efficiency of the enzyme was 36-fold increased compared to free CA. They found out that functionalization with octa(aminophenyl)silsesquioxane (OAPS), an amine modified polyhedral oligomeric silsesquioxane, gave the best results. Based on this finding they reported OAPS functionalized Fe₃O₄@SiO₂ particles as efficient composite for immobilization of CA (Scheme 1.3).^[184]

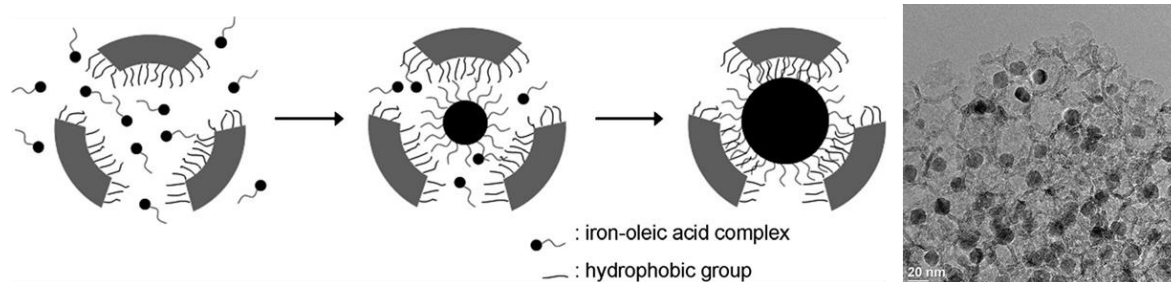


Figure 1.26: Schematic illustration of the growth of iron oxide particles inside spherical MCF pores. Iron-oleic acid precursors grow to a magnetic particle until the hydrophobic residues at the pore surface stop the growth due to steric hindrance. The TEM image depicts the distribution of the dark iron oxide particles (ca. 20 nm) inside the porous network. This figure is reprinted with permission from Wiley-VCH.^[179]

Not only greenhouse gases pollute the environment but also carcinogenic and mutagenic polyaromatic hydrocarbons (PAH) which can be oxidized and hence detoxified. Laccases have been immobilized in SBA-15 and bimodal carbons by several groups.^[180,207–209] Bautista et al. performed the degradation of naphthalene as a model compound to show the effective oxidation by the biocatalyst.^[207] Magnetic $\text{Fe}_3\text{O}_4@ \text{SiO}_2$ particles have been recently used as a support for catechol-1,2-dioxygenase that was immobilized by complexation of its His-tag onto Ni^{2+} introduced to the particles surface. The enzyme was able to cleave the aromatic ring structure and detoxify catechol.^[182]

As discussed in 1.3.1.4 the combination of porous materials with magnetic nanoparticles is a simple separation strategy. Some recent publications reported the successful implementation of this strategy in *Green chemical* applications.^[193,210,211] Lee et al. synthesized iron oxide nanoparticles inside siliceous MCFs (Figure 1.26). They introduced iron oleic complexes, which grew inside the cage-like pores of hydrophobic functionalized MCF until the hydrophobic residues stopped the growth. They used this material for adsorption of CALB and have proven the efficiency of this composite material in biocatalysis.^[179]

1.3.3.2 Enzyme cascades and cofactor regeneration

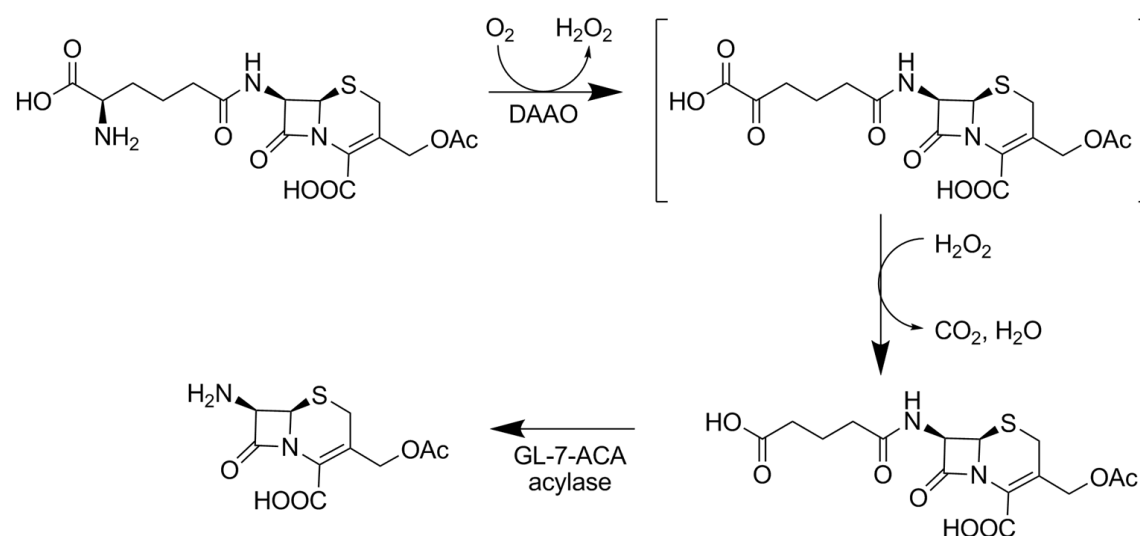
In the near future cascade reactions with immobilized enzymes will be more and more applied to perform complex reaction cycles. For this purpose the knowledge based on previous research experience has to be combined for multiple enzymes. Two general possibilities exist to generate cascade reactions with immobilized enzymes.^[30] The co-

immobilization of enzymes on one carrier is beneficial for the diffusion of products, cofactors and substrates since the proteins are adjacent to each other. On the other hand the design of a support (pore size, surface charge) that fits both enzymes can be complex owing to different affinities of the enzyme to the support. The immobilization on two separate supports facilitates the design of the supports as well as immobilization procedure and reaction conditions but the diffusion limitations are quite high since the first product has to get from one support to the next. Another advantage arises from the possible separation of toxic or inhibiting products on two different carriers.

Some reports on multienzyme catalysis in nanoporous materials already exist.^[10,101,119,212,213] During the design of multienzymatic reaction cascades the attention has to be especially drawn to the facile adjustment of the ratio of the enzymes. The combination of GOx and horseradish peroxidase (HRP) inside of porous hollow silica spheres reached the highest conversion of 4-aminoantipyridine and phenol with an excess of HRP.^[214] The encapsulation of both enzymes inside the hollow spheres stabilized both enzymes and encouraged the authors to use their material for the oxidation of PAHs performed by GOx and hemoglobin as a pseudoperoxidase in a stirred tank reactor. However, in this reaction cycle the immobilization of hemoglobin was more efficient on mesoporous silica. Hence, the oxidation of PAHs occurred on two separate materials with a high excess of hemoglobin better than the co-immobilization of both enzymes.

Recently, benzene and ethane PMOs with SBA-16-like structures and pure SBA-16 were used to immobilize a two enzyme cascade of D-amino acid oxidase (DAAO) and glutaryl-7-amino cephalosporanic acid acylase (Gl-7-ACA acylase) that converts cephalosporin C to glutaryl-7-amino cephalosporanic acid (Scheme 1.4), an important precursor for the synthesis of antibiotics.^[119] The best results for the immobilization of DAAO exhibited the best results on the ethane-bridged PMO obtaining increased stability and activity compared to SBA-16 immobilized DAAO. GL-7-ACA acylase was most active in the ethane-bridged PMO but this material had the lowest loading of protein. The authors assumed that the mass transfer resistance in the other materials led to reduced activity. Since both systems were studied independently they have to be combined in the future. Owing to different performances in adsorption and catalysis the

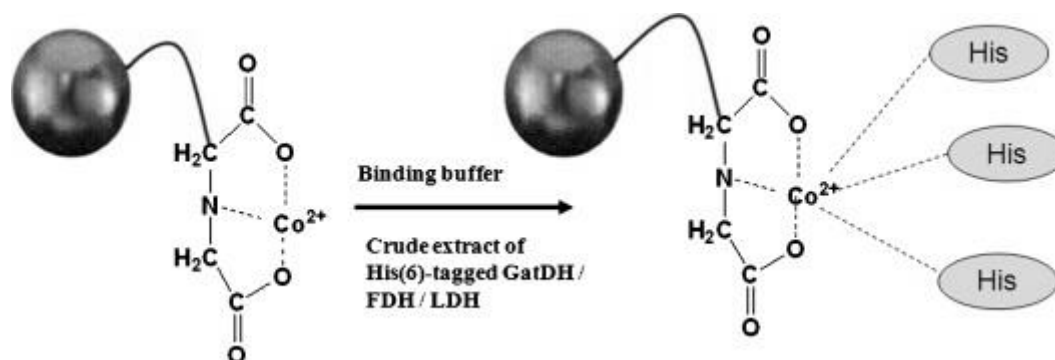
enzyme would be probably not co-immobilized but immobilized on two separate materials.



Scheme 1.4: Biocatalytic approach to cephalosporin C to glutaryl-7-amino cephalosporanic acid by DAAO and GL-7-ACA acylase.

Multienzyme-cascades have been also performed on magnetic composite materials.^[190,204,215,216] In the context of biomass hydrolysis Yang et al. performed a co-immobilization of α -amylase and glucoamylase on magnetic chitosan beads. The effectivity of starch hydrolysis was greatly enhanced compared to the use of single enzymes since the starch was hydrolyzed at different glycosidic bonds.^[204]

Many enzymes use expensive cofactors (e.g. NADPH, NADH) to catalyze reactions thus it is important to develop new methods for regeneration, immobilization or surrender of the cofactor.^[10–12,170,217–219] One approach is the enzymatic regeneration of cofactors. This approach was recently studied by Rocha-Martin et al. with a variety of enzymes attached covalently to different supports. In their multienzyme cascades co-immobilized enzymes performed better than separately immobilized ones. They were able to locate both enzymes using confocal laser scanning microscopy and obtained a homogenous mixture of both.^[219]



Scheme 1.5: Illustration of one-step purification and immobilization of His-tagged GatDH, FDH and LDH onto iminodiacetic acid modified magnetic nanoparticles. Co^{2+} is complexed by iminodiacetic acid and the His-tag of the respective protein. Thus the protein is recovered from the solution. Reprinted with permission from Elsevier.^[170]

Another approach is the immobilization of cofactor and enzyme. The co-immobilization of cofactors is an easy straightforward process to circumvent the difficulty of cofactor recycling. Alcohol dehydrogenases (ADHs) are NAD^+ or NADP^+ dependent enzymes that are often applied in redox reactions. Galarneau et al. encapsulated alcohol dehydrogenase and NAD^+ in a sponge-like mesoporous silica.^[220] Simple adsorption of NADP^+ in SBA-15 was reported by Vittorini et al. for the reduction of 6-methyl-5-hepten-2-one by ADH.^[221] This reaction was performed in a two-phase system where the organic phase was able to sufficiently solubilize the hydrophobic educt. The regeneration of NADPH was achieved in the aqueous phase by oxidation of 2-propanol by ADH. The benefit of this approach is the simultaneous oxidation and reduction performed by only one protein and hence the simple design of only one support. The third approach is the complete avoidance of cofactors. Weber et al. immobilized only the heme domain of monooxygenase and not the whole enzyme. The isolation of the heme domain and immobilization on SBA-15 proofed the successful application in hydroxylation of different organic substances.^[75]

Two very interesting multienzymatic pathways combined with cofactor regeneration were performed by Demir et al.^[170] Affinity iron oxide beads (Scheme 1.5) have been used as support and simultaneously for purification of His-tagged galactitol dehydrogenase (GatDH). Two cascades were built up, one for the synthesis of 1,2-propanediol by GatDH with cofactor regeneration by formate dehydrogenase (FDH) and the second one for the synthesis of L-tagatose with GatDH and lactate dehydrogenase (LDH) as cofactor regenerator NADH/NAD^+ . This approach shows that

versatile and effective catalytic cycles can be obtained having cofactor regenerating enzymes.

2 CHARACTERIZATION TECHNIQUES

2.1 POWDER X-RAY DIFFRACTION (PXRD)

Powder X-ray diffraction (PXRD) is a technique mainly used for the identification of crystalline phases, the determination of crystallite size and the identification of structural defects. The sample is irradiated with a monochromatic X-ray beam which is diffracted at the crystal lattice planes. The obtained diffraction patterns are a result of constructive (Figure 2.1) or destructive interference of the scattered X-rays.

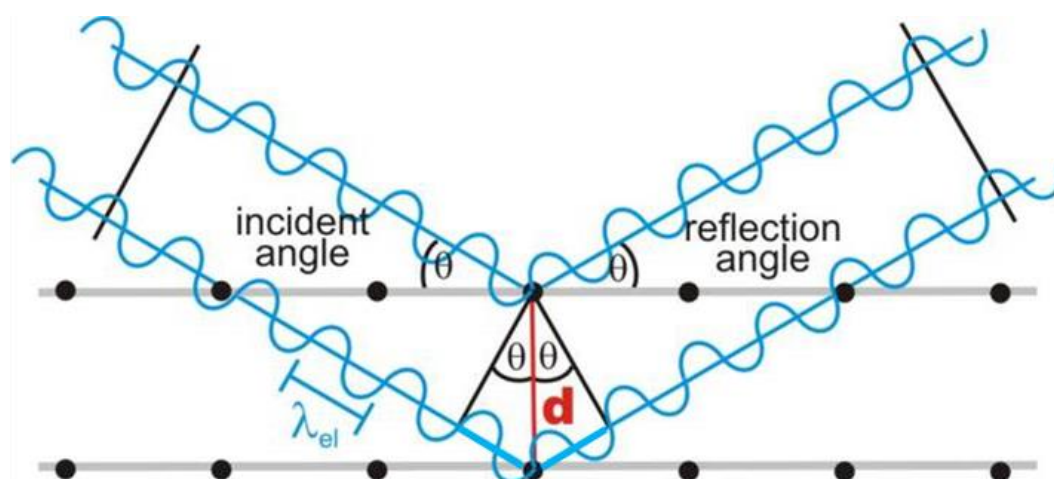


Figure 2.1 Illustration of Bragg's law at crystal lattice planes with an interplanar spacing d . Constructive interference is obtained when the path difference of the diffracted X-ray beam equals a multiple integer of the wavelength λ_{el} of the incident beam with an angle θ .

According to Bragg's law (Equation 2) constructive interference is observed when the path difference of the diffracted beam is a multiple integer of the wavelength of the incident beam.

$$2d\sin\theta = n\lambda \quad (2)$$

d = interplanar spacing

θ = diffraction angle

λ = wavelength

Not only amorphous materials can be analyzed by XRD but also amorphous materials with periodic structures. Mesoporous silicas, for example, have highly periodic structures that result in reflections in the region of small angles. For materials, polymers or liquid crystals with even larger periodicity, small-angle X-ray scattering (SAXS) is a useful method. SAXS is a technique similar to conventional PXRD with much smaller incident angles that allow detecting periodicities of up to 150 nm.

2.2 CHARACTERIZATION OF POROSITY

Different regimes of porosity (Figure 2.2; micro-, meso-, macropores) usually require different techniques to obtain information about pore size distribution (psd), surface area, pore volume, porosity and many more. Whereas those parameters can be easily accessed for micro- and mesoporous materials by gas physisorption the filling of macropores larger 200 nm is not possible with for example nitrogen or argon. Mercury porosimetry is the only method that covers a pore size range of several magnitudes including meso- and macroporous samples. A combination of gas adsorption and mercury porosimetry offers an extensive investigation of materials with micro-, meso- and macroporosity.

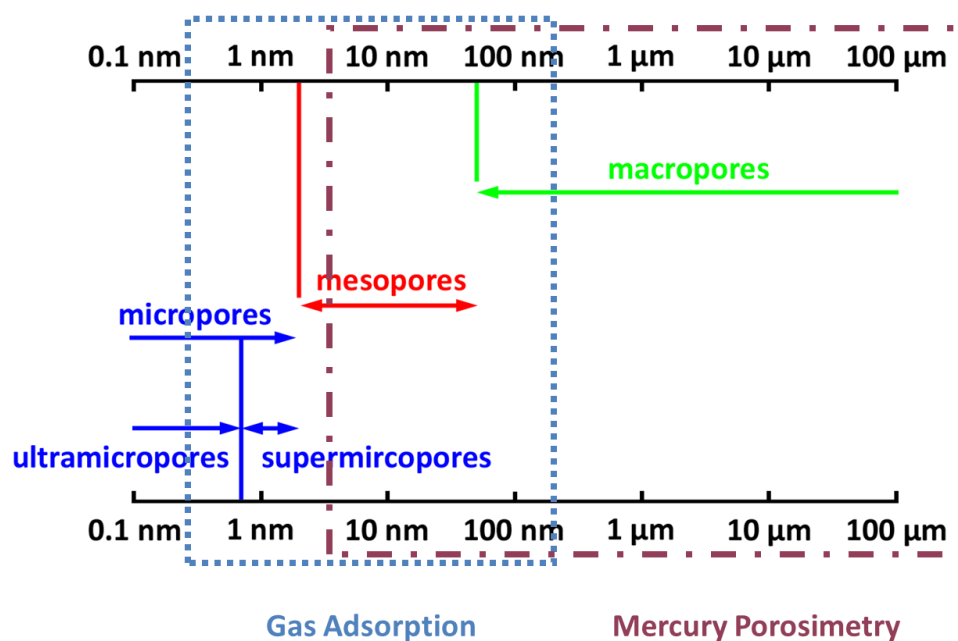


Figure 2.2: Classification of porous materials according to the *Union of Applied Chemistry* (IUPAC) and respective analytical methods.

The nature of the porous surface is another important aspect where gas adsorption can give further information. Solid-state NMR, vibrational spectroscopy, zeta potential, thermal analysis are common techniques that are applied to further elucidate the surface groups. But sorption in general can add important information concerning the interaction with different molecules. Water vapor sorption for example is a technique that is highly sensitive towards the hydrophobicity of materials.

2.2.1 VOLUMETRIC NITROGEN PHYSISORPTION

The physisorption of a gas (adsorptive) onto a solid material (adsorbent) is a reversible process that occurs spontaneously whenever a gas is brought in contact with a surface. The resulting adsorbate consists of the matter in the adsorbed state. Dispersion forces are the main forces leading to adsorption, less often ionic or dipole interactions are present. An important peculiarity of nitrogen is its quadrupole moment that can lead to additional interactions with polar solids. This effect is further discussed in the section of surface area analysis.

The IUPAC defined six different isotherm types (Figure 2.3) that are generally obtained whereas type I and IV isotherms are the most common ones.^[222] All isotherms exhibit a strong increase in amount of adsorbed gas approaching p/p_0 that is associated to the condensation of the bulk adsorptive. Gas adsorption in microporous solids commonly gives a type I isotherm. The characteristic steep increase in amount of adsorbed gas at low p/p_0 is associated to a minimum in the potential energy created by a potential overlap of neighboring walls. Thus the adsorption process in micropores is dominated by fluid-wall interactions and proceeds continuously.

In contrast, the filling of mesopores consists of monolayer and multilayer formation accompanied by capillary condensation at higher p/p_0 (type IV isotherm). During monolayer coverage fluid-wall interactions are dominant whereas fluid-fluid interactions lead to capillary condensation and multilayer formation. For mesoporous materials with pores larger 4 nm the isotherm usually shows hysteresis. Hysteresis H1 is usually observed for mesoporous materials with cylindrical pore geometry. This type of hysteresis is assigned to the intrinsic properties of the vapor-liquid phase transition. It is usually discussed in terms of a nucleation barrier that arises due to the formation of a

new interface during capillary condensation. Since the desorption proceeds via a receding meniscus without the effort to build new interfaces it is in thermodynamic equilibrium. H2-H3 hystereses cannot be explained by a so-called “single-pore model” since they are associated with network effects in interconnected pore networks. H2 hysteresis is usually observed in ink-bottle pores where cavitation or pore blocking phenomena occur. The nearly horizontal hysteresis H3 is a less common hysteresis type caused by specific geometrical assemblies of pores or particles. H4 hysteresis is observed for slit-shaped pores, for example in carbons with micro- and mesoporosity.

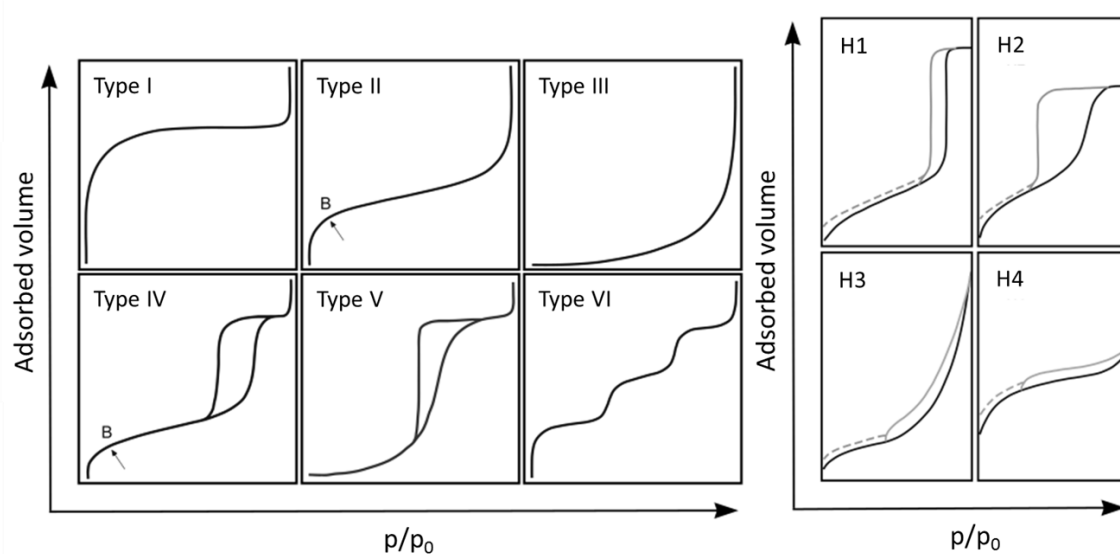


Figure 2.3: Classification of the adsorption isotherms and corresponding hysteresis curves according to IUPAC.

The adsorption in non-porous and macroporous materials proceeds via layerwise adsorption (type II). Type III and V isotherms are characteristic for materials with low adsorbent-adsorbate interactions. The less common Type VI isotherm denotes stepwise multilayer adsorption whereas the monolayer capacity can be obtained from each the step.

Determination of the specific surface area

Most methods for the determination of a specific surface area of a porous material are based on the prediction of the adsorbate molecules needed to cover the surface with a monolayer. One of the first methods is the Langmuir isotherm that is similar to the type I

isotherm. However, this model is today only used for chemisorption since it is limited to a few molecular layers.

The BET method named after the inventors Brunauer, Emmett and Teller, is the most widely used technique.^[223] It is an extension to the Langmuir theory based on the formation of multiple layers. A few assumptions the BET theory is based on are still highly discussed. For example it is stated that the adsorption sites are energetically equivalent and that there is no interaction of the adsorbate molecules in the layers. However, it is still the method of choice for mesoporous as well as microporous materials since it allows a good comparability of the materials. The linear form of the BET equation (Equation 3) directly relates the surface occupancy to the partial pressure. Thus a monolayer capacity and from that the specific surface area can be obtained.

$$\frac{\frac{p}{p_0}}{n \left(\frac{1-p}{p_0} \right)} = \frac{1}{n_m C} + \frac{C-1}{n_m C} \left(\frac{p}{p_0} \right) \quad (3)$$

p = vapor pressure of the adsorptive

p_0 = saturation pressure of the adsorptive

n_m = monolayer capacity

n = amount of adsorbate

C = BET constant

Another major problem associated with the BET theory is the cross-sectional area of the adsorptive nitrogen. Since nitrogen is a quadrupole it interacts with polar surfaces and thus increases its cross-sectional area (0.162 nm²). It is assumed that the BET surface area overestimates the surface area of silicas up to 25 % using the common cross-sectional area of nitrogen.

Determination of the pore size distribution

Two kinds of approaches exist to analyze the pore size distribution of materials. Macroscopic approaches (e.g. Barrett-Joyner-Halenda (BJH)) are based on the Kelvin equation and therefore on the assumption that the pore fluid can be described as bulk

liquid. Molecular approaches (e.g. Nonlocal DFT (NLDFT)) have established electron density profiles for the confined adsorbate in the pores. These profiles give a much better insight into the thermodynamic state of the pore fluid. The most important methods are discussed here shortly.

The BJH method was one of the first to connect the partial pressure of the capillary condensation to the pore radius.^[224] This approach considers the capillary condensation as a shifted phase transition from bulk gas to bulk liquid. This simplification underestimates pore sizes of up to 30 % since the preadsorbed layer is neglected. Although it is known that this is a simplification of the state of the confined pore fluid, this theory is still widely used especially for pore sizes larger 20 nm. With increasing pore size the adsorbed fluid becomes more and more a bulk fluid.

Approaches that are based on density functional theory (DFT), eg. nonlocal DFT (NLDFT), quenched solid DFT (QSDFT), describe the state of the pore fluid more exact since they approach from the molecular level.^[225,226] These methods calculate a set of model isotherms (kernel) for a set of pore sizes and compare it to the experimental data. Since the fluid-solid interactions are implemented in this theory each pore shape or model has its own set of isotherms. The QSDFT is a relatively new extension of the NLDFT that takes the inhomogeneity of the pore wall into account.^[225]

2.2.2 GRAVIMETRIC WATER VAPOR SORPTION

In contrast to the physisorption of gases that are not sensitive to the surface chemistry, like argon or nitrogen, water is interacting with polar surfaces.^[227] Thus, the analysis and interpretation of water vapor adsorption data is not straightforward and the theories are still widely discussed. Nevertheless, some facts on the interpretation and mechanism of water adsorption are already known:

- 1) The water molecules are either physisorbed or chemisorbed.
- 2) The polar structure of water allows the molecules to create hydrogen bonds to the adsorbent as well as among themselves.

3) The uptake of water in porous materials is not only influenced by their hydrophobic/hydrophilic nature but also strongly by their porosity, especially their pore volume.

A mesoporous more hydrophilic material, like SBA-15, has not necessarily a higher water uptake than a microporous carbon. Since water has a small kinetic diameter (0.28 nm) it can access even very small pores. But weak interactions between water and adsorbent shift the adsorption to higher p/p_0 and reduce the theoretically accessible pore sizes so that large mesopores are not filled.^[228]

Water adsorption onto porous materials can give information on the stability of compounds in aqueous solution, their water sorption capacity as well as their hydrophilicity. But a simple classification into hydrophilic and hydrophobic materials is not as easily made since the definition of hydrophobicity is not straightforward. Therefore, different so-called hydrophobicity indices (χ) have been proposed in the last decades.^[227] Some of the approaches are based on thermogravimetric data and some on adsorption measurements. The thermogravimetric analysis was applied by Anderson et al. who compared the mass loss of water at two different temperatures.^[229] They assumed that loosely adsorbed water was evaporated prior to 150 °C and strongly adsorbed water above 150 °C. This definition was extended for porous solids by Giaya et al. who compared the volume of strongly adsorbed water to the pore volume of the solid.^[230] Another classification of water adsorption in porous solids can be done by their adsorption isotherms that have been discussed in chapter 2.2.1. Type I, II, IV and VI denote hydrophilic materials whereas hydrophobic or low hydrophilic materials are characterized by type III and V isotherms.

For highly hydrophobic materials that exhibit water adsorption capacities lower than their pore volume a linear increase with a flat slope (type VII) is observed (Figure 2.4). However, these isotherms are not suited to compare or quantify the hydrophilic/hydrophobic behavior of porous materials. First attempts have been made to use the slope at low coverage for a comparison but the different isotherm shapes make a reliable quantification impossible.^[231] Weitkamp et al. compared the adsorption of water vapor sorption and hydrocarbons to quantify the hydrophilicity of materials.^[232] Although this method is a good tool for the water affinity it is limited due to the

exhaustive measurement process. Thommes et al. defined a more simple approach for the analysis of nanoporous materials.^[233] The χ related the ratio of the adsorbed volume of a completely wetting liquid (e.g. Ar, N₂) to water as a partially wetting liquid at different p/p_0 .

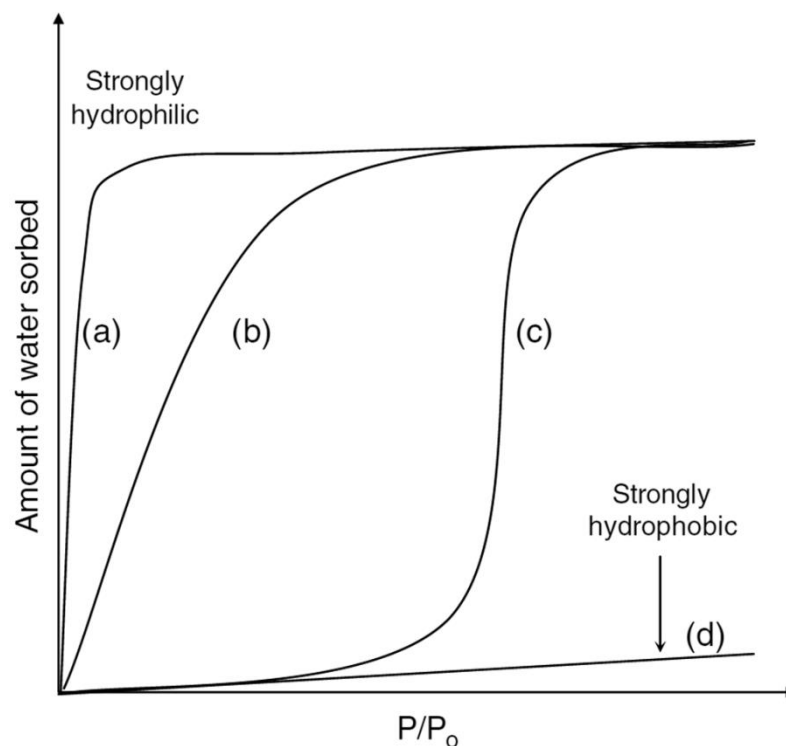


Figure 2.4: Adsorption isotherms type I (a,b), type V (c) and type VII (d) for materials with the same pore volume. The hydrophilicity is decreasing from a to d. a and b denote a type I isotherm where the slope can be directly correlated to the hydrophilicity. Adsorption of water at lower p/p_0 is observed for sample a indicating higher hydrophilicity. The spontaneous increase of adsorbed water for sample c denotes the point of cluster condensation. The strongly hydrophobic material has an adsorption capacity lower than its pore volume. Reprinted with permission from Elsevier.^[234]

The mechanism of water vapor adsorption in porous materials was extensively discussed in the last decade.^[227,235–238] Mesoporous silica is one of the most investigated materials in that field. The amorphous character of silica leads to a number of silanol groups on the surface that are more or less part of the adsorption process. In the region of low p/p_0 the silanol groups are rehydroxylated depending on the pretreatment of the sample. Usually, the desorption of water from a silica surface is not complete since a part of the water is chemisorbed at the surface. The terminal silanols are the most acidic sites and bind water first. In the next step the formation of water clusters occurs. Then the hydrophobic isolated silanols as well as the siloxane bridges are taking part in the

adsorption process. In most cases a hysteresis in the adsorption isotherm occurs. In the term of adsorption of completely wetting adsorptives the adsorption proceeds via multilayer coverage. In terms of water adsorption a so-called water-mediated cluster filling is proposed.^[239,240] The water clusters are built due to hydrogen-bonds between the water molecules. Ice-like clusters are believed to be the most stable and they are further stabilized via intercluster hydrogen bonds. After a critical size, dependent on the relative humidity, exceeded capillary condensation is observed. The critical size denotes the moment where the potentials of the clusters are overlapping and an energy minimum is reached. Desorption proceeds by molecular evaporation in equilibrium. A highly discussed topic was the location of the water-cluster formation. Dubinin et al. proposed that functional groups are the preferred cluster sites but other researchers showed that carbon without any oxygen groups shows cluster-formation too.^[240]

All in all the combination of physisorption of wetting adsorptives and water vapor sorption offers a variety of information. The determination of water adsorption capacity was proven to be a useful tool in enzyme immobilization in the last years especially for the immobilization of lipases in hydrophobic silicas.

2.2.3 MERCURY POROSIMETRY

Mercury porosimetry is a widely used technique to access the surface area, pore size distribution, pore volume, tortuosity, permeability, compressibility, density and network effects of meso- and macroporous solids.^[241–245] Whereas the pore volume is directly measured all other parameters are derived from pore volume and applied pressure and have more or less high source of errors in their calculation. The pore size distribution can be calculated straightforward from the data using the Washburn equation that is derived in this chapter. Washburn proposed that a porous solid behaves like the assembly of small cylindrical capillaries.^[246] Therefore, the intrusion of mercury can be considered in terms of capillarity.

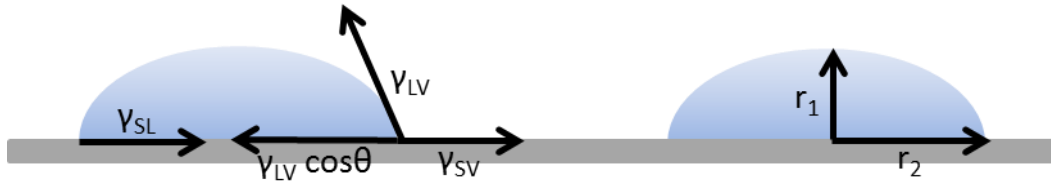


Figure 2.5: Direction of interfacial forces present in a liquid drop (left). The interfacial tension between solid and liquid (γ_{SL}) as well as the cosine of the tangentially liquid-vapor tension (γ_{LV}) act towards the center of the particle. In contrast, the solid-vapor tension (γ_{SV}) tends to spread the particle on the substrate. Depiction of the radii of curvature across a liquid drop (right).

In contrast to water vapor sorption on hydrophilic materials as well as gas physisorption, mercury porosimetry deals with a non-wetting liquid. The wettability of a solid by a liquid is depending on three adhesive or cohesive forces (Figure 2.5) applied at the interfaces. The interfacial energy γ_{SV} between solid and vapor is produced by a film of liquid molecules on the solid produced by the vapor pressure. This phenomenon draws the liquid further to the outside. In contrast the tension γ_{LV} between liquid and vapor as well as between solid and liquid γ_{SL} is directed towards the center of the liquid drop. An equilibrium between these forces results in a stable liquid drop.

As shown in Equation 4 (Young equation), the contact angle θ is a direct measure of the wettability. Contact angles larger 90° define situations of non-wettability and smaller 90° of wettability. The contact angle of mercury is still a highly discussed issue since it changes due to the substrate. For comparability reasons a contact angle of 140° is used since it was found to be an adequate mean for contact angles on several substrates.^[247]

$$\cos\theta = \frac{\gamma_{SV} - \gamma_{SL}}{\gamma_{LV}} \quad (4)$$

The Young-Laplace equation (Equation 5) describes the pressure difference Δp across a liquid surface in terms of the radii of curvature (r_1 and r_2) and the surface tension γ .

$$\Delta p = \gamma \left(\frac{1}{r_1} + \frac{1}{r_2} \right) \quad (5)$$

Non-wetting liquids like mercury have to be forced inside a capillary since they underlay capillary depression. The meniscus in a capillary with spherical cross-section is

spherical and hence r_1 and r_2 from Equation 5 are equal. Thus the equation is simplified to:

$$\Delta p = \frac{2\gamma}{r} \quad (6)$$

Taking into account the relation for the pore radius in a cylindrical capillary the Washburn equation (Equation 7) that directly relates the pore radius to the pressure difference is obtained. Δp can be described as p since the evacuation of the capillary in the case of mercury intrusion diminishes the external pressure and only the internal pressure p induced by the surface curvature applies.

$$pr = -2\gamma \cos\theta \quad (7)$$

However, one has to be aware that the Washburn equation is only related to cylindrical pores. Nevertheless, it provides a simple conversion of the measured parameters to the pore size.

Intrusion-extrusion curves for the wide pressure range are obtained by two different experimental setups. The low pressure measurement is performed with a pneumatic apparatus and the high pressure measurement with a hydraulic apparatus. The pressure and the volume of intruded mercury are monitored during the experiment whereas the contact angle (140°) and surface tension of mercury (0.484 Nm^{-1} at 25°C) are constant. The first step is to evacuate the sample cell to remove contaminants and air, afterwards the mercury is pressurized stepwise to enter the sample cell. The intruded volume is monitored by measuring the capacitance between the mercury column and a metal plate. Thus by increasing pressure the mercury is moving upwards in the capillary stem, the length of mercury in the capillary is decreasing and the capacitance is correlated to the intruded volume. The first data point is usually obtained at pressures of 3000-4000 Pa. Measurements at lower pressure can be done but are highly questionable since the pressure difference (head pressure) through the sample is very high.

For high pressure measurement the penetrometer is transferred into the high pressure station where an electromotor increases the pressure up to 400 MPa. In

general, two methods exist to obtain high pressure analysis: The incremental mode increases the pressure gradually until equilibrium is obtained. This method is pretty time-consuming and reduces the number of data points but assures that the equilibrium is reached for each data point. The continuous mode is a fast method that acquires a lot of data points to ensure that every detail in the sample composition is measured. However, if the rate of intrusion is too fast the equilibrium is not reached and temperature effects can occur.^[242]

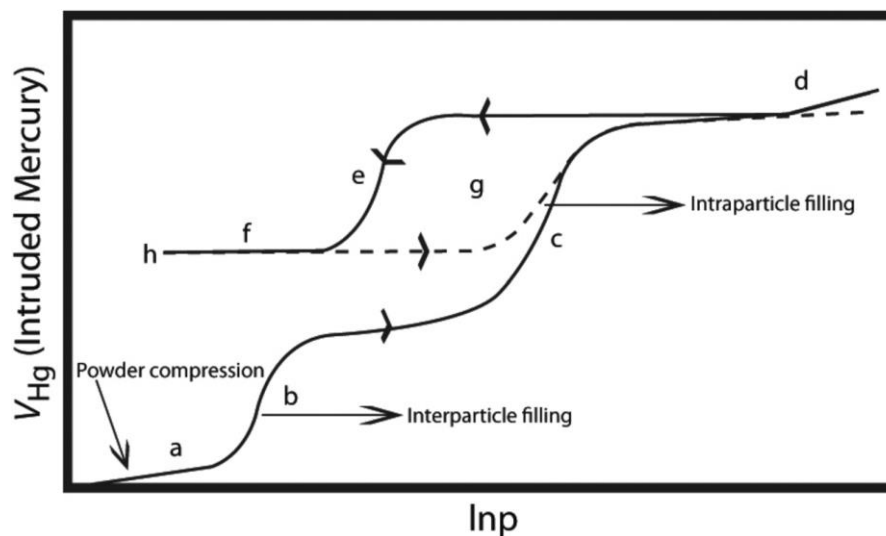


Figure 2.6: Schematic plot of the applied pressure and the intruded volume of mercury (intrusion-extrusion curve) showing several possible steps. Starting with the densification (a) of a powder and interparticle filling (b). Afterwards mercury enters the porous network (c) and sometimes higher pressure leads to reversible or irreversible compression (d) of the solid. In the extrusion process a hysteresis (e) is observed that usually closes (g) after the second intrusion. Mercury remains trapped in the pores after the first (f) and following cycles (h). Figure reprinted with permission from Elsevier.^[244]

A schematic intrusion-extrusion diagram is depicted in Figure 2.6. The rearrangement of particles in powders gives a small increase in intruded volume (a) prior to filling of interparticle voids (b). Both steps are not obtained with monolithic materials or large granules. The pore filling (c) is usually the step with the largest increase in intruded volume. In some solids reversible or irreversible compressibility (d) is obtained at high pressure. The extrusion is never following the same path as the intrusion curve. A more or less large hysteresis (e) is obtained. The origins of hysteresis were extensively discussed.^[241,243] In general discrimination between “single-pore” and network models is made. One of the first “single-pore” models proposed a different contact angle for receding and advancing mercury.^[248] However, this was questionable in

thermodynamically point of view and was not able to explain the differences in the shape of hysteresis. Today, it is generally believed that a mixture of structural effects and an energy-barrier during extrusion leads to a delayed extrusion of mercury.^[243] The energy barrier or sometimes called nucleation barrier is due to the formation of new interfaces during extrusion. Thus the increase in interfacial energy needs to be overcome by an excess pressure. The structural effects result from pore blocking and percolation effects also known from gas physisorption. Since the effect leads to a delayed extrusion the pore size is always determined from the intrusion. Mercury entrapment (f) is obtained in all experiments. Theoretic and experimental results show that the extrusion and intrusion is conducted via mercury bridges. During the extrusion process the mercury bridges can rupture at junctions or small restrictions even at a rough surface. Thus not all mercury can be removed from the sample. If a next intrusion cycle is performed the loop closes (g) and no additional entrapment (h) occurs.

2.3 LIGHT SCATTERING TECHNIQUES

Light scattering techniques are widely used to obtain information about sizes as well as the surface of particles. The measurement of these parameters benefits from the ability of solid matter to scatter light. Different scattering forms are observed depending on the wavelength of the light source and the size of the scattering object.

When the wavelength of light and the object are of similar size, asymmetrical Mie scattering is observed. In contrast, considering a monochromatic laser beam with a wavelength of 633 nm that interacts with a very small object like a nanoparticle, Rayleigh scattering is observed. The light is scattered homogeneously by the particle. In the techniques discussed below such quasi-elastic scattering is observed and from the detection of the scattered light information about the scattering object is extracted. Although both techniques are based on the scattering of light several differences in the experimental setup, the detection and processing of the data are present.

In the following chapters a short introduction of zeta potential measurements as well as dynamic light scattering for particle size determination is given.

2.3.1 DYNAMIC LIGHT SCATTERING (DLS)

Light scattering experiments are divided in static and dynamic methods that are distinguished by the detection periods of the scattered Rayleigh radiation (with classical lasers). Static light scattering, generally used for size determination of macromolecules, uses periods in the millisecond-range whereas much shorter (nano- to microseconds) are used for the dynamic light scattering (DLS). The short time frame for the DLS allows measuring the particle movement in dispersions that is induced by collision of the particles with solvent molecules due to thermal energy.^[249] This random movement is called Brownian motion and contains size information of the dispersed particles. The hydrodynamic diameter of an object is correlated to the diffusion since large particles will be slower than the diffusion of smaller particles. The Stokes-Einstein equation (Equation 8) mathematically relates the hydrodynamic diameter d_H of a spherical object to the diffusion coefficient D .^[250]

$$d_H = \frac{kT}{3\pi\eta D} \quad (8)$$

Although the size is one of the most important influence factors for the diffusion properties, the viscosity η and the ionic strength of the solvent are important to consider. To simplify a size measurement the viscosity of the solution is held constant. The nature of the surface of the particles can significantly alter the hydrodynamic radius since it changes the thickness of the double layer.

The setup of a DLS experiment is shown in Figure 2.7. A monochromatic laser beam is focused onto the sample compartment. After entering the sample compartment most of the beam leaves the cuvette unscattered while a smaller part of the light is scattered (Rayleigh-scattering) by the particles in solution. Since the scattering is quasi-elastic the detection of light is possible in every direction to the sample compartment. Here an angle of 173° is used to minimize the effect of multiple scattering. The intensity of the laser light is measured by a detector. Due to the random Brownian motion of the particles the intensity of the scattered light at one position is fluctuating. The fluctuation rate is monitored and correlated to the size of the particles by the diffusion coefficient.

A digital correlator monitors the randomly fluctuating intensities detected at defined time intervals τ in the μs -range and compares the intensity. The similarity of the signals is decreasing with time or in other words, the correlation is decreasing with time. The steepness of the correlation curve is directly related to the size of the particles.

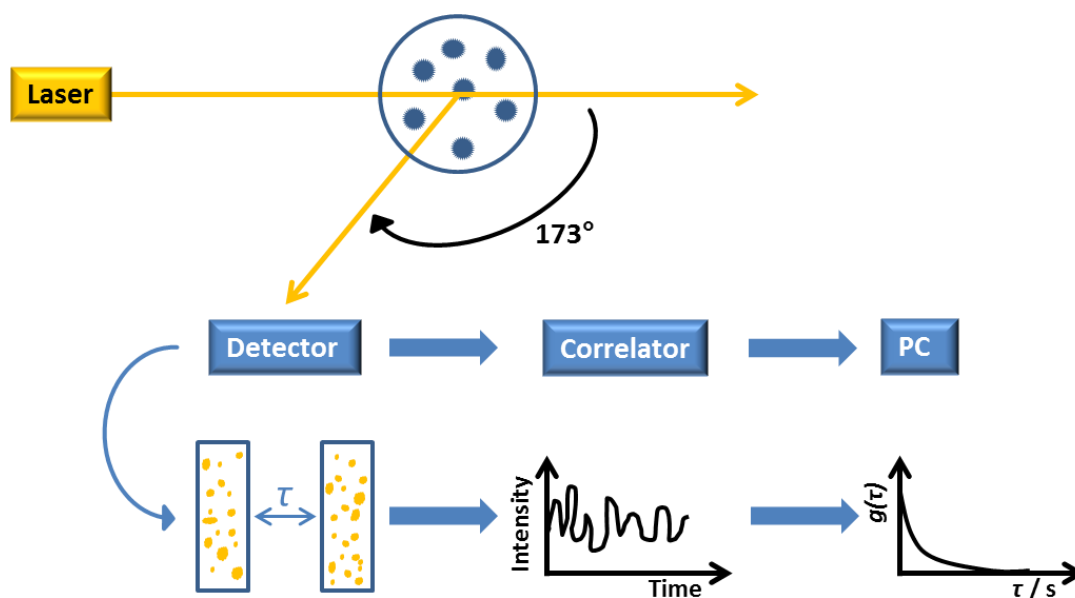


Figure 2.7: Schematic illustration of a DLS experiment. The particles in a sample compartment scatter a part of the incident laser light. The scattered laser light is measured at periodic time intervals τ by a detector. The similarity or so called correlation at these time intervals is processed by a digital correlator and the correlation curve is derived from several algorithms in the corresponding software.

To obtain a result for all measurements the obtained data is further processed by multiplication of both intensities ($I(t)$, $I(t+\tau)$) and afterwards an average over all measurements is created by an autocorrelation function (Equation 9):

$$g(\tau) = \langle I(t) \cdot I(t + \tau) \rangle \quad (9)$$

After applying the correlation function, several algorithms can be used to derive the intensity based size information. A simple exponential decay (“Cumulants analysis”, Equation 10) can be fitted to the correlation function of monodisperse samples with the baseline A and intercept B . The function Γ relates the correlation function to the diffusion coefficient D and the scattering vector length q .

$$g(\tau) = A[1 + B \cdot e^{(-2\Gamma\tau)}] \quad (10)$$

$$\Gamma = Dq^2$$

$$q = \frac{4\pi n_0}{\lambda} \sin\left(\frac{\theta}{2}\right)$$

A more complex method (e.g. "CONTIN") that uses the sum of exponential decays for all obtained sizes is used for polydisperse particles. Both methods use the obtained diffusion coefficient to solve the Stokes-Einstein relation and obtain the hydrodynamic radius. Generally, the distribution data is obtained from an algorithm that fits the sum of exponential decays since this allows generating the size information for all size measurable with this technique. On the other hand the cumulants analysis is related to the direct size information like the polydispersity index (Pdl) and the Z-average. The Z-average is the intensity-based mean size information derived from the cumulants analysis whereas the Pdl gives information on the broadness of the distribution and hence if a sample is mono- or polydisperse (Pdl > 0.05).

The intensity based size information obtained by this method can be further converted to a volume or number distribution. Since the radius is introduced exponentially into volume and number distribution the error obtained with both distributions can be very high. However, the number distribution is the method that is most comparative. In a polydisperse sample smaller particle can diminish in the volume and intensity distribution compared to larger ones.

2.3.2 ZETA POTENTIAL MEASUREMENTS

The zeta potential or electrokinetic potential is a measure to describe the charge environment of a particle in a liquid at defined conditions.^[251,252] From the zeta potential information on the electrostatic interaction of the particle with other charged objects or between the particles itself can be derived. The particle interactions are the main driving forces for the stabilization or destabilization of colloidal systems addressed by the DLVO theory (named after the scientists Derjaguin, Landau, Verwey and Overbeek). Although it is based on several assumptions the DLVO theory is still suitable and descriptive for

particle interactions in solution. The surface of the particles is simplified as infinite uniform and flat with a homogeneous charge density. Electric potential of the particle surface as well as ion concentration are assumed to be constant in the colloidal system. The DLVO theory mainly takes repulsive electrostatic and attractive van der Waals forces into account. Another very small contribution to the total potential energy of the colloid is added by the potential energy provided by the solvent. The potential of the attractive van der Waals forces V_A is based on the following equation that is directly correlated to the particle distance D with the Hamaker constant A :

$$V_A = \frac{-A}{(12\pi D^2)} \quad (11)$$

The repulsive forces are generated by the electrostatic repulsion of the electric double layer. Thus the potential V_R is directly related to the zeta potential ζ and the particle distance D according to the following equation with the solvent permeability μ , the particle radius r and the Debye length κ :

$$V_R = 2\mu r \zeta^2 e^{-\kappa D} \quad (12)$$

In Figure 2.8 the addition of attractive and repulsive forces to the total potential energy (interaction energy) as a function of the distance of two approaching particles is shown. When the function of the potential energy reaches a maximum that is larger 10 kT a repulsive barrier is created that cannot be overcome by Brownian motion. Thus flocculation is prevented and a stable colloid is obtained. If the secondary minimum is lower than zero the particle attraction is high and flocculation occurs.

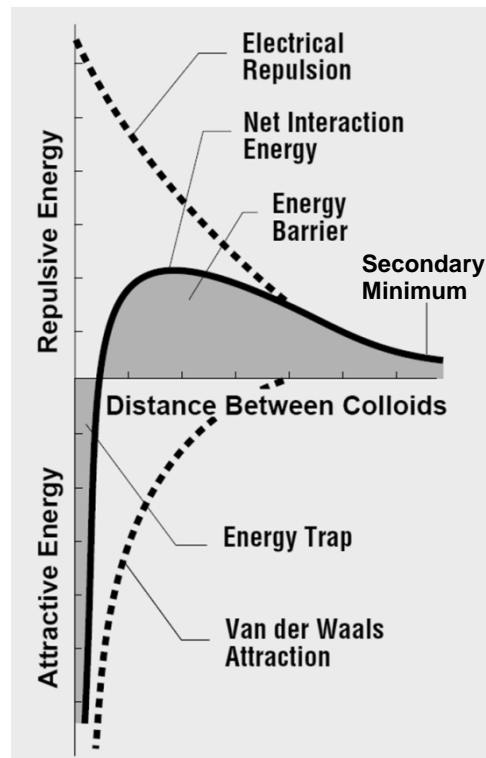


Figure 2.8: Potential energy of two particles as a function of their distance. The net interaction energy consists of van der Waals attraction as well as electrostatic repulsion of the electric double layers. If two particles are in very close contact a so-called “energy-trap” is created by the high attraction of the particles and thus aggregation is observed. An energy barrier of about 10 kT is considered as the border for stable colloids. At some conditions, like high ionic strength media, a secondary minimum of the net energy is observed where flocculation occurs. Usually, high salt concentrations lead to a reduction of the electric double layer thickness and hence less electrostatic repulsion.^[253]

The electrostatic forces in a colloidal system can be described with the model of the electrical double layer (Figure 2.9).^[252] The formation of an electric double layer is a direct result of an electrically charged surface. The first layer (Stern layer) of counter ions is directly associated to the surface of the particle to compensate the Nernst potential present at the surface. The potential at this strongly attached layer is called Stern potential. The second part of the double layer is a diffuse layer (Gouy-Chapman layer) of counter ions that are attracted by the solid particle and repelled by the ions in the Stern layer. The concentration of counter ions decreases with the distance from the solid surface.

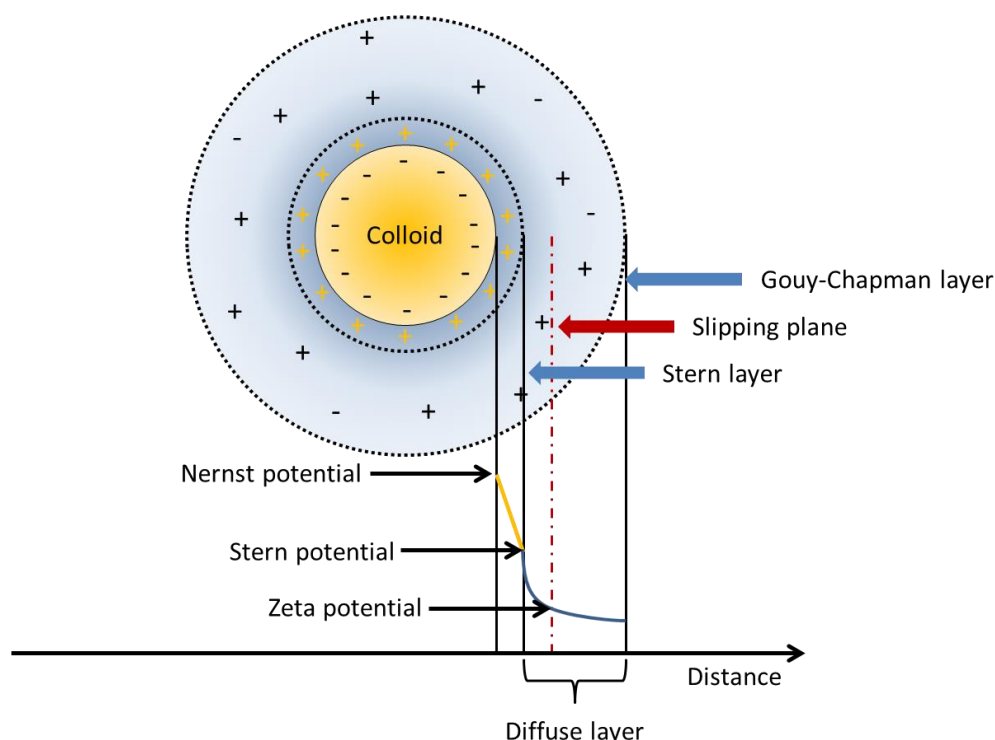


Figure 2.9: Schematic description of the charged environment of a particle in a solvent. The electrical double layer is built of the Stern layer and a diffuse layer. Within the thin Stern layer all ions are tightly bound to the particle. The potential is linearly dropping. The counter ion concentration is decreasing with the distance from the particle but until the slipping plane the ions still move in the particle boundary during particle movement. The potential at the slipping plane is called zeta potential.

A particle under Brownian motion has a border within the diffuse layer where the ions and solvent molecules directed toward the particle surface are dragged with the motion of the particle while another part stays in place. The potential at this so called shear or slipping plane between the charged colloid and the surrounding solution is called the zeta potential. The magnitude of the zeta potential is strongly dependent on the thickness of the double layer which can be modified changing the ionic strength or pH of a solution. Therefore it is reasonable to clearly define the measurement conditions and to perform titrations at various pH values. As a rule of thumb an absolute zeta potential larger than 30 mV denotes stable colloids whereas the lowest stability is observed at the isoelectric point (zeta potential = 0).

The zeta potential is directly related to so-called electrokinetic effects that occur when mobility of charged particles in a solvent is observed.^[252] The direction of the movement can either result from the charged surface or the solvent. Electrokinetic effects include: Electro-osmosis, electrophoresis, sedimentation and streaming

potential. The measurement of the zeta potential is mainly based on capillary electrophoresis. The electrophoretic mobility describes the motion of a particle in an applied field opposed by viscous forces of the solvent. Capillary electrophoresis is a common technique to determine the zeta potential of particles. The Henry equation (Equation 13) directly transfers the electrophoretic mobility U_E to the zeta potential ζ by known viscosity η and dielectric constant ϵ of the solvent.^[254,255] The Henry's function $f(\kappa a)$, that is the ratio of particle radius to the thickness of the electrical double layer, is treated as a constant. The equation is a combination of the equations derived by Smoluchowski and Hückel. The Smoluchowski approach ($f(\kappa a) = 1.5$) is applied working in aqueous solution with moderate electrolyte concentration and larger particles ($> 200 \mu\text{m}$). In contrast, dispersion in non-aqueous solvents with very small nanoparticles are represented by the Hückel approximation ($f(\kappa a) = 1$).

$$U_E = \frac{2\epsilon\zeta f(\kappa a)}{3\eta} \quad (13)$$

Although this equation is quite simple, the data processing and detection method is not straightforward. In electrophoretic measurements the experiment is performed in a capillary electrophoretic cell with a potential applied at the electrodes at both ends of the capillary. The particles are moving towards one of the electrodes depending on their charge. The polarization of the applied potential is periodically changed either in the slow (SFR) or fast field reversal mode (FFR). One problem arising with the SFR is the occurrence of electro-osmosis in the capillary. The applied field additionally increases the amount of counter ions moving to the respective electrode. The migrating ions drag the surrounding solvent with them and generate a flow towards one electrode and a backflow in the middle of the capillary. Therefore the measurement position is crucial since the flow would disturb the electrophoretic movement of the particles. At the stationary layer where both flow directions cancel each other out a measurement is possible but only a small part of the sample is measured. Changing the polarization fast so that the terminal velocity of the particles is reached, but the electro-osmosis is delayed, allows measuring a large part of the sample. Hence, the amount of particles

measured is high but the measurement time is too low to yield reliable distribution data. The combination of both methods consecutively provides both a reliable size and distribution data.

The detection of the particle movement is performed by Laser Doppler Velocimetry (LDV). Therefore, the incident laser beam is splitted prior to entering the capillary in a reference and a scattering beam. The latter enters the capillary filled with the sample and is scattered by the particles moving in solution. According to the Doppler Effect the light scattered by a moving object experiences a phase shift. Due to its high frequency the phase shift of the scattered laser beam is not directly detectable. Thus a modulated beam is generated by combining reference and scattered beam after leaving the sample area. This optical modulator approach leads to a lower frequency after constructive and destructive interference of both beams and thus can be detected. The modulated beam frequency is afterwards compared to the reference beam frequency that was obtained by modulation with a beam generated by an oscillating mirror. The Doppler Shift between both modulated beams contains the information of the particle mobility which is further converted to the zeta potential by the Henry equation.

2.4 ULTRAVIOLET-VISIBLE SPECTROSCOPY (UV-Vis)

An incident electromagnetic wave can interact in several ways with matter: reflection, scattering and absorption. The absorption of light in the ultraviolet and visible range transfers the molecules in electronic excited states. Thus the absorption of energy at distinct wavelength from the incident light causes a reduction of the intensity of the light that passes through the sample. The measure that is usually monitored is the transmittance given by the ratio of transmitted to incident light.

In general, UV-Vis spectroscopy is used for quantitative analyses according to the Lambert-Beer law or kinetic measurements. Qualitative analysis is less often performed since the broadness of the bands for the electronic transitions is a problem for obtaining good qualitative analyses. For protein analysis kinetic enzyme activity measurements and determination of the protein concentration are widely used techniques. While the kinetic measurements usually monitor the conversion of a substrate that absorb in the

UV-Vis region, protein concentration assay use colored dyes to determine the concentration. The direct measurement of the protein concentration due to the absorbance of the aromatic amino acids is possible but in many cases not feasible.

2.5 ELECTRON MICROSCOPY

One of the major advantages of an electron microscope in contrast to a conventional light microscope is the use of an electron beam as radiation source. The high energy and focusability of the electron beam allows obtaining very high magnification and resolution images of a sample. An electron beam is generated under high vacuum by an emission source and accelerated towards the sample. Electromagnetic lenses as well as deflection coils focus the electron beam.

The differences in TEM and SEM are mainly due to the detection of the secondary signals. While SEM detects mainly secondary and backscattered electrons, transmission electron microscopy detects transmitted electrons. Therefore, thin samples (less than 200 nm) are prepared for TEM to increase the number of transmitted electrons. The magnification that can be obtained with TEM (< 0.1 nm) is even higher than for SEM (>1 nm) when aberration corrections are used. Electron diffraction is an additional technique that is used to derive crystallographic information.

Several elastic and inelastic interactions of the electrons with the solid are observed (Figure 2.10). The primary signal that can be detected is the loss of energy of the incident electrons due to collisions and deceleration phenomena. However for SEM, most of the topographical information is generated from secondary signals (electrons and photons). Most important are backscattered (BSE) and secondary electrons (SE). BSE are obtained whenever a primary electron collides with an atom core of the solid matter. The electron is hence elastically scattered backwards. Since collisions with the small core of an atom are more seldom the intensity of the BSE is usually lower compared to secondary electrons. The contrast obtained by BSE is strongly dependent on the atomic number of the element whereas the SE intensity is mainly affected by the energy of the primary electron beam. The origin of SEs is the ionization of atoms by

collision. Incident electrons knock out electrons of the inner shells of the atoms. Thereby they lose part of their energy and exhibit a change in their path.

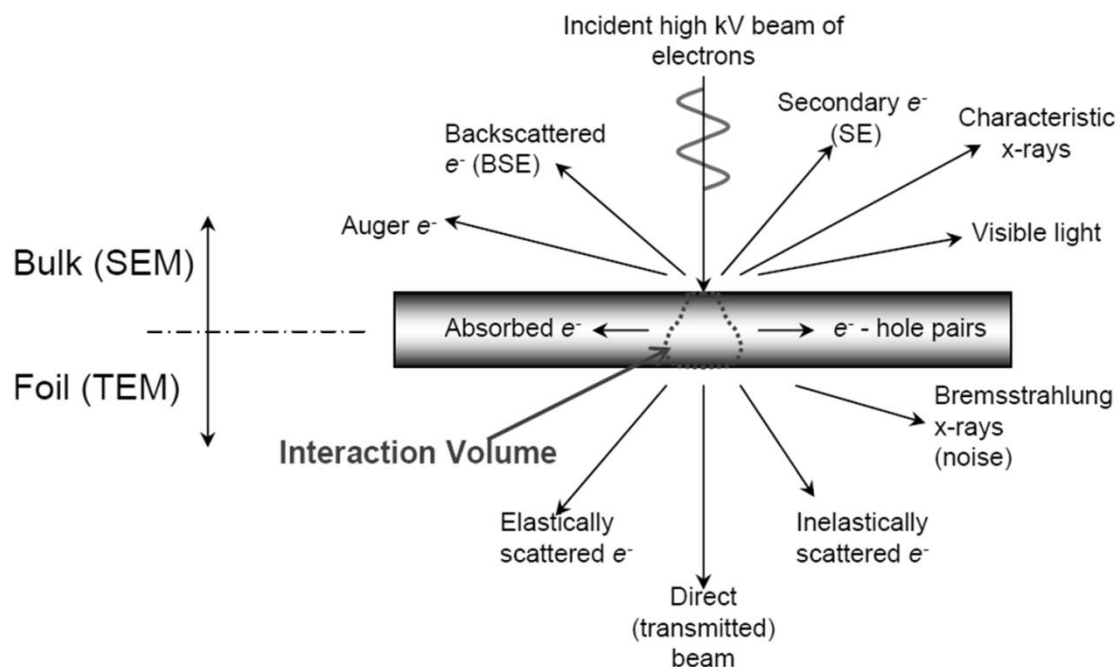


Figure 2.10: Interactions of electrons with solid matter. Some of the electrons are transmitted whereas the other part is reflected from the sample surface. Emitted electrons and photons are observed in a small interaction volume called “plume”. Depending on their energy the depth of the emitted electrons varies significantly. High energy backscattered electrons are obtained up to a penetration depth of 1 μm compared to secondary electrons (< 10 nm).

The detection of backscattered and secondary electrons can generate images with very high spatial resolution. If the incident electron beam is focused on a kink or surface roughness the incident angle changes and the current of electrons from the sample to the detector is varied. The differences in the electron current are detected by BSE and SE detector and transferred into an image that depicts the topography of the material.

2.6 THERMAL ANALYSIS (TG/DTA/MS)

Thermal analysis offers a wide range of analytical methods to determine physical and chemical characteristics of samples or mixture under a distinct temperature program. One of the most popular methods is the thermogravimetric analysis (TG) that monitors the mass of a substance during a heating program. Depending on the nature of the

substance weight losses (e.g. decomposition, dehydration) or more seldom weight gains (e.g. oxidation) are observed. Using an inert gas inside the sample chamber redox reaction can be suppressed. The weight loss is usually determined with a magnetic microbalance to assure a high precision of the data.

Differential scanning calorimetry (DSC) and differential thermal analysis (DTA) are two methods that give insides into the energetic behavior, namely the enthalpy, of the processes that occur during heat treatment. Both methods are similar in their experimental setup as well as in their data, but the DSC is a method that allows obtaining quantified data. In both methods a reference sample additionally to the substance material is heated and the temperature of both is monitored by separate thermal elements. The DTA now observes the temperature difference that is obtained for the sample when a combustion or transformation is observed. In DSC experiments a heating devices always keeps the temperature of the reference and the sample equal and monitors the additional heating power for the sample.

Simultaneous measurements of TG and DSC/DTA are highly favorable since they allow a precise interpretation and assignment of all thermal effects that occur during the measurement. Additional information is gained when the gaseous combustion products are further analyzed by IR, mass spectrometry or gas chromatography.

2.7 INFRARED (IR) SPECTROSCOPY

Infrared spectroscopy measures the absorption of light by a molecule. The photons collide with electrons of the sample and excite the molecules in higher vibrational and rotational energy levels. Photon absorption occurs when the molecules excitation leads to a change of its electric dipole moment. Therefore vibrations of molecules symmetric to inversion are invisible in the IR spectra whereas they can be detected with Raman spectroscopy. The complementary of both techniques allow obtaining comprehensive information about the vibrational states of the sample.

The IR spectrum, usually recorded from 400 up to 4000 cm^{-1} , is commonly divided in two parts. Typical vibrations of functional groups are located at higher wavenumber due

to their high energy whereas the fingerprint region (400 and 1500 cm^{-1}) is used to identify substances.

2.8 MATRIX ASSISTED LASER DESORPTION/IONIZATION-TIME OF FLIGHT MASS SPECTROMETRY (MALDI-TOF)

MALDI-TOF is a special type of mass spectrometry to determine the molecular mass and in some cases the structure of high molecular weight compounds, such as proteins. MALDI is a very gentle ionisation method that suppresses the fragmentation of the large molecules. The analyte is embedded in a matrix that is usually composed of hydroxylated benzoic acid derivatives or cinnamic acid. Therefore, analyte and matrix components are dissolved in a solvent and placed on a target plate. Under reduced pressure the solvent is evaporated and the matrix crystallizes around the analyte. In the MALDI experiment the target is charged and an UV laser pulse is irradiated onto the sample spot. The UV irradiation excites the π -System of the aromatic system in the matrix component and thus leads to spontaneous evaporation of the matrix. The analyte is released and ionized in one step. Since the matrix absorbs most of the energy and transfers only part of it to the analyte the technique produces less fragmented analyte molecules and proteins can be detected as complete molecules.

The separation is usually performed with a time-of-flight system. Therefore, the quasi-molecular ions are accelerated by an applied voltage into a field-free zone. In the TOF system the ions are separated according to their mass-to-charge ratio.

2.9 MAGNETOMETRY

In general the characterization of magnetic materials includes the analysis of their magnetic properties like strength and direction of the magnetic field. Therefore an external magnetic field induces a magnetization in the respective sample material that is recorded. Different magnetometer setups have been used for such measurements, whereas SQUID and vibrating sample magnetometry (VSM) are the most frequently used techniques. Here, vibrating sample magnetometry is discussed in detail.

In a VS magnetometer an external homogenous magnetic field is applied that leads to a magnetization of the respective sample. Since the sample is continuously vibrating the magnetic field starts to oscillate. The oscillation induces a voltage in detector coils parallel to the external magnetic field. The induced voltage is compared to a magnetic reference material and a magnetization value is obtained.

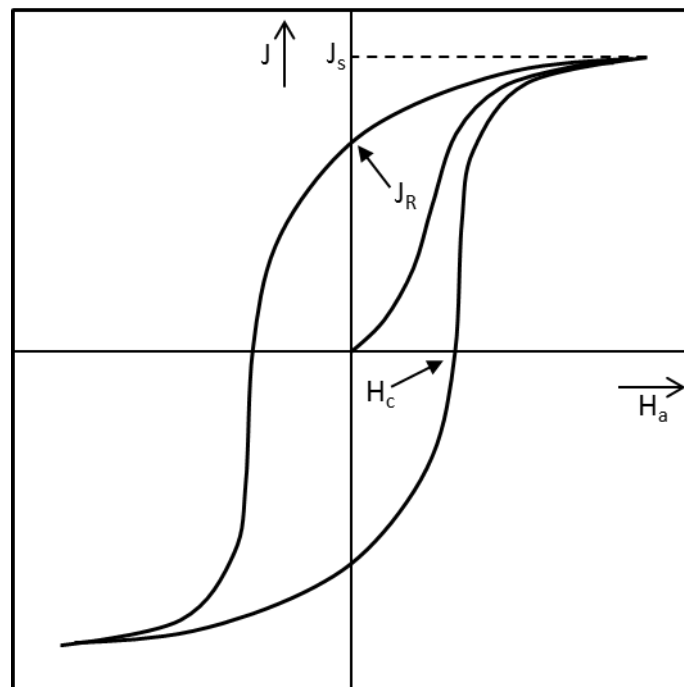


Figure 2.11: Schematic description of a hysteresis curve observed with variation of the external field strength H_a for ferri- and ferromagnetic materials. Saturation magnetization J_s , coercivity H_c , remanence J_r and the magnetic susceptibility χ_0 can be directly derived from that data.

In a conventional magnetometric measurement the sample magnetization J is monitored with varied external field strength H_a . For ferro- and ferrimagnetic materials (not for superparamagnetic materials) a hysteresis curve is observed (Figure 2.11). With increasing H_a the magnetic domains are aligned until at a saturation magnetization J_s all spins are aligned. When the external field is adjusted to zero hysteresis is observed due to a remanence magnetization J_r . The coercivity H_c is reached when J_s becomes zero.

3 MOTIVATION

In the last decade the establishment of inorganic-biohybrid materials in catalytic applications became increasingly important since the use of biocatalysts is often associated with environment friendly processes. These processes are generally referred to as *Green chemistry* approaches. Since the working conditions (e.g. temperature, pH) of enzymes are usually very mild and the catalysis is very efficient (yield, selectivity) they are suitable to perform in *green* processes. The products that are obtained by using enzymes as catalysts in large-scale processes are very pure and only a low amount of waste is produced. However, problems can arise due to the instability of the enzymes as well as the difficult separation from the reaction mixture. These are the main driving forces for the immobilization of enzymes onto carrier materials. The immobilization can lead to a rigidification of the enzyme structure and thus to a significant stabilization against thermal or chemical deactivation. Additionally, the use of solid biocatalysts facilitates the separation of the enzyme from the reaction mixture.

Based on the promising concept of immobilized enzymes in *Green chemistry* two different topics have been investigated as a part of the present thesis:

The first approach dealt with the use of solid biocatalysts in the regeneration of NADPH. Up to now, the cofactor regeneration is a main research topic, since many enzymatic reactions are based on expensive cofactors. Therefore, stable enzymatic regenerating systems are necessary for *green chemical* processes. Additionally, catalytic enzymatic cascades are mostly based on at least one cofactor dependent enzyme. On this account the immobilization of glucose-6-phosphate dehydrogenase in nanoporous materials was performed to obtain an efficient NADPH regeneration system. Mesoporous materials have been used in the last decade to yield stabilization of enzymes due to their confinement. A series of nanoporous materials based on silica and carbon were investigated on this purpose. To yield an optimum stabilization for G6PDH not only the type of the material was changed but also its surface functionalization. The properties of the materials in terms of porosity and surface charge was intensively investigated and correlated to the behavior of the enzyme during and after

immobilization. The uptake of enzyme from solution, the activity and stability of the biocatalyst and the leaching of enzyme from support is discussed further in terms of enzyme-support interactions.

The application of biocatalysts in the degradation of renewable feedstocks to biofuels or to building blocks for chemical synthesis is another important topic in *Green chemistry*. Many renewable feedstocks, e.g. corn, do however interfere with the human food production and are therefore less adequate for the production of fuels or chemicals. In this context cellulose is an attractive alternative source of biomass that exists in larger amounts. One general problem arising from the use of cellulose as feedstock is the difficult degradation of the biopolymer. Today, high temperature and acidic conditions are used to decompose the cellulose in smaller glucose units. Cellulosomes are protein complexes that degrade cellulose highly efficient and are therefore feasible sources for the cellulose degradation.

The second topic in this thesis deals with the assembly of a cellulosome onto inorganic magnetic particles. Silica particles were established as a model system to investigate the coupling chemistry and immobilization behavior of the single cellulosome components. In the first step a protein unit consisting of cohesin, a protein necessary for the assembly of the respective proteins, and the cellulose-binding module (CBM), which mediates the interaction with the cellulose surface, were covalently attached either by an active ester or a click-chemistry approach. In the next step another protein unit consisting of dockerin, responsible for the assembly with cohesin, and the enzymatic active unit, a cellulase is immobilized. This biohybrid material was then introduced in the degradation of cellulose.

Besides the assembly of the cellulosome onto silica nanoparticles as model system the synthesis of silica coated magnetite particles was investigated to obtain easy separation of the biocatalyst in the future. Therefore the coating conditions were varied to obtain a stable support for the degradation of cellulose.

4 TAILORING POROUS MATERIALS FOR G6PDH IMMOBILIZATION³

4.1 INTRODUCTION

Enzymes offer higher selectivity and often higher turnover rates of their catalytic conversions compared to other catalysts. Considering these benefits, enzymes are perfectly suited for industrial applications but are often sensitive to harsh reaction conditions, such as organic solvents, high/low pH, and high temperatures, or need expensive cofactors.^[256] To reduce the costs enzymatic cofactor regeneration has become an important issue in the last few decades.^[257,258] Glucose-6-phosphate dehydrogenase (G6PDH) is an important enzyme in cofactor regeneration cycles.^[259] It generates the reduced form of the cofactor nicotinamide adenine dinucleotide phosphate (NADPH) during the conversion of glucose-6-phosphate to 6-phosphogluconate in the pentose phosphate way. NADPH can be used to activate different proteins that act in a reaction cycle with G6PDH.^[11] For such biocatalytic cycles, stabilization of the protein is very important for cost efficiency. Additionally, recovering G6PDH is a major problem that needs to be resolved to stop the reaction cycle and to separate product and catalyst. Both, stability and recoverability of the enzyme can be increased by immobilization onto solid supports. It was shown in previous publications that the activity of particular enzymes can be maintained or even increased after immobilization.^[137]

Mesoporous silicas turned out to be ideal supports for immobilization of biomolecules because of their suitable properties: Silica is a biocompatible, non-toxic material which makes it adequate for applications in biological and medical applications.^[3] Other options like mesoporous carbons have been investigated to achieve mainly hydrophobic interactions with proteins.^[260] The use of porous materials in general, including macroporous and hierarchical systems, offers a high variability of uniform, well-ordered structures with different channel systems, which allow the transport of various substrates and proteins. Channel geometry and connection determine the enzymatic reaction rate and have to be well chosen in order to allow a

³ Parts of this chapter have already been published.^[99]

continuous flow of the substrate and a sufficient enzyme uptake. The high surface areas of porous materials offer the possibility of high protein loadings and therefore high specific activities. Protection of the enzymes derives from enclosing the molecules in the pores so that aggregation and autolysis can be strongly reduced. The environment of the pore stabilizes the protein structure by decreasing its mobility. The pore size has to be chosen carefully. Leaching and low stabilization occur when using a porous material, in which the pores are larger than the enzyme itself, whereas pores that are too small lead to pore blocking and deactivation of the enzyme.^[36,84,86] There are several ways to immobilize an enzyme onto a porous material: covalent attachment, encapsulation, entrapment, adsorption, and adsorption followed by cross-linking. Covalent bonding is possible with almost all materials but leads generally to partial deactivation of the enzyme, whereas adsorption is a mild immobilization technique. During entrapment, encapsulation, and cross-linking the enzyme is in contact with chemicals that can cause deactivation. Adsorption is the most widely used method for protein immobilization in porous materials because of the possible retention of activity; however, leaching from the support can become an obstacle.

To avoid this problem it is important to adjust the interactions between protein and support surface. The interactions that occur during the adsorption process are either hydrophobic or electrostatic interactions or hydrogen bonding. If performing the immobilization near the isoelectric point of the protein, electrostatic interactions between the enzymes are low and hydrophobic interactions are the controlling forces. However, the isoelectric point (pI) is often not at the pH at which the protein is most stable. If performing the immobilization at a pH lower or higher than the pI, electrostatic interactions control the adsorption process.^[3,31,37,110] The silica surface can be easily modified by post-synthetic functionalization with various silanes to match the electrostatic interactions between protein and support, whereas carbon surfaces are harder to functionalize. Oxidation is one means of hydrophilization of the carbon surface to make it accessible for proteins.^[161]

In this chapter the immobilization of the large protein G6PDH from *Leuconostoc mesenteroides* on various porous materials is discussed. Adsorption (undirected) as well as directed and undirected covalent immobilization is used to compare several techniques and supports. Mesoporous siliceous cellular foams and hierarchical porous

carbons are tailored to maximize uptake, activity and stability of the protein. In the beginning of this chapter several MCFs with differently charged surfaces have been used for G6PDH immobilization to gain insight into the immobilization behavior. In the next step amine-containing supports have been varied (spacer chain length, type of amine and location of the charged amine) in order to fine-tune the performance of the biocatalyst. The undirected covalent immobilization was performed by Schiff base reaction between the support and the materials.

The best performing biocatalyst was then applied in a reaction sequence with 6-phosphogluconate dehydrogenase (6PGDH).

4.2 RESULTS AND DISCUSSION

4.2.1 CHARACTERIZATION OF NANOPOROUS SUPPORTS

4.2.1.1 Siliceous mesostructured cellular foams (MCF)

Variation of MCF synthesis parameters

One of the key parameters that had to be taken into account for G6PDH ($d_H > 13$ nm) immobilization was a suitable pore size of the porous support. Since mesoporous silicas showed good performance in enzyme immobilization in the past, MCF was supposed to be an adequate support since pore sizes up to 45 nm are accessible according to the literature.^[63] MCF (see 1.3.1.1 and Figure 4.1) has spherical pores connected by smaller windows thus one of the major issues was to enlarge the cell entrance so that the enzyme is able to enter the main pore. In the synthesis of MCF NH_4F is added to enlarge the window size by erosion of the silica whereas the size of the main pore is mainly influenced by hydrothermal temperature and oil/polymer (TMB/P123) ratio (Table 4.1).

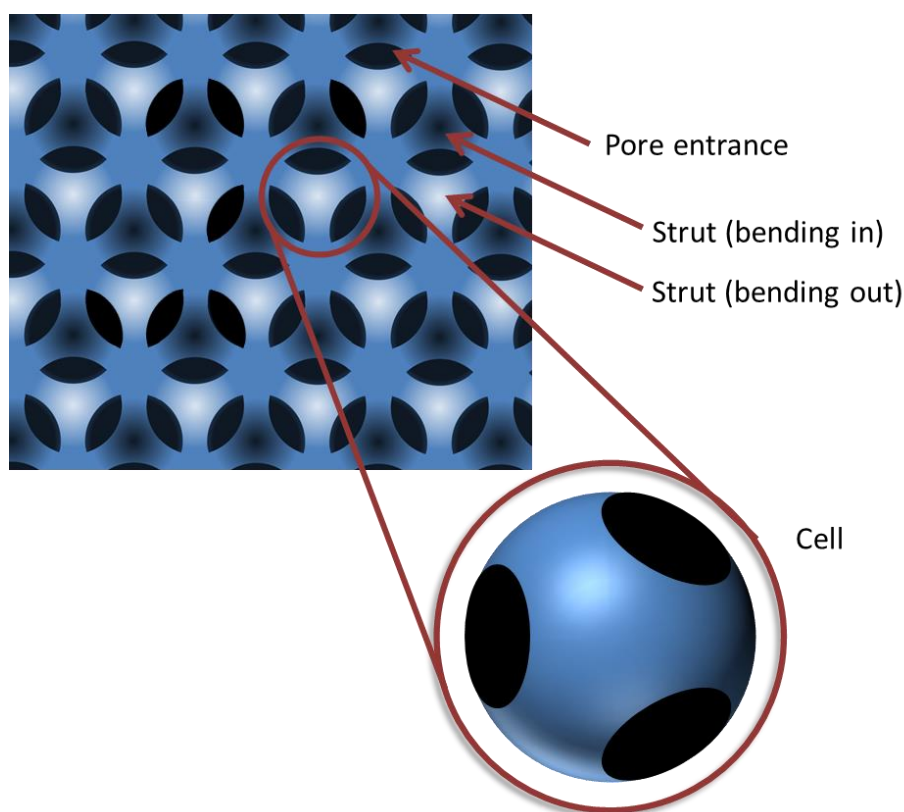


Figure 4.1: Schematic illustration of MCF. The inset depicts a single cell with the pore entrances to a spherical pore.

Table 4.1: Structural properties (BET surface area (S_{BET}), pore size from adsorption and desorption branch ($D_{\text{p,des/ads}}$) and pore volume (V_{p}) of MCF supports prepared at 100, 120 and 140 °C with varying TMB/P123 ratio with or without addition of NH_4F .

Hydrothermal T / °C	TMB/P123 (w/w)	NH_4F	$S_{\text{BET}} / \text{m}^2 \text{g}^{-1}$	$D_{\text{p, ads}} / \text{nm}$	$D_{\text{p, des}} / \text{nm}$	$V_{\text{p}} / \text{cm}^3 \text{g}^{-1}$	
100 °C	0	w/o	622	7.6 ^a	7.6 ^b	0.89	
		w	915	8.1 ^a	7.6 ^b	1.06	
	0.30	w/o	711	9.9	7.2	1.31	
		w	576	19	12	2.07	
	0.50	w/o	656	22	10	1.95	
		w	528	26	13	2.06	
	0.75	w/o	667	23	10	2.16	
		w	599	23	12	2.13	
	1.00	w/o	697	22	8.4	1.99	
		w	554	26	12	2.27	
	1.5	w/o	750	27	8.6	2.24	
		w	557	29	13	2.31	
	120 °C	0	w/o	597	8.4 ^a	8.5 ^b	1.03
			w	470	9.3 ^a	9.5 ^b	1.08
0.30		w/o	493	20	10	1.00	
		w	480	21	13	1.97	
0.50		w/o	485	23	11	2.03	
		w	440	28	14	2.17	
0.75		w/o	524	25	11	2.04	
		w	437	29	15	2.26	
1.00		w/o	661	25	11	2.57	
		w	475	32	15	2.49	
1.5		w/o	595	28	11	2.56	
		w	536	31	14	2.93	
140 °C		0	w/o	441	10 ^a	10 ^b	1.06
			w	392	10 ^a	10 ^b	0.9
	0.30	w/o	356	27	16	1.79	
		w	339	37	23	2.45	
	0.50	w/o	350	33	16	1.93	
		w	332	39	23	2.74	
	0.75	w/o	427	31	18	2.42	
		w	356	35	23	2.20	
	1.00	w/o	398	32	20	2.24	
		w	357	35	22	2.39	
	1.5	w/o	401	36	20	2.26	
		w	307	45	26	2.47	

a: determined by NLDFT (kernel: cylindrical pores adsorption), b: determined by NLDFT (kernel: cylindrical pores equilibrium model) ; w = with; w/o = without

Without addition of TMB as an oil component no swelling and thus no formation of spherical micelles occurs. In this case a hexagonal SBA-15 ($p6mm$) is obtained as indicated by the (100), (110) and (200) peaks in the small-angle PXRD pattern (Figure 4.2). Additionally a decrease in intensity with increasing temperature can be assigned to a reduction of crystallographic order. All other samples showed no peaks in the PXRD due to their disordered structure as well as an increased wall to wall distance.

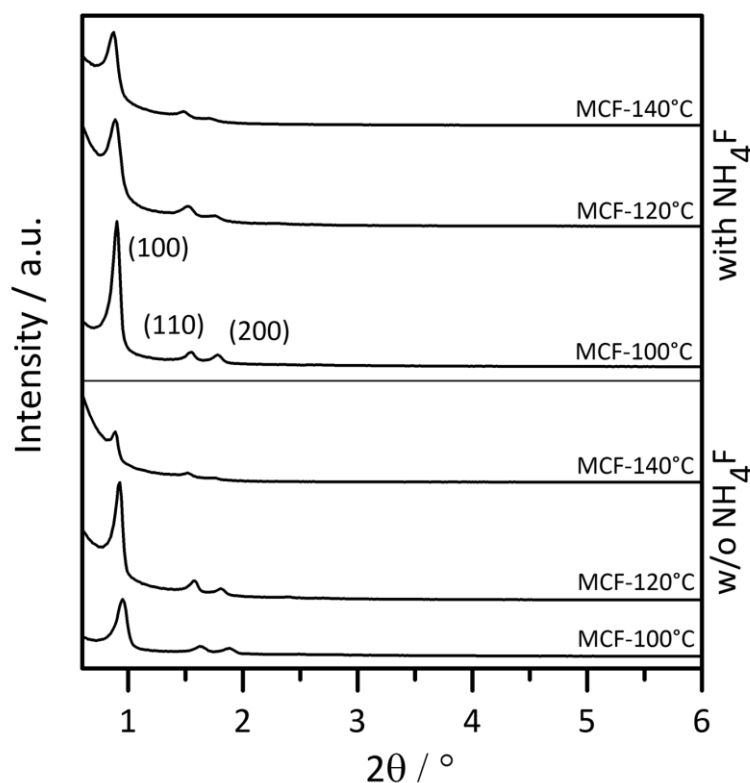


Figure 4.2: Powder diffraction patterns of mesoporous silicas prepared without addition of TMB with assigned peaks. The peaks indicate the presence of the hexagonal $p6mm$ phase of SBA-15. With increasing temperature a decrease in intensity is observed due to the reduction of periodic order as well as a peak shift due to an increased wall to wall distance.

From the respective d -values determined for the peak assigned to the (100) plane the lattice constant and hence the wall thickness was determined (Table 4.2).⁴ As a general trend the lattice constant is increasing with increasing temperature whereas the wall thickness decreases, due to the enlargement of the pore diameter.

⁴ The wall thickness was determined by the following equation valid for materials with hexagonal symmetry: $h_{\text{hex}} = a - D$, with a determined from the XRD pattern and D derived from nitrogen physisorption.

Table 4.2: Lattice constants and wall thickness for SBA-15 samples prepared at 100, 120 and 140 °C with or without addition of NH₄F.

Sample	NH ₄ F	d ₁₀₀ / nm	a / nm	h _{hex} / nm
MCF-100 °C	No	9.21	10.6	3.0
MCF-120 °C	No	9.53	11.0	2.5
MCF-140 °C	No	9.92	11.5	1.5
MCF-100 °C	Yes	9.55	11.0	3.4
MCF-120 °C	Yes	9.84	11.4	1.9
MCF-140 °C	Yes	10.8	11.6	1.6

d: diffraction plane spacing, a: lattice constant, h_{hex}: wall thickness

Some general trends are derived from nitrogen physisorption at 77 K shown in Figure 4.3, Figure 4.4, Figure 4.5 and Table 4.1. The BET surface area decreases with addition of NH₄F up to 25 % as well as with increasing temperature according to the loss of structural order with increasing temperature as well as increasing pore diameters. A hydrothermal temperature of 100 °C leads to surface areas between 550-800 m²g⁻¹ but at 140 °C only 310-440 m²g⁻¹ are observed.

All samples have type IV isotherms with H1 hysteresis curves whereas the width of the hysteresis is depending on the amount of TMB and the temperature of the hydrothermal treatment. For samples without addition of TMB the pore size distribution was determined by NLDFT since the PXRD proofed the hexagonal phase of SBA-15. The match of both pore sizes determined from adsorption as well as desorption branch further confirms the presence of a SBA-15 structure with cylindrical pore geometry. For all MCFs the BJH method was used to determine the size of the pore body from adsorption and the neck size from the desorption branch.

With increasing TMB/P123 ratio a broadening of the hysteresis is obtained which is a result of the increasing difference between pore and window size, since the adsorption branch is shifted to higher p/p₀ by an increasing pore size triggered by the swelling effect of TMB. In contrast, the hysteresis is broadening with decreasing temperature due to the shift of adsorption and desorption branch. At higher p/p₀ the difference between the two branches is smaller since the relative pressure is related logarithmically to the pore size. Thus this effect is only due to the mathematical correlation and no occurrence of network effects since most of them would lead to a H2 hysteresis.

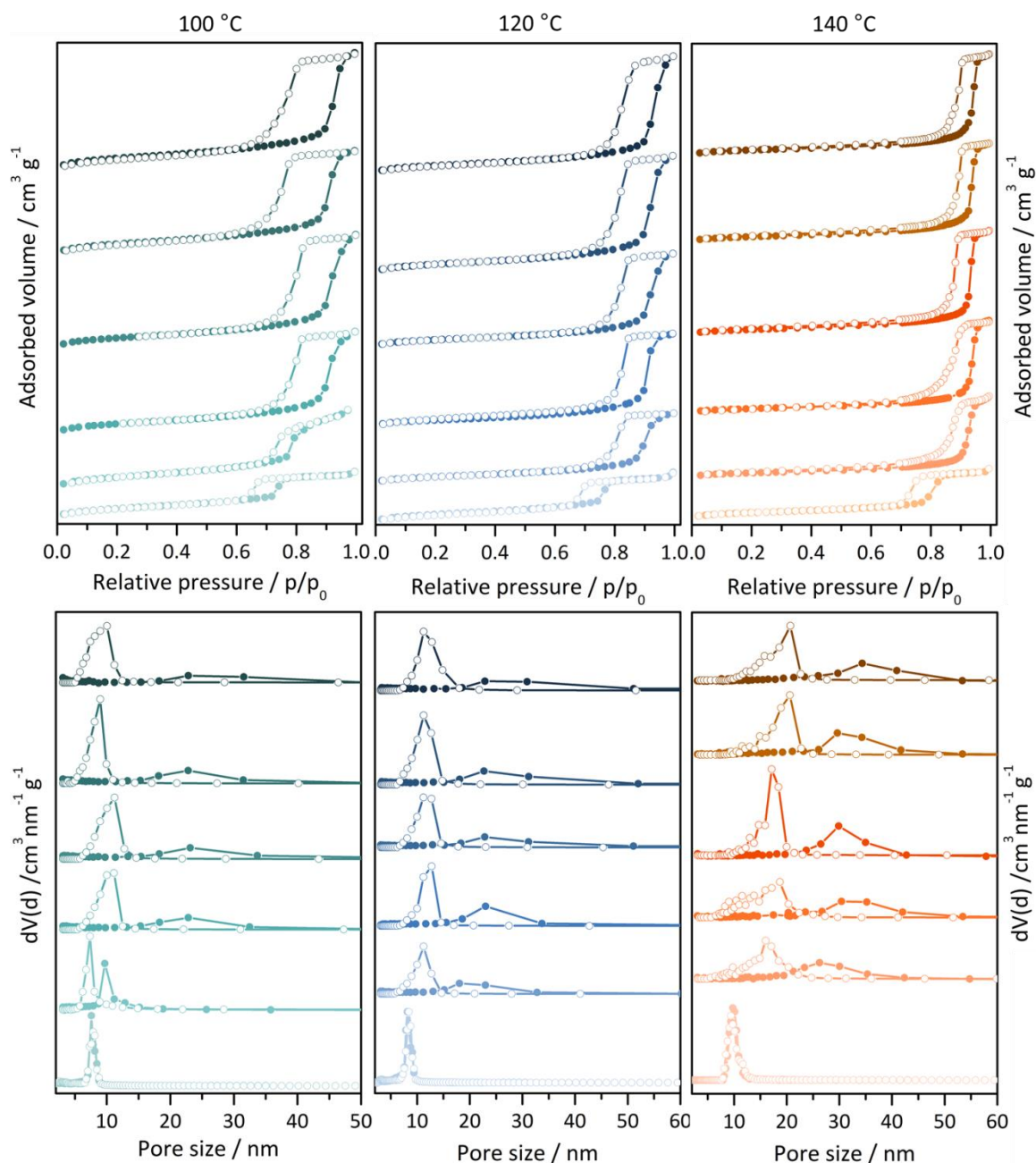


Figure 4.3: Nitrogen physisorption isotherms (77 K) with adsorption (filled symbols) and desorption (empty symbols) and respective BJH pore size distributions of MCF synthesized without addition of NH_4F at hydrothermal temperatures of 100, 120 and 140 °C. TMB/P123 ratios of 0, 0.33, 0.50, 0.75, 1.0 and 1.5 (light to dark color) have been used.

Not only a broadening of the hysteresis is observed with increasing TMB content but also a shift of the adsorption branch to higher relative pressure. This shift indicates that a higher TMB/P123 ratio indeed leads to an increase of the size of the pore body. This effect is most dominant from TMB/P123 ratios of 0 to 0.3 and less pronounced between

0.5 and 1.5. The size of the pore body additionally increases with increasing temperature.

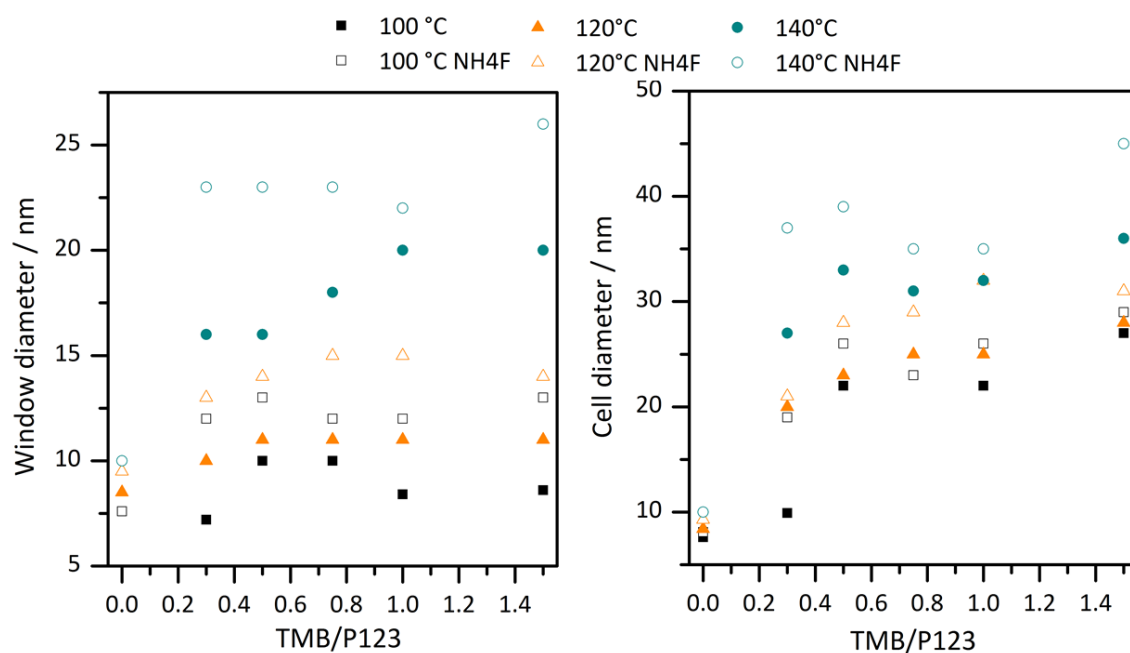


Figure 4.4: Development of window and cell diameter with increasing TMB/P123 ratio obtained for hydrothermal temperatures of 100, 120 and 140 °C with and w/o addition of NH_4F .

The size of the pore window is less affected by the TMB/P123 ratio and the temperature but is strongly dependent on the addition of NH_4F . The addition of fluoride widens the pore windows about 3-4 nm. Pore volume as well as pore size correlate strongly with the amount of TMB indicated by an increasing adsorbed volume of nitrogen and a shifted adsorption branch.

Most of the trends described above are strictly followed for hydrothermal temperatures of 100 °C and 120 °C but less for 140 °C. A hydrothermal temperature of 140 °C increases the structural disorder and leads to broad pore size distributions and hence broader neck size distributions. In that case the amount of TMB has a strong influence on the neck size. In general the pore volume correlates with the pore size but not with the neck size since a larger window does not affect the available volume.

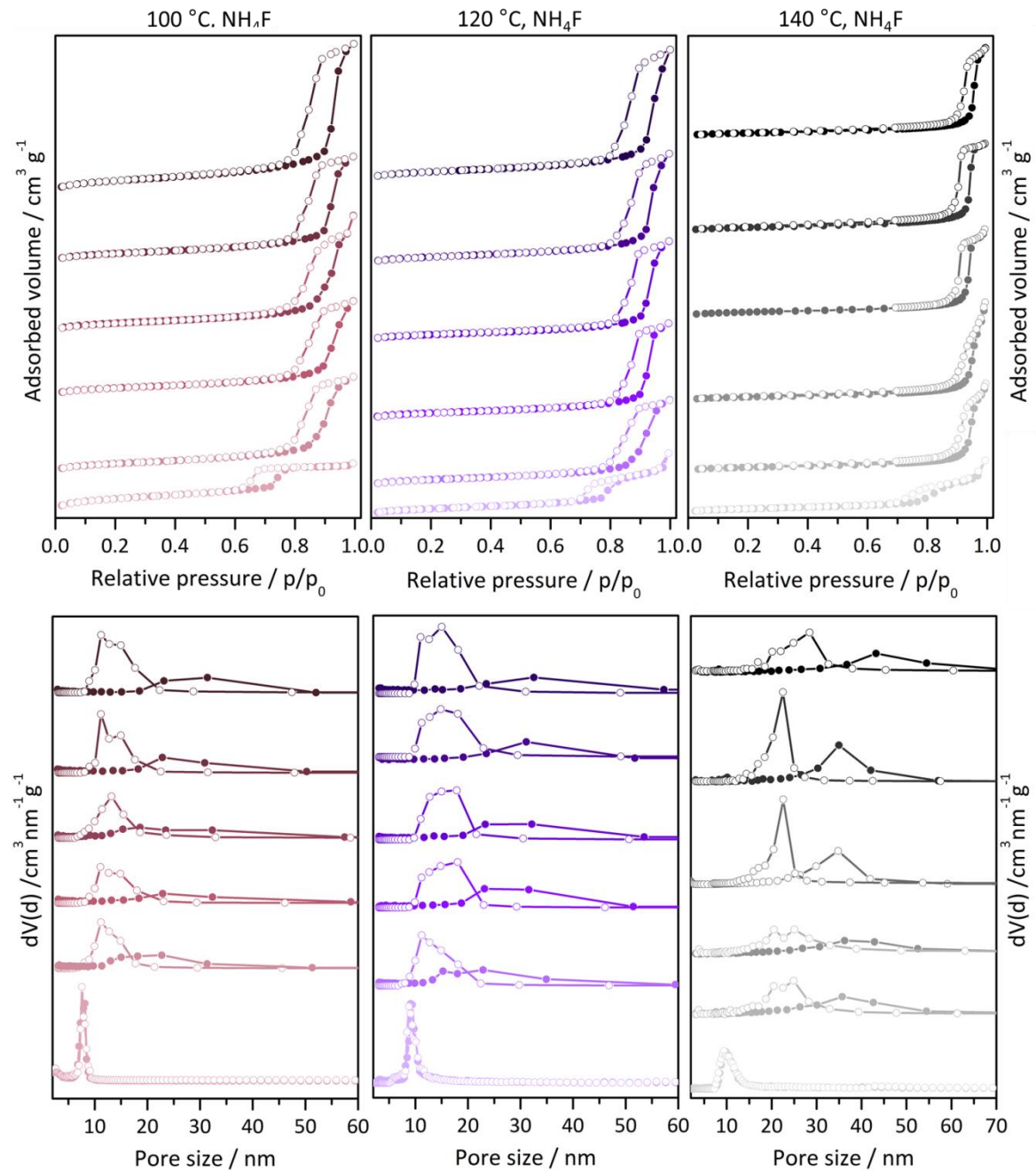


Figure 4.5: Nitrogen physisorption isotherms (77 K) with adsorption (filled symbols) and desorption (empty symbols) and respective BJH pore size distributions of MCF synthesized with addition of NH_4F at hydrothermal temperatures of 100, 120 and 140 °C. TMB/P123 ratios of 0, 0.33, 0.50, 0.75, 1.0 and 1.5 (light to dark color) have been used. As a general trend an increase in the entrance and main pore size with increasing amount of TMB is observed.

Characterization of MCF for G6PDH immobilization

As mentioned above, the neck size is the limiting parameter for the enzyme adsorption. Thus a MCF support for G6PDH immobilization was chosen according to its neck diameter. Since the enzyme exhibits a hydrodynamic radius of 13 nm, syntheses at 140 °C with addition of NH_4F lead to the favored neck size above 15 nm. A pronounced increase in pore volume and neck size was obtained for a TMB/P123 ratio of 0.5 to 0.75. Therefore the synthesis parameters of MCF for the immobilization of G6PDH were fixed at those parameters. The structure of the respective MCF support was further characterized by electron microscopy and small-angle X-ray scattering.

The morphology of the MCF support was characterized by SEM (Figure 4.6). The particles exhibit a high degree of surface roughness with a cauliflower-like morphology. As mentioned in a chapter 1.3.1.2 rough surfaces feature high external surface areas which can lead to cumulated adsorption onto the external surface. The particle size distribution of MCF is very broad and shows mainly particles in the μm range (centered at 2-20 μm).

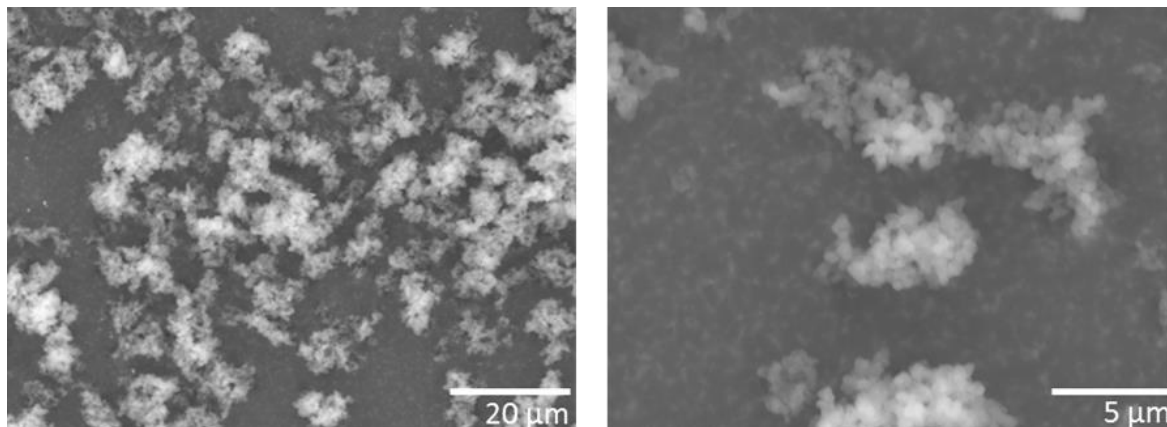


Figure 4.6: SEM images showing particle size and morphology of MCF particles. The particle size distribution is rather broad between 2-20 μm and the particles exhibit cauliflower morphology.

The TEM image of MCF, depicted in Figure 4.7, proves the foam-like structure of this material. At thinner regions of the sample the walls of the spherical pores can be clearly seen. The wall thickness determined from TEM is about 6 nm which is in good agreement with the literature.^[63]

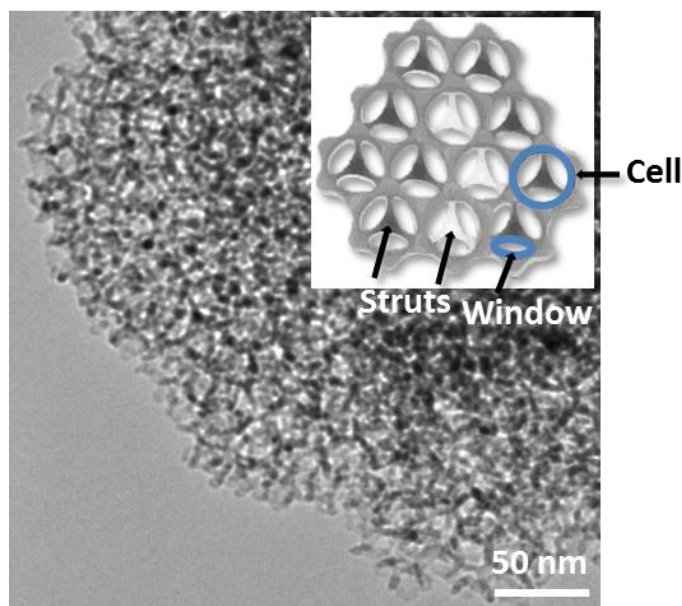


Figure 4.7: TEM image of MCF with a schematic cross-section of the pore system of MCF (inset). The inset shows the spherical pores (cells) of MCF with entrance windows that are built from struts bending out (dark grey) and away (light grey) from the drawing plane.

Additionally, the MCF was analyzed by SAXS (Figure 4.8) where one primary peak and three higher order peaks were observed, indicating uniformly shaped cells with a relatively narrow pore size distribution. The SAXS data was fitted to the scattering of vesicular shaped particles, which is in good agreement with the experimental data. The diameter of the pore (33 nm, walls including pore: 39 nm) and the wall thickness (3 nm) were calculated with this model. Whereas the pore size is in good agreement with the data obtained from nitrogen physisorption, the determined wall thickness is smaller than obtained by TEM. Since the fit for the experimental SAXS data is not perfectly in accordance the wall thickness from the TEM images is supposed to be more reliable. Thus the pore size of the spherical pore would be about 33 nm which is in good agreement to the data obtained from nitrogen physisorption measurements at 77 K (35 nm).

To sum up, MCF synthesized at 140 °C with a TMB/P123 ratio of 0.75 was considered as one possible support for the immobilization of G6PDH due to its large pore size and volume. The addition of NH_4F led to sufficiently large pore entrances to provide enough space for diffusion of G6PDH inside the pore network.

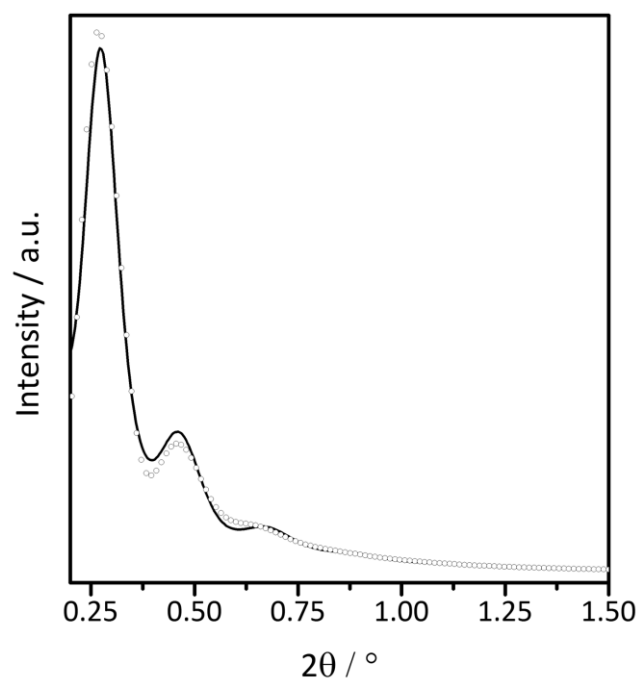
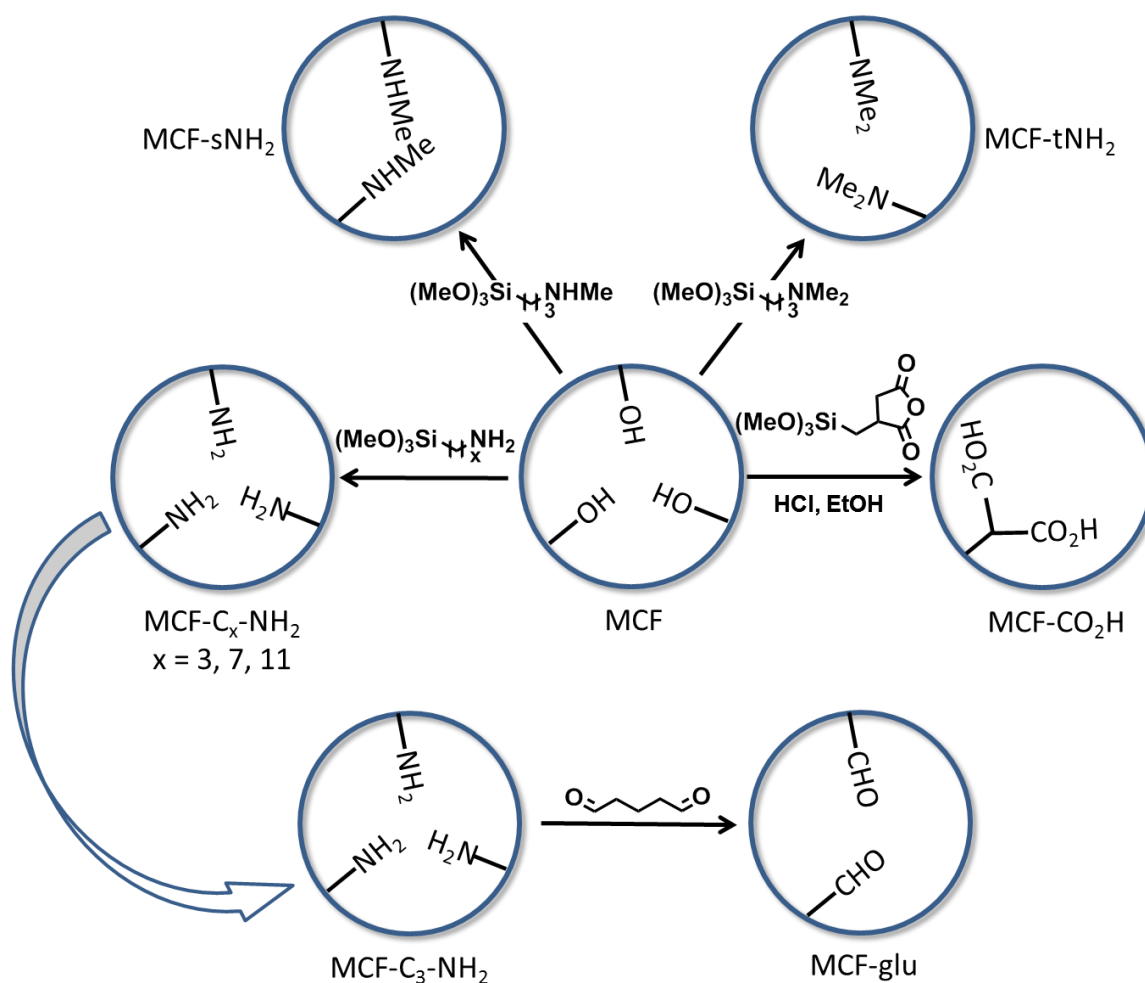


Figure 4.8: SAXS pattern at rt of MCF synthesized at 140 °C with addition of NH_4F and a TMB/P123 ratio of 0.75. Three higher order peaks besides the primary peak are an indication of uniform pores. The experimental data (line) is in good agreement with a fit (dots) for spheres.

4.2.1.2 Organosilane functionalized MCF

Several forces are responsible for the immobilization of enzymes onto solids including hydrophobic, van der Waals and electrostatic forces as well as covalent bonds. In order to screen several immobilization techniques, the MCF support was functionalized by postsynthetic silylation with organosilanes. An overview of the modifications with their respective abbreviations is given in Scheme 4.1.



Scheme 4.1: Functionalization of MCF with various organosilanes. Cycles illustrate a model pore with the respective functionalization attached at the pore walls. For simplification purposes the carbon chain is not drawn inside the pore. The starting material was MCF with free silanol groups that have been further modified by silylation. Amine modified MCF is additionally reacted with glutardialdehyde.

Characterization of MCF-CO₂H, MCF-C₃-NH₂ and MCF-glu⁵

In order to proof the successful functionalization of MCF with the respective organosilanes nitrogen physisorption at 77 K, IR spectroscopy as well as TG/DTA/MS measurements were performed. On one hand the results of nitrogen physisorption (Table 4.3, Figure 4.9) can give a hint if a modification was successful, on the other hand pore blocking effects by organosilanes can be evaluated.

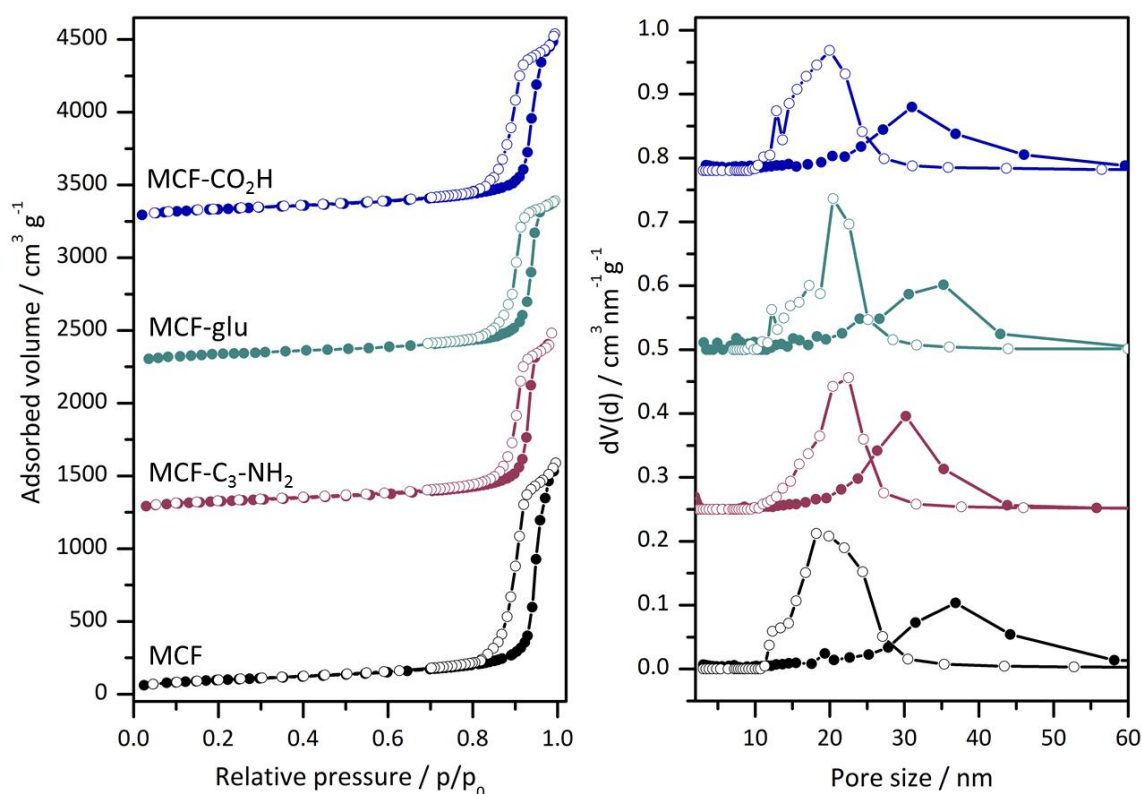


Figure 4.9: Nitrogen physisorption isotherms (at 77 K) and BJH pore size distributions determined from the adsorption (filled symbols) and desorption branch (empty symbols) for functionalized MCF samples. The isotherms are shifted by 1250, 2250, and 3250 cm³g⁻¹. BJH pore size distributions are shifted by 0.25, 0.50 and 0.75 cm³nm⁻¹g⁻¹. With the functionalization the peaks of the pore size distribution are shifted towards smaller diameter.

The decrease in the pore size as well as the reduced pore volume are indicated in the reduction of the amount of adsorbed nitrogen and the shift of the adsorption branch to lower partial pressure. The reduction in the mass specific parameters S_{BET} and V_p confirms an increased mass due to the introduced organosilanes whereas the reduction

⁵ Amine-functionalized MCFs (except MCF-C₃-NH₂) are discussed in the next paragraph for comparability reasons.

of D_p additionally direct towards a functionalization at the internal surface area. The high pore volume and surface area of MCF-CO₂H is due to low functionalization densities ρ_F of these samples (see TG/DTA/MS).

Table 4.3: Nitrogen physisorption (at 77 K) data for functionalized MCFs and the respective MCF starting material.

Sample	$S_{\text{BET}} / \text{m}^2 \text{g}^{-1}$	$D_{\text{p,entr}} / \text{nm}$	D_p / nm	$V_p / \text{cm}^3 \text{g}^{-1}$
MCF	356	23	35	2.20
MCF-C ₃ -NH ₂	277	21	30	1.74
MCF-glu	274	22	30	1.64
MCF-CO ₂ H	305	20	31	1.81

For all supports the complete coverage of the surface by post-synthetic modification was attempted to assure that only few residual silanol group affect the interactions. The amount of organic residues was determined by thermogravimetric and differential thermal analysis coupled to a mass spectrometer (TG/DTA/MS) (Table 4.4, Figure 4.10, Figure 4.11). The mass loss during the TG measurement is divided into two parts. The first part (< 250 °C) can be attributed to the evaporation of water adsorbed to the silica framework. The mass loss between 250 °C and 700 °C is assigned to the combustion of organic residues on the surface. At temperatures above 700 °C a mass loss due to the condensation of the silica species (0.4 %) is observed. From the combustion step ρ_F can be calculated to determine the degree of functionalization. Calculations of ρ_F are found in the Appendix (9.1.2).

Table 4.4: Functionalization density and mass loss derived by TG/DTA/MS.

Sample	Mass loss / %		$\rho_F / \text{mmol g}^{-1}$
	< 250 °C	< 750 °C	
MCF-C ₃ -NH ₂	2.2	6.2	1.14
MCF-glu	3.1	14.6 (6.4) ^a	1.16
MCF-CO ₂ H	3.1	10.7	0.753

a: amount of glutardialdehyde functionalization

For 3-aminopropyl modified MCF (MCF-C₃-NH₂) the functionalization density (ρ_F) is near the theoretical limit of 1.2 mmol g⁻¹ (Table 4.4).^[261] After the loss of adsorbed water

a two step decomposition can be observed in the TA (Figure 4.10a). The first dominant exothermic step (300 °C) is a result of the decomposition of the carbon chain. H_2O^+ , CO^+ , CO_2^+ and NO^+ are detected by the MS as decomposition products of the modification. In the second step (450-600 °C) the rest of the gaseous products diffuse out of the pores.

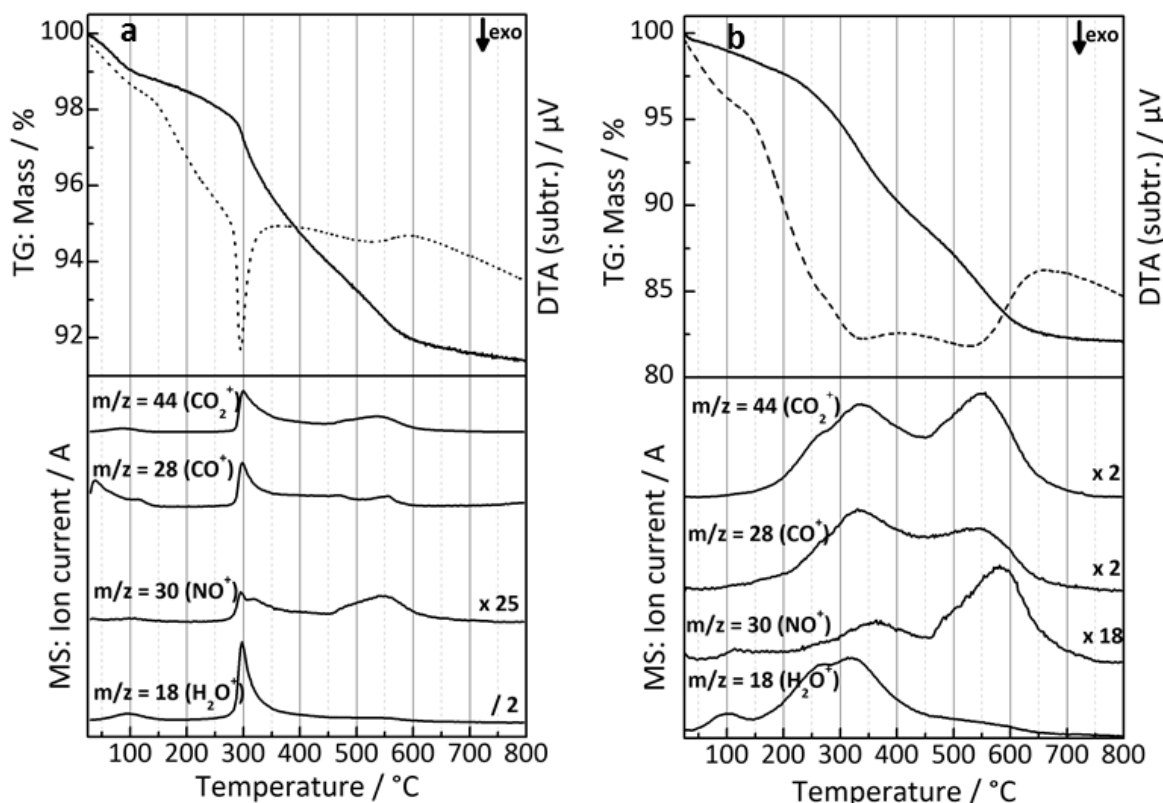


Figure 4.10: TG/DTA/MS of MCF-NH₂ (a) and MCF-glu (b) in synthetic air. The diagram at the top shows the TG (solid line) and DTA (dotted line) curve whereas the ion currents detected by a mass spectrometer are depicted at the bottom. An increase in mass loss and a broadening of DTA and MS peaks is observed after modification of MCF-NH₂ with glutardialdehyde.

After modification with glutardialdehyde (MCF-glu) all amine residues of MCF-C₃-NH₂ are bound to glutardialdehyde giving the same functionalization density for this material (Table 4.4). Due to an increased chain length the decompositions of the organic moieties becomes broadened over a wide temperature range (Figure 4.10b). Thus the two peaks in the DTA and the MS pattern overlap.

The modification of MCF with carboxylic acid moieties (MCF-CO₂H) results in lower ρ_F , but a similar amount of organic residues as a result of two carboxylic groups on every silane. The decomposition of the organic chain proceeds over one single step between

250 and 500 °C accompanied by a loss of water and carbon dioxide/monoxide detected by MS (Figure 4.11a).

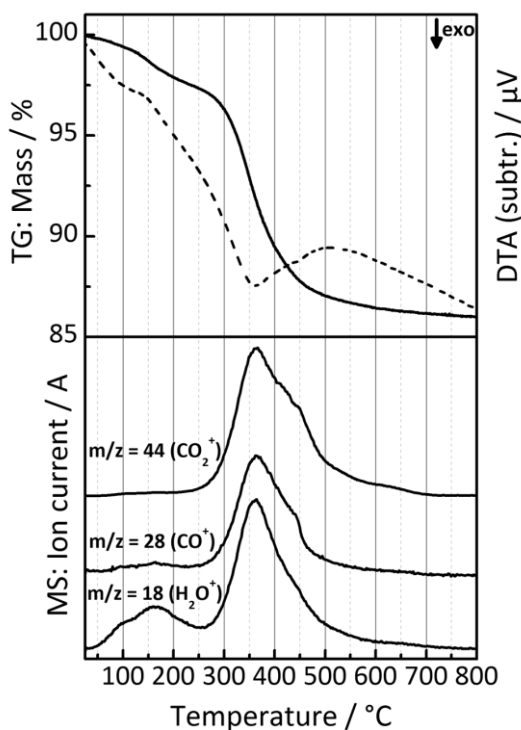


Figure 4.11: TG/MS/DTA of MCF-CO₂H in synthetic air. The diagram at the top shows the TG (solid line) and DTA (dotted line) curve whereas the ion currents detected by a mass spectrometer are depicted at the bottom of each diagram.

IR spectroscopy (Figure 4.12) was used to gain further information about the kind of organic functionalization at the silica surface. Most of the detected bands belong to vibrations of the silica network (Table 4.5) since most of the material is silica. The organic compounds are only a small part of the material. Thus the bands corresponding to the organic groups are usually very weak. For all modified MCFs small bands arising from the CH₂ stretching vibrations (2930, 2865 cm⁻¹) are present. MCF-CO₂H and MCF-glu show a characteristic band for the C=O stretching vibration. All vibrations are summarized in Table 4.5.

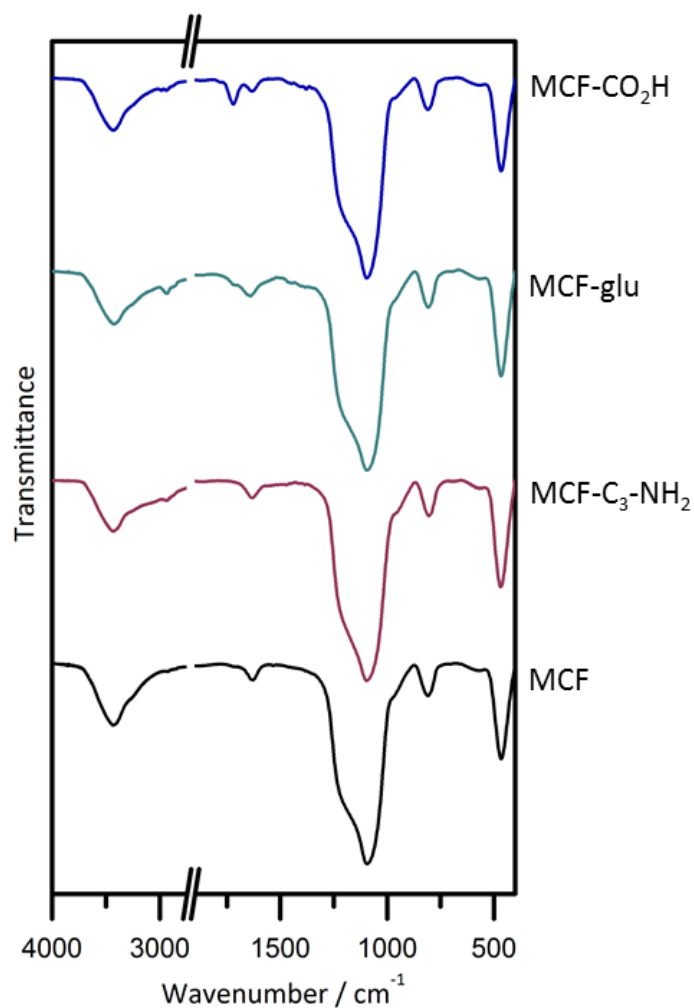


Figure 4.12: Normalized IR spectra of functionalized MCFs. Most of the vibrations can be assigned to the silica network whereas some weaker bands indicate the presence of the organic moieties attached to the walls of the MCF.

Table 4.5: IR bands and vibrations for the respective MCFs. The bands for pure MCF occur as well for the modified samples.

Sample	Wavenumber / cm^{-1}	Vibration
MCF	3427	Hydrogen bonds
	1628	Adsorbed water
	1209	ν_{as} (Si-O-Si)
	1095	ν_{as} (Si-O-Si)
	953	ν (Si-OH)
	808	ν_s (Si-O-Si)
	466	δ (Si-O-Si)
Modified MCF	2930	ν_{as} (CH_2)
	2865	ν_s (CH_2)
MCF- CO_2H	1722	ν (C=O)
ν_{as} : asymmetric stretching, ν_s : symmetric stretching, δ : deformation		

Characterization of amine-functionalized MCF

The functionalization of MCF with aminoalkylsilanes was performed with various silanes in order to obtain MCF modified with primary, secondary and tertiary amine functionalities. Not only the type of the amine was varied but also the chain length of the silanes. In Table 4.6 the maximal theoretical chain length, assuming a straight alignment of the carbon chain with sp^3 carbons (109.5°) is depicted. The calculation is an geometrical estimation derived from the relationship of the respective bonds and bond angles of the organic chain.

Table 4.6: Chain length of the respective organic residue of MCF organosilicas. The length was calculated according to the respective chain length and bond angles in the organic moieties.

Sample	Chain length/ nm
MCF-C ₃ -NH ₂	0.46
MCF-C ₇ -NH ₂	0.96
MCF-C ₁₁ -NH ₂	1.5
MCF-sNH ₂	0.52
MCF-tNH ₂	0.52

Length and mass of the respective organic residues have an influence on the porosity of the porous materials. Therefore nitrogen physisorption at 77 K was measured. A decrease in the adsorbed volume and a shift of the adsorption branch in comparison to pure MCF is depicted in the nitrogen isotherms (Figure 4.13). This corresponds to a decrease in the BJH pore size and in the pore volume observed for all MCF samples after functionalization (Table 4.7, Figure 4.13). The additional mass of the organosilanes condensed to the walls of the MCF leads to a reduction of the BET surface area and the pore volume.

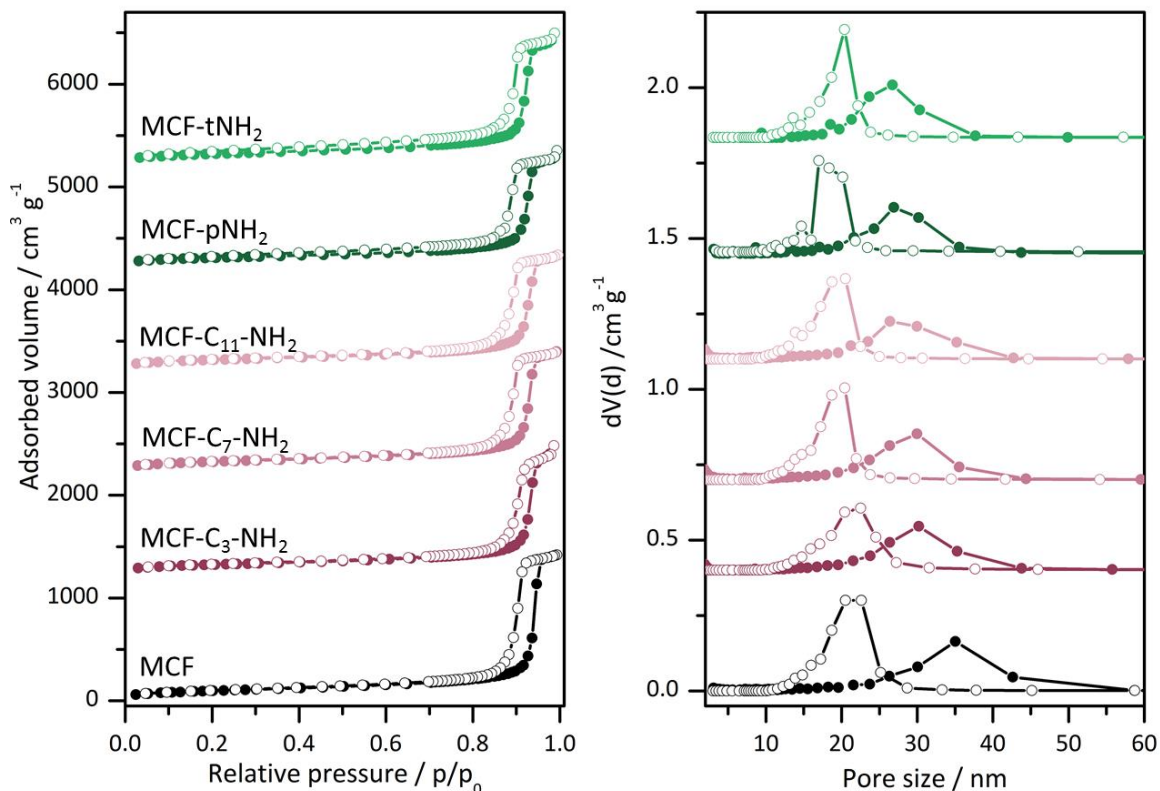


Figure 4.13: Nitrogen physisorption isotherms (at 77 K) and BJH pore size distributions determined from the adsorption (filled symbols) and desorption branch (empty symbols) for amine functionalized MCF samples. The isotherms are shifted by 1250, 2250, 3250, 4250 and 5250 $\text{cm}^3 \text{g}^{-1}$. BJH pore size distributions are shifted by 0.40, 0.70, 1.1, 1.5 and 1.8 $\text{cm}^3 \text{nm}^{-1} \text{g}^{-1}$. With the functionalization the peaks of the pore size distribution are shifted towards smaller diameter.

The extension of the carbon chain from three to eleven carbon atoms leads to a stepwise reduction of the cell pore size and volume caused by an increased steric demand of the silane (Table 4.6). Although a complete straight alignment of the carbon chain for MCF-C₇-NH₂ and MCF-C₁₁-NH₂ seems unlikely even a coiling would increase the occupied space and thus decrease pore volume and pore size.

Table 4.7: Nitrogen physisorption (at 77 K) data for functionalized MCFs and the respective MCF starting material.

Sample	$S_{\text{BET}} / \text{m}^2 \text{g}^{-1}$	$D_{\text{p,entr}} / \text{nm}$	D_{p} / nm	$V_{\text{p}} / \text{cm}^3 \text{g}^{-1}$
MCF	350	21	35	2.16
MCF-C ₃ -NH ₂	277	21	30	1.74
MCF-C ₇ -NH ₂	294	19	29	1.71
MCF-C ₁₁ -NH ₂	266	19	28	1.61
MCF-sNH ₂	238	18	28	1.57
MCF-tNH ₂	284	20	26	1.82

The decrease of the BJH pore size is usually stronger for the main pore, since most of the functionalization occurs there. A reduction of the pore entrance size is less pronounced due to the thin walls and thus the presence of less silanol groups. An increased functionalization at the entrance site would be less favorable due to possible pore blocking effects and a minor functionalization density at the spherical pore. The differences in the porosity of MCF-sNH₂ and MCF-tNH₂ compared to the other materials are not due to steric effects since the size of the molecule is similar. Those differences arise due to a different functionalization density determined by TG/DTA/MS (Figure 4.14, Table 4.8).

Table 4.8: Functionalization density and mass loss derived by TG/DTA/MS.

Sample	Mass loss / %		$\rho_F /$ mmol g ⁻¹
	< 250 °C	< 750 °C	
MCF-C ₃ -NH ₂	2.2	6.2	1.2
MCF-C ₇ -NH ₂	1.3	10.6	1.1
MCF-C ₁₁ -NH ₂	0.7	14.4	1.0
MCF-sNH ₂	2.0	11.0	1.7
MCF-tNH ₂	0.8	12.0	1.6

Primary (MCF-C₃-NH₂), secondary and tertiary amine functionalized samples exhibit three exothermic steps in the TG/DTA corresponding to the loss of adsorbed water, the combustion and evaporation of the organic residues indicated by a release of the respective combustion gases (H₂O, NO, CO/CO₂). The comparison of the TG/DTA/MS data shows that the signals of the DTA are broadened with increasing amount of methylene residues of the aminosilane due to the increased complexity of the organic moiety. The mean combustion temperature is highest for the primary amine functionalization (300 °C) and lowest for the secondary amine (260 °C) indicating a higher thermal stability for primary and tertiary amines. The high functionalization densities (Table 4.8) are the reason for the reduction of surface area, pore size and pore volume mentioned above.

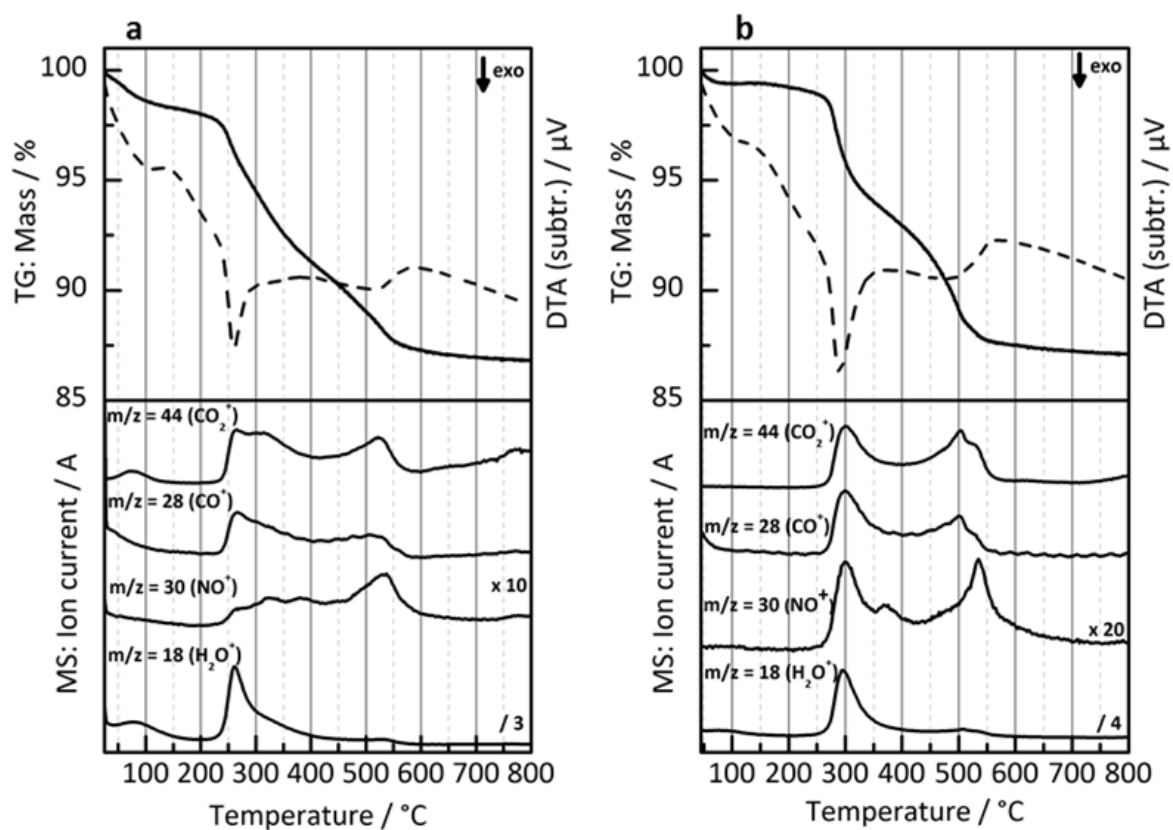


Figure 4.14: TG/MS/DTA of MCF-sNH₂ (a) and MCF-tNH₂ (b) under synthetic air. The diagram at the top shows the TG (solid line) and DTA (dotted line) curves whereas the ion currents detected by a mass spectrometer are depicted at the bottom of each diagram.

The TG/DTA/MS for amine functionalized MCF with C3, C7, C11 chain length (Figure 4.15, Figure 4.10) consist of the same three steps as primary, secondary and tertiary amines. With increasing chain length a broadening of the DTA/MS signals can be observed resulting from additional amount of organic that needs to be oxidized and evaporated. Due to this effect a reduction of the combustion temperature is observed from 300 °C for MCF-C₃-NH₂ to 250 °C for MCF-C₁₁-NH₂.

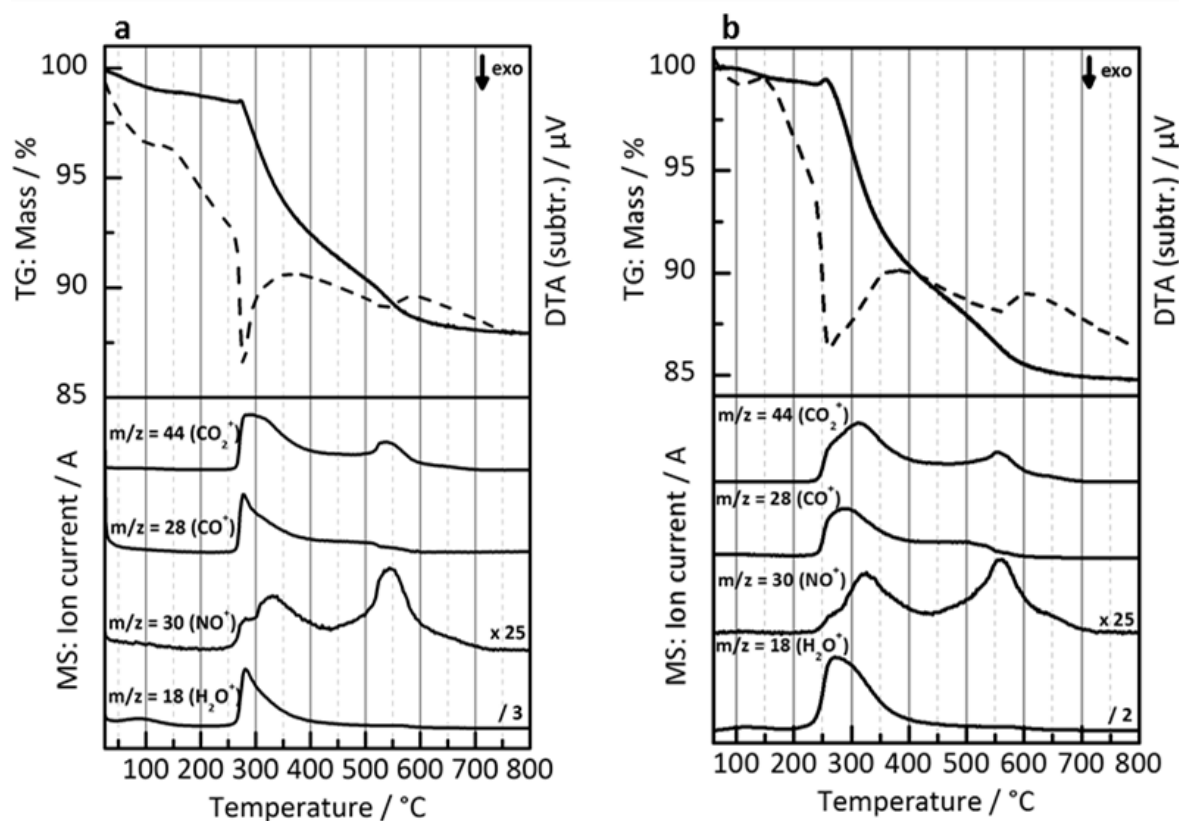


Figure 4.15: TG/MS/DTA of MCF-C₇-NH₂ (a) and MCF-C₁₁-NH₂ (b) under synthetic air. The diagram at the top shows the TG (solid line) and DTA (dotted line) curves whereas the ion currents detected by a mass spectrometer are depicted at the bottom of each diagram.

For all amine-modified MCFs bands arising from the silica network (Table 4.5) are present in all IR spectra (Figure 4.16). The bands for the N-H stretching vibrations are overlapped by the broad peak associated with the hydrogen bonds of the silanol groups and are thus not detectable. Several bands that can be assigned to the C-H vibrations (Table 4.9) of the CH₂ and CH₃ are observed. With increasing chain length from MCF-C₃-NH₂ to MCF-C₁₁-NH₂ the intensity of the CH₂ vibrations is enhanced. For MCF-sNH₂ and MCF-tNH₂ additional bands appear for the C-H vibrations of the methyl groups.

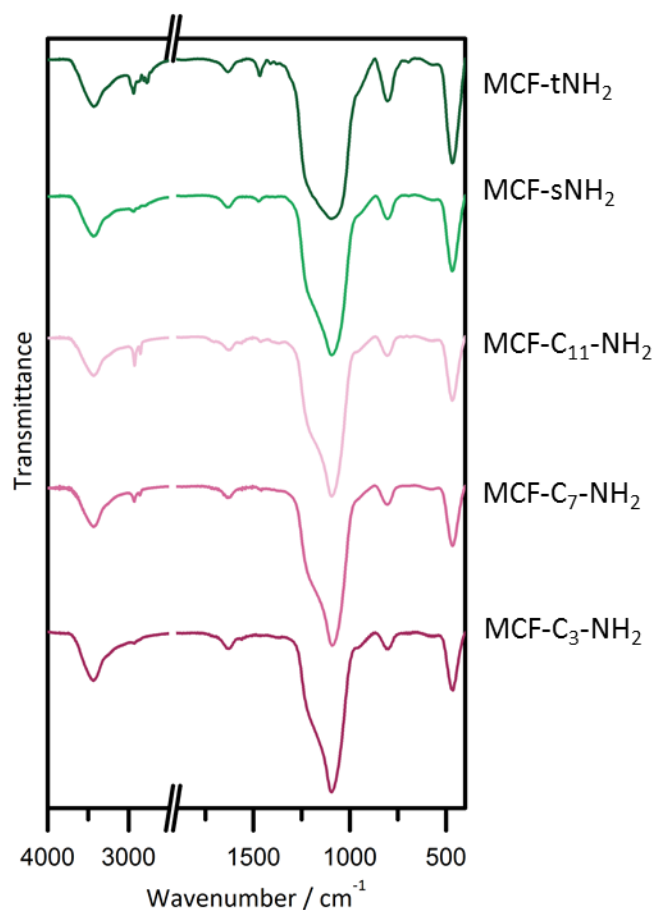


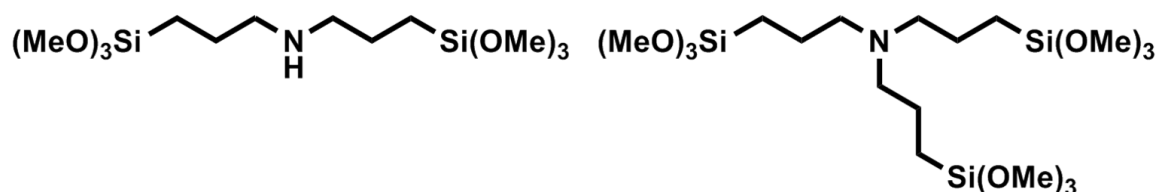
Figure 4.16: Normalized IR spectra of amine-modified MCFs. Most of the vibrations can be assigned to the silica network whereas some weaker bands indicate the presence of the organic moieties attached to the walls of the MCF.

Table 4.9: IR bands and vibrations for the respective amine-modified MCFs. Bands assigned to the silica network are depicted in Table 4.4.

Sample	Wavenumber / cm^{-1}	Vibration
MCF-C ₃ /C ₇ /C ₁₁ -NH ₂	2930	ν_{as} (CH ₂)
	2865	ν_s (CH ₂)
MCF-s/tNH ₂	2941	ν_{as} (CH ₂), ν_{as} (CH ₃) overlapped
	2870	ν_s (CH ₂), ν_s (CH ₃) overlapped
	2815	ν_s (CH ₂)
	1467	δ_{as} (CH ₃)
	1411 ^a	δ_s (CH ₃)
	1377 ^a	δ_s (CH ₃)
ν_{as} : asymmetric stretching, ν_s : symmetric stretching, δ : deformation, a: only observed for MCF-tNH ₂		

4.2.1.3 PMOs with alkyl-amine bridged precursors⁶

Periodic mesoporous organosilicas have been included as support materials into the immobilization studies in order to investigate the effect of their high content of organic compound that is directly included into the pore walls and not extended to the inside of the pore. Two amine-containing precursors (Scheme 4.2) have been used in the synthesis of PMOs without condensation with TEOS or other precursors. The secondary amine precursor (BTMPA) exhibits two silane groups for the condensation into a 3-dimensional structure whereas the tertiary amine precursor (TTMPA) exhibits higher connectivity due to its three silanes as connecting points. Three different PMOs are presented here: Two of them are powdered materials prepared with OTAC as a SDA under acidic conditions, one prepared by condensation of TTMPA (t-PMO) and one with BTMPA (s-PMO). Additionally, an aerogel was obtained after supercritical drying of a gel prepared from TTMPA under basic conditions with OTAC (PMO-Aerogel).



Scheme 4.2: Precursors for the synthesis of amine-containing PMOs: Bis-(trimethoxypropyl)amine (BTMPA) and Tris-(trimethoxypropyl)amine (TTMPA).

Since highly ordered PMOs are up to now not accessible with large pores (> 10 nm) and narrow pore size distributions the materials presented here have a fairly broad pore size distribution (Figure 4.17, Table 4.10). Although the materials presented here exhibit no periodic order they are still referred to as PMOs since they are synthesized without addition of any monosilylated precursor or TEOS. The nitrogen physisorption isotherms for s- and t-PMO exhibit a broad hysteresis and a moderate uptake of nitrogen whereas the uptake of the PMO-Aerogel was almost 10-fold increased. However, the high uptake

⁶ The G6PDH immobilization in amine-bridged PMOs was performed in cooperation with Sven Martens from our group. The syntheses and parts of the characterization of the PMOs was part of his diploma thesis: "Synthese und Charakterisierung periodisch mesoporöser Organosilicas (PMOs) mit stickstoffhaltigen Brückenfunktionen" (Hamburg, 2012).

of the aerogel can only give a hint to its pore volume since the pores cannot be completely filled up to a p/p_0 close to 1. Thus mercury intrusion was performed to access the complete porosity of the material but the aerogel collapsed during the high pressure measurement.

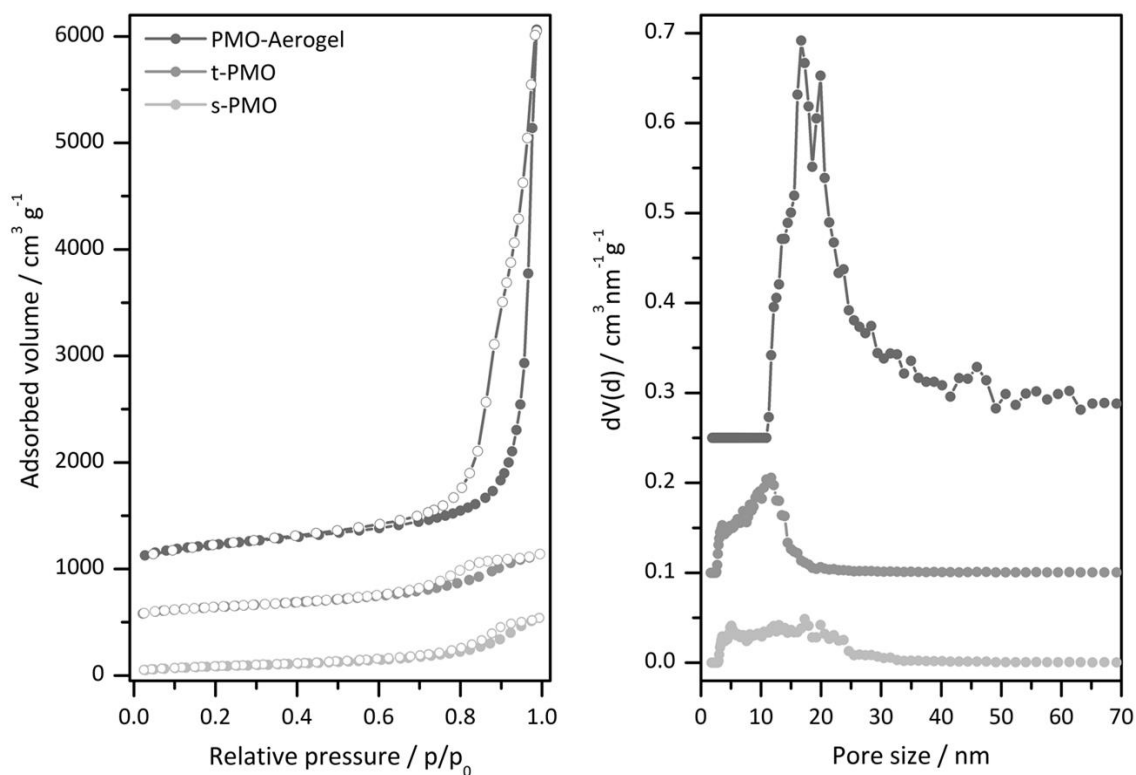


Figure 4.17: Nitrogen physisorption isotherms (at 77 K) and NLDFT pore size distributions (kernel: cylindrical pores, equilibrium model) of amine-PMOs. The adsorption (filled symbols) and desorption branch (empty symbols) are shifted by 1000 and 500 cm³g⁻¹. NLDFT pore size distributions are shifted by 0.25 and 0.10 cm³nm⁻¹g⁻¹.

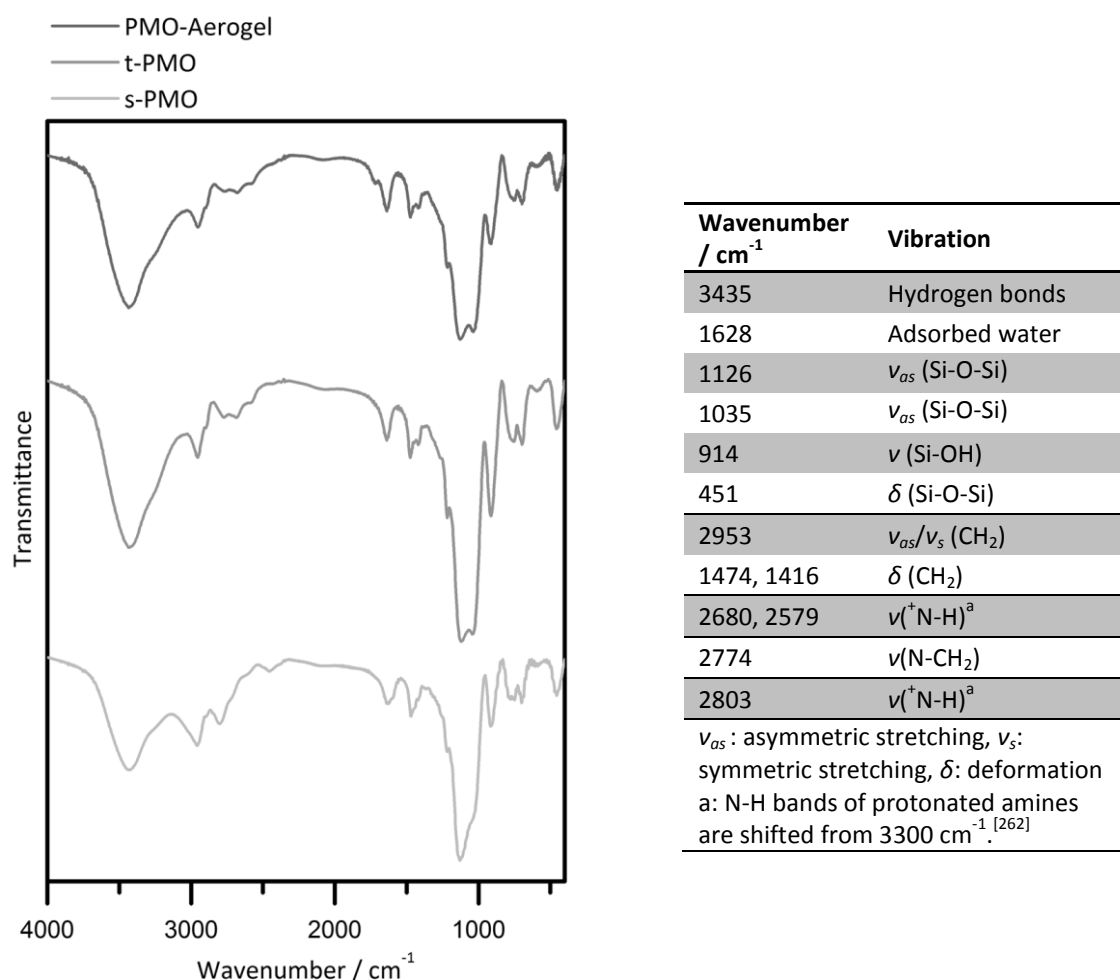
Surface area, pore volume as well as pore sizes for the three PMOs determined from nitrogen physisorption at 77 K are summarized in Table 4.10. The pore size was determined by NLDFT from the desorption branch for cylindrical pores. According to the obtained data, G6PDH could enter the pores of all materials but the large pore volume and pore size of the aerogel in particular could be beneficial for the adsorption of G6PDH.

Table 4.10: Nitrogen physisorption (at 77 K) data for PMO samples.

Sample	$S_{\text{BET}} / \text{m}^2 \text{g}^{-1}$	$D_{\text{p,NLDFT}} / \text{nm}^a$	$V_{\text{p}} / \text{cm}^3 \text{g}^{-1}$
s-PMO	306	4-24 (14)	0.784
t-PMO	517	8-14 (11)	0.926
PMO-Aerogel	854	12-32 (18)	$>7.83^b$

a: medium D_{p} in brackets; b: not completely accessible by nitrogen physisorption

IR spectra were recorded (Figure 4.18) in order to obtain information about the presence of the organic bridges inside the PMO materials.


Figure 4.18: IR spectra of amine-containing PMOs with the respective vibrational bands summarized.

The thermal stability as well as the composition of the PMOs was investigated by thermal analysis (Figure 4.19, Figure 4.20, Table 4.11) in synthetic air between 25 and

900 °C. The mass loss of the PMO materials consist of two major steps: The loss of adsorbed water led to a mass loss between 7 and 8 % below 170 °C. Above 170 °C the thermal combustion of the bridging groups led to the main mass loss between 43 and 46 %. During the combustion step several gaseous combustion products were detected that can be assigned to the combustion of the carbon chain (H_2O^+ , CO_2^+ , CO^+) and the amine group (NO^+ , NO_2^+). Additionally, traces of Cl^+ ($m/z = 35$) as chloride counter ions from synthesis (HCl) or SDA extraction have been detected by mass spectrometry. The residual mass is assigned to SiO_2 .

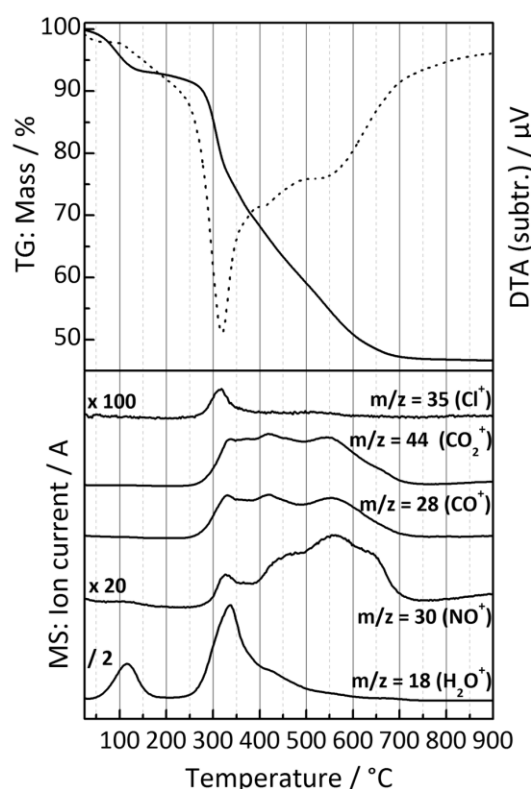


Figure 4.19: TG/MS/DTA of s-PMO measured in synthetic air. The diagram at the top shows the TG (solid line) and DTA (dotted line) curves whereas the ion currents detected by a mass spectrometer are depicted at the bottom of each diagram.

Interestingly, the decomposition of the s-PMO started at higher temperatures compared to the t-PMO and the aerogel. Usually, networks consisting of more connection points are supposed to be more stable but decomposition of the s-PMO started at 200 °C (determined from the DTG curve) whereas the PMO materials made of the three-connecting precursor already started to decompose at 170 °C.

Table 4.11: Mass loss of PMO samples determined by TG/DTA/MS.

Sample	Mass loss / %	
	< 170 °C	< 800 °C
s-PMO	7.5	45.9
t-PMO	7.8	43.7
PMO-Aerogel	6.8	42.5

Since the synthesis of the aerogel PMO was not performed in diluted hydrochloric acid the ion current of Cl^+ is much weaker compared to the other samples indicating that less chloride ions are present in the samples.

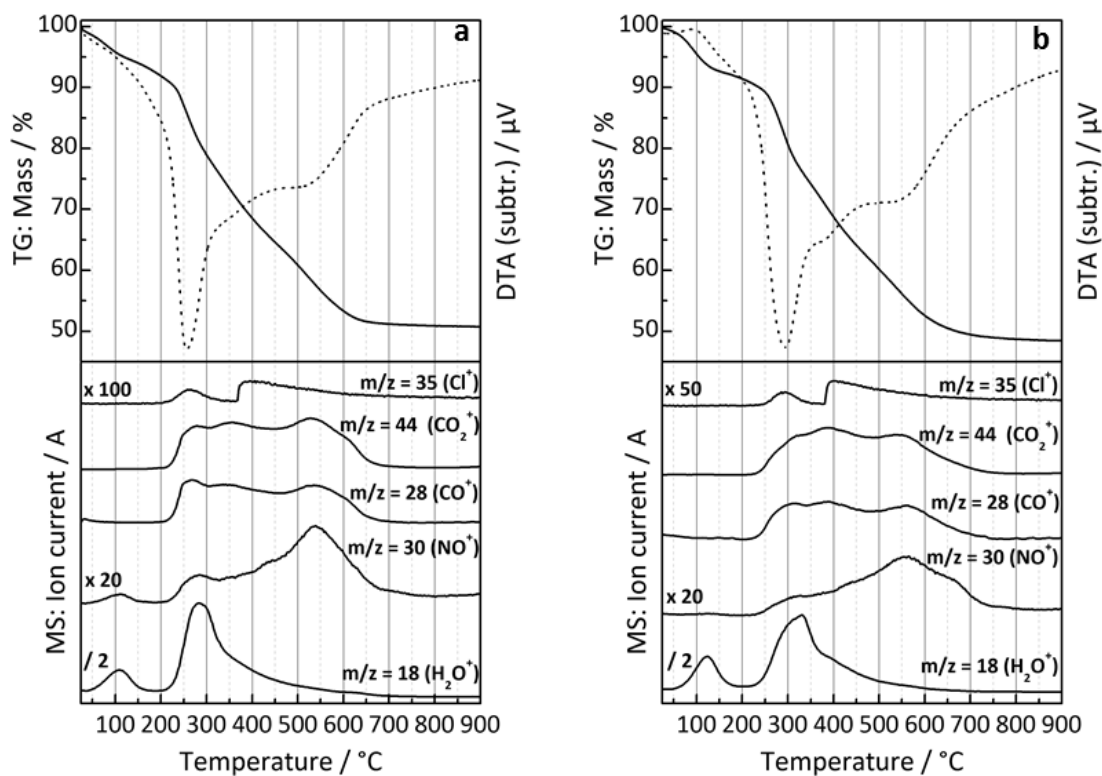


Figure 4.20: TG/MS/DTA of PMO aerogel (a) and t-PMO (b) measured in synthetic air. The diagram at the top shows the TG (solid line) and DTA (dotted line) curves whereas the ion currents detected by a mass spectrometer are depicted at the bottom of each diagram.

4.2.1.4 Hierarchical porous carbon

Synthesis and characterization of hierarchical porous carbon

A porous carbon was chosen in order to provide a distinct hydrophobicity as well as bimodal porosity. It was suggested that a mesoporous-macroporous hierarchical system can improve the diffusion through a pore system by loading only one pore system with the large molecule and leaving one pore system open for diffusion of smaller molecules like reactants or substrates.^[263,264] The synthesis of the hierarchical support was accomplished via an assembly of nanosized PMMA spheres (Figure 4.21). Monodisperse PMMA spheres were prepared by emulsion polymerization. The size of the particles was 400 nm with a polydispersity index (PDI) of 0.01 (monodisperse) determined by DLS.⁷

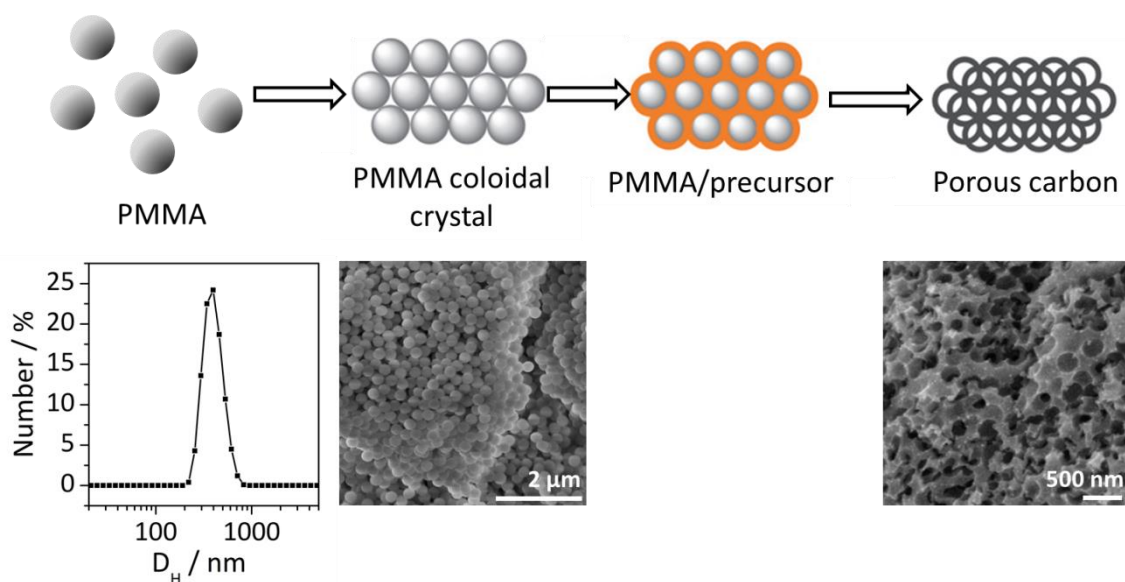


Figure 4.21: Synthesis of hierarchical macro-mesoporous carbon. PMMA spheres with a hydrodynamic diameter (D_H) of 400 nm, determined by DLS (left), were assembled to a PMMA monolith (middle). The monolith was impregnated with a resol-TEOS precursor solution and after solvent evaporation and thermal curing a PMMA-carbon composite was obtained. In the last step PMMA removal, silica removal by hydrofluoric acid treatment and carbonization were performed resulting in a porous carbon network (right).

After the assembly of the PMMA particles by sedimentation, PMMA monoliths were obtained. The particles in the monolith were not assembled in high order but a contact area between the particles was observed in SEM in most cases. The replication of the sphere assembly was performed with a precursor solution of TEOS, prepolymerized

⁷ The PDI is a general measure for the dispersity of a colloidal system. Below a PDI of 0.05 colloidal particles are considered as monodisperse.

phenol-formaldehyde resin and Pluronic F127 as a SDA for mesopores. After infiltration, solvent evaporation and thermal curing a PMMA/precursor composite was obtained that was further treated at high temperature to remove the PMMA and carbonize the material. The synthesized macro-/mesoporous carbon (Macro-C) has pore sizes of about 300-350 nm as can be seen in the SEM image (Figure 4.21). The smaller pore diameter is caused by shrinkage of the PMMA particles and the pores due to thermal treatment.

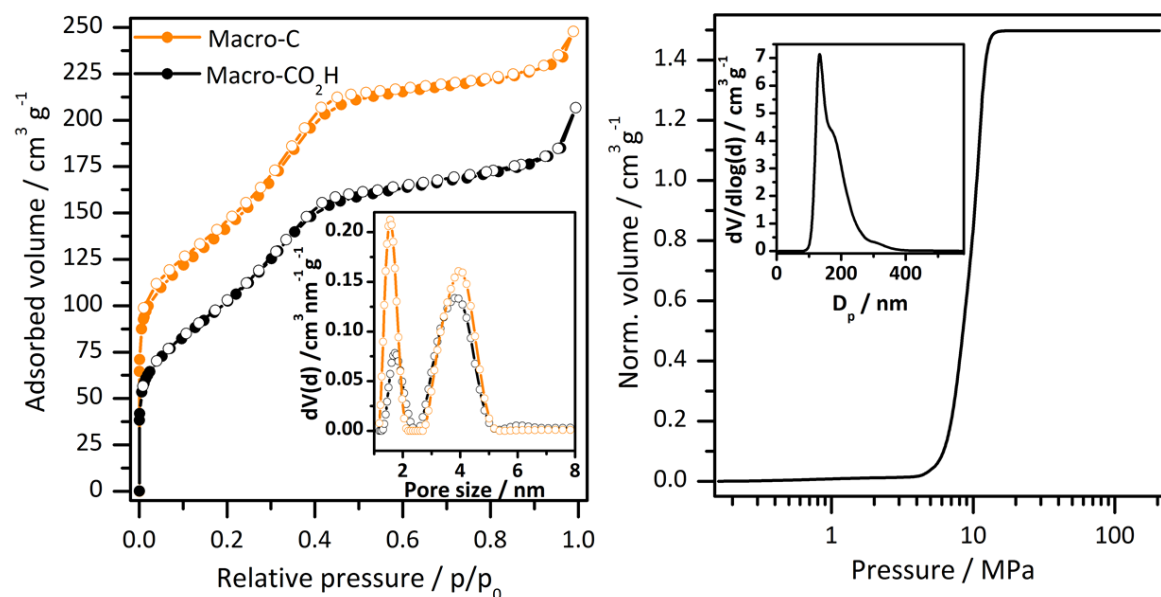


Figure 4.22: Nitrogen physisorption (left) measured at 77 K of Macro-C (orange) and Macro-CO₂H (black) with adsorption (filled symbols) and desorption (empty symbols). The inset shows respective pore size distributions determined by QSDFT (kernel: cylindrical pores equilibrium branch). Mercury intrusion with the respective pore size in the inset is shown for Macro-C on the right side.

Additionally to the imaging techniques, mercury intrusion as well as nitrogen physisorption was performed to gain further information about the porosity of the material. The physisorption isotherms (Figure 4.22) show a steep increase at low p/p_0 indicating the presence of micropores. The pore size distribution was obtained using QSDFT for cylindrical pores. The micropores have a diameter of 1.7 nm. A further increase in adsorbed volume of nitrogen can be assigned to the filling of the mesopores. No hysteresis is observed in this case since the diameter of the mesopores introduced into the walls of Macro-C by using Pluronic F127 was 3.8 nm and thus too small to show hysteresis. The small pore size did not allow the G6PDH to enter the pore system. The mesopore volume determined by QSDFT ($0.34 \text{ cm}^3 \text{ g}^{-1}$) was determined from nitrogen

physisorption whereas the macropore volume ($1.50 \text{ cm}^3 \text{ g}^{-1}$) was accessed by mercury porosimetry. The entrances to the macropores were investigated by mercury porosimetry. The intrusion curve and the pore size distribution based on the Washburn equation are shown in Figure 4.22. Since mercury intrusion in monoliths does not involve any packing effects only the filling of the macropores leads to an increase in intruded volume. Owing to the disordered structure of the material the distribution of the entrance diameter is quite broad (100-250 nm). The pore diameter cannot be accessed due to the reasons discussed in chapter 2.2.3. All data derived from mercury porosimetry and nitrogen physisorption are summarized in Table 4.12.

Table 4.12: Nitrogen physisorption data of Macro-C and Macro-CO₂H.

Sample	$S_{\text{BET}} / \text{m}^2 \text{ g}^{-1}$	$D_{\text{p,entr}} / \text{nm}$	$D_{\text{p}} (\text{macro}) / \text{nm}$	$D_{\text{p}} (\text{meso}) / \text{nm}$	$V_{\text{p}} (\text{macro}) / \text{cm}^3 \text{ g}^{-1}$	$V_{\text{p}} (\text{meso}) / \text{cm}^3 \text{ g}^{-1}$
Macro-C	518	100-250 ^a	300-350 ^b	3.8	1.5 ^a	0.35
Macro-CO ₂ H	388	-	-	3.8	-	0.27

a: determined by mercury porosimetry, b: determined by SEM

Oxidation and characterization of hierarchical porous carbons

Carbons are usually hydrophobic materials that need activation in order to optimize their performance for biomolecule uptake. One problem with hydrophobic materials is that they repel charged biomolecules, but even more difficult is their poor suspension behavior in buffers. Solutions to these problems would be the use of organic solvents or more hydrophobic proteins but neither of these possibilities could be applied here. The high stability of carbon powders against water was the reason to attempt optimizing the carbon surface for G6PDH uptake. Oxidation with ammonium persulfate (APS) is an established procedure to oxidize carbons. Treatment with APS can be easily controlled so that the porosity of the carbons is not altered too much and the surface is sufficiently accessible for water molecules. Successful functionalization is proven by nitrogen physisorption (Figure 4.22, Table 4.12) and IR spectroscopy (Figure 4.23).

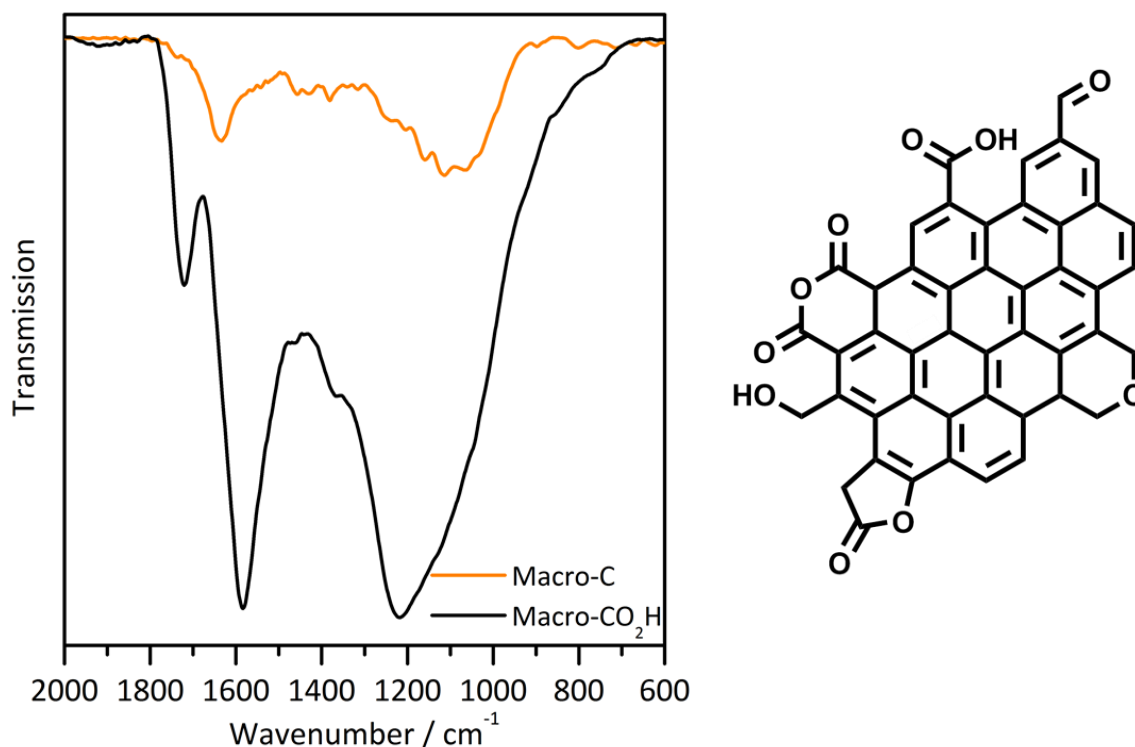


Figure 4.23: IR spectra of hierarchical macroporous carbons. C-O, C=C and C=O bands are increased or appear upon oxidation of Macro-C.

After oxidation of the carbon, various functional groups evolve that can interact in different ways with biomolecules.^[260,265–267] Carboxylic acid moieties are most important for interaction with proteins by hydrogen bonding and Coulomb interactions. A broad band in the FTIR spectra around 1220 cm^{-1} (C-O stretch) and at 1700 cm^{-1} (C=O stretch) are assigned to carboxylic acid groups. The aromatic C=C stretching vibrations (1590 cm^{-1}) are known to be increased by carbonyl groups conjugated to the aromatic system.^[267] The reduction of S_{BET} and V_p can be explained by the erosion of the carbon during oxidation and absolute weight increase by the addition of the oxygen.

Water vapor sorption (Figure 4.24) was performed in order to proof the different behavior of the porous carbons towards water. The uptake of water vapor was monitored at $25\text{ }^\circ\text{C}$ at relative humidity between 5-95 %. The isotherms can be classified according to IUPAC as type V isotherms. The type V isotherm is observed for materials that are hydrophobic or low hydrophilic. During adsorption the surface of the porous carbon is covered by water clusters until at a certain pressure capillary condensation in the mesopores takes place. The shift of the onset of capillary condensation to lower relative humidity after oxidation of the carbon can be assigned to the increased

hydrophilicity that leads to an increased adsorption at lower humidity. Additionally, the amount of adsorbed water at low humidity is strongly increased after oxidation. This indicates the successful hydrophilization of the porous carbon by oxidative treatment. The change of the hysteresis shape is due to a stronger interaction of adsorptive and adsorbent.

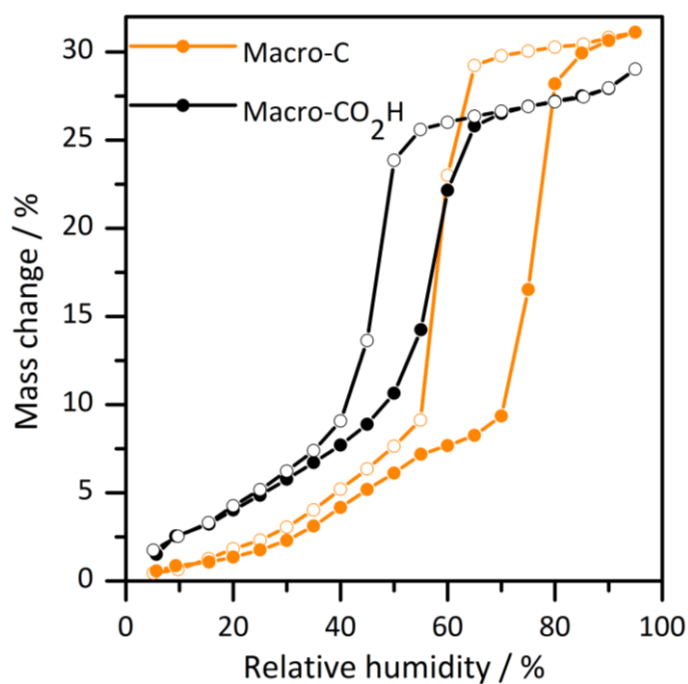


Figure 4.24: Water vapor sorption isotherms of macroporous carbons with adsorption (filled symbols) and desorption (empty symbols) measured at 298 K between a relative humidity of 5 and 95 %.

The reduction of the total amount of adsorbed water is caused by the reduction of surface area and pore volume observed after oxidation with APS.

4.2.2 IMMOBILIZATION OF G6PDH WITHIN NANOPOROUS SUPPORTS

The immobilization of G6PDH was first performed in nanoporous materials with different surface properties (charge, hydrophobicity) in order to evaluate a wide range of immobilization methods and applying forces. In order to investigate whether a material can be considered as a support or which forces apply during the immobilization procedure further insight into the enzyme crystal structure is necessary.

Structure and surface of G6PDH

The crystal structure of G6PDH from *Leuconostoc mesenteroides* was determined almost 10 years ago.^[14] From the crystal structure many important information is derived. One of the most important is the size of the enzyme that is the limiting parameter for the immobilization in porous materials. The diameter of the molecule is about 12.4 nm and the hydrodynamic radius larger than 13 nm.

Besides the size of the enzyme knowledge about the properties of the enzyme surface are mandatory for the immobilization process. Different interactions between the amino acids on the surface of the enzyme and the supports can occur: hydrogen bonding, Coulomb interactions, hydrophobic interactions as well as covalent bonding. These forces affect the uptake, amount of protein adsorbed, leaching behavior, activity and stability. The pI of the enzyme is 4.6, thus the enzyme has a negative net charge at neutral pH.^[268] The red color in the Coulombic surface mapping (Figure 4.25a) marks the negatively charged residues that mostly cover the surface of the enzyme. The strongly charged surface leads to a very hydrophilic behavior of the enzyme that further connects to its large hydrodynamic radius. The hydrophilic surface of the enzyme is shown in Figure 4.25b. The blue color assigns areas with hydrophilic amino acid residues whereas those with red color are hydrophobic residues. The surface charge of the enzyme and the hydrophilicity are key parameters for the immobilization of G6PDH onto the solid supports that span a wide range of charge as well as hydrophilic/hydrophobic behavior.

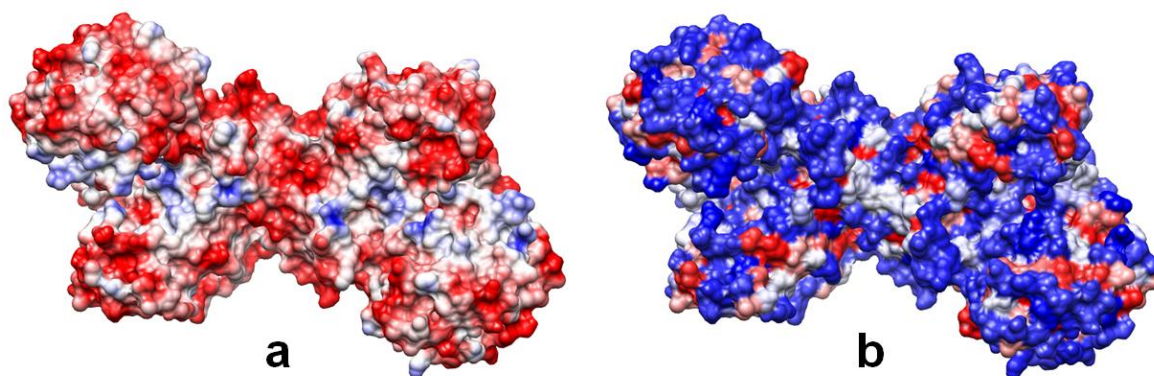


Figure 4.25: Mapping of the Coulomb surface potential (a, negatively charged (red) and positively (blue) and non- (white) charged areas) and hydrophilic surface (b, hydrophilic (blue)), hydrophobic (red) areas) of the G6PDH dimer.

Hierarchical carbons and MCF samples have been used for adsorption and covalent immobilization. A covalent attachment was achieved by an established method: a Schiff base reaction between glutardialdehyde-modified MCF (MCF-glu) and the surface amine groups of the enzyme. Besides the most frequently used lysine residues, the N-terminus can be covalently attached to an aldehyde as well. The covalent immobilization by an imine is considered in literature as a multipoint attachment method, which means that an enzyme is attached to the support with more than one amino acid. Due to the presence of many lysine residues this method is considered as unspecific, meaning that the immobilization cannot be directed.

Multipoint attachment is generally believed to improve the stability of an enzyme but to strongly reduce the activity due to rigidification. Another problem that can arise during multipoint attachment of multimeric enzymes to supports is the dissociation of their subunits that is accompanied by deactivation of the enzyme.

Immobilization, uptake and leaching of G6PDH

As mentioned above, simple adsorption was mainly used as immobilization technique. Only on MCF-glu G6PDH was covalently bound. The experimental procedure involved an incubation period of G6PDH with the respective support of 24 h at 25 °C and pH 7.4. During the immobilization samples were withdrawn at distinct time intervals to monitor the uptake of enzyme by the support. The amount of enzyme left in the solution was

determined by bicinchoninic acid protein assay (BCA)⁸ in order to calculate the protein that was taken up by the porous material. In Figure 4.26 the relative uptake with respect to the amount of enzyme in solution is shown.

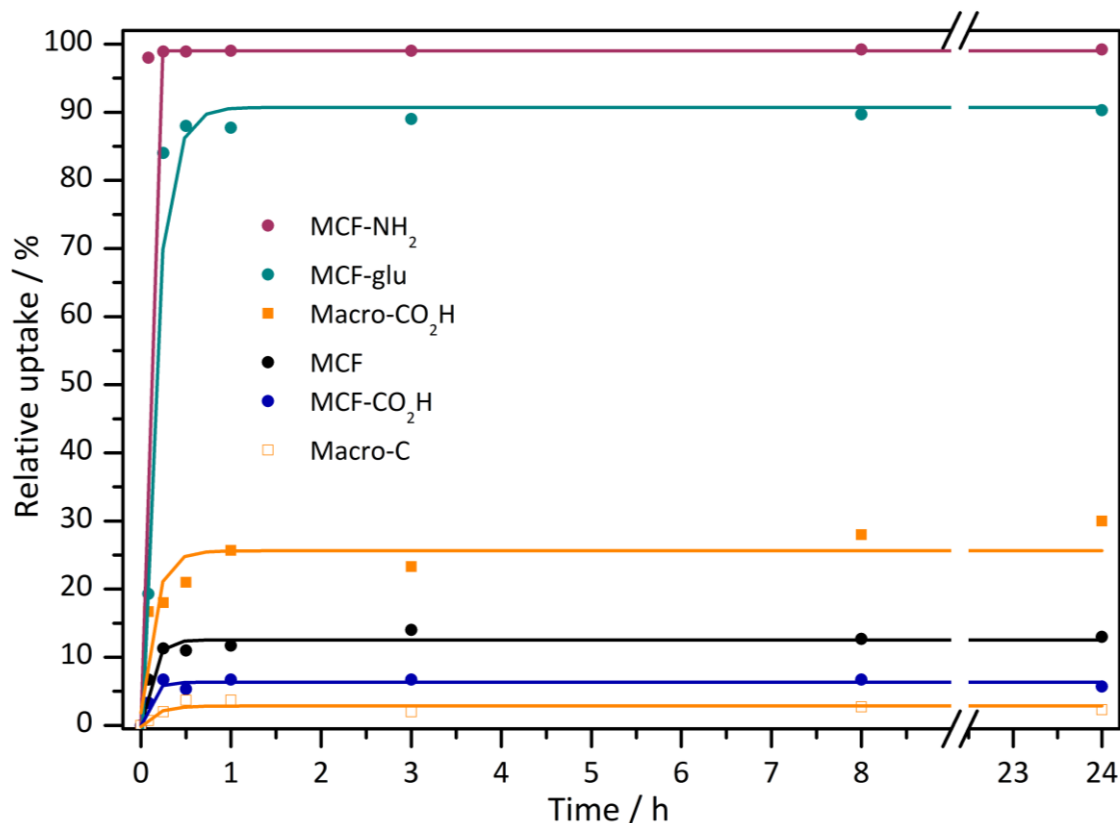


Figure 4.26: Relative uptake curves of G6PDH by nanoporous materials at 25 °C with asymptotic fit as a guide to the eye. The plateau was reached very fast for all supports. Most of the enzyme was taken up by MCF-glu and MCF-NH₂ whereas the other materials show moderate or low uptake.

Differences in the velocity of the enzyme adsorption or binding as well as the amount of enzyme have been observed. In all cases the enzyme was taken up very fast from solution. After one hour the plateau of the uptake curve was reached with all nanoporous supports. The maximum of adsorption was achieved by most materials after 30 minutes, whereas the amine-modified MCF reached the adsorption equilibrium after 15 minutes and Macro-CO₂H not until one hour.

⁸ The BCA assay is based on the reduction of Cu(II) to Cu(I) by the amide bonds of the protein. The reduced copper ion is then complexed by two molecules BCA and the formed purple complex is used for quantification of the protein.

The presence of the enzyme in MCF samples was additionally proven by IR and nitrogen physisorption at 77 K. After the immobilization bands for the stretching vibrations of the amide band occurred in the spectra. The band at 1656 cm^{-1} can be assigned to the C=O stretching vibration and the band at 1533 cm^{-1} to the N-H stretching vibration.

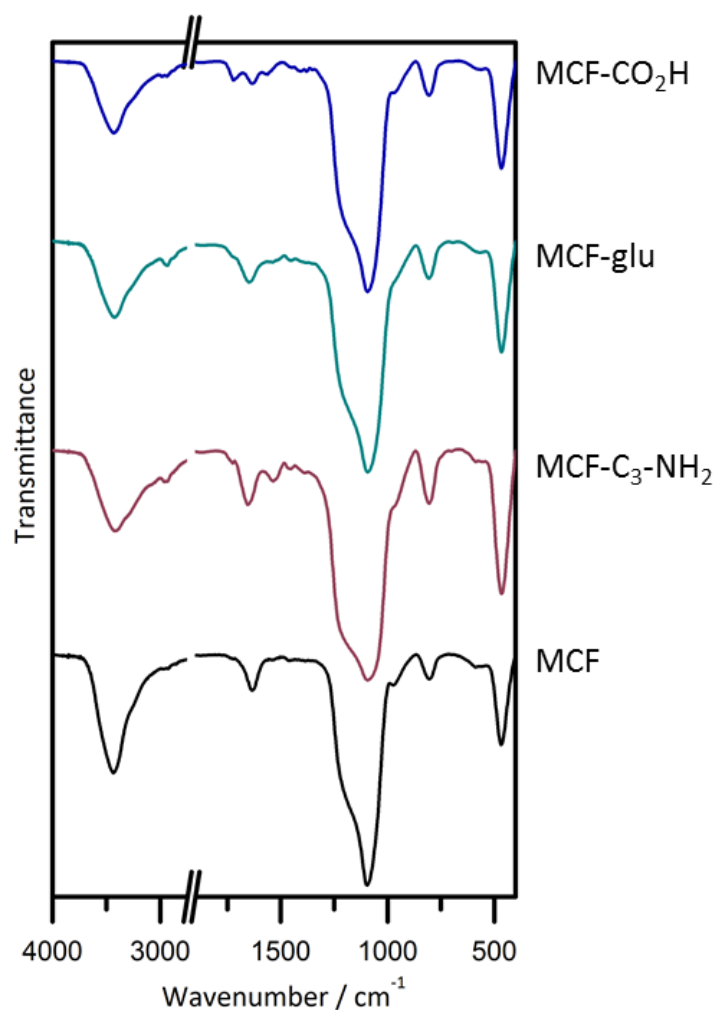


Figure 4.27: IR spectra of immobilized G6PDH. All samples show the respective bands for the amide stretching vibrations except the pure MCF since the amount of enzyme was too low.

The nitrogen physisorption data is summarized in Table 4.13. Reduced surface areas and pore volumes are observed as expected due to additional mass and reduced space inside the pores. However, this is only a hint that the enzyme is located in the pores and not outside the material. Since the amount of measured sample is very low the data is prone to errors. Also, the addition of an enzyme inside the pores does not necessarily

lead to a reduction of the surface area or pore volume since the enzyme itself creates surface and cavities. The amount of space required by the enzyme is also dependent on the folding of the enzyme after treatment at reduced pressure.

Table 4.13: Nitrogen physisorption data (77 K) for immobilized G6PDH onto MCF samples.

Sample	$S_{\text{BET}} / \text{m}^2 \text{g}^{-1}$	$D_{\text{p,entr}} / \text{nm}$	D_{p} / nm	$V_{\text{p}} / \text{cm}^3 \text{g}^{-1}$
MCF	361	21	31	2.23
MCF-P	352	20	31	2.21
MCF-NH ₂	277	21	30	1.74
MCF-NH ₂ -P	238	22	32	1.63
MCF-glu	274	22	30	1.64
MCF-glu-P	270	20	30	1.55
MCF-CO ₂ H	305	20	30	1.90
MCF-CO ₂ H-P	297	21	31	1.81
P = protein				

The net uptake of the enzyme by the nanoporous supports was not only expressed by the adsorption kinetic but also by the protein content (Figure 4.26) that was left after separation of the solid from the solution. The kinetic uptake curves show a high uptake for the adsorption onto the surface of MCF-NH₂ and the covalent immobilization by imine bond in MCF-glu. The total uptake of protein from solution (Figure 4.28) after 24 h reached almost 100 % for the amine-modified support material and almost 90 % with the covalent method. All other materials exhibited less affinity and thus less uptake of protein. Only the oxidized carbon sample (Macro-CO₂H) showed a moderate uptake performance (30 %).

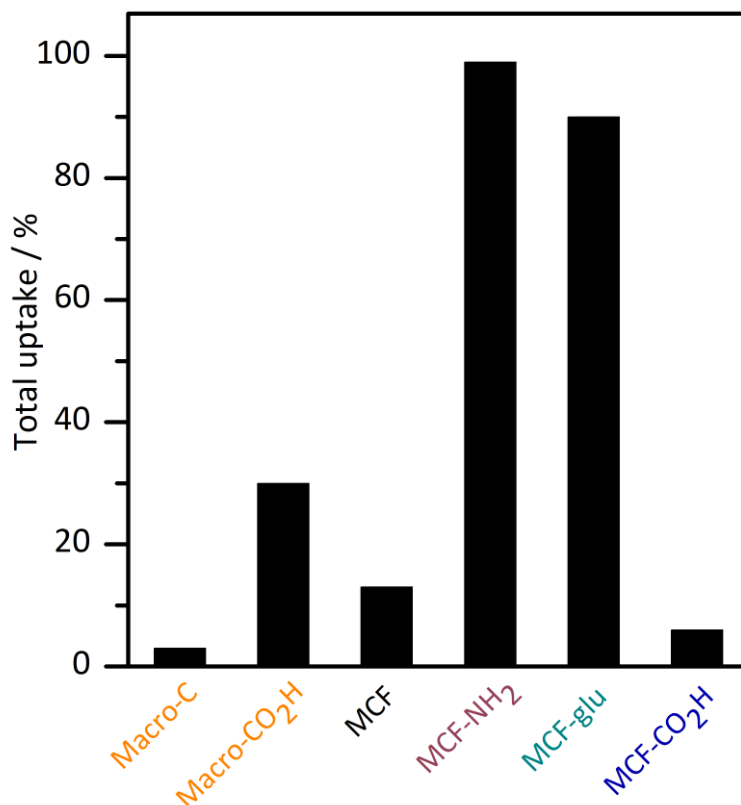


Figure 4.28: Total uptake of G6PDH from solution by nanoporous supports respective to the enzyme content in solution.

The total protein content before and after washing cycles is another measure to illustrate the affinity of the respective support to the material. The mass specific protein content for each sample is expressed in mg enzyme per g support (Figure 4.29). The amount of enzyme after three washing steps is commonly subjected to the loss of loosely attached enzyme molecules and thus to a small reduction in the mass specific enzyme content. In this case a minor reduction of the enzyme content was observed for most samples. Only the protein content of the carbon materials was greatly reduced after washing indicating that the interactions were not strong enough to overcome the leaching from the support. The large macropore size additionally supported this effect. Nonetheless, the protein content after oxidation of Macro-C was significantly enhanced due to hydrophilization of the surface.

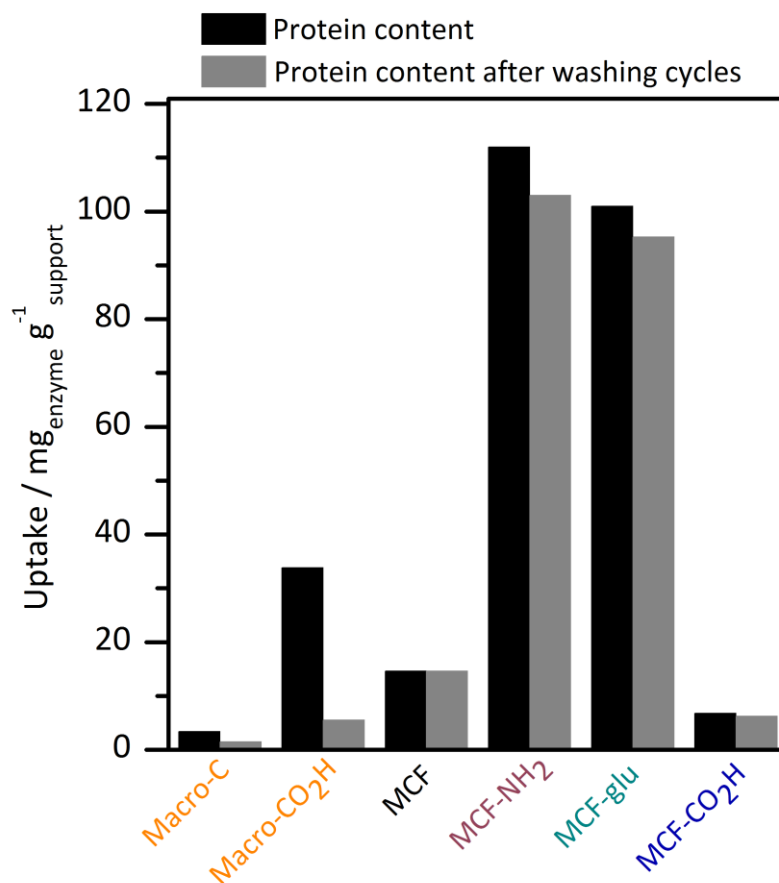


Figure 4.29: Protein content of nanoporous samples prior and after applied washing cycles. The mass specific uptake is presented in mass of enzyme respective the mass of the support material.

But how can these differences be explained? In general the uptake of enzymes is directed by different interactions between the amino acids on the surface of the protein and the support: hydrogen bonding, Coulomb interactions, hydrophobic interactions as well as covalent bonding. Thus the support as well as the enzyme has to be evaluated for possible interactions they can contribute to the immobilization. The silica network offers hydrophobic parts that are created by the siloxane bridges and more hydrophilic silanol groups. But the hydrophilic nature of these supports is mainly caused by the organic moieties that have been introduced by postsynthetic modification. However, these residues can also contribute to hydrophobic properties due to their organic chains. The hydrophilic part of the organic residue is usually extended into the inner of the pore. Thus silicas provide hydrophobic as well as hydrophilic nature.

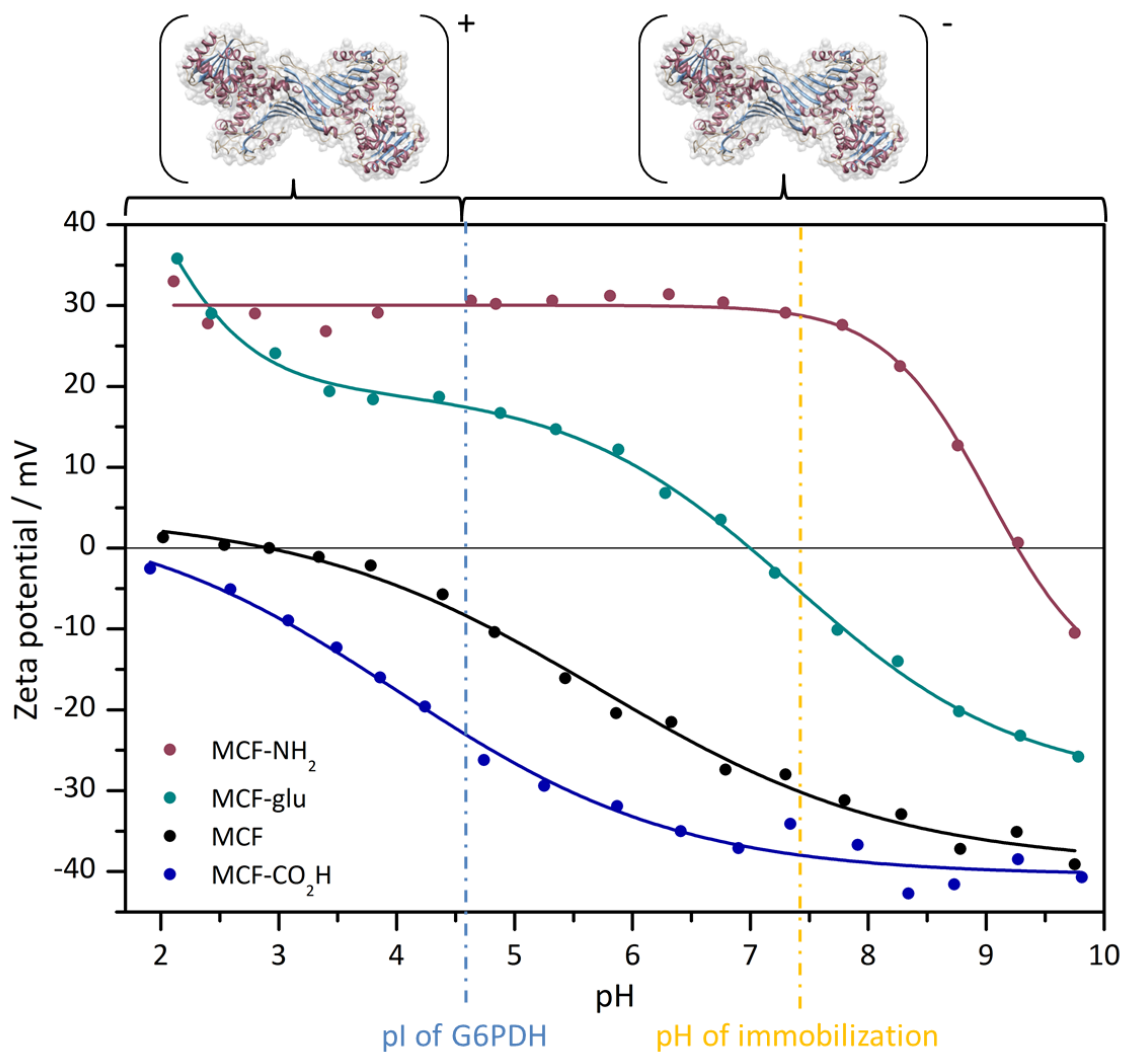


Figure 4.30: Zeta potential titrations of the mesoporous silica supports. Below their isoelectric point materials and the enzyme ($pI = 4.6$) are positively charged, above negatively. At the pH of immobilization (pH 7.4) the enzyme, MCF and MCF-CO₂H exhibit a negative net charge whereas MCF-glu is essentially non-charged and MCF-NH₂ positively.

Additionally, the silanols polar functional group can contribute to the creation of hydrogen bonds. The strongest non-covalent forces are Coulombic forces that are part of charged species in the materials. To evaluate the protonation/deprotonation behavior of the silica supports zeta potential titrations (Figure 4.30) between pH 2 and 10 have been performed. It has to be mentioned here, that not only the functional groups of modified MCFs take part in the acid/base reactions but also free silanols left in the material. Thus these measurements depict always an equilibrium between the acid/base behavior of the silanol groups and the functional group. MCF-CO₂H and pure MCF are deprotonated almost during the complete pH range thus their pI is reached at very low

pH. Both materials have strongly acidic behavior leaving the silanol or carboxylic acid groups deprotonated. In contrast the amine-functionalized silica is positively charged until its pI is reached at pH 9.3 due to the protonation of the amine groups. MCF-glu has an isoelectric point at neutral pH and is thus almost neutral or slightly negatively charged at pH 7.4. Since the aldehyde groups are not able to contribute to the charge behavior, the protonated imine group (base) is almost neutralized by silanol groups (acid). A summary of the results of the zeta potential titrations is found in Table 4.14.

Table 4.14: Isoelectric points of nanoporous samples with the respective charged group at the pH of immobilization and possible types of interaction.

Sample	MCF	MCF-CO ₂ H	MCF-glu	MCF-NH ₂	Macro-C	Macro-CO ₂ H
pI	2.9	<2	7.0	9.3	n.d.	n.d.
Charged group (at pH 7.4)	Si-O ⁻	-CO ₂ ⁻	Si-O/ =NH-	-NH ₃ ⁺	None	-CO ₂ ⁻ , -O ⁻
Type of interaction ^a	Coulomb (-) H-bonds HI	Coulomb (-) H-bonds HI	Covalent H-bonds HI	Coulomb (+) H-bonds HI	HI	HI Coulomb (-) H-bonds

a: possible interactions in order of their probability and strength

n.d.: not determinable; HI: hydrophobic interactions; H-bonds: hydrogen bonds

Due to their poor dispersibility and the high light absorption of the carbons it was not possible to generate zeta potential measurements of the hierarchical carbon samples with the available optical setup.

The zeta potential titrations delivered insight into the charge of the materials but some light has still to be shed onto the enzyme as a counterpart during the immobilization. At the beginning of the chapter the general surface properties of the enzyme were summarized. G6PDH is an enzyme with a hydrophilic surface that exhibits a negative net charge at neutral pH. In the following paragraphs the surface is studied in more detail with respect to possible interactions with the nanoporous materials.

To sum up, all nanoporous materials (except Macro-C), have the ability to built hydrogen bonds to the enzyme. The silicas have their functional groups as well as the silanols whereas the oxidized carbons have oxygen-containing functional groups for the attachment. In Figure 4.31 polar amino acids on the surface of G6PDH are marked that can act as hydrogen bonding sites.

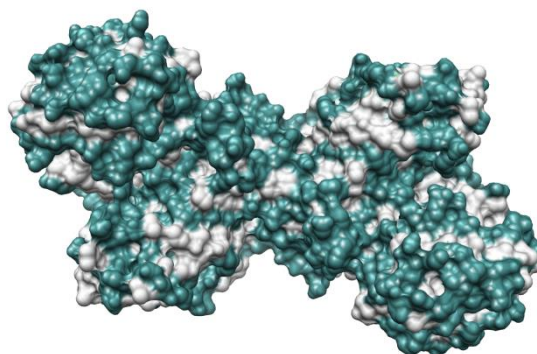


Figure 4.31: Polar amino acids at the surface of G6PDH colored in cyan. The polar amino acid residues are possible H-bond sites.

Since both carbons studied here can be considered as hydrophobic supports, they will interact mostly with hydrophobic amino acids (Figure 4.32a) in the enzyme. The aromatic portion of the carbons is probably directed towards aromatic amino acids (Figure 4.32b). As can be seen in Figure 4.32 hydrophobic and aromatic amino acids are not directly located at possible contact areas but more hidden in small pockets of the enzyme so that they are not directly exposed to the hydrophilic aqueous exterior.

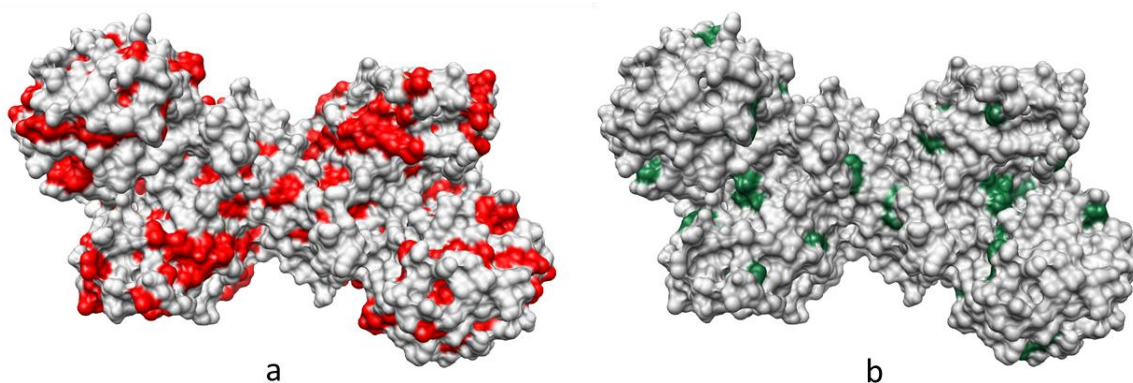


Figure 4.32: Surface of G6PDH with hydrophobic amino acids (a, red) and aromatic amino acids (b, green). Most of these amino acids are hidden from the external aqueous environment.

The most prominent interactions that direct the uptake of an enzyme are commonly Coulomb forces. Most materials used here exhibit a negative net charge (Table 4.14) at the pH of immobilization whereas MCF-NH₂ is the only material with a positive charge. As discussed at the beginning of the chapter the enzyme exhibits a negative net charge at pH 7.4 due to its isoelectric point (pH 4.6). Charged amino acids are depicted in Figure 4.33.

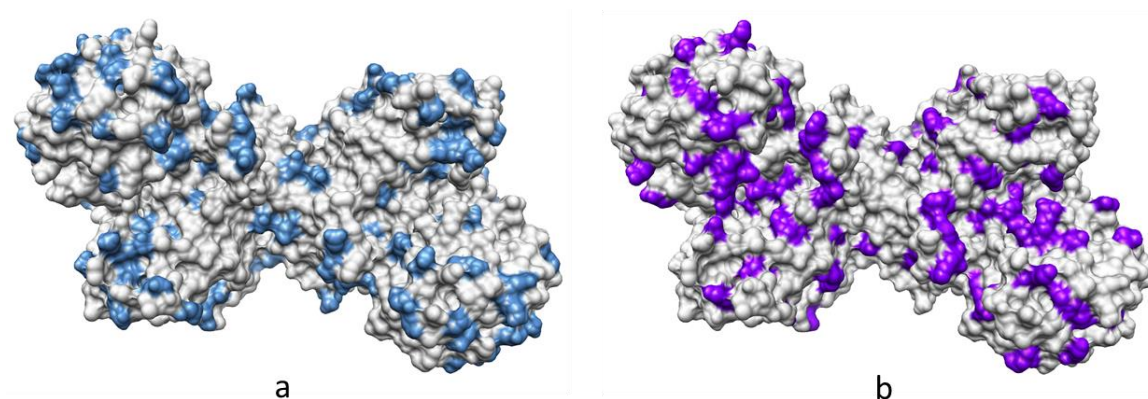


Figure 4.33: Surface of G6PDH with negatively charged amino acids (a, blue) and positively charged amino acids (b, violet).

In this context the uptake kinetics can be discussed. A rapid and complete uptake of enzyme, like that observed with MCF-NH₂, is usually governed by strong attractive forces that are obviously present between the positively charged amine-modified silica and the negatively charged amino acid residues at the surface of the enzyme. In contrast the negatively charged silicas (MCF-CO₂H, MCF) exhibit very low uptake of G6PDH due to strong repulsive forces of the equally charged residues. That supports the assumption that mainly electrostatic attraction and repulsion occur between the protein and the support. The differences in the uptake of MCF and MCF-CO₂H can be explained by the orientation of the residues. The silanols groups are attached directly at the wall and do not, like the carboxylic acid chains extend into the inner of the pore. Additionally, two carboxylic acid residues are present at one carbon chain increasing the local negative charge concentration. Thus the carboxylic acid groups do have a stronger repulsion towards the enzyme.

Hydrogen bonding is another type of attractive forces that may apply but it is less attractive. That does usually not only lead to lower amount of adsorbed enzyme but also to a slower adsorption. Since hydrogen bonds are directed forces in contrast to Coulomb interactions the orientation of the enzyme inside the porous system is less rapid. The slowest adsorption was observed with the hierarchical carbons (Macro-C and Macro-CO₂H) due to the still hydrophobic nature of these materials. Macro-C exhibits a very low uptake of protein but after oxidation (Macro-CO₂H) the total uptake was much higher. These differences can be assigned to the hydrophilicity of the carbon materials

as well as the possible creation of hydrogen bonding for Macro-CO₂H. It has to be pointed out that the protein was almost completely washed out of the oxidized carbon after three washing cycles. The reasons are the large pores and the weak interactions in this material. G6PDH is an enzyme with hydrophilic amino acids on the surface and is obviously not attracted by hydrophobic interactions that are reported for example for lipases in hydrophobic materials.

However, the amount of adsorbed protein on Macro-CO₂H was much higher than for MCF-CO₂H. This effect is most likely caused by the native high presence of various not necessarily negatively charged oxygen-containing groups on the surface of the carbon material (see Figure 4.23) whereas the immobilization onto the silica surface is mainly inhibited by the repulsion of the negatively charged carboxylic acid groups.

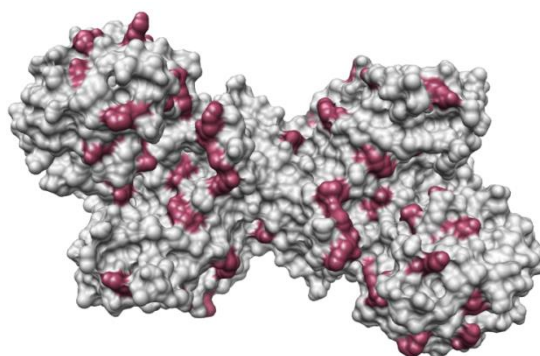


Figure 4.34: Surface of G6PDH with marked lysine residues that are exposed to the outside of the molecule. Lysines are the main anchors in proteins for covalent anchors.

Glutardialdehyde modified MCF (MCF-glu) was used to covalently attach the G6PDH. Almost 90 % of the protein in solution was taken up very fast by the porous support. The fast uptake is due to the low electrostatic repulsion of the almost non charged aldehyde modified support to the negatively charged protein. Therefore the diffusion in the pores is less hindered. Due to the absence of opposite charges the binding of the G6PDH is not electrostatically but rather covalently at the lysine residues of the protein (Figure 4.34).

The distributions of the amino acids that are responsible for the respective association of the enzyme to the support are widely distributed over the enzyme. Thus no specific areas for the binding are present and a discussion of the orientation of the enzyme towards the wall of the nanoporous materials is not possible in terms of specific

areas of amino acids. However, a maximization of contacts between wall and enzyme would be feasible for the enzyme considering the concept of attractive opposite charges or covalent bonding. Thus, when the enzyme is immobilized onto MCF-NH₂ and MCF-glu an orientation along its extended surface (Figure 4.35b) is more probable whereas the reduction of contacts to the negatively charged walls of the other supports is preferred to reduce the repulsion. In that case the enzyme would be oriented at one of its “tips” (Figure 4.35a).

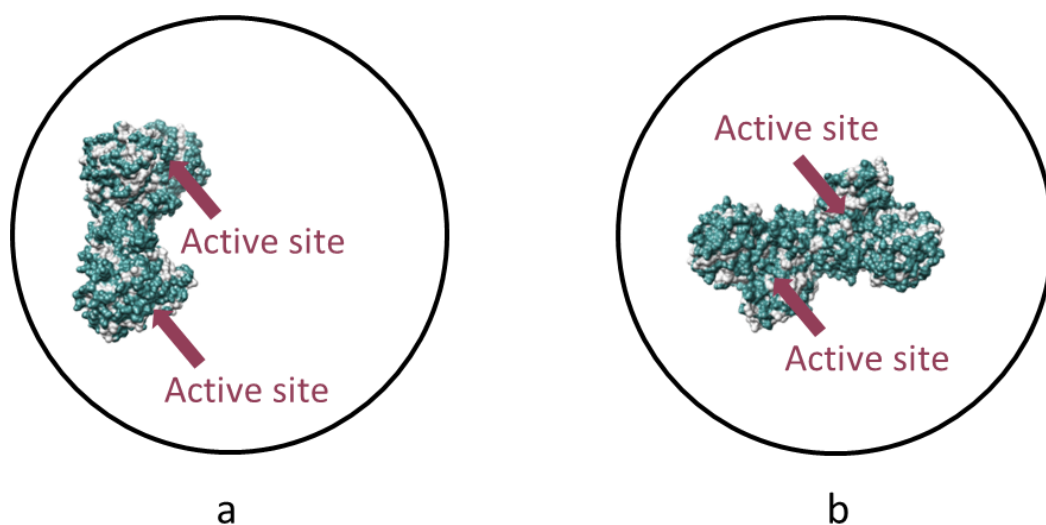


Figure 4.35: Schematic illustration of possible orientations of G6PDH. The adsorption onto negatively charged MCFs leads to a repulsion of the negative net charged enzyme and the negatively charged pore walls. Hence a reduction of contact area (b) is preferred. A maximization of the contact area of enzyme and pore wall would be favorable for situations with strong attractive interactions (a).

For all support materials there was no leaching detected but for the sample Macro-CO₂H (25 % after 24 h) where the protein leached out of the pores due to the reasons mentioned above.

Activity of G6PDH

Besides the amount of enzyme in the nanoporous materials the activity and stability of the enzymes inside the nanopores are key parameters that need to be addressed. In most cases the activity is reduced after the immobilization whereas the stability is increased. The loss of activity can have several reasons:

- 1) The active site is located next to the pore wall or another enzyme hindering the substrate to diffuse towards the active site.
- 2) The movement of the enzyme is hindered due to rigidification.
- 3) Unfolding occurs as a result of “spreading” (maximization of the contact surface) or due to the nature of the substrate.
- 4) Diffusion problems arising from the porosity of the support.
- 5) Adsorption of one of the substrates or the product by the support.
- 6) Partitioning effects (different microenvironment inside the confined space).

Since so many factors influence the activity of an enzyme it is usually not possible to differentiate how the enzyme is deactivated. One of the reasons often forgot is the different microenvironment in a pore that can affect the charge density, pH and hydrophilicity of the solution inside the pore compared to the buffer solution outside the microenvironment. This environment affects the stability and activity of the enzyme as well as the diffusion of substrate and/or product.

In the case of G6PDH immobilization point 2) of the above mentioned influence parameters can be almost excluded, except for covalent immobilization, from the discussion. Due to the restricted space, mobile proteins may be deactivated after immobilization. The B-factor (crystallographic measure for the thermal movement) gives information on the mobility of the G6PDH. A high B-factor (Figure 4.36, red) assigns regions with high mobility. As can be seen from Figure 4.36 the protein has a predominantly stiff structure. During the binding of NADP^+ and G6P only small conformational changes are observed.

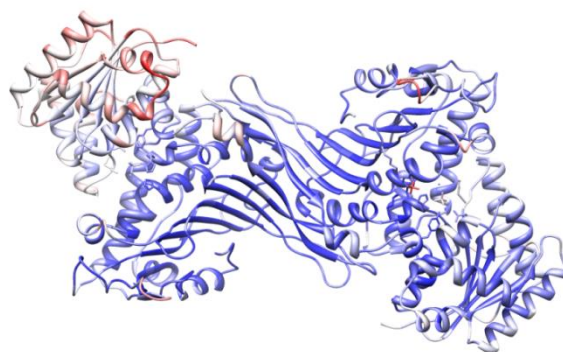
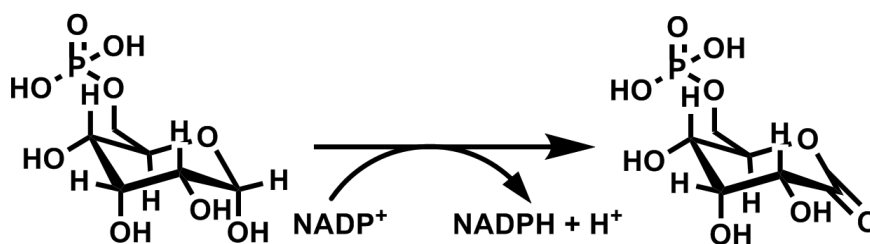


Figure 4.36: Mobility of G6PDH. The red areas are assigned to regions of higher mobility whereas blue region are assigned to stiff regions.

The enzyme catalyzes the conversion of glucose-6-phosphate to 6-phosphogluconolactone by reduction of NADP^+ to NADPH (Scheme 4.3). The absorbance of NADPH was monitored at 340 nm by UV/Vis spectrometry to calculate the activity. In all stability studies the activity is depicted as relative activity to make the comparison of the materials easier.



Scheme 4.3: Conversion of glucose-6-phosphate to 6-phosphogluconolactone by reduction of NADP^+ to NADPH catalyzed by G6PDH.

The retention of activity was determined as relative activity (Figure 4.37) compared to the free enzyme after immobilization.

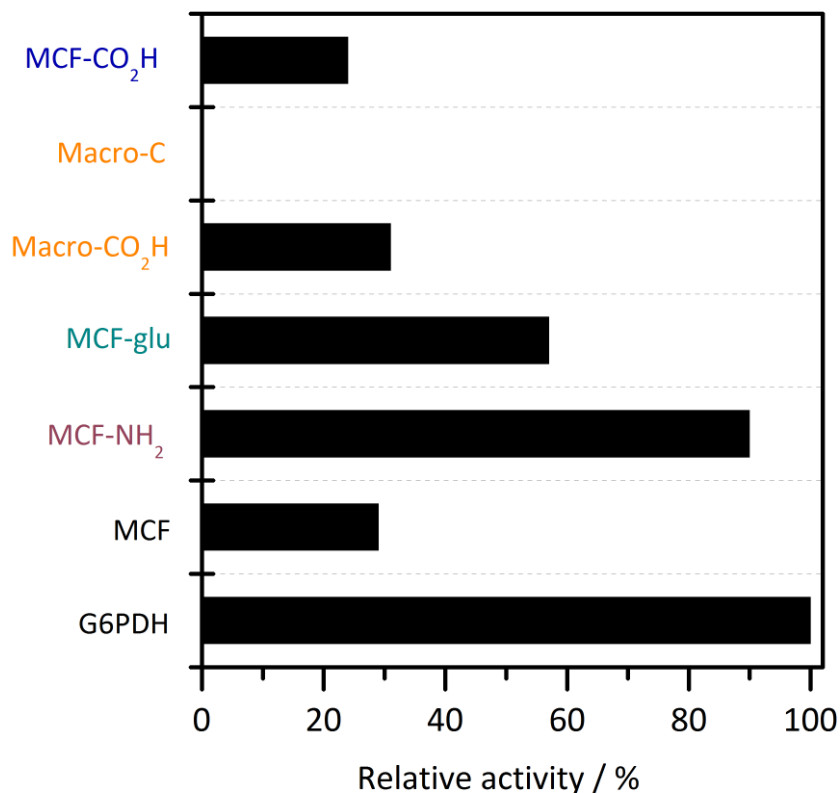


Figure 4.37: Relative activity of immobilized G6PDH compared to the activity of the free enzyme.

The total activity per mg support and enzyme is also shown in Table 4.15 to compare the respective materials. The electrostatic attachment of G6PDH onto MCF-NH₂ achieved very high activity retention of 90 % whereas the activity of Macro-CO₂H, MCF-CO₂H and MCF is relatively low (20 and 30 %).

Table 4.15: Relative and total activities for immobilized and free G6PDH.

Sample	Relative activity / %	Activity / U mg ⁻¹ enzyme	Activity / U mg ⁻¹ support
G6PDH	100	336	n.d.
MCF	29	99	1.44
MCF-NH ₂	90	302	31.1
MCF-glu	57	191	18.3
MCF-CO ₂ H	31	103	0.64
Macro-C	n.d.	n.d.	n.d.
Macro-CO ₂ H	24	79	0.47

n.d.: not determinable

After the covalent immobilization of G6PDH on MCF-glu almost 60 % of the initial activity remained. For covalent techniques this is an excellent result because less than 50 % remaining activity is a common result obtained after covalent immobilization.^[269,270] The loss of activity is most likely due to rigidification of the enzyme due to multipoint attachment. Since the active site is more or less buried in a cleft direct covalent attachment of the glutaraldehyde to an amino acid next to the active site is unlikely. No activity was detected for Macro-C due to the low loading.

As already mentioned above, a loss in activity can have several reasons. One possible explanation is the shielding of the active site. As described above orientations with a maximization or minimization of contacts between enzyme and pore wall are possible. But in both cases the active site would not be completely shielded (Figure 4.38). Since the active site is in a cleft of the enzyme even an orientation of the active site against the pore wall would only enhance the diffusion resistance of substrate and product. A complete deactivation due to blocking of the active site would not occur.

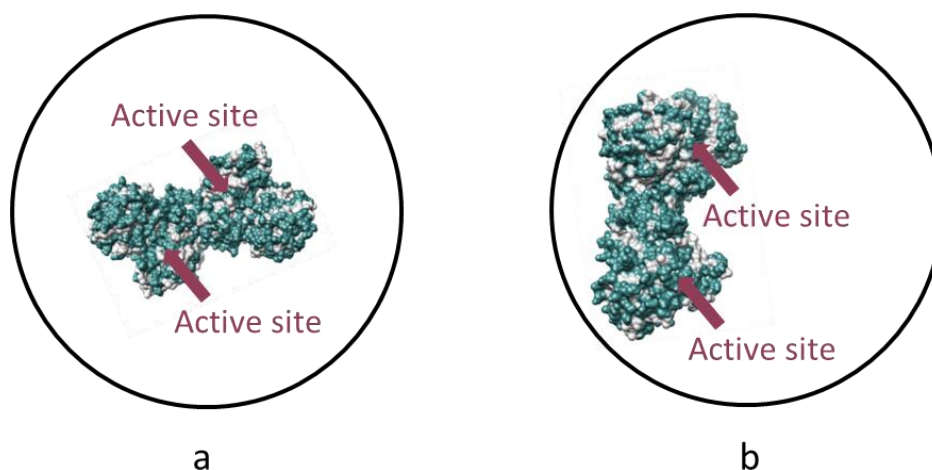


Figure 4.38: Schematic illustration of possible orientations of G6PDH with its active sites. Although the enzyme has two possible active sites only one at a time is active.

The most important issue in the discussion of activity reduction is the consideration of the environment inside the pore being completely different from the solution outside the porous network. On one hand the confinement of the protein inside the pore can lead to steric hindrances that have been discussed above, on the other hand so-called partitioning effects arise.^[31,271] These effects can lead to changed conditions in the vicinity to the surface. Thus inside a pore an environment arises that exhibits different salt concentration and pH compared to the buffer outside. MCF-NH₂ acts basic and is thus easily protonated whereas MCF-CO₂H and pure MCF materials are more acidic. Since the catalytic activity of an enzyme is strongly influenced by the pH the activity is can be either reduced or increased. The activity of G6PDH has its maximum at slightly basic conditions (pH 7.4-7.8) so that a basic interior inside the pores would benefit the conversion of G6P.^[17] Thus MCF-NH₂ exhibits higher activities than the acidic supports MCF-CO₂H, MCF and the respective carbons. Since MCF-glu exhibited almost no charge at pH 7.4 the activity will not be affected by the pH inside the pores.

The last issue that has to be considered in the context of enzyme activity in porous materials is diffusion. Cofactor and substrate have to diffuse into the pores of the material and to the active site or the cofactor binding site. After the release of the product it has to diffuse out of the material to be detected. In the activity assay the substrate is applied in 3-fold excess so that the availability of the cofactor is more important. To investigate the uptake behavior for the cofactor by the respective

materials, cofactor adsorption experiments have been performed. A solution containing NADP^+ was incubated with the samples to adsorb the cofactor to some extent. Afterwards the solid was separated and the concentration of NADP^+ in the supernatant was tested. Since the detection of NADP^+ is much more prone to errors, the cofactor was converted to NADPH by addition of G6P and G6PDH. The absorbance of NADPH is then detected at 340 nm. The plots for the respective samples are shown in Figure 4.39.

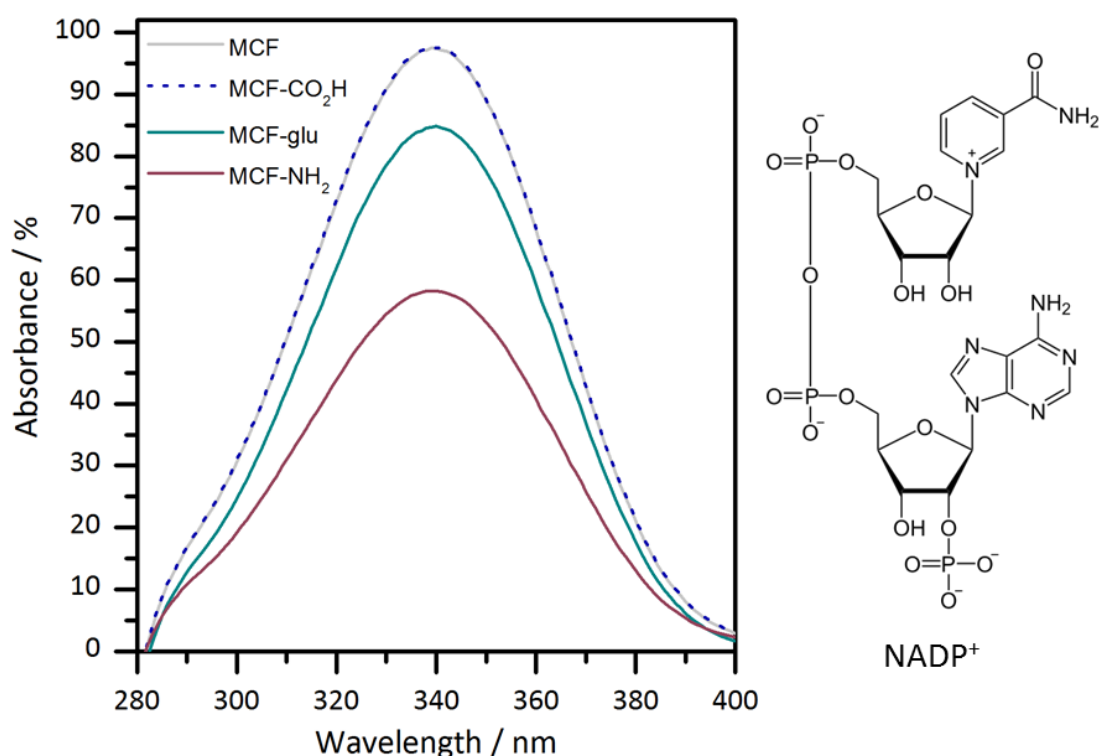


Figure 4.39: Adsorption of NADP^+ in nanoporous materials. After conversion to NADPH the residual NADPH was quantified in the supernatant. The absorbance of the respective supernatants is shown here relative to the absorbance of the used NADP^+ solution.

The adsorption of NADP^+ shows that the affinity of MCF-NH_2 and MCF-glu towards the cofactor is much higher. Plain silica as well as carboxylic acid-modified silica showed no adsorption of NADP^+ . This is mainly due to electrostatic reasons, since the negatively charged phosphate residues of NADP may lead to repulsion with negatively charged support materials whereas it is attracted towards positively charged MCF-NH_2 . Thus the diffusion of the cofactor into the pore system and thus to the binding site might be enhanced for MCF-NH_2 and hindered for negatively charged supports.

To conclude, the partitioning effect inside the porous system affects the diffusion as well as the pH inside the pore system. It has a positive effect on the activity for G6PDH immobilized on MCF-NH₂ whereas a reduction of activity is observed for negatively charged materials.

Stability of immobilized G6PDH

The remaining activity of the protein after the immobilization process is of course an important number but even more important is the stability of the enzyme inside the pores of the specific host. The storage stability at 4 °C, the thermal stability and the cycle stability of the respective biocatalysts were compared to the stability of the native protein. The stabilization phenomenon that is associated with the confinement inside the pores is usually discussed in the context of the following reasons:

- 1) Rigidification due to the attachment onto the pore walls.
- 2) Partitioning effects:
 - a) No deactivation by microbial fouling, gas bubbles or shear forces inside the pores.
 - b) Different microenvironment inside the pore as a confined space compared to the external environment.

The storage stability at 4 °C (Figure 4.41, Table 4.15) of the G6PDH immobilized on all MCF supports was very high, meaning that the loss of activity during a certain period is very low. Thus, the immobilization on the pore wall, either electrostatical or covalent, provided enough stability for the enzyme at 4 °C and acted as a diffusion barrier to prevent diffusion out of the pores. G6PDH immobilized on Macro-CO₂H was not stable due to leaching that was reported above from the support. The large pores of the carbon as well as the weak immobilization forces led to diffusion out of the pores even at 4 °C. In the solution the leached protein is subjected to the same denaturation phenomena as the free protein in solution.

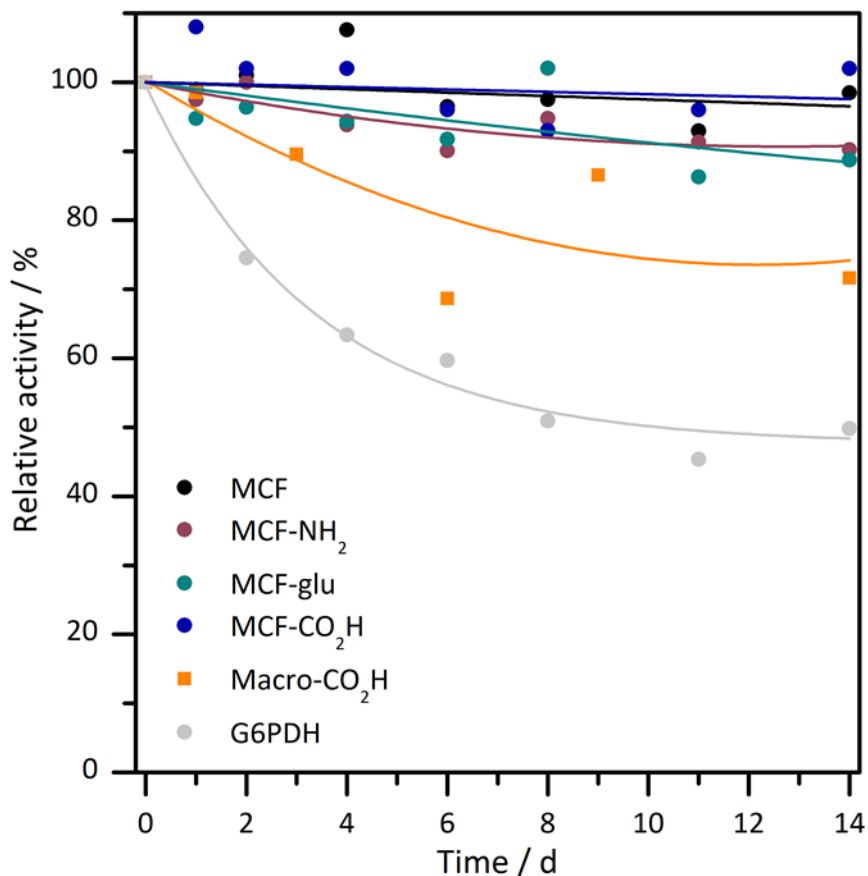


Figure 4.40: Storage stability at 4 °C for immobilized and free G6PDH. Solid lines are guide to the eye. Immobilization in MCF led to a significant stabilization whereas immobilization in the macropores of the carbon materials did not enhance the stability.

Heating the buffer suspensions of each material to 37 °C gives information on the thermal stability of the protein. Usually, the phenomena described for the storage stability are enhanced at 37 °C due to enhanced thermal movement and diffusion. As can be seen in Table 4.15 and Figure 4.41 the thermal stability is high for the protein immobilized in MCF-NH₂ and MCF-CO₂H indicating that the forces between protein and support surface stabilize the protein even at higher temperature. The activation phenomenon observed for MCF-NH₂ is further discussed in the next chapter. The stabilization of the protein in MCF-CO₂H is mainly caused by hydrogen bonding not by electrostatic interactions due to the repulsive forces at the immobilization pH between negatively charged support and enzyme. The observed stabilization effect is lower for the covalent attachment and the immobilization via interactions with the silanol groups on pure MCF. The difference between both negatively charged residues is the extension of the residues into the pore. Whereas the carboxylic acid groups are extended into the

pore the silanol groups are located directly at the pore wall. The extension of the negatively charge residues still provides the possibility of binding to positively charged residues of the protein.

The reduction of stability at higher temperatures due to low intermolecular forces is not a possible explanation for the activity loss that occurred on MCF-glu. One reason might be that the higher temperature results in switching the equilibrium of the imine formation towards the free protein. This would lead to protein leaching into the solution, which could not be detected because the concentration was below the detection limit. Another issue could be “spreading” of the protein. This phenomenon occurs when a protein tries to maximize its contact areas with a surface and thus leads to unfolding of the protein at a certain extent.

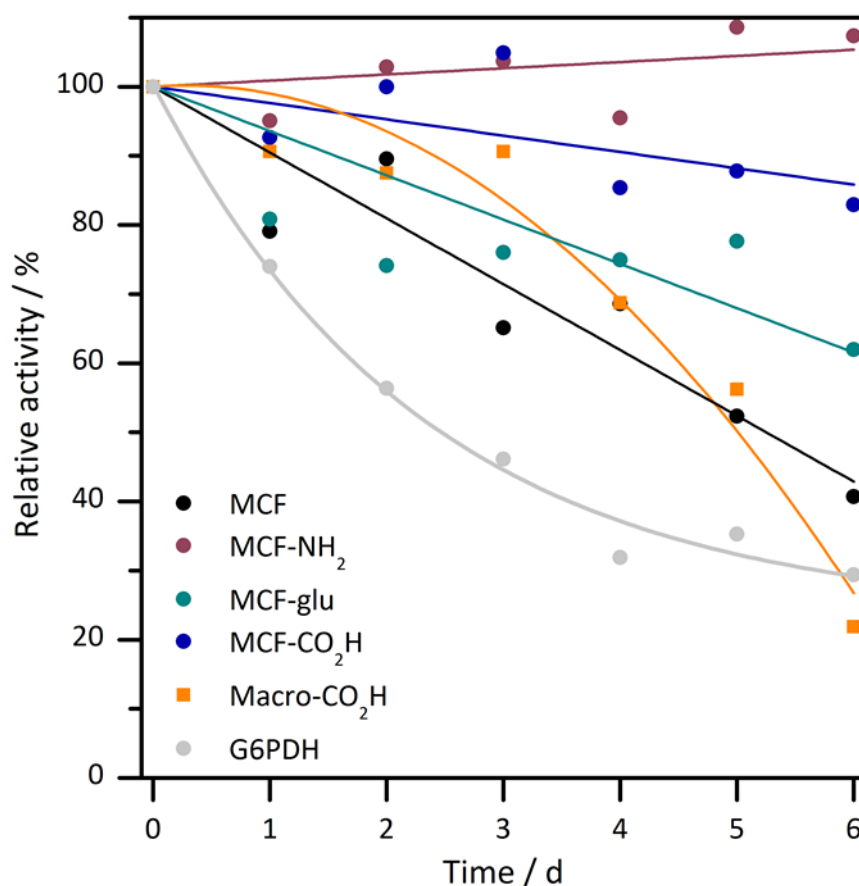


Figure 4.41: Thermal stability of free and immobilized G6PDH at 37 °C. Solid lines are guide to the eye. Free G6PDH and G6PDH immobilized onto oxidized carbon (Macro-CO₂H) show a drastic decrease of their activity after 14 days whereas all other nanoporous supports offer a stabilizing environment for G6PDH.

Macro-CO₂H shows low stabilization due to leaching. Compared to the trend observed at 4 °C the immobilized enzyme shows some kind of lag-phase due to diffusion barriers and not an immediately drop of activity like at 37 °C.

Table 4.16: Stability of free and immobilized G6PDH after respective periods.

Sample	Relative activity / % (4 °C, 14 d)	Relative activity / % (37°C, 6 d)	Relative activity / % (37 °C, 5 Cycles)
G6PDH	48	29	n.d.
MCF	97	43	80
MCF-NH ₂	91	105	98
MCF-glu	89	61	81
MCF-CO ₂ H	98	86	96
Macro-C	n.d.	n.d.	n.d.
Macro-CO ₂ H	74	27	75

n.d.: not determinable; All values are estimated from the respective fit.

The cycle stability (Figure 4.42, Table 4.16) for all materials follows a similar trend as the thermal stability. The highest stabilities were observed for MCF-CO₂H and MCF-NH₂ due to the confinement effect inside the pores. Again, Macro-CO₂H exhibits low cycle stability due to leaching. However, there is another issue that influences the cycle stability namely the recovery of the sample. After each cycle at 37 °C, the sample is separated by centrifugation. Some of the samples showed bad separation behavior due to the nature of the modification or particle size. Due to bad pelletization behavior of MCF and MCF-glu parts of the samples were withdrawn with the supernatant. Thus a lower activity was detected in the next cycles.

During the activity measurements a release of protons occurs due to NADP⁺ reduction. To verify that the pH does not change during the measurements the pH was monitored for 30 min. (see 9.1.3). No influence of the catalytic reaction to the pH was detected.

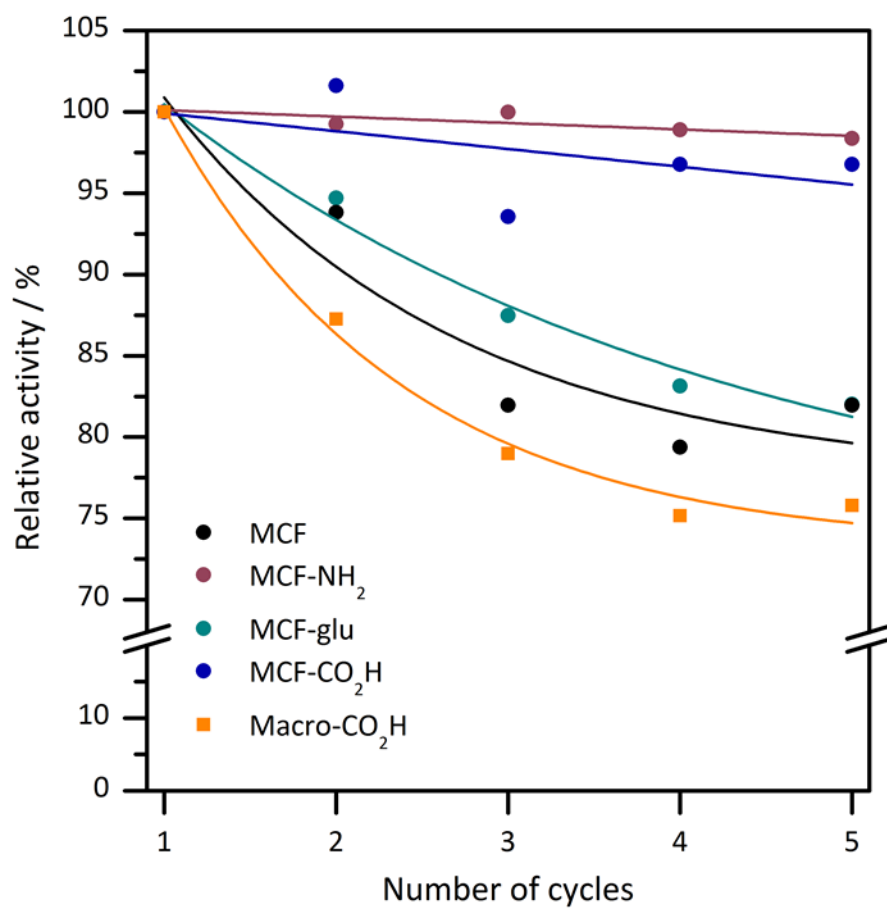


Figure 4.42: Cycle stability of immobilized G6PDH at 37 °C with solid lines as guide to the eye. While MCF-NH₂ and MCF-CO₂H almost retained their activity after five cycles the activity of the other samples dropped about 15-25 %.

4.2.3 INFLUENCE OF THE TYPE OF AMINE-MODIFICATION ON THE IMMOBILIZATION OF G6PDH

The results shown in the last chapter underlined that the amine-functionality of the support material is beneficial for the immobilization, activity and stability of G6PDH. Thus a further investigation of the amine moieties and their influence on the behavior of G6PDH seemed necessary. In this chapter the type of amine-containing support materials was varied in different directions. A contrast between hydrophobic and electrostatic interactions was introduced using primary n-alkyl amines of different chain length (MCF-C₃-NH₂, MCF-C₇-NH₂, MCF-C₁₁-NH₂). Additionally, the type of the amine was modified by postsynthetic grafting of MCF with primary (MCF-C₃-NH₂), secondary (MCF-sNH₂) and tertiary aminosilanes (MCF-tNH₂) with short alkyl chains (C3). Periodic mesoporous organosilicas (PMOs) with tertiary and secondary amines in their bridging group have been included in these studies to evaluate whether the extension of the amines into the pore or their location in the walls of the porous network is beneficial. These materials were characterized, apart from the general characterization in chapters 4.2.1.2 and 4.2.1.3, to evaluate their hydrophobicity and their electrostatic behavior towards G6PDH.

The encouraging results of MCF-C₃-NH₂ presented in the last chapter led to the conclusion to evaluate this material in more detail. Thus the beginning of this chapter is dedicated to the evaluation of the kinetics and the maximum G6PDH uptake of MCF-C₃-NH₂. The results of these studies have given further insights into the behavior of G6PDH in amine-modified materials.

4.2.3.1 Maximum uptake capacity of MCF-C₃-NH₂

The maximum uptake capacity of G6PDH (Figure 4.43) and its influence on the activity (Figure 4.44) of the immobilized enzyme was investigated. Therefore, concentrations between 0-3.3 mg mL⁻¹ have been evaluated. Additionally, only half the amount (5 mg) of MCF-C₃-NH₂ has been used in order to increase the amount of enzyme per mg silica and to yield a reasonable content of enzyme since only a limited amount of G6PDH was available. All other parameters have been held constant compared to earlier immobilizations.

The total uptake of G6PDH from solution was almost completely achieved at low G6PDH concentrations ($< 0.5 \text{ mg mL}^{-1}$) but dropped linearly to less than 70 % at an enzyme concentration of $3300 \mu\text{g mL}^{-1}$. This effect can be easily explained by diffusion constrictions that arise from the already immobilized enzyme molecules inside the pores. Considering one occupied pore another enzyme can hardly diffuse through this pore. At least the pore would be filled with two enzyme molecules and thus the entrance blocked for other enzymes. Since the enzyme has a high affinity to the pore walls it is most likely that it will immobilize in the pores near the surface and it becomes more difficult for other enzymes to be immobilized.

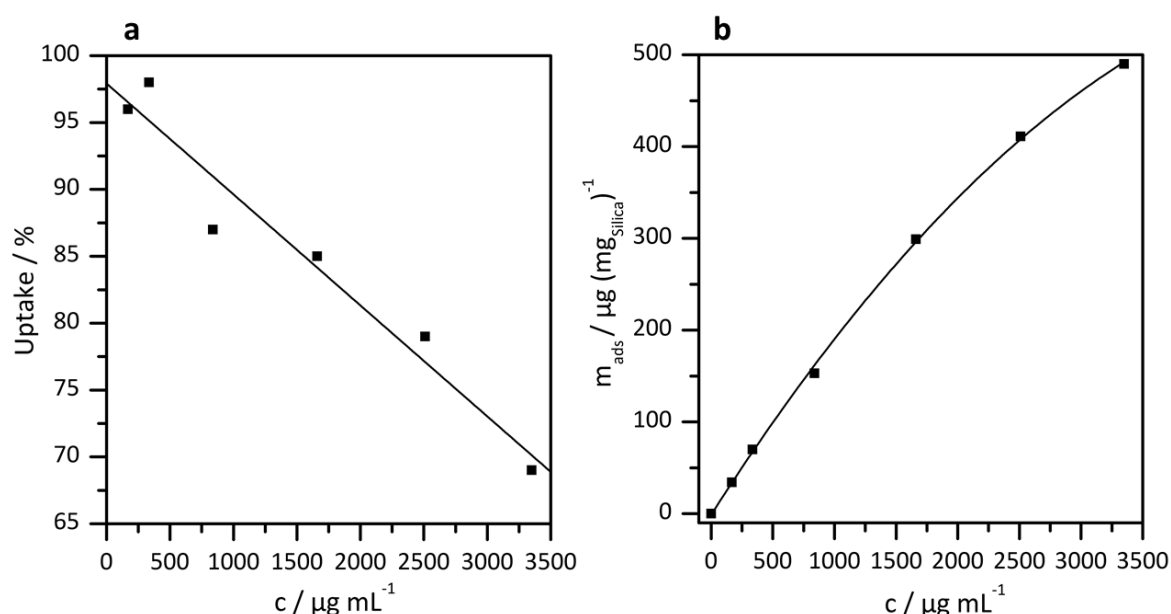


Figure 4.43: G6PDH uptake capacity for MCF-C₃-NH₂. (a) The total uptake in % decreases linearly with increasing G6PDH concentration in solution. (b) With increasing concentration of G6PDH the relative amount of adsorbed enzyme approaches a plateau that is not reached during these experiments.

The mass specific amount of enzyme per mg silica with increasing enzyme concentration is depicted in Figure 4.43b. Below a concentration of 2 mg mL^{-1} the adsorbed amount of G6PDH seems to behave linearly whereas the curve above these values seems to reach a plateau. Unfortunately, due to the limited amount of enzyme it was not possible to further increase the enzyme concentration. It has to be noted here that at the highest concentration 50 % G6PDH relative to the mass of enzyme was taken up. This is an extremely high amount for such a large enzyme. The large amount of

enzyme definitely is an indicator for an immobilization of enzyme inside the pore network since the external surface would already be covered at lower concentrations.

Additionally to the enzyme content the activity for all immobilized samples was checked. The absolute activity (Figure 4.44) increased consistently with the amount of enzyme per sample but the mass specific activity (relative to 1 mg enzyme) was almost linear with increasing amount of enzyme. An exception was the high activity that was observed for low enzyme concentrations. An explanation for this observation could be the location of the enzyme after immobilization. A low amount of enzyme can be easily taken up from the external surface of the particles and from pores directly accessible from the solution. Thus the diffusion of substrates, cofactors and products would be not diffusion limited in contrast to enzyme molecules immobilized with a larger distance from the surface. These observations again support the theory of enzyme molecules immobilized in the inside of the porous system. According to these results, the immobilization inside the inner pore network starts above a concentration of about $250 \mu\text{g mL}^{-1}$.

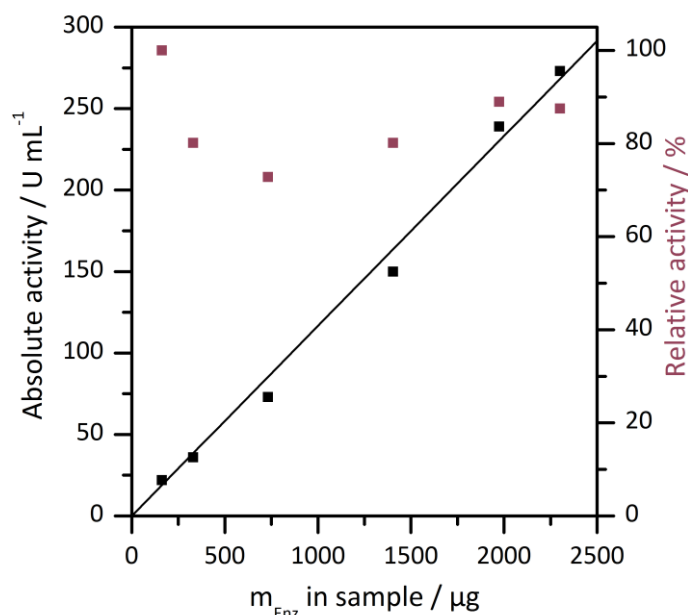


Figure 4.44: Development of relative and absolute activity in units/ mL^9 of G6PDH with increasing enzyme amount in MCF- $\text{C}_3\text{-NH}_2$. The absolute activity is linearly increasing with increasing enzyme content whereas a nearly constant mass specific relative activity is shown.

⁹ 1 unit oxidizes $1 \mu\text{mol}$ of D-glucose 6-phosphate to 6-phospho-D-gluconate per min in the presence of NADP^+ at pH 7.4 at 37°C .

Due to the obtained results the enzyme concentration for the immobilization experiments was fixed between 700 and 1000 $\mu\text{g mL}^{-1}$ for 10 mg silica in the following experiments. This region was a compromise between activity, enzyme loading and availability as well as high uptake.

4.2.3.2 Michaelis-Menten kinetics of MCF-C₃-NH₂

The kinetic parameters Table 4.17 for the free and immobilized enzyme were determined using the Michaelis-Menten (Equation 13) with either fixed amount of cofactor or substrate.

$$v_0 = \frac{v_{\max} [S]}{K_m + [S]} \quad (14)$$

A double reciprocal plot (Lineweaver-Burk plot) was established from the determined values for the initial reaction rate v_0 and the substrate concentration $[S]$. Thus the maximal reaction rate v_{\max} and the Michaelis-Menten constant K_m were determined from the slope and the y-intercept of the determined linear fit. According to the literature and the linearity of the Lineweaver-Burk plots (see appendix) the Michaelis-Menten theory is applicable to G6PDH.^[17,272–274]

Table 4.17: K_m and v_{\max} values experimentally determined for free and on MCF-C₃-NH₂ immobilized G6PDH in HEPES buffer (0.2 M, pH 7.4) at 37 °C. For comparison K_m values obtained for free and encapsulated G6PDH are shown. No literature data was found for v_{\max} .

	Varied	K_m / mM	K_m / mM^a	$v_{\max} / \text{mmol (L min)}^{-1}$
Free G6PDH	G6P	0.123	0.185	0.0418
	NADP ⁺	0.025	0.837	0.0387
Immobilized G6PDH	G6P	0.617	1.07	0.0210
	NADP ⁺	0.205	1.98	0.0355
a: Data obtained from literature. Conditions: phosphate buffer (0.2 M, pH 7.0); enzyme encapsulated in silica gel. ^[272]				

The K_m constant is considered in Michaelis-Menten kinetics as a measure for the enzymes substrate affinity at the employed conditions. However, it is a relatively vague number and the Lineweaver-Burk plot is prone to errors. Thus the values found in

literature are usually in a very broad range. Nonetheless, the changes in the kinetic constants are important numbers to characterize differences in the enzyme behavior prior and after immobilization.

A reduction of v_{max} and an increase of K_m (reduced substrate affinity) that was obtained after immobilization of G6PDH in MCF-C₃-NH₂ is a typical result for immobilized enzymes in general. Some examples of immobilized G6PDH are available in literature and all report an increase of K_m but no data for v_{max} .^[272–274] The increase of the Michaelis-Menten constant and the reduction of the maximal reaction rate after immobilization arises usually from increased diffusion restrictions, electrostatic interactions of the matrix towards product or substrate or an altered affinity of the enzyme towards the substrate due to partitioning effects. Due to these versatile effects and the difficulties arising from inactive or shielded amounts of enzyme the kinetic constants after immobilization are usually referred to as “apparent” constants.

The maximum reaction rate v_{max} of G6PDH is reduced to about 66 % after immobilization with varied G6P concentration compared to the free enzyme. A varied NADP⁺ concentration however leads to a minor reduction of 8 % after immobilization. A reason for this effect could be the above mentioned partitioning effect. It was shown in chapter 4.2.2 that the affinity of NADP⁺ was very high for MCF-C₃-NH₂ leading to a beneficial environment for the catalytic reaction of the enzyme. This would explain the minor reduction of v_{max} obtained with varied NADP⁺ concentration. The increase of v_{max} is probably attributed to diffusion constrictions that arise from the immobilization of the enzyme inside the porous material.

4.2.3.3 Effect of spacer length and hydrophobicity

As a result of the last chapter electrostatic interactions have been figured out as a main reason for the immobilization performance of G6PDH within the pores of MCF-C₃-NH₂. In this chapter the elongation of the aminosilane carbon chain length introduces an increasing hydrophobicity and thus the increasing strength of hydrophobic interactions. Therefore, MCF was modified with aminosilanes of various carbon chain length (C3, C7, C11). Not only the effect of increased hydrophobicity was investigated but also the theoretically increased enzyme-to-wall distance. Since the hydrophobicity was increased

with increasing carbon chain length the dispersion behavior of MCF-C₇-NH₂ and MCF-C₁₁-NH₂ was poor in aqueous solution. Thus the experiments were repeated with a small amount of DMSO to increase the hydrophobicity of the solvents. In the following figures samples with addition of DMSO are represented with empty symbols and dotted lines for clarification.

Immobilization and uptake of G6PDH

The adsorption of G6PDH within amine-functionalized MCF samples was performed as described in the previous chapter. G6PDH was incubated with the respective support for 24 h at 25 °C and pH 7.4. As mentioned at the beginning of this chapter DMSO was added to enhance the dispersibility of the hydrophobic samples MCF-C_{7,11}-NH₂. During the immobilization samples were withdrawn at distinct time intervals to monitor the uptake of enzyme by the support. The amount of enzyme left in the solution was determined by BCA assay in order to calculate the protein that was taken up by the porous material.

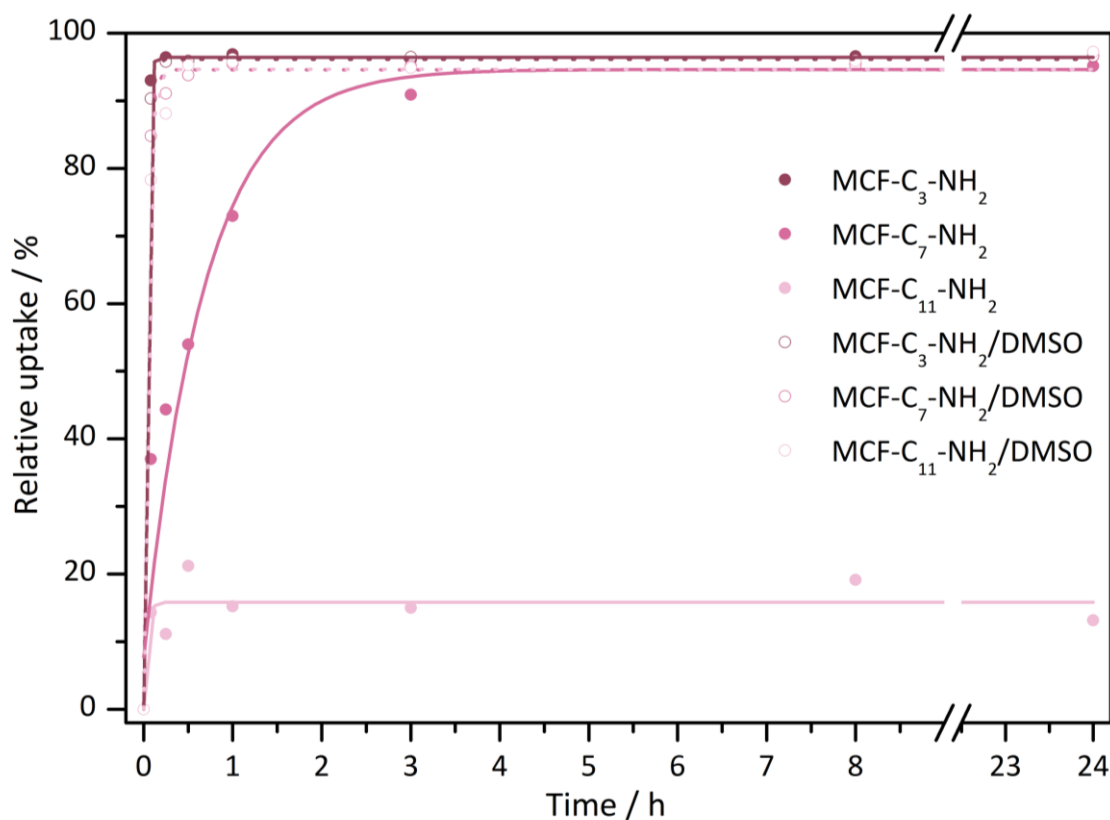


Figure 4.45: Relative uptake curves of G6PDH by amine-modified MCF at 25 °C with asymptotic fit. The plateau was reached very fast with most materials except MCF-C₇-NH₂. The addition of DMSO leads to a significantly enhanced uptake for materials with longer chain length.

The relative uptake curves are shown in Figure 4.45 with asymptotic fits as a guide to the eye. A complete uptake was achieved for MCF-C₃-NH₂ as well as for MCF-C₇-NH₂ but the velocity of the adsorption was significantly reduced with an increased chain length. Only a low amount of enzyme (17 %) was adsorbed to MCF-C₁₁-NH₂.

The addition of DMSO to the immobilization mixture significantly enhanced the uptake of G6PDH to MCF-C₇-NH₂ in terms of reaction velocity and MCF-C₁₁-NH₂ concerning the amount of enzyme taken up. All samples exhibited an total uptake of more than 90 % of G6PDH from solution (Figure 4.46).

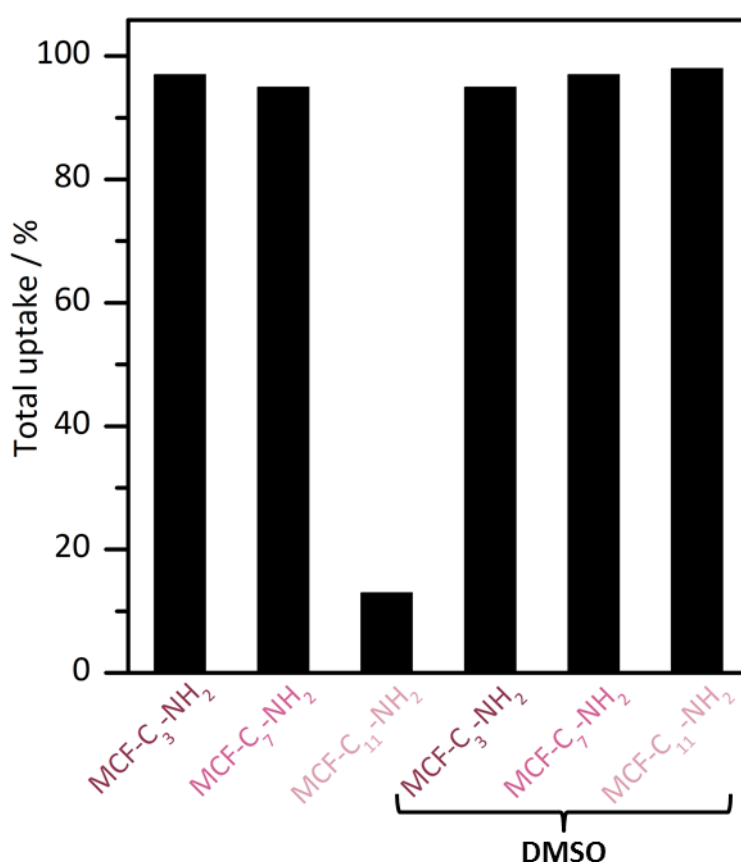


Figure 4.46: Total uptake of G6PDH from solution by amine-functionalized MCF respective to the enzyme content in solution.

The enhanced uptake after the addition of DMSO indicates that the increased hydrophobicity of the solvent was beneficial for the adsorption of G6PDH to hydrophobic MCF. Maybe an enrichment of DMSO at the hydrophobic solid surface increased the affinity for the enzyme, acting as a kind of mediator. The slow uptake

kinetics of G6PDH adsorbed on MCF-C₇-NH₂ were affected by the hydrophobic nature of the material, similar to the low uptake of enzyme by MCF-C₁₁-NH₂ prior to the addition of DMSO that was caused by the hydrophobicity of the material. The low but fast uptake of this material indicated a loose attachment at the external surface. The effect of the hydrophobicity of the supports has two possible effects on the adsorption of G6PDH:

- 1) The buffer was not able to penetrate the porous network of the material and thus the enzyme was not able to enter the system.
- 2) The enzyme was sterically inhibited and/or not attracted by the hydrophobic residues.

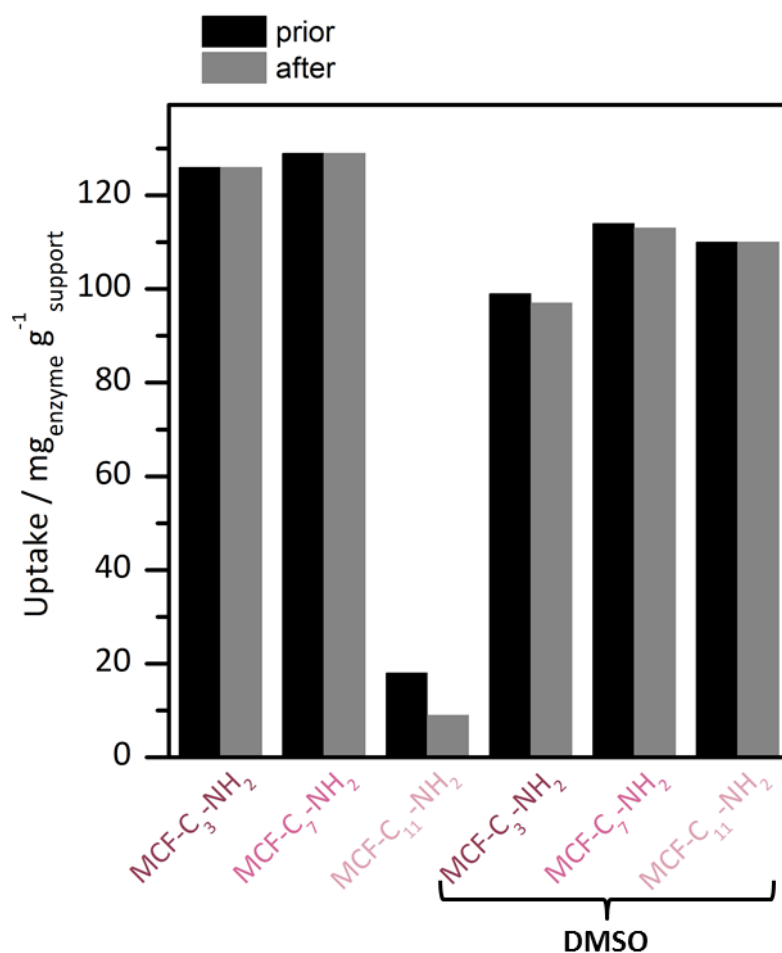


Figure 4.47: Protein content of amine-functionalized MCF supports prior and after applied washing cycles. The mass specific uptake is presented in mass of enzyme respective to the mass of the support material.

A loose attachment of the enzyme or repulsion is also detectable by monitoring the protein content prior and after the immobilization (Figure 4.47). All samples showed no or only minor loss of adsorbed enzymes after three washing cycles whereas a strong reduction of adsorbed G6PDH was observed for MCF-C₁₁-NH₂.

The increase of hydrophobicity was not only apparent to the eye but was also quantified by water vapor adsorption. The water adsorption isotherms of all silicas show an open hysteresis due to the at 25 °C irreversible rehydroxylation of the silica surface. Additionally all samples exhibit a low total uptake of water since the surface of silica with and without organic modifications is more hydrophobic. The capillary condensation is not observed in this case since only small mesopores are completely filled by water. Nevertheless the onset of capillary condensation is present for MCF-C₃-NH₂. The increase in hydrophobicity with increasing chain length is indicated by a decrease of the slope of the adsorption branch at low relative humidity.

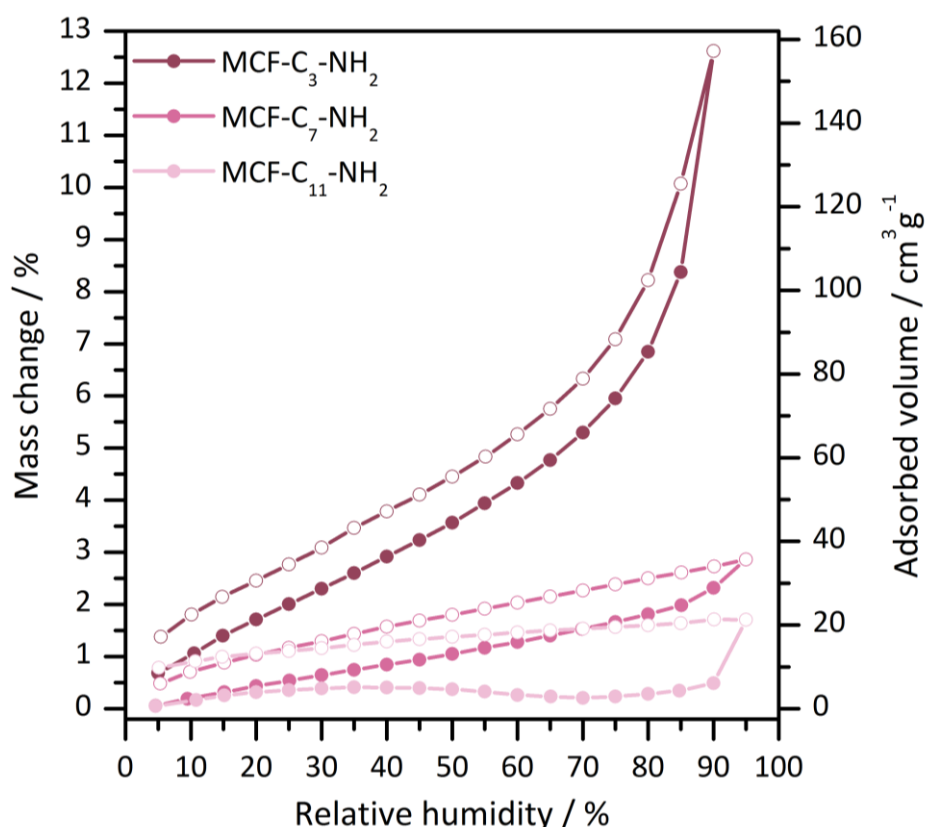


Figure 4.48: Water vapor isotherms (adsorption branch: filled symbols, desorption branch: empty symbols) of amine-modified MCF materials with different chain length performed between 5-95 % relative humidity at 25 °C. All samples were degassed under reduced pressure at 120 °C for 20 h. A relative decrease of the amount of adsorbed water is obtained with increasing chain length indicating an increase in hydrophobicity.

In order to derive quantification two different hydrophobicity indices (χ) have been calculated from the obtained data. A hydrophobicity index for combined micro- and mesoporous materials was defined by Thommes et al. in order to quantify the hydrophobicity of zeolites.^[233] Therefore the adsorption of water as a not completely wetting adsorptive was compared to argon as a completely wetting adsorptive. From the argon physisorption the micropore volume was determined at $p/p_0=0.15$ and the total pore volume at the upper closure point of the hysteresis ($p/p_0=0.92$). The determined pore volumes allow now with the density of water at 298 K (0.997 g cm^{-3}) to calculate the degree of pore filling with water from the water isotherm. The ratio of both values is referred here as χ_2 . A total filling of the pores with water in the case of complete wetting would lead to a χ_2 of 1.

Unfortunately, this index is not strictly transferrable to the MCF materials since no micropores are present in the MCF materials and no upper closure point is reached for the water isotherms due to the large mesopores. Nonetheless, the degree of pore filling was determined for the last point measured in the water vapor sorption and compared to that value determined from the argon isotherms. A comparison of the BET surface area determined from the argon and nitrogen physisorption is shown in Table 4.18. Although nitrogen is an adsorptive that is completely wetting, argon physisorption is used to calculate a correct value for S_{BET} . As can be seen from the deviations of the BET surface areas determined by the two adsorptives, the nitrogen physisorption leads to a larger error in the case of MCF-C₃-NH₂. This is due to the enhanced polarity of the material that leads to an increased interaction with the quadrupole of nitrogen. Therefore, the decrease in the deviation of both methods is an additional proof for the hydrophobicity of the respective MCF materials.

Table 4.18: BET surface area determined by nitrogen (77 K) and argon (87 K) physisorption.

Sample	MCF-C ₃ -NH ₂	MCF-C ₇ -NH ₂	MCF-C ₁₁ -NH ₂
$S_{BET}(\text{N}_2) / \text{nm}^2$	277	294	266
$S_{BET}(\text{Ar}) / \text{nm}^2$	255	290	265
Deviation / %	7.9	1.4 ¹⁰	0.4

¹⁰ The deviation between the argon and nitrogen physisorption was determined from another equally synthesized sample ($S_{BET}(\text{N}_2) = 291 \text{ m}^2\text{g}^{-1}$, $S_{BET}(\text{Ar}) = 287 \text{ m}^2\text{g}^{-1}$) since not enough sample was left to perform a reliable determination of the surface area according to BET.

Additionally, the derived values for χ_2 exhibit a strong increase in the hydrophobicity from MCF-C₃-NH₂ to MCF-C₇-NH₂ and MCF-C₁₁-NH₂. Since χ_2 is linked to several difficulties that arise with the large pores of the material, another hydrophobicity index (χ_1) is defined here. In terms of enzyme adsorption the effect that is most interesting is not the water uptake that is governed by the porosity of the materials but the one derived from the surface chemistry. The surface chemistry is accessed in the region of low p/p_0 . Therefore, from the uptake of water in that region the monolayer capacity was determined according to the BET equation. The derived monolayer capacity from the water sorption isotherm was then compared to a theoretical monolayer capacity under the assumption of complete wetting, determined from the BET surface area of the argon isotherm.¹¹ The determined values for χ_1 (Table 4.19) show the same trend as those derived from χ_2 .

Table 4.19: Carbon chain length, pI and hydrophobicity indices χ for MCF samples with varied chain length.

Sample	MCF-C ₃ -NH ₂	MCF-C ₇ -NH ₂	MCF-C ₁₁ -NH ₂
Chain length /nm	0.46	0.96	1.5
pI	9.2	9.7	10.2
χ_1	0.30	0.10	0.05
χ_2	0.40	0.05	0.02

All the above mentioned differences in the affinity of the enzyme towards the respective supports have been stated due to hydrophobicity of the materials but the question arises, if the amine group is still involved in the adsorption. To evaluate the basicity of the amine groups and thus their capability to take part in acid base reactions zeta potential titrations of both materials have been performed.

¹¹ All calculations were performed with a cross-sectional area for water of 10.5 Å and a molecular weight of 18.015 g mol⁻¹.

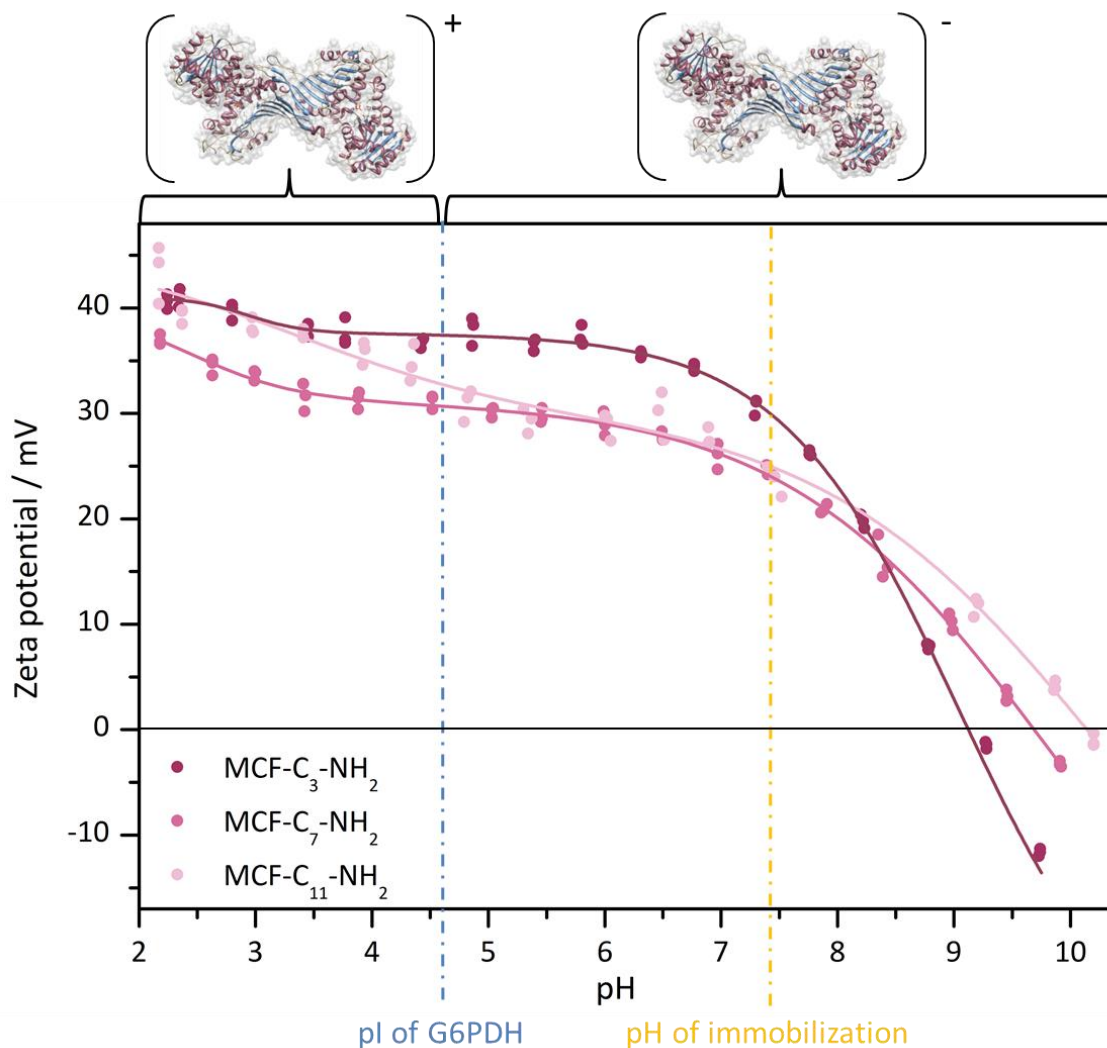
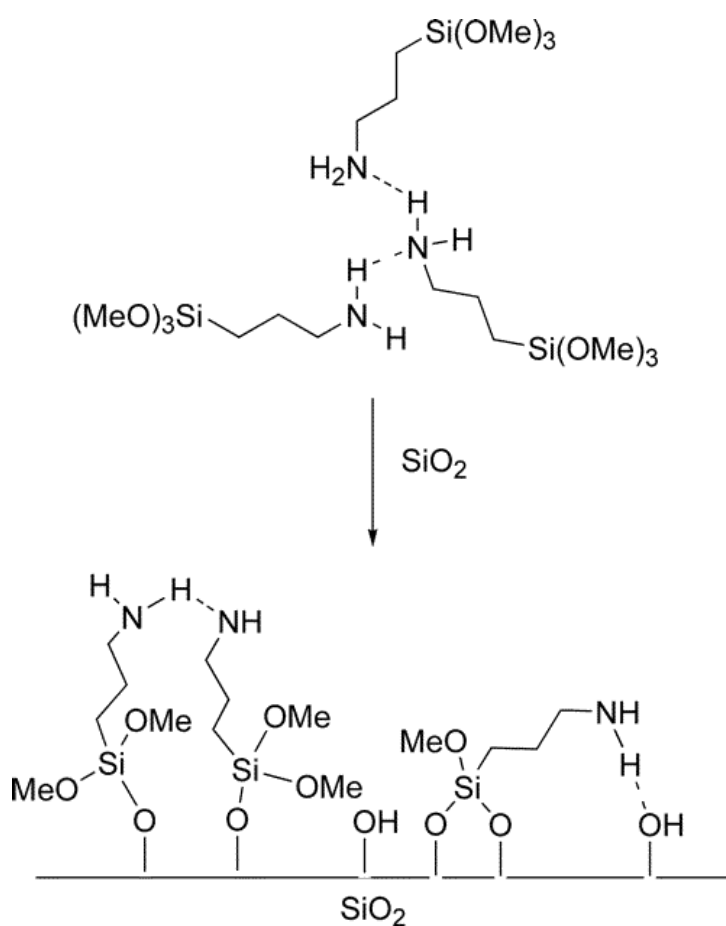


Figure 4.49 Zeta potential titrations of the amine-modified MCFs with varied chain length with sigmoidal curve fit. Below their isoelectric point materials and the enzyme ($pI = 4.6$) are positively charged, above negatively. At the pH of immobilization (pH 7.4) the enzyme exhibits a negative net charge whereas all amine-modified MCF supports have a positive net charge.

Two interesting features have been observed. First, the zeta potential of all amine-modified MCFs is highly positive at pH 7.4 (pH of immobilization) and thus the electrostatic interactions should still be favorable for the adsorption of G6PDH. However, the orientation of the amine group is a major issue that will be discussed in the next paragraphs. Second, the pI of the MCF supports is increasing with increasing chain length. The observed values however, will probably not affect the immobilization, since all materials exhibit a highly positively charged surface at the point of immobilization. Looking at the pK_a values of amines with increasing amine chain length

almost no change is observed: Aminoethane (10.67), aminooctane (10.65) and aminodecane (10.64).^[275] Thus the increase in the pI has a different origin.

The orientation of the carbon chains and thus the amine groups is an important factor for explaining the pIs as well as the hydrophobicity/hydrophilicity of the support materials. In literature, the functionalization of porous silicas with amine groups is a highly discussed topic.^[276–279] In general, all experiments are performed with 3-aminopropyltriethoxy (APTES)- or -chlorosilanes, a short chained aminosilane. However, the effect of the long carbon chains becomes more significant with increasing chain length.



Scheme 4.4: Grafting of a silica surface with APTES. In solution a clustering process is observed due to the basicity of the amine group. The amine group can interact in many ways with the silica surface.

At first, a short overview (Scheme 4.4) is given for the general considerations during and after the functionalization of silicas with aminosilanes. The major difference during and after the grafting process with aminosilanes compared to other silanes is the ability

of the amine group to create intermolecular hydrogen bonds with itself or the silanol groups. This leads to cluster formation already in solution but more important to numerous interactions on the silica surface. Even a high degree of aminosilane coverage of the surface does not prevent the presence of residual silanol groups, either from the organosilanes or the silica surface. Thus an orientation of the aminosilane towards the silanol groups at the silica surface is possible. In water at pH 7 this would even lead to an electrostatic attraction since the acidic silanol is deprotonated and the basic amine protonated. Additionally, amine-amine hydrogen bonds are possible between aligned aminosilanes, if the amine groups are not completely protonated. Protonated amines can additionally act as hydrogen bond acceptor in combination with water as an hydrogen bond donor.

Now, the possibilities that aminosilanes are interacting with their environment are clarified. But what happens when the chain length increases and hydrophobic interactions and van der Waals interactions become more and more favorable. Unfortunately, no information of aminosilane grafting was available on the topic of varied chain length but the behavior of alkylammonium surfactants gives a proper insight into the situation. The adsorption of alkylammonium surfactants with C10 to C18 carbon chains onto a quartz surface leads to highly aligned structures and changes the pI with increasing chain length towards lower electrolyte concentration.^[280] Another example of highly aligned carbon chains are the so-called SAMs (Self-assembled monolayers) that have been established even on porous silicas. Thus, it is assumed here, that an increasing chain length will lead to an alignment of the carbon chains. However, since the silica surface is not smooth and interactions with the surface silanols cannot be completely excluded thus no perfect monolayer is formed. A hint to the alignment of the carbon chains are the high functionalization densities that have been observed for C7 (1.1 mmol g⁻¹) and C11 (1.0 mmol g⁻¹). In literature a shielding of the available aminosilanes by already grafted octylsilanes led to a reduction of grafted amount.^[281] The alignment of the alkyl chains leads to an additional alignment of the amine "head" group and thus to enhanced hydrogen bonding between the amines. Additionally, zwitterionic species between silanols and amines are reduced and thus to an increase of the basicity of the material and hence an increased pI. The difference in the pI between MCF-C₇-NH₂ and MCF-C₁₁-NH₂ is most likely a phenomenon of reduced order. A shorter

carbon chain leads to less interactions between the carbon chains and thus to more packing defects. The increase of defects with medium length carbon chain was also reported in literature.^[281] Firestone et al. grafted a planar silica surface with halosilanes of alkyl chain length C_n ($n = 2, 3, 8, 11, 15$) and investigated the order of the chain alignment. They obtained highly ordered structures with C11 and C15 but high gauche defects with C8 alkyl chains. The reduction of the order was explained with the lower amount of van der Waals interactions for the intermediate chain length.

To conclude, both electrostatic attraction and hydrophobic interactions strongly influence the adsorption in amine-modified MCFs. The crucial effect is the increasing hydrophobicity of the materials that lead to a reduced uptake of enzyme in aqueous solution. The addition of DMSO as a more hydrophobic mediator, however, can eliminate this effect. Additionally, the orientation of the amine is believed to be aligned with C7 and C11 alkyl chain length but more or less disordered with C3.

Activity of G6PDH

The maximum of activity of G6PDH is shown in Figure 4.50 plotted relative to the activity of G6PDH immobilized onto MCF-C₃-NH₂. Since this chapter is dedicated to amine-modified MCF MCF-C₃-NH₂ is always used as reference. It has to be noted, that the activity of G6PDH was increased for some samples during the first weeks (see “Stability of G6PDH”). Here, the maximum activity was taken for the calculations.

Table 4.20: Relative and total activities for immobilized G6PDH.

Sample	Relative activity / %	Activity / U mg ⁻¹ enzyme	Activity / U mg ⁻¹ support
MCF-C ₃ -NH ₂	100	292	43
MCF-C ₇ -NH ₂	11	31	4
MCF-C ₁₁ -NH ₂	12	34	1
MCF-C ₃ -NH ₂ /DMSO	39	115	11
MCF-C ₇ -NH ₂ /DMSO	3	9	1
MCF-C ₁₁ -NH ₂ /DMSO	1	3	2

Two trends can be generated from the data: First, the initial activity is significantly reduced for C7- and C11-functionalized silica. Second, the initial activity obtained for

G6PDH immobilized on materials with the respective chain length was reduced by the addition by DMSO about 30 %.

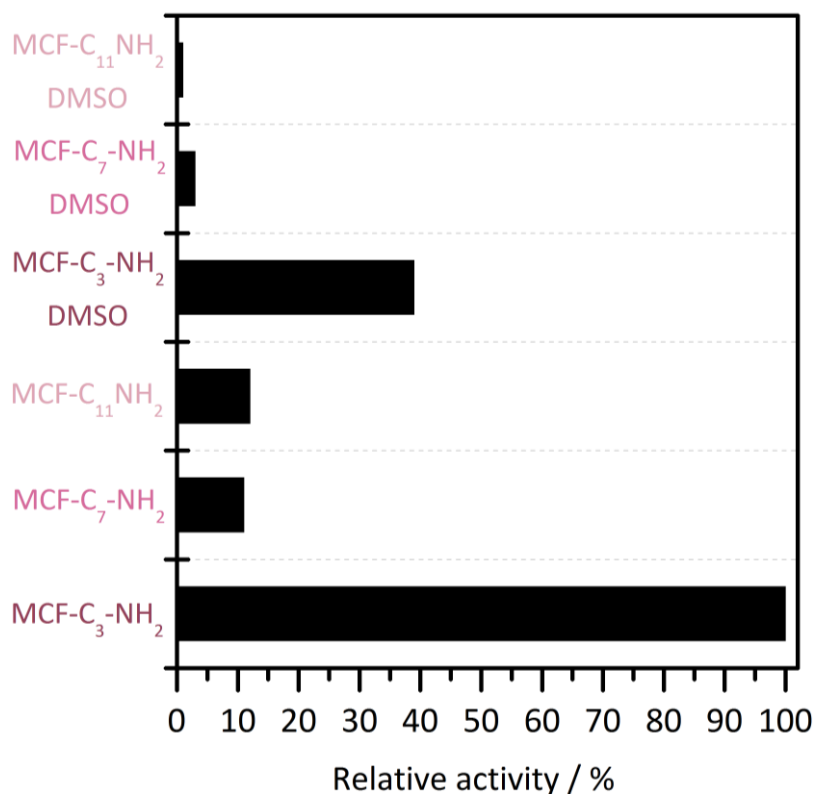


Figure 4.50: Relative activity of immobilized G6PDH compared to the activity of the enzyme adsorbed on MCF-C₃-NH₂.

To further evaluate the deactivation of G6PDH Michaelis-Menten kinetics have been performed with varied DMSO concentrations. For these studies the free G6PDH was used to diminish effects of diffusion or partitioning inside the pore network and focus on the deactivation. Since neither K_m nor v_{max} stayed constant common inhibition mechanisms (competitive, noncompetitive) could be excluded. On the one hand the K_m constant decreased with increasing DMSO concentration, indicating that the affinity for the substrate was increased with increasing DMSO constant. On the other hand the reaction velocity decreased with increasing DMSO concentration. In the literature this effect was already reported for G6PDH.^[282] Viola et al. found out that this behavior was not only observed with DMSO but with many nonpolar organic solvents. Thus the increased affinity was not a result of specific binding of DMSO to the enzyme but a matter of the hydrophobic/hydrophilic contrast. With addition of the solvent the

solution was more hydrophobic and this led to an increased affinity of G6P to the enzyme (partitioning). The reduction of the maximum reaction velocity was assigned to the slowed hydrolysis of the lactone and hence to an increase in the back reaction.

Table 4.21: Michaelis-Menten kinetics for free G6PDH with varied G6P and DMSO concentration performed at 37 °C in HEPES buffer.

DMSO / HEPES	Varied	K_m / mM	v_{max} / mmol (L min) ⁻¹
1/100	G6P	0.123	0.042
1/30	G6P	0.083	0.041
1/15	G6P	0.068	0.026

Thus, the reduction of activity with increasing DMSO content was explained but the drastic reduction of activity of G6PDH immobilized onto MCF-C₇-NH₂ and MCF-C₁₁-NH₂ remains still unclear. In general, a longer spacer length between support and enzyme is considered as favorable since it does increase the mobility and hence the activity of the enzymes. This is definitely not the case here but additionally an increased carbon chain length leads to an increase in hydrophobicity which affects not only the interactions of the enzyme towards the material but also the diffusion of the substrates. Thus, the adsorption of NADP⁺ (Figure 4.51) at the respective silicas was investigated. The NADP⁺ adsorption of the C7- and C11-modified silicas was enhanced after addition of DMSO supporting the hypothesis of DMSO as a mediator for the diffusion inside the pores by increasing the hydrophobicity of the solvent. The uptake of NADP⁺ however was decreased with increasing chain length of the materials. That would explain the general reduction of activity with C7 and C11 chain length but not the lacking activity between both samples. Thus, other effects have to take part in the deactivation process.

One reasonable explanation is the unfolding of protein to expose its hydrophobic amino acid residues towards the materials surface. This effect was reported in literature for myoglobin immobilized onto a flat silica surface.^[283] A deactivation was spectroscopically investigated by measuring the Soret band of the heme domain. With carbon chain length of C11 and C15 a deactivation due to unfolding after 1 h was proven but was not observed with a C8 carbon chain. This would however be contrary to the

observation that the same degree of deactivation was observed for C7 and C11 modified silica. Nevertheless, it cannot be totally excluded since G6PDH is not myoglobin.

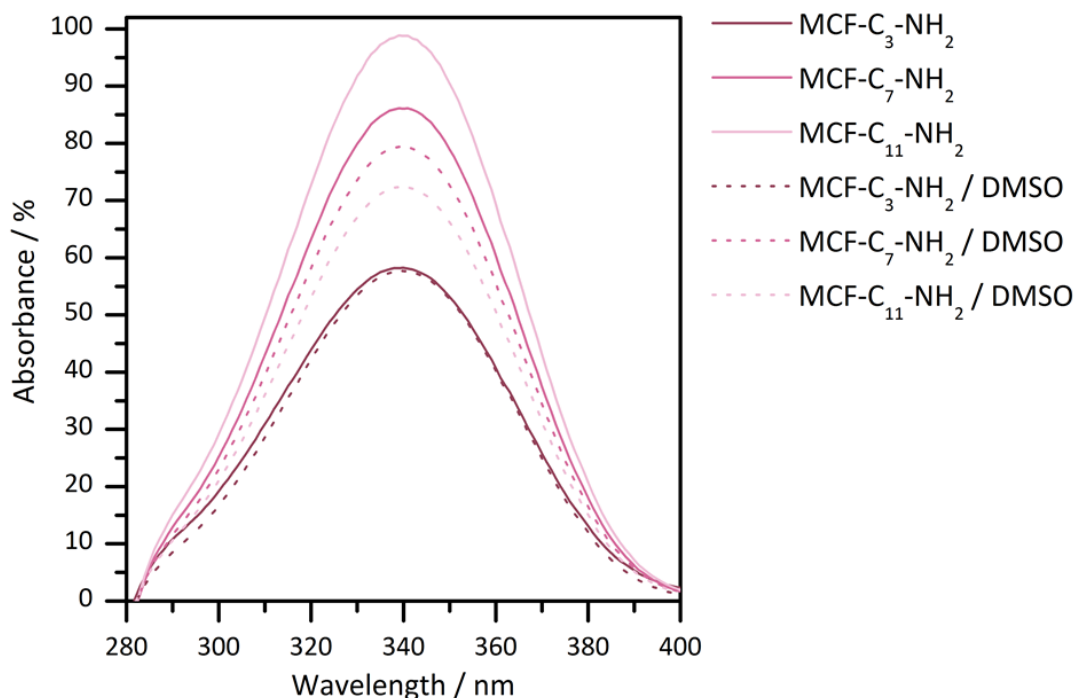


Figure 4.51: Adsorption of NADP⁺ in nanoporous materials. After conversion to NADPH the residual NADPH was quantified in the supernatant. The absorbance of the respective supernatants is shown here relative to the absorbance of the used NADP⁺ solution.

Another reason for the deactivation would be the penetration of the active site by the hydrophobic residues of the silica surface that in general is likely for G6PDH immobilized onto MCF-C₇-NH₂ and MCF-C₁₁-NH₂.

Stability of G6PDH

The stability of G6PDH immobilized in amine-functionalized MCF with varying chain length was monitored at 4 °C and 37 °C. A summary of the data can be found in Table 4.22. As discussed already for the uptake the main driving forces of stabilization or destabilization at the surface of the amine-modified MCF samples are either electrostatic interactions with the charged amine groups or hydrophobic interactions with the carbon chains.

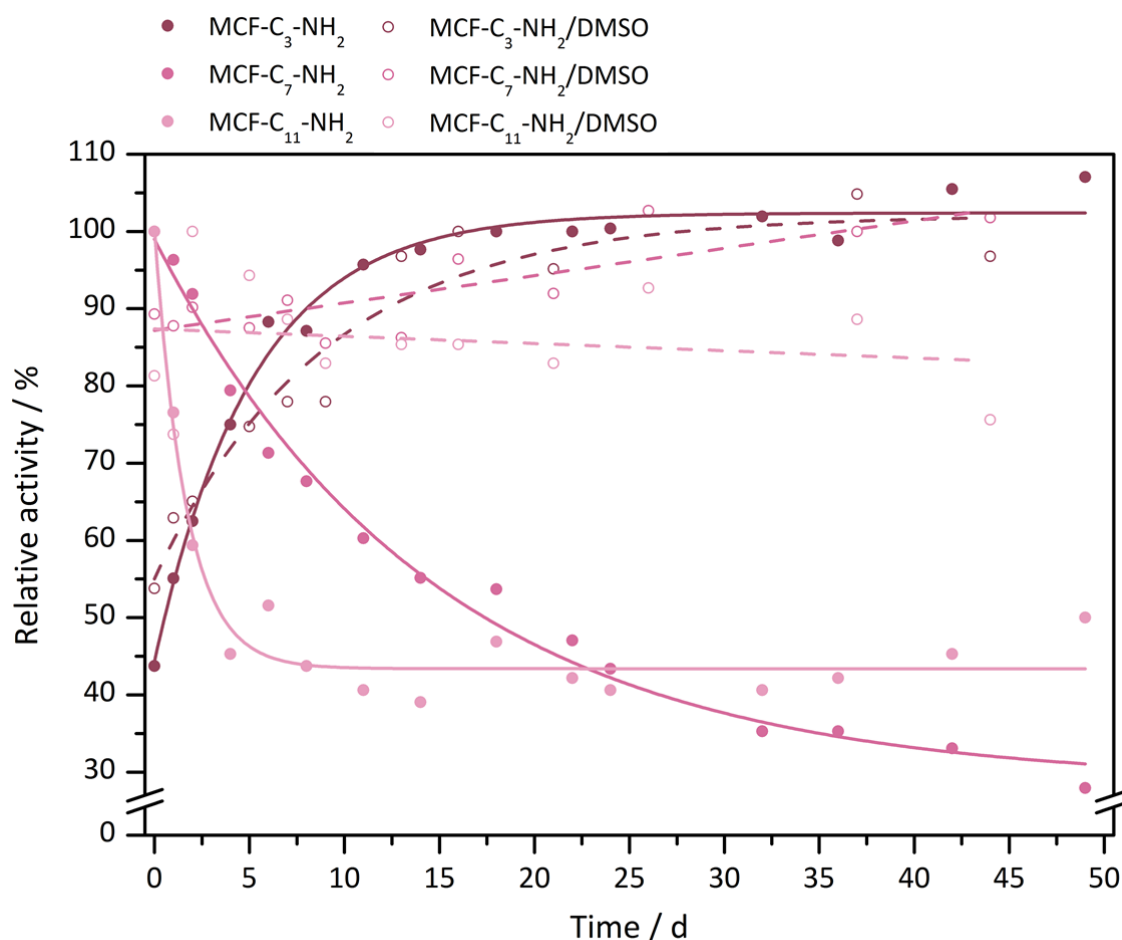


Figure 4.52: Storage stability at 4°C for immobilized G6PDH. Immobilization in MCF-C₃-NH₂ led to a significant stabilization whereas immobilization in MCF-C₇-NH₂ and MCF-C₁₁-NH₂ had no stabilization effect. The increase of hydrophobicity of the solvent by addition of DMSO showed to enhance the stability of G6PDH immobilized in hydrophobic silicas. Solid lines are guide to the eye.

Samples stored at 4°C (Figure 4.52) without addition of DMSO show an exponential increase or decrease with time. For MCF-C₃-NH₂ an increase in activity of more than 50 % is observed. The activity approaches the maximum activity and is stable for more than 50 days. The increase of the activity was not observed in that amount compared in the example showed in the last chapter (Figure 4.40) although the immobilization was performed in both cases on the same MCF-C₃-NH₂ batch. The reasons for that are not clearly identifiable since the immobilization and storage procedure was kept constant. One explanation might be differences in the enzyme batches.

In contrast to the increase in activity observed for G6PDH in MCF-C₃-NH₂, the activity of G6PDH immobilized in MCF-C₇-NH₂ and MCF-C₁₁-NH₂ exponentially decreases with storage time, whereas MCF-C₁₁-NH₂ asymptotically approaches 43 % relative activity.

The enhanced activity for MCF-C₃-NH₂ is also reported in literature but the reason was never proven.^[284,285] One of the authors subjects the increase in the activity to a process of desorption of the enzyme from the support.^[284] Some of the non-covalent bonds built during the immobilization were thought to interfere with the catalytic activity. After they are cleaved the initial activity is restored. The second hypothesis is an activation during the defolding process prior to deactivation.^[285] It is proposed here, that the defolding leads to an exposure of the active site in the first place and thus to an enhanced diffusion of the substrate to the active site. In the second step deactivation is observed due to further defolding. This hypothesis, however, cannot explain why the stability is unchanged for such a long period. So, a restoring of the initial activity is more likely than activation due to unfolding. The restoring of the initial activity can be caused by the above mentioned breaking of non-covalent bonds but this would eventually lead to less stabilization and enhanced leaching due to a loosely bound enzyme. Both is not the case here (Figure 4.52, Figure 4.53). Another possibility of restoring the initial activity is either refolding of protein denatured prior to the immobilization or subunit recombination at the surface of the mesoporous silica.

Table 4.22: Relative activity at 4 °C and 37 °C for MCF supports with varied chain length.

Sample	Relative activity / % (4 °C, 14 d)	Relative activity / % (4 °C, 30 d)	Relative activity / % (37°C, 6 d)
MCF-C ₃ -NH ₂	98	100	87
MCF-C ₇ -NH ₂	56	38	0
MCF-C ₁₁ -NH ₂	43	43	0
MCF-C ₃ -NH ₂ /DMSO	86	100	47
MCF-C ₇ -NH ₂ /DMSO	92	98	0
MCF-C ₁₁ -NH ₂ /DMSO	92	85	0
All values are estimated from the respective fit.			

The instability of G6PDH in C11- and C7-modified silicas is a result of low interactions present between enzyme and support. Additionally, high leaching values for MCF-C₁₁-NH₂ have been found that underline these observations. The limited uptake was also taken as a hint for immobilization of G6PDH only on the external surface of MCF. The addition of DMSO to the immobilization mixture yielded a significantly higher stability for G6PDH immobilized on both materials triggered by the “mediator” role of

DMSO explained above. The decrease in hydrophilicity of the solvent led to an enhanced transport of the enzyme into the pores and hence a stabilization due to hydrophobic interactions and thus reduced leaching for MCF-C₁₁-NH₂. The increase of the relative activity for G6PDH immobilized onto MCF-C₃-NH₂ upon addition of DMSO was delayed compared to the samples without DMSO but also reached a constant value.

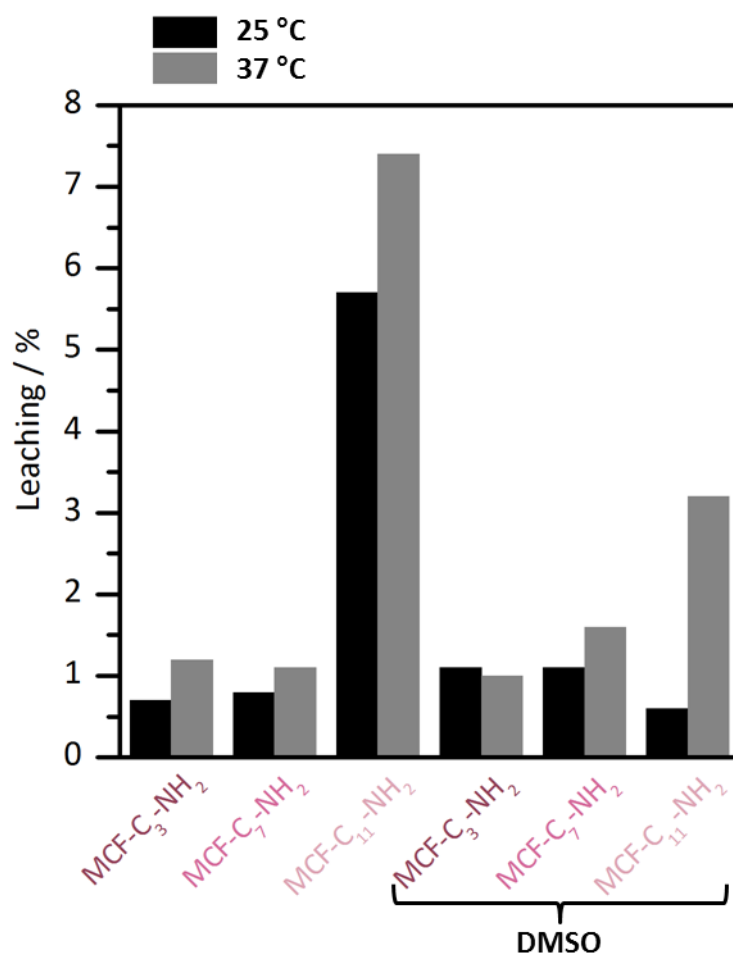


Figure 4.53: Leaching of G6PDH from amine-functionalized supports at 25 and 37 °C.

Thermal stability studies at 37 °C (Figure 4.54) showed a very fast deactivation (< 4 days) for all samples with or without addition of DMSO except G6PDH immobilized onto MCF-C₃-NH₂. Usually, all effects that are obtained during the stability studies at 4 °C are more dominant at higher temperatures but this is not the case here. The fast deactivation of all samples could be triggered by an increase of thermal movement in the long alkyl chains of the silanes that could lead to enhanced leaching of the enzyme and thus deactivation in solution. Indeed, the leaching is much higher for samples at

37 °C but this cannot be the only influencing component since the leaching of MCF-C₃-NH₂ and MCF-C₇-NH₂ is almost the same. Therefore, an effect of the long carbon chains has to take part in the deactivation process. Maybe, an enhanced defolding of the enzyme is triggered by an increased hydrophobicity due to disordering of the carbon chains. Thus the chains would be more or less exposed and the defolding of the enzyme would be facilitated to reduce the hydrophilic exterior of the enzyme.

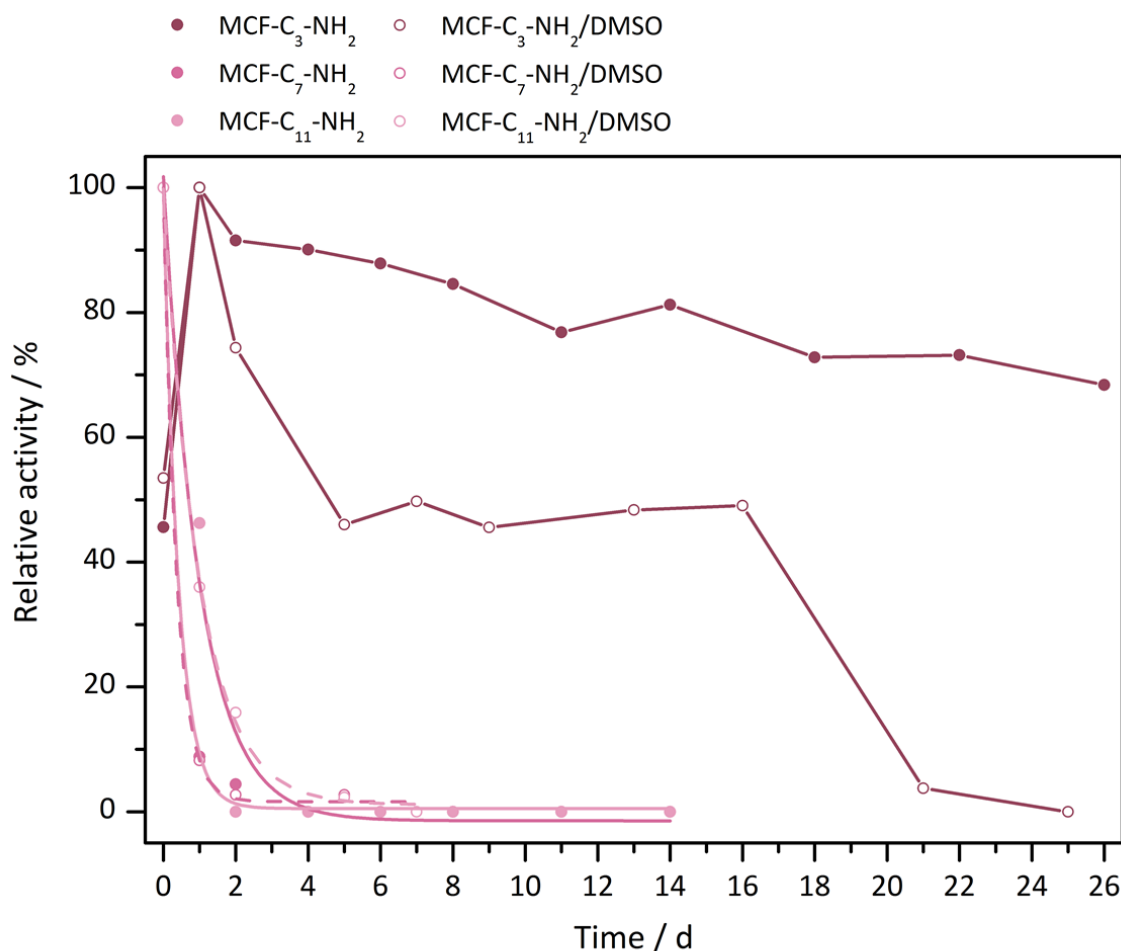


Figure 4.54: Thermal stability at 37 °C for immobilized G6PDH. Immobilization in MCF-C₃-NH₂ led to a significant stabilization whereas immobilization in MCF-C₇-NH₂ and MCF-C₁₁-NH₂ had no stabilization effect. The increase of hydrophobicity of the solvent by addition of DMSO showed to have no effect on the stability of hydrophobic silicas.

4.2.3.4 Effect of type (primary, secondary, tertiary) and site of amine moieties

The last chapter was mainly focused on the competition of hydrophobic and electrostatic interactions between the enzyme and the support surface. Varied chain

length of aminosilanes introduced both effects. In this chapter PMO materials with secondary (s-PMO) and tertiary amine precursors (t-PMO, PMO-aerogel) and MCF materials grafted with primary (MCF-pNH₂), secondary (MCF-sNH₂) and tertiary (MCF-tNH₂) short-chain (C3) aminosilanes are discussed. Therefore, electrostatic and hydrophobic interactions are still a part of this chapter but the electrostatic interactions will occur in pronounced form. The main difference of PMO and grafted MCF materials is the site of the amine modification either in the walls of the PMOs or extended into the pore. Due to the high organic content in PMOs they are usually referred to as more hydrophobic as grafted silicas.

Immobilization and uptake

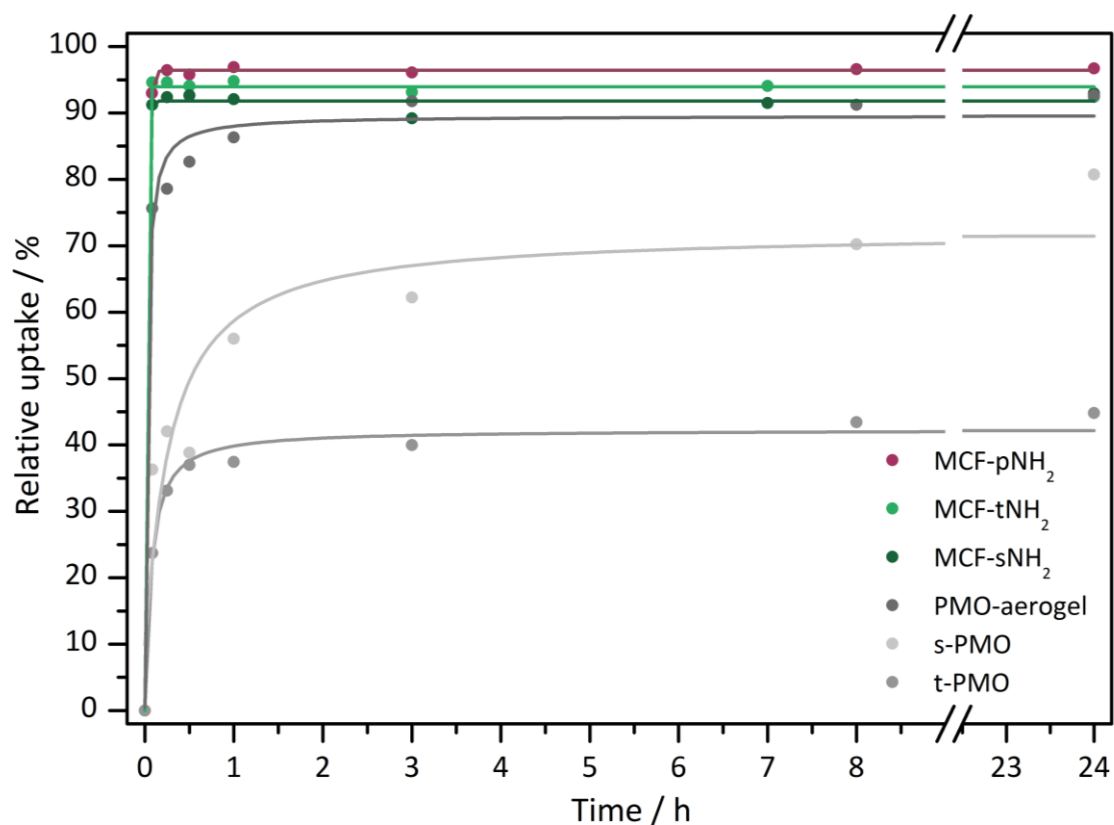


Figure 4.55: Relative uptake curves of G6PDH by amine-modified MCF at 25 °C with asymptotic fit. The plateau was reached very fast with all MCF supports whereas the adsorption to all PMO materials was slower.

The relative uptake (Figure 4.55) of G6PDH from solution shows significant differences between the uptake of the PMOs and the MCF materials. The uptake by all MCF materials occurred spontaneous and very fast (< 15 min.) indicating that no

diffusion limitations occurred for the enzyme. In contrast, the diffusion of G6PDH into the pores of s-PMO was not finished until 4-8 h of immobilization time. Both PMOs with tertiary bridging amines showed saturation after 1 h. Differences were not only observed in the uptake rate but also in the amount of adsorbed G6PDH (Figure 4.56). No significant trend was observed for the amount of adsorbed enzyme onto MCF-p-,s- and t-NH₂ since the adsorbed amount onto MCF-pNH₂ reached about 97 % and the latter yielded about 92 %. This and the fast uptake is an indicator for the presence of strong electrostatic attraction that is not significantly altered between the different materials. The PMOs, however, varied in their uptake behavior. Most of the enzyme was taken up by the aerogel-type material whereas the s-PMO adsorbed only about 80 % and the tertiary PMO less than 50 %. This trend is not dedicated to the nature of the precursor but to the differences in the pore size of the PMO materials that decreases in this direction.

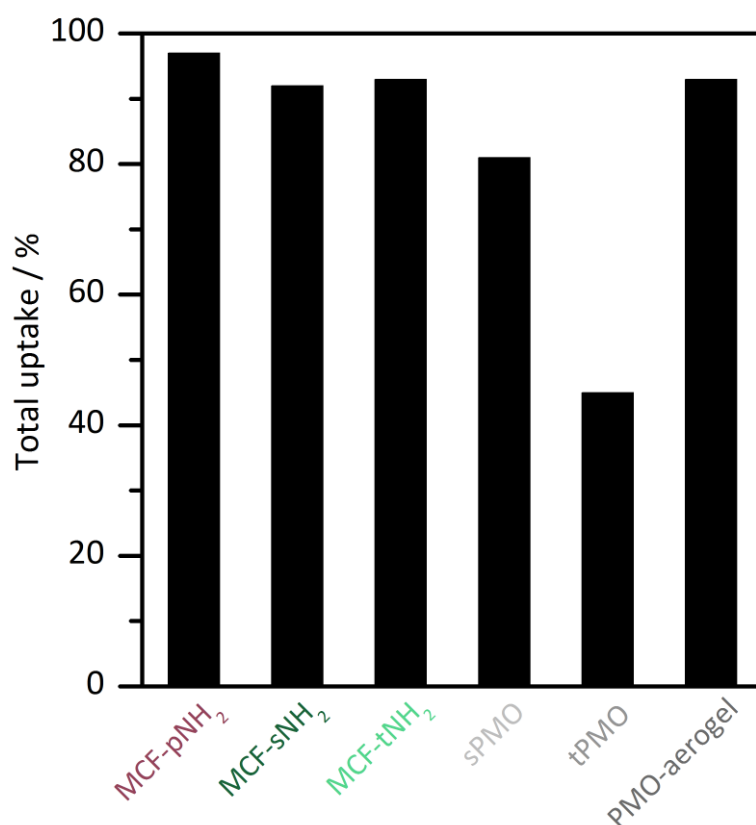


Figure 4.56: Total uptake of G6PDH from solution by amine-functionalized MCFs and PMOs respective to the enzyme content in solution.

This theory was additionally underlined by monitoring the protein content prior and after washing cycles (Figure 4.57) in the respective materials. s- and t- PMO exhibited only marginal loss of protein due to the confinement in the small pores whereas much of the enzyme was washed out of PMO-aerogel with its large pores. The differences observed in the total amount of protein compared to the relative amount in the samples (for example the high amount of enzyme in s-PMO) was caused by the varying protein content in the stock solution between the MCF and PMO materials. Nonetheless, the adsorption behavior can be comparatively discussed since both the relative and total uptakes are depicted.

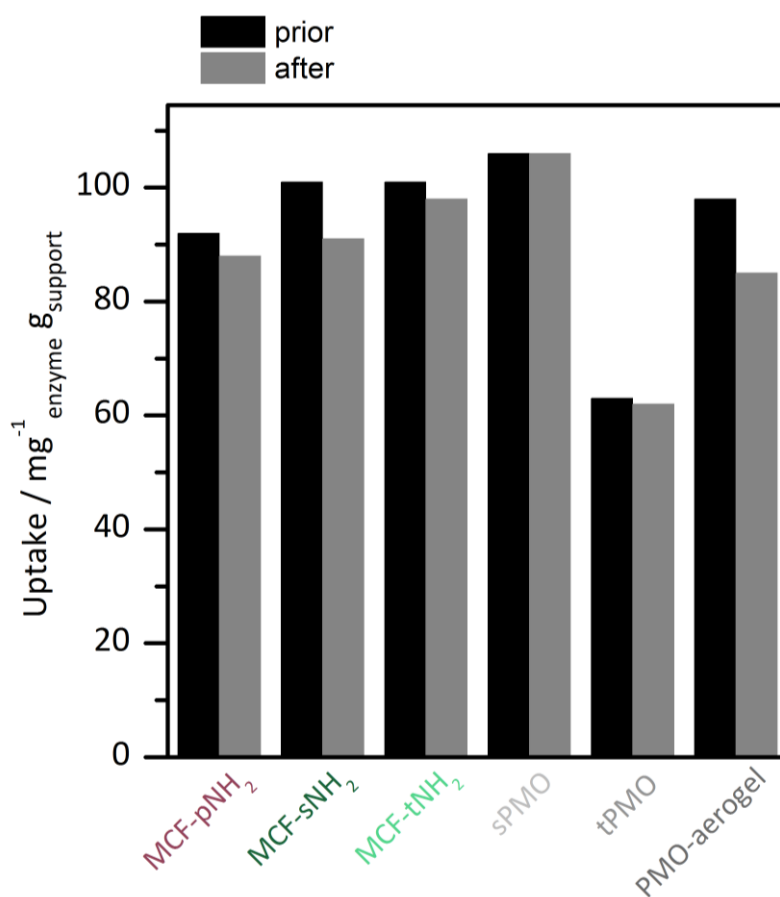


Figure 4.57: Protein content of amine-functionalized MCF supports and PMOs prior and after applied washing cycles. The mass specific uptake is presented in mass of enzyme respective to the mass of the support material.

To evaluate whether the hydrophobicity of the PMO materials affects the uptake behavior water sorption measurements at 25 °C were performed. The water vapor isotherms (Figure 4.58) show an almost simultaneously increasing adsorption of water

vapor at low relative humidity (5 - 35 %) and thus a nearly identical hydrophobicity. Additionally $\chi_{1,2}$ were calculated according to the procedure described in the last chapter.

Table 4.23: BET surface area derived from argon (87 K) and nitrogen (77 K) physisorption.

Sample	s-PMO	t-PMO
$S_{\text{BET}}(\text{Ar}) / \text{nm}^2$	196	467
$S_{\text{BET}}(\text{N}_2) / \text{nm}^2$	306/177 ^a	517
Deviation / %	36/-9.7	9.0

a: Sample not stable during heat treatment.
Surface area prior and after Ar physisorption.

The onset of capillary condensation was reached earlier for the t-PMO due to the presence of smaller micropores. Both samples reached no complete filling of the pores with water due to the presence of larger mesopores. The hysteresis was not closed for both samples due to chemisorption of water onto the siloxanes that led to rehydroxylation and thus surface silanol groups.

The hydrophobicity of all amine-functionalized MCF samples will not significantly differ from the hydrophobicity of the primary amine-modified investigated in the last chapter since the addition of one or two methyl groups does not have a strong influence on the hydrophobicity. All values are summarized in Table 4.24. Since the hydrophobicity of the PMO materials is constant for PMOs synthesized with the secondary and tertiary precursor it is not anticipated to have any effect on the uptake behavior between the respective PMO materials. Although the hydrophobicity indices suggest a higher hydrophilicity for the PMOs the surface of PMOs is still more hydrophobic due to the higher organic/silica ratio. The higher hydrophobicity indices are a result of the different porosity of the PMOs compared to the MCFs like discussed above. The reduced and slower uptake of the PMOs compared to the MCF materials, however, is possibly caused by the hydrophobicity of the materials despite their different pore sizes.

The hydrophobicity indices χ_1 and χ_2 were determined according to the procedure for the MCF materials described in the last chapter. One problem that arises with the PMO materials is the presence of large pores that are not even completely filled with argon. Hence no upper closure point for the adsorption isotherm with argon is detected.

Therefore, the validity of χ_2 is not given and the values determined from water adsorption are larger than those for argon adsorption. Since the PMOs exhibit a minor amount of micropores, χ_2 at $p/p_0=0.15$ is additionally determined.

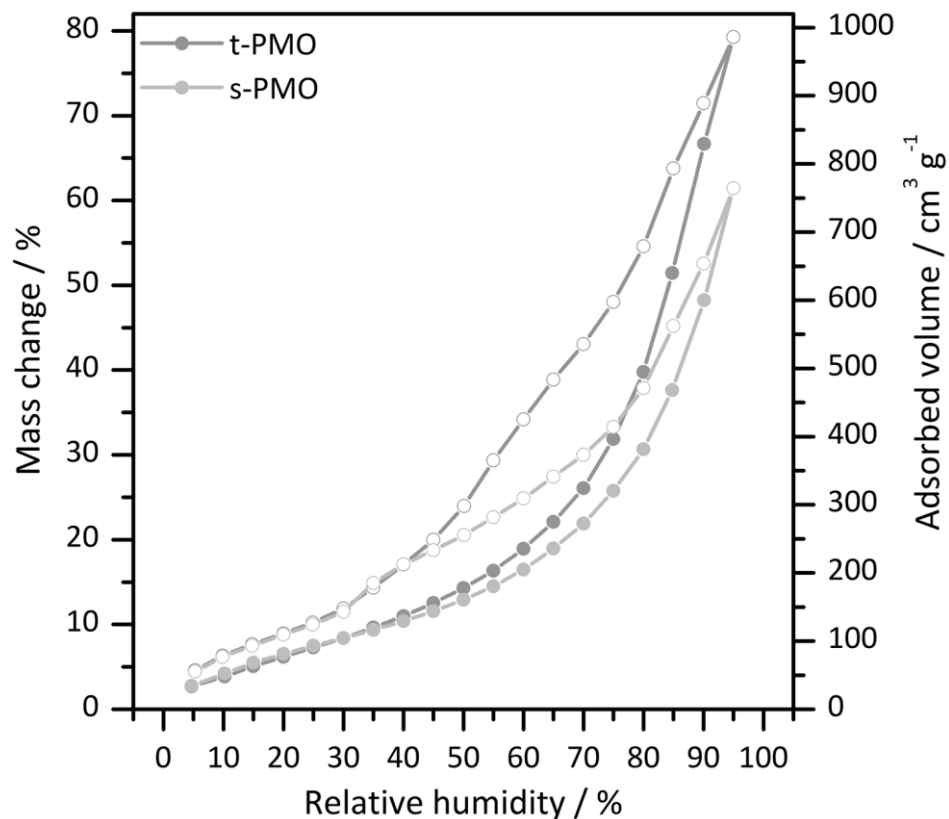


Figure 4.58: Water vapor sorption isotherms for s- and t-PMO measured at 25 °C between a relative humidity of 5-95 %.

Another problem arises from the instability of s-PMO that was obviously not stable during heat treatment. Therefore, the obtained values underestimate the hydrophobicity since an additional outgassing of the sample was needed that reduced the surface area prior to the argon measurement.

The hydrophobicity indices determined here are due to the microporosity of the samples not comparable to the results of MCF. They only can be used to compare similar materials to each other. The PMO prepared from the tertiary bridged amine precursor seems to be more hydrophobic than the one obtained for s-PMO. However, this is due to the instability of this PMO discussed above. According to the precursors used a similar hydrophobicity should be detected for both materials as was indicated by the

simultaneous progress in the adsorption branch of the water vapor isotherm at low p/p_0 .

Table 4.24: Hydrophobicity indices and pIs of MCF and PMO samples.

Sample	MCF-pNH ₂	MCF-sNH ₂	MCF-tNH ₂	s-PMO	t-PMO	PMO-aerogel
pl	9.2	9.5	9.5	10.0	9.4	9.3
χ_1	0.30	/	/	1.3	0.59	/
χ_2	0.40	/	/	1.3 ^a 0.82 ^b	1.1 ^a 0.34 ^b	/

a: Index determined at p/p_0 of 0.95

b: Index determined at p/p_0 of 0.15

Additionally, zeta potential titrations (Table 4.24, Figure 4.59, Figure 4.60) have been performed in order to evaluate the role of the pl for the adsorption process. In general, the pl of amines is similar between primary and secondary amines of the same kind but reduced for tertiary amines.^[275] Tertiary amines are not able to create intermolecular hydrogen bonds with water and thus the solvation of the ions is reduced and hence the tendency to be protonated.^[286] However, as discussed above the free silanol groups on the silica surface are an important factor for the acid-base behavior of the functionalized materials. The zwitterionic coordination of amines or the acidic function of the silanol group can change the isoelectric point of the material. All PMO and MCF materials discussed here have pIs in the range between pH 9-10. Thus the basicity of the materials is similar. Differences between primary-, secondary- and tertiary-modified MCF are very small and cannot be accounted to a change in surface chemistry. Those materials should therefore behave similarly and exhibit strong electrostatic attraction to G6PDH.

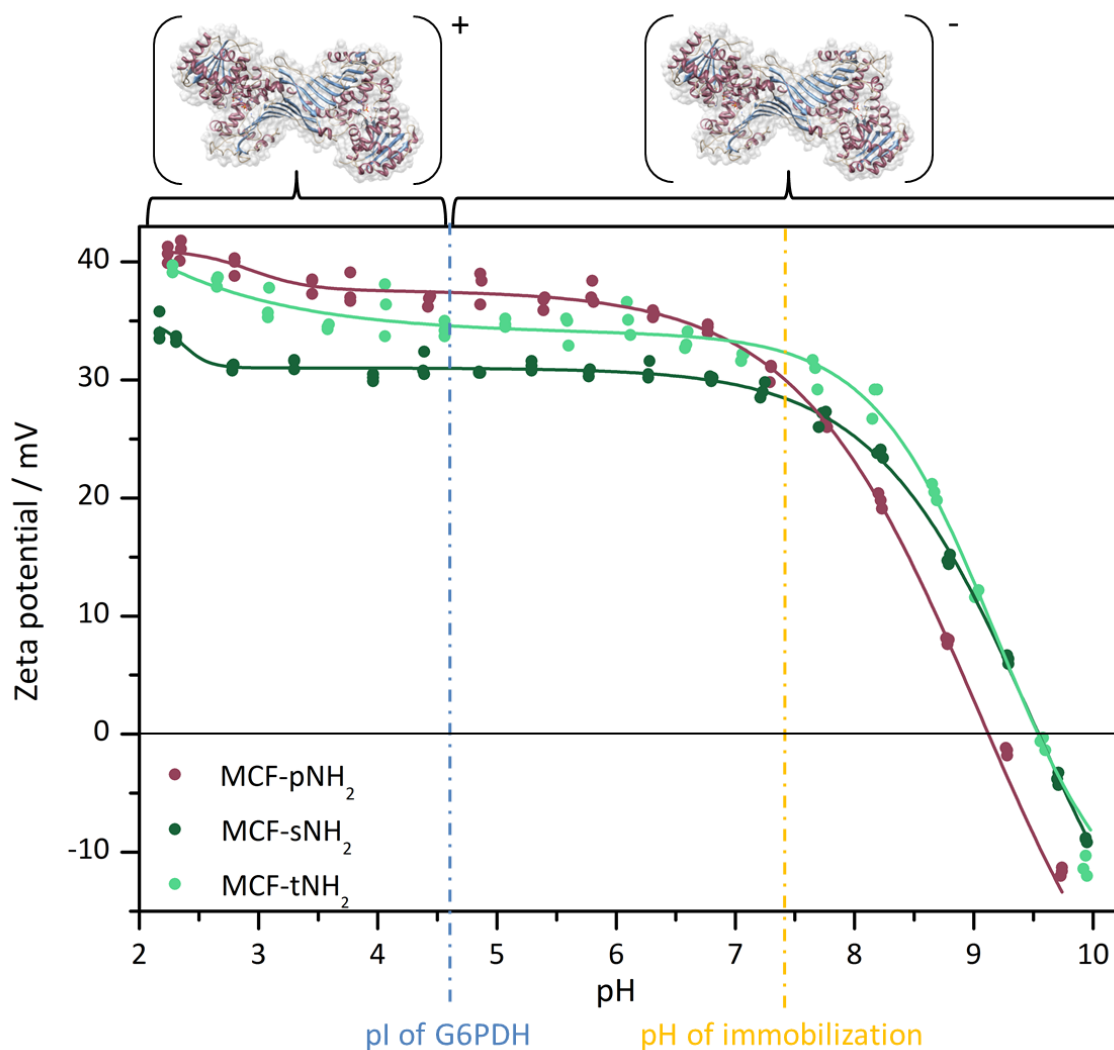


Figure 4.59: Zeta potential titrations of the amine-modified MCFs with sigmoidal curve fit. Below their isoelectric point materials and the enzyme ($pI = 4.6$) are positively charged, above negatively. At the pH of immobilization (pH 7.4) the enzyme exhibits a negative net charge whereas all amine-modified MCF supports have a positive net charge.

The zeta potential titration of the PMO materials showed not only a variation of the pIs but also of the maximum zeta potential. The curves of s- and t-PMO exhibited a much lower zeta potential compared to the aerogel-type PMO. This is a result of less surface charge and is often assigned to instability of particles. Both PMOs synthesized from a tertiary amine-precursor have similar pIs (Table 4.24) whereas the pI of the PMO containing a secondary amine in the organic bridge is much higher. However, all PMOs are charged highly positive at the pH of immobilization and hence the electrostatic behavior is not responsible for differences in the uptake.

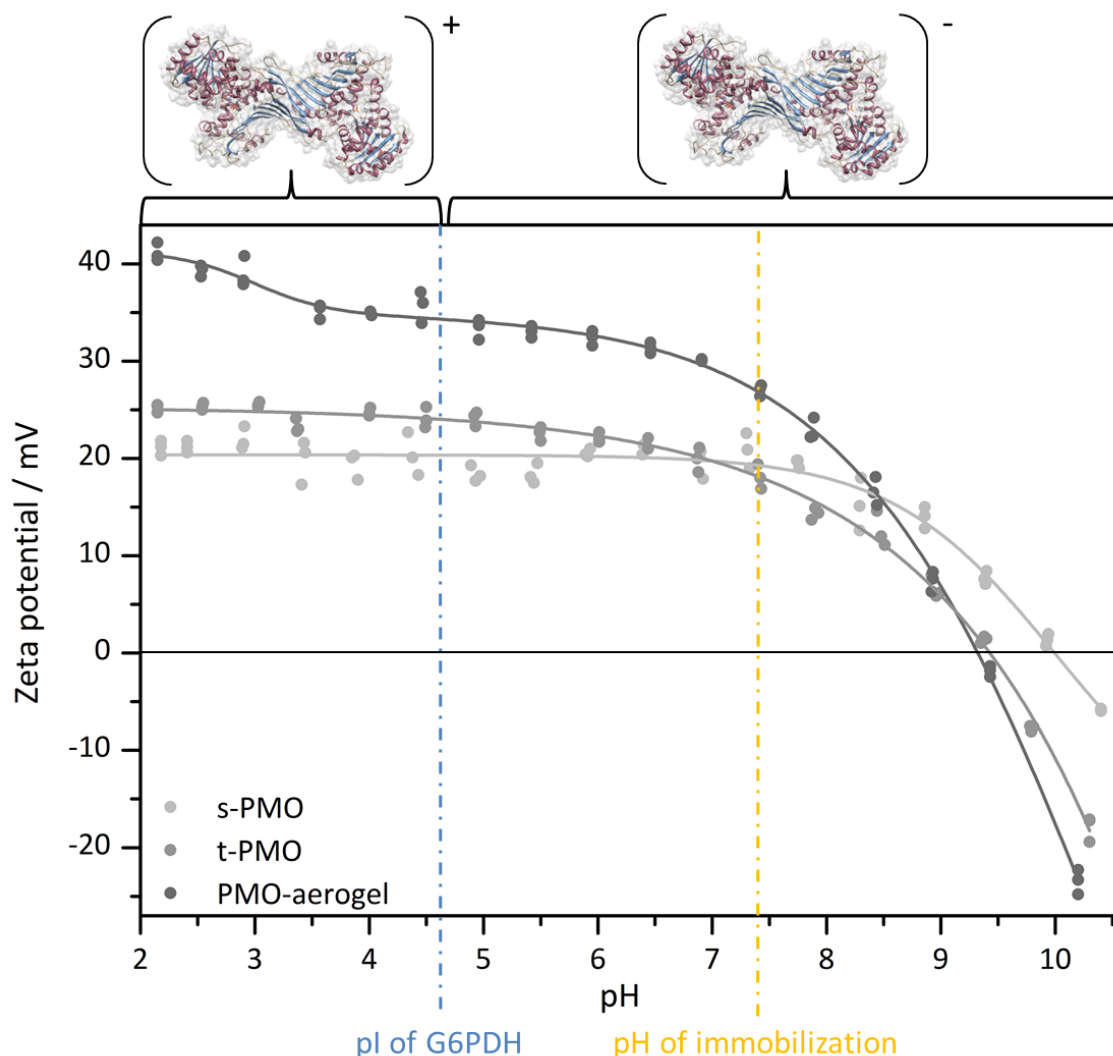


Figure 4.60: Zeta potential titrations of the amine-containing PMOs with varied chain length with sigmoidal curve fit. Below their isoelectric point materials and the enzyme ($pI = 4.6$) are positively charged, above negatively. At the pH of immobilization (pH 7.4) the enzyme exhibits a negative net charge whereas all amine-modified MCF supports have a positive net charge.

Activity of G6PDH

The maximum total activity of G6PDH adsorbed onto PMO and MCF supports was investigated after adsorption. Since an increase of activity was observed for G6PDH immobilized on MCF materials the maximum of the activity obtained for G6PDH immobilized onto MCF- pNH_2 was used for all materials as a comparison. The plot of the relative activity shows clearly the separation into two groups namely G6PDH adsorbed onto MCFs and PMOs. Very high retention of activity (> 90 %) was observed for G6PDH immobilized on MCF- pNH_2 , MCF- sNH_2 and MCF- tNH_2 whereas a reduction of 70 % compared to MCF- pNH_2 was observed for all PMO materials.

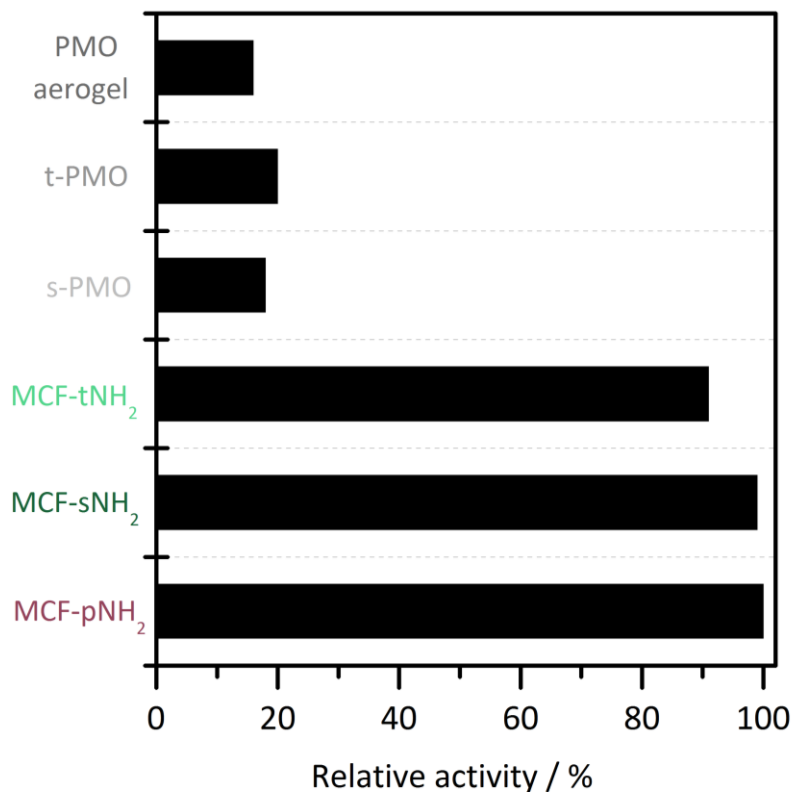


Figure 4.61: Relative activity of immobilized G6PDH compared to the activity of G6PDH immobilized onto MCF-pNH₂.

Besides the relative activity absolute activities (Table 4.25) respective to the amount of enzyme and carrier have been determined. All show similar group behavior of MCF and PMO supports.

Table 4.25: Relative and absolute activity of immobilized G6PDH at 37°C.

Sample	Relative activity / %	Activity / U mg ⁻¹ enzyme	Activity / U mg ⁻¹ support
MCF-pNH ₂	100	341	45
MCF-sNH ₂	99	336	46
MCF-tNH ₂	91	311	46
s-PMO	18	48	5
t-PMO	20	54	4
PMO-aerogel	16	48	4

One possible reason for the difference in the relative activities of G6PDH is related to the diffusion of the cofactor. The comparison of the uptake of NADP⁺ (Figure 4.62) however seems not to have an influence on the activity. All materials exhibited a more

or less pronounced reduction of the absorbance of NADPH in the supernatants and thus an uptake of NADP^+ . The absorbance of NADPH for the MCF materials was very similar but a slightly higher uptake was observed for the tertiary amine probably caused by the high functionalization density with organosilane. These findings support the assumption that there is almost no difference in the electrostatic interactions between the MCF materials.

The amount of NADP^+ adsorption increased continuously from the aerogel-type PMO to t-PMO to s-PMO. Since the hydrophobicity of the materials was comparable other reasons have to be responsible for this trend. Since both tertiary PMOs (PMO-aerogel, t-PMO) are composed of the same precursor they are chemically very similar. The porosity is the main distinctive feature between both materials. The higher NADP^+ uptake of t-PMO is mainly triggered by the enhanced adsorption potential in the small mesopores of this material. The lowest absorbance in the supernatant and thus the highest adsorption of NADP^+ was obtained with the secondary PMO.

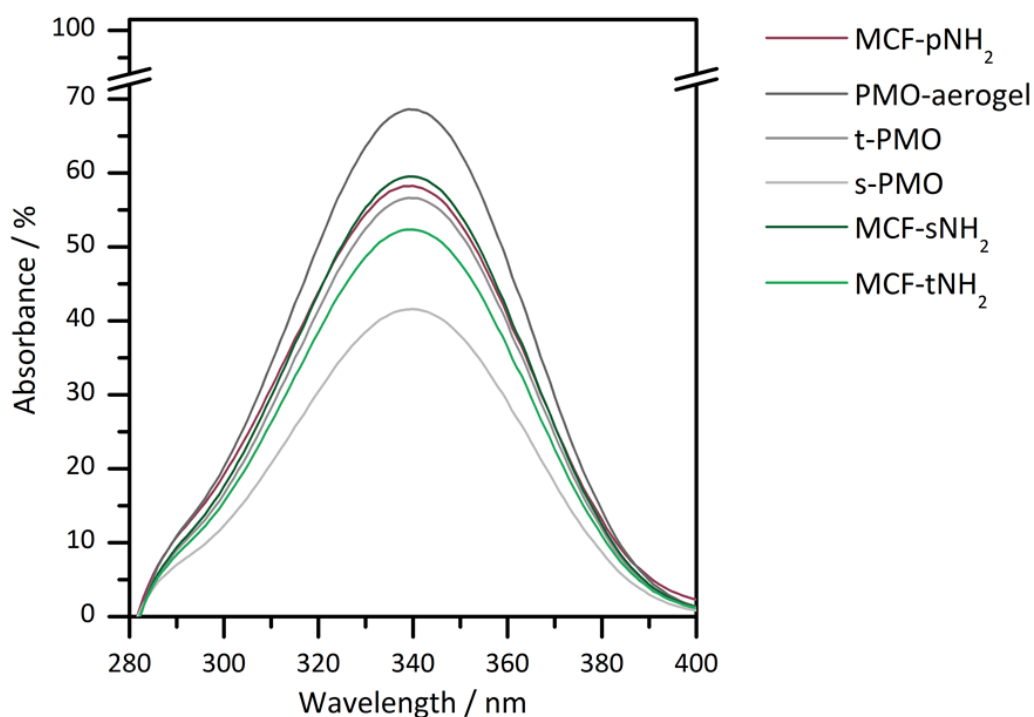


Figure 4.62: Adsorption of NADP^+ in PMO and MCF materials. After conversion to NADPH the residual NADPH was quantified in the supernatant. The absorbance of the respective supernatants is shown here relative to the absorbance of the used NADP^+ solution.

Since its pore size was larger than the pore size of the t-PMO it is no valid explanation here. But the isoelectric point of the secondary PMO was much higher than observed for the other materials. Thus the increased basicity of the interior of the PMO might be a reasonable explanation.

Since the diffusion of the cofactor was excluded as a possible reason for the different activities of MCF supports compared to the PMO supports the interactions are discussed here as a possible parameter. The main difference between the PMOs and the MCFs is the hydrophobicity as discussed earlier. An increase in hydrophobicity was assigned to the drop of the activity of G6PDH immobilized onto MCF-C₇-NH₂ and MCF-C₁₁-NH₂ in the last chapter. This is apparently also obtained for the PMO materials. The extension of the amine residues into the pore compared to their presence in the walls of the PMO is additionally changing the interactions with the enzyme.

Stability of G6PDH

The activity of G6PDH was monitored at 4 °C and 37 °C over a period of 50 or 30 days to determine thermal and storage stability of the enzyme. The relative activities of immobilized G6PDH are shown in Figure 4.63. G6PDH shows an exponential decay of the activity typically observed for free enzymes in solution whereas an increase of the activity was obtained for G6PDH immobilized onto MCF functionalized with primary, secondary and tertiary amine groups. The maximum of the activity was reached after 15 days prior to a slow linear decrease of the activity. The increase of the activity was caused, as already mentioned in the last chapter, by refolding or liberation processes of the enzyme. The high stability of G6PDH immobilized onto MCF supports can be mainly assigned to the favorable electrostatic interactions of the material with enzyme and substrate whereas the PMOs behaved more hydrophobic. Like already observed in the uptake behavior no significant differences between the MCF supports are present. This is an additional indicator that the type of the amine is not essential for the interactions between support and enzyme.

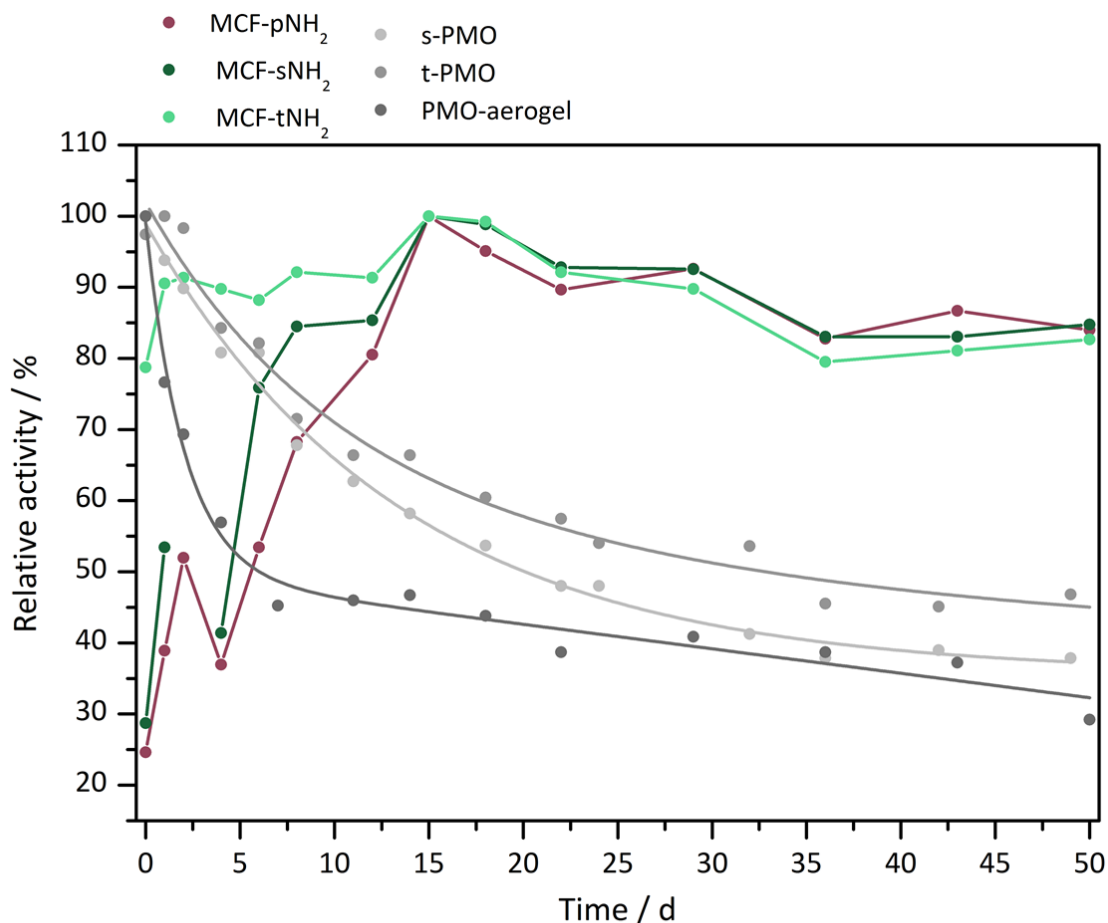


Figure 4.63: Storage stability at 4 °C for immobilized G6PDH. Immobilization in MCF materials led to a significant stabilization whereas G6PDH immobilized in PMO materials showed an exponential decay of activity during storage. Solid lines are plotted as guide to the eye.

In contrast to the stabilization effect of the MCF, the exponential decay observed for G6PDH immobilized in PMOs is a result of continuous enzyme inactivation. Thus, no stabilization effect is present for the immobilized enzyme inside the pores of the PMOs. However, the decay curves of the samples show a trend that can be directly correlated to the pore size of the PMOs. The pore size decreases in the order: t-PMO, s-PMO and PMO-aerogel whereas the stability is increased. This shows that the pore size still does have a positive effect on the stability caused by stabilization due to confinement effects (Figure 4.64) or due to leaching for the enzyme immobilized in the aerogel.

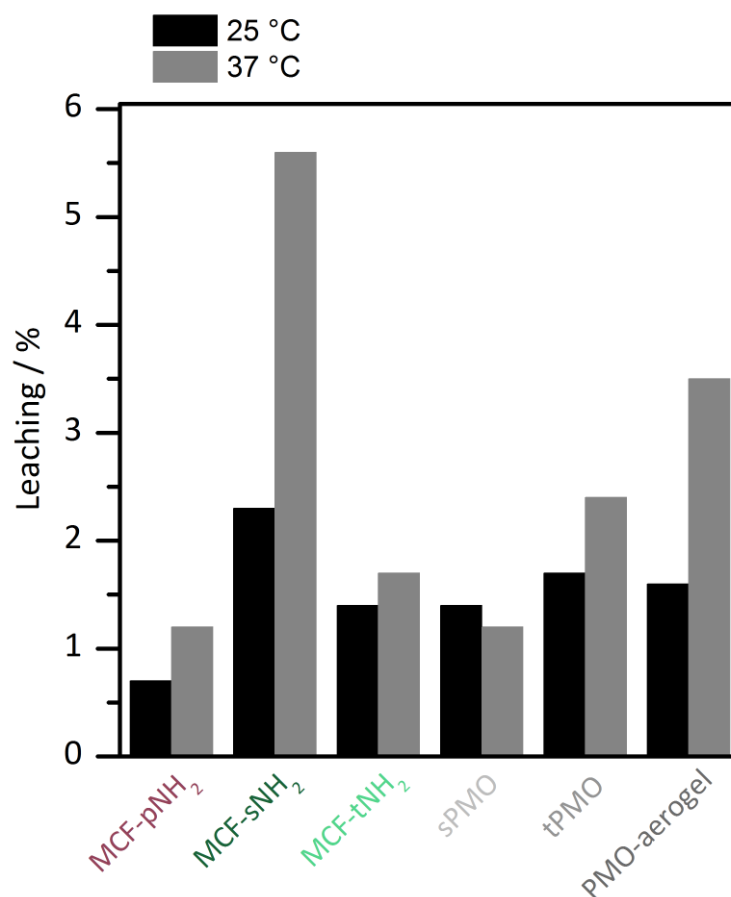


Figure 4.64: Leaching of G6PDH from PMO and MCF samples.

Increasing the temperature during leaching experiments from 25 to 37 °C enhances the leaching significantly due to enhanced Brownian motion. In general, increased leaching was observed for the PMO-aerogel and MCF-sNH₂. The high content of leached enzyme from the aerogel-type material is caused by the large pores of this material but the explanation for the leaching of MCF-sNH₂ has to be influenced by different parameters since the pore size of the primary and secondary amine-modified MCF supports are similar as well as the functionalization density. Up to now, no possible explanation was found that can clarify these observations.

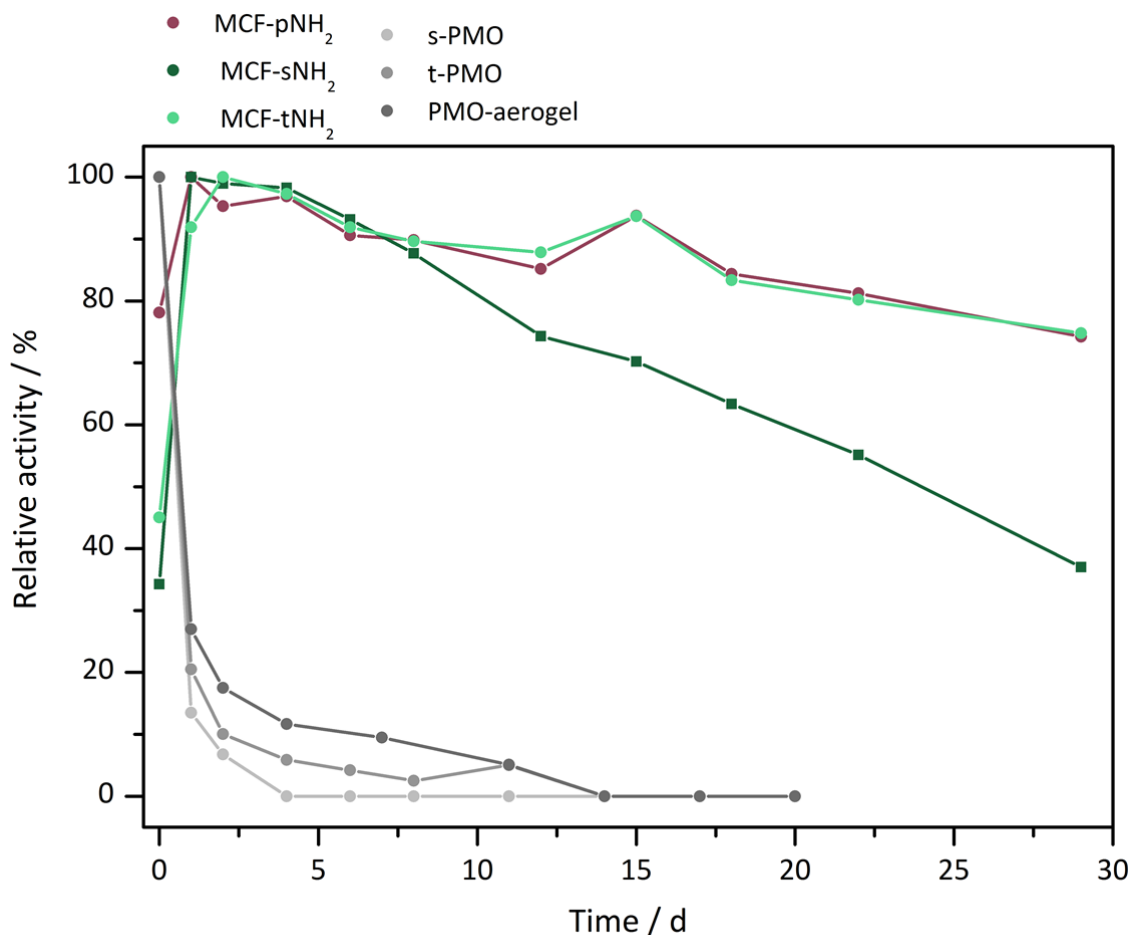


Figure 4.65: Thermal stability at 37 °C for immobilized G6PDH. Immobilization in MCF materials led to a significant stabilization whereas the immobilization in PMO materials had no stabilization effect. Solid lines are shown as guide to the eye.

The trends observed for the stability at 4 °C were found similar but more emphasized at 37 °C. The exponential decay of the activity for the PMO materials was much faster than observed at lower temperatures. After less than 15 days none of the samples showed any residual activity. The MCF samples were much more stable although the MCF-sNH₂ showed a much faster decay of the activity. This is mainly caused by the enhanced leaching of the enzyme from the support. The difference of PMO and MCF samples is mainly due to the difference in the interacting forces with G6PDH. Hydrophobic interactions present in the PMOs due to their organic groups seems to destabilize the enzyme whereas the electrostatic interactions between the amine groups of the MCF samples with the enzyme seem to have a rigidification effect and thus a higher stability is obtained. All obtained data are summarized in Table 4.26.

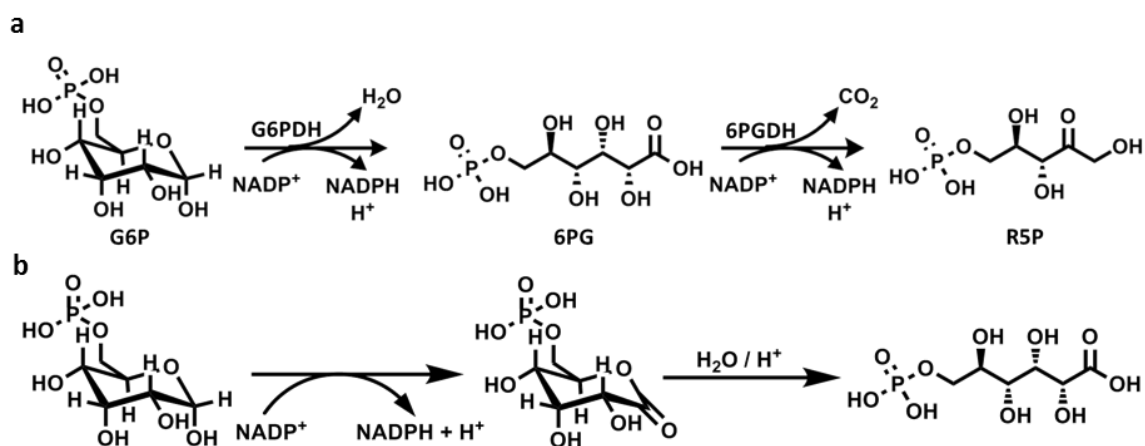
Table 4.26: Stability of G6PDH immobilized onto PMO and MCF support materials.

Sample	Relative activity / % (4 °C, 14/15 d ^a)	Relative activity / % (4 °C, 30 d/ 29 d ^a)	Relative activity / % (37°C, 6 d)
MCF-pNH ₂	100	93	91
MCF-sNH ₂	100	93	93
MCF-tNH ₂	100	90	92
s-PMO	58	51	4
t-PMO	64	42	0
PMO-aerogel	45	39	9

All values are determined from the respective data points or the respective fit if present.
a: 15 d for MCF samples, 14 d for PMO samples

4.2.4 CONVERSION OF GLUCOSE-6-PHOSPHATE TO RIBULOSE-5-PHOSPHATE BY G6PDH AND 6PGDH¹²

A short reaction sequence (Scheme 4.5) was established with G6PDH from *Leuconostoc mesenteroides* and 6-phosphogluconat dehydrogenase (6PGDH) from *Bacillus stearothermophilus* in order to proof the potential of these enzymes in a cascade reaction. Two general ways exist for the application of immobilized enzymes in a sequence of reactions. Participating enzymes can be bound to one carrier in a co-immobilization process.^[219,274] The diffusion of substrates, cofactors and products is usually enhanced due to the vicinity of both enzymes but toxic byproducts or inhibition are common side-effects. On the other hand the immobilization onto two different carriers allows the separation of the enzymes and products but the reaction sequence is diffusion-limited.^[219,287] The immobilization onto two different materials additionally allows to tailor a support according the respective enzyme and to independently control the immobilized amount of enzyme on the carrier.



Scheme 4.5: Two-enzyme sequence consisting of G6PDH and 6PGDH. (a) G6P is converted by G6PDH to 6PG that is further oxidized to R5P. Both reaction steps are accompanied by the reduction of NADP⁺. (b) The first reaction of the sequence (G6P to 6PG) proceeds via 6-phosphogluconolactone that is rapidly hydrolyzed to 6PG in solution.

¹² The presented work is a result of a cooperation with M. Dreifke from our group, Lutz Hilterhaus and Jan Simons from the Technical University Hamburg-Harburg. The immobilization of 6PGDH was performed by M. Dreifke.

Here a separate immobilization approach was chosen in order to allow a specific treatment of each enzyme during immobilization and to prevent an inhomogeneous distribution of the enzymes in the pore network of a carrier. Further it is planned in the future to apply the enzymes in separate reactors with different reaction conditions. Both enzymes are immobilized onto 3-aminopropyl-modified MCF (MCF-C₃-NH₂). The catalytic reaction performed with immobilized G6PDH and 6PGDH is shown in Scheme 4.5a. G6PDH catalyzes the first reaction step that is the oxidation of glucose-6-phosphate (G6P) to 6-phosphoglucono lactone. The lactone is rapidly hydrolyzed in aqueous environment to 6-phosphogluconic acid (6PG) (Scheme 4.5b). 6PG is the substrate of 6PGDH that decarboxylizes the acid in the last step to ribulose-5-phosphate (R5P). Both catalytic steps are accompanied by the reduction of NADP⁺ to NADPH which will be monitored during the cascade reaction.

In order to establish a successful cascade the kinetic of both immobilized enzymes is analyzed at the respective reaction conditions. Since 6PGDH was less stable than G6PDH according to our results, the conditions were adapted to this enzyme. Thus the reaction was performed in phosphate buffer at 25 °C. Since both enzymes follow the Michaelis-Menten according to literature the K_M and v_{max} values were determined.^[17,272,288] The MM kinetics for G6PDH have been extensively discussed in chapter 4.2.3. The obtained values of K_m for 6PGDH are higher than the ones obtained for free 6PGDH from literature, as expected, due to diffusion restrictions and/or partitioning effects. The data are not directly comparable since the measurement conditions varied but it is used here as a guidance value. The Lineweaver-Burk plots can be found in the appendix.

Table 4.27: K_M and v_{max} values for G6PDH and 6PGDH determined at 25 °C in phosphate buffer (50 mM, pH 7.5) either by varied substrate or cofactor concentration.

Immobilized enzyme	Varied	K_m / mM	v_{max} / mmol (L min) ⁻¹
G6PDH	G6P	0.264	0.015
	NADP ⁺	0.024	0.017
6PGDH ^a	6PG	0.071	0.013
	NADP ⁺	0.015	0.006
a: K_m (6PG) = 0.016 mM; K_m (NADP ⁺) = 0.017 mM ^[288] conditions: Tris-HCl (pH 8.0), 30 °C			

However, the important conclusions for the cascade are drawn by comparing the kinetic parameters to each other not the values of immobilized and free enzymes. Most important are the values for v_{max} that are higher for immobilized G6PDH than for 6PGDH. Thus more 6PG is produced than it can be converted by 6PGDH. Usually, a more balanced reaction equilibrium is favored due to inhibition effects, accumulation of one product or back reactions. The back reaction however is not possible since the hydrolysis of the lactone is irreversible. Nevertheless, a lower concentration for G6P was chosen in order to reduce the reaction velocity of G6PDH. The NADP^+ concentration was chosen to exceed the G6P concentration in order to allow a complete conversion of the substrate in the first and second reaction step.

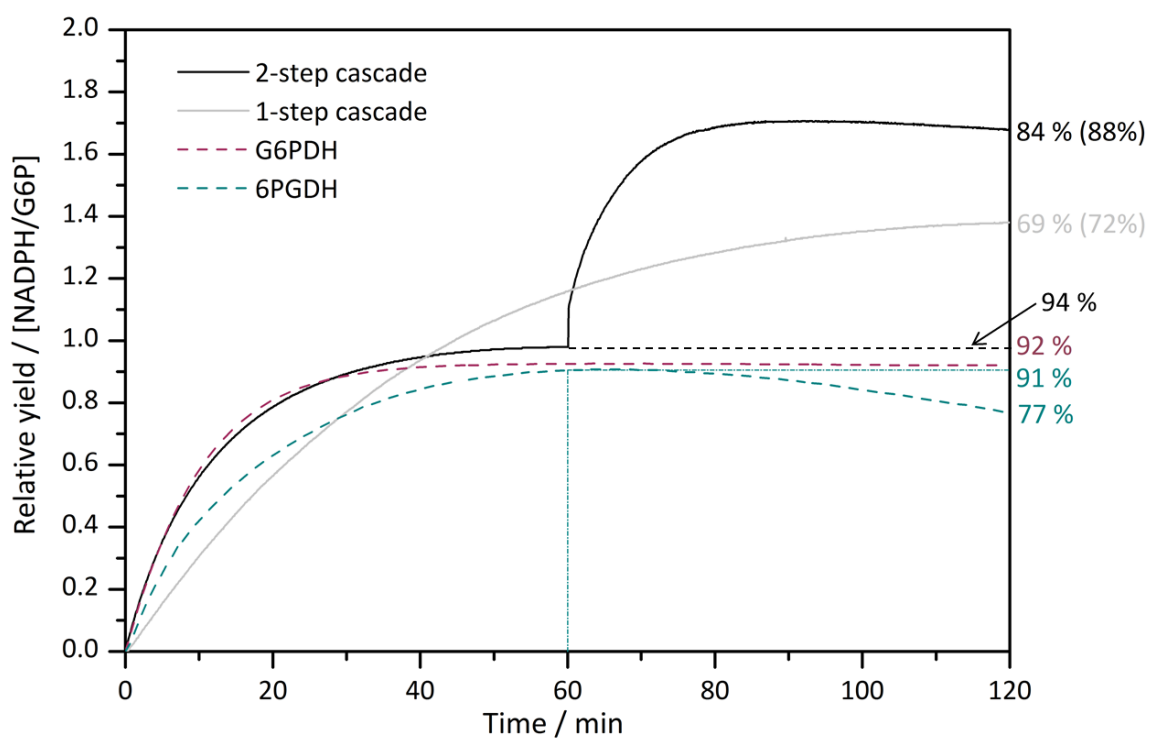


Figure 4.66: 1- and 2-step cascade reaction of 6PGDH and G6PDH. Additionally both half reactions have been carried out under the cascade conditions (phosphate buffer 50 mM, pH 7.5; NADP^+ : 0.50 mM, G6P: 0.12 mM). For the reaction of 6PGDH 6PG was added. The yields of each reaction are depicted at the right side of the figure. The yield in brackets is respective to the maximum yield achieved by G6PDH under the applied conditions. The maximum yield of the 6PGDH reaction after 60 min prior to the decrease in activity is also shown.

Besides both half reactions of either G6PDH or 6PGDH two model cascades have been established. In one cascade both immobilized enzymes were added simultaneously to the solution (1-step cascade) and in the other 6PGDH was added after the catalytic

reaction of G6PDH reached a plateau (2-step cascade). The results (Figure 4.66) are plotted against the yield expressed in the relative concentrations of the formed cofactor NADPH to the concentration of substrate applied. A complete conversion of 1 mol G6P could lead to 1 mol NADPH for each half reaction and thus a total yield of 2 mol for the reaction sequence.

The half reaction for G6PDH approaches a maximum conversion of 92 % after about 50 min. During the rest of the reaction time the absorption of NADPH stays almost constant. Little losses in the relative yield (0.004) can only be assigned to the slow degradation of NADPH ($\tau = 28$ h) since the hydrolysis of the lactone prevents the back reaction.^[287] In contrast the second half reaction of 6PGDH reaches its maximal conversion (91 %) much slower and decreases afterwards. The slower conversion is mainly due to the smaller maximal reaction velocity. The reduction of the NADPH concentration can have different reasons. One explanation would refer to the degradation of NADPH one to a possible back reaction. The degradation of NADPH is much slower than the decay observed here but a possible back reaction due to solubilized CO₂ was already observed in literature for 6PGDH from *Candida utilis* by Hanau et al.^[289] A complete conversion of the substrate is not reached in both cases due to inhibition effects. Both enzymes exhibit no product inhibition but competitive inhibition of NADPH and NADP⁺.^[17,288] The more NADPH is produced the more the inhibition is favored.

Considering an optimal reaction progress the 2-step cascade would simply be an attachment of both half reactions. But as can be seen here, the reaction yield (84 %) is lower than the expected yield (91 %). A small part of the loss is as already mentioned dedicated to the back reaction but the larger part is assigned to an increased NADPH concentration in the second half reaction and thus a stronger inhibitory effect for 6PGDH. But nonetheless a conversion of more than 80 % is a good result. The yield of the first half reaction is slightly increased up to 94 % due to errors in the experimental and/or detection part.

The 1-step cascade exhibits much slower conversion of the substrates to the product due to diffusion effects. Here, the substrates and cofactors have not only to enter one porous system but also after leaving the material filled with G6PDH the products have to enter the MCF filled with 6PGDH. But even if this is taken into account the overall yield

will not reach the yield observed for the 2-step cascade. Possible reasons are inhibitory effects that are not easily accessed due to the educt/product mixture during the reaction sequence.

4.3 EXPERIMENTAL SECTION

4.3.1 CHARACTERIZATION TECHNIQUES - INSTRUMENTAL DETAILS

Powder X-ray diffraction (PXRD)

The diffraction patterns in the region of small angles ($< 10^\circ$) were performed with $\text{Cu}_{K\alpha}$ radiation (1.541874 Å) with a *MPD X'Pert Pro* from *Panalytical* in theta-theta geometry. The detector was operated at a voltage of 45 kV and a current of 40 mA. Speed: 25 s/step (step size: 0.0131°).

Small-angle X-ray scattering (SAXS)

SAXS measurements were performed in transmission mode with a setup from *Seifert* (X-ray generator and rotating anode setup DRF-Cu 0.3) with $\text{Cu}_{K\alpha}$ radiation. The data was analyzed by using the “*Scatter*” software.

Volumetric nitrogen physisorption

Nitrogen physisorption isotherms were performed at 77 K in a relative pressure range of $p/p_0 = 0.02\text{--}0.99$ on an *Autosorb 6* or *Quadrasorb (Quantachrome Instruments)*. Prior to adsorption, all samples were degassed at 120°C for 20 h under reduced pressure. Pore size distributions were obtained by using the BJH method and quenched solid and nonlocal DFT methods and the surface area by using the BET equation (for p/p_0 values of 0.05–0.25).

Gravimetric water vapor sorption

Gravimetric water vapor sorption was performed on an *AquaDyne* from *Quantachrome Instruments*. The samples were outgassed at 120 °C for 20 h at reduced pressure as well as treated at 80 °C with dry air prior to the measurement. All experiments were performed at 25 °C from 5-95 % relative humidity (RH) in steps of 5 % RH.

Mercury porosimetry

Mercury intrusion was performed using a *PoreMaster 33* from *Quantachrome Instruments*. The pressure was increased from 20-33000 psi in a continuous mode using

the slowest possible autospeed mode. For all measurements a mercury contact angle of 140° and a surface tension of 0.480 N m^{-1} were assumed.

Zeta potential titrations

Titrations of the zeta potential were performed at 25°C with a *Zetasizer Nano SZ* in combination with a multipurpose *MPT-2* titrator from *Malvern Instruments*. A 4 mW HeNe laser ($\lambda = 633 \text{ nm}$) was used as a light source. The detection of the scattered light was performed at an angle of 13° relative to the incident beam. The *M3-PALS* technique (patented by Malvern instruments), a combination of FFR and SFR and LDV (see 2.3.2), was used to measure and process the data derived from the sample. The pH was varied from pH 2-10 in steps of 0.5 (± 0.2) used 0.1 M NaOH as a base and 0.1 M HCl as an acid source. All samples were dispersed under sonication in ultrapure water. The Smoluchowski approximation was used to solve the Henry equation.

UV-Vis spectroscopy

All biochemical characterizations were performed with a *Biomate3S* spectrophotometer from *Thermo Scientific*.

Electron microscopy

The TEM images were recorded on a *CM30-ST* from *Philips* with an acceleration voltage of 300 kV. The SEM images were obtained by using a *Leo-1550* from *Carl Zeiss NTS* with an acceleration voltage of 5 kV.

Thermal analysis (TG/DTA/MS)

TG/DTA/MS experiments were performed on a thermobalance *STA 449 F3 Jupiter* and a coupled *QMS 403 C Aëolos* Quadrupol mass spectrometer from *Netzsch*. All measurements were performed under synthetic air (argon/oxygen (8:2)) and a gas flow of 20 mL min^{-1} . About 20 mg sample were heated in an aluminium oxide crucible with a heating rate of 5 K min^{-1} from room temperature to 600°C . The assignment of the particular combustion steps was done by analysis of the differential mass loss curve (DTG).

Infrared spectroscopy (IR)

FTIR spectra were recorded by using a *Vertex 70* from *Bruker* in transmission with a KBr pellet for solids or NaCl plates for liquid samples.

NMR spectroscopy

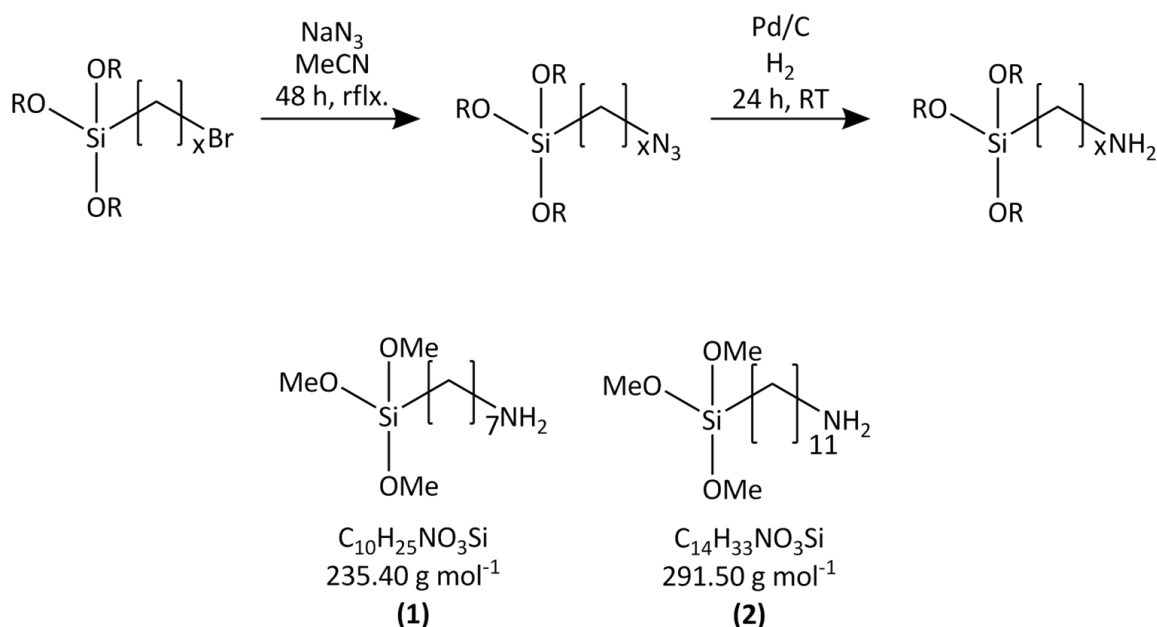
NMR spectra were recorded on a *Bruker AVANCE 400* with tetramethylsilane as an internal standard.

4.3.2 SYNTHESIS AND FUNCTIONALIZATION OF NANOPOROUS SUPPORTS

4.3.2.1 Synthesis of mesostructured cellular foams (MCF)

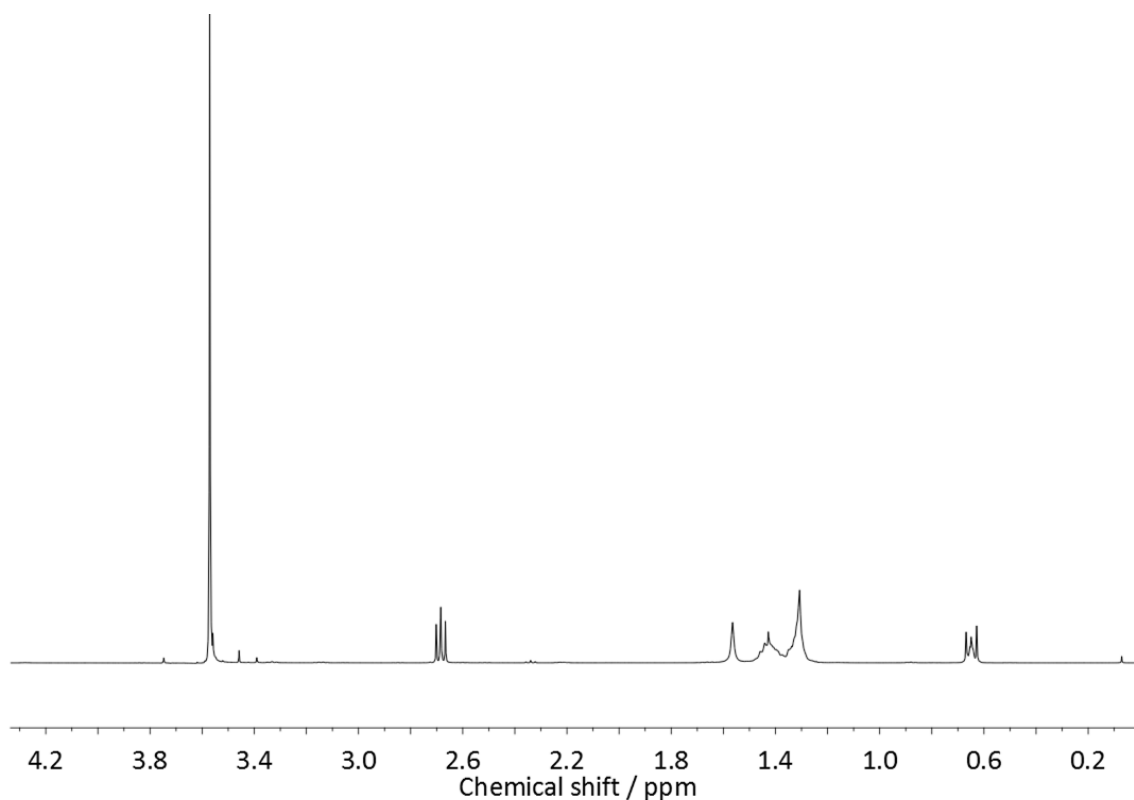
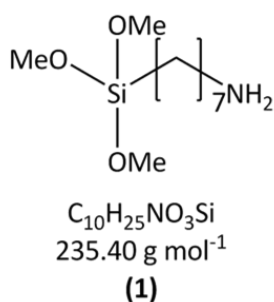
MCF was prepared according to the literature.^[63] Pluronic P123 (2.4 g, 0.41 mmol) was dissolved in 1.9 M HCl (90 mL) at RT. After the addition of the respective amount of mesitylene (TMB/P123 = 0, 0.30, 0.50, 0.75, 1.0, 1.5) and NH_4F (28 mg, 0.76 mmol), the mixture was heated to 40 °C and stirred. After 1 h, TEOS (5.3 g, 5.7 mL, 25.4 mmol) was added and the mixture was further stirred for 20 h at 40 °C. The mixture was transferred to an autoclave and aged at 100 - 120 °C under static conditions for 24 h. The resulting white powder (MCF) was filtered off, washed with water and ethanol and dried for 24 h at 60 °C. Removal of the template was achieved by calcination for 5 h at 550 °C (heating rate = 1 K min⁻¹).

4.3.2.2 Functionalization of MCF

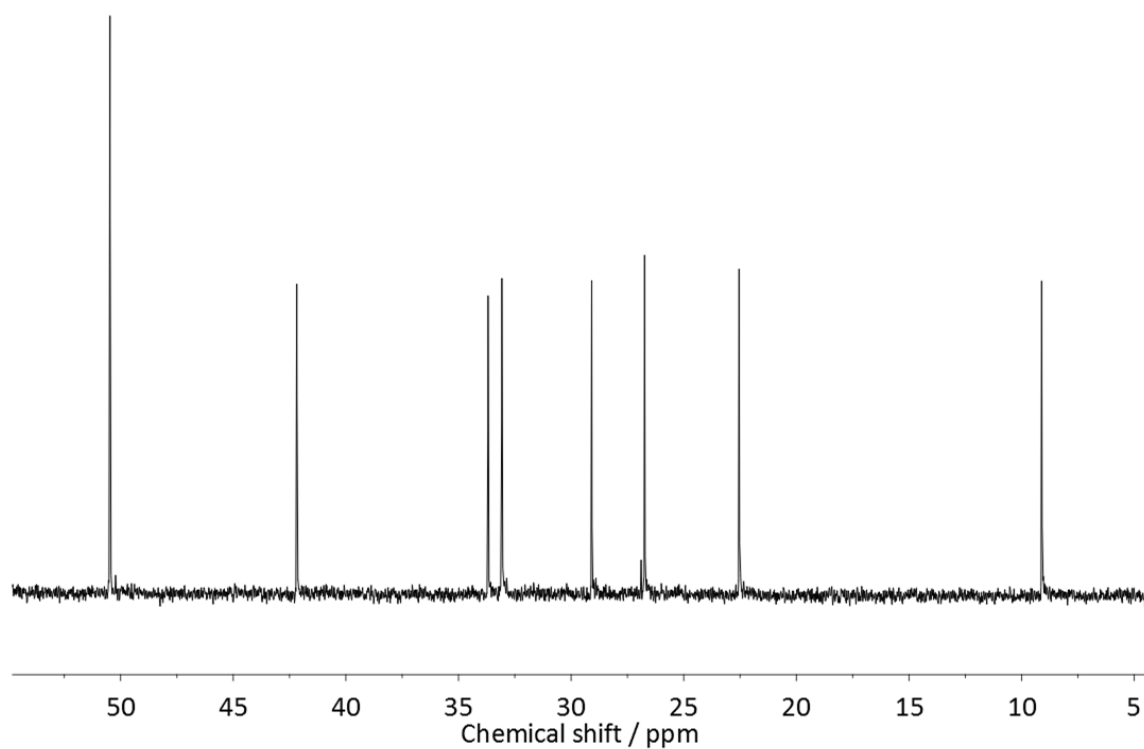
Synthesis of 7-aminoheptyl- and 11-aminoundecyl-trimethoxysilane

The two-step procedure for the synthesis of the respective aminosilanes consists of a bromide-azide transfer and a hydration step performed according to literature.^[290]

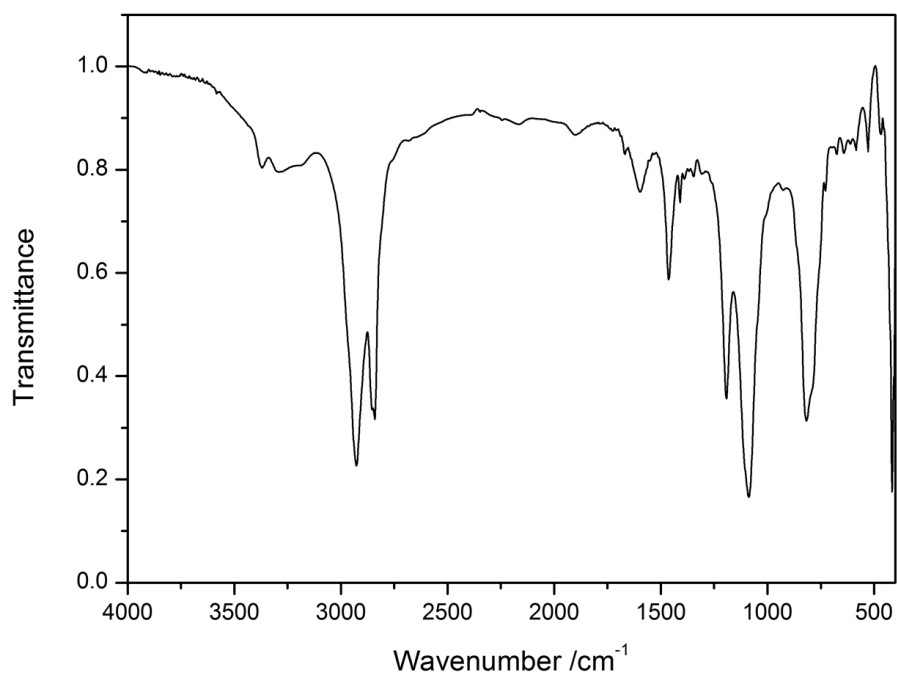
2.8 mmol of the the respective bromosilanes were solubilized in 15 mL acetonitrile. An excess of NaN_3 (9.8 mmol) was added to the solution that was refluxed for 48 h. The solvent was evaporated under reduced pressure. The residual mixture was diluted with 15 mL cyclohexane prior to the separation of the inorganic salts and the product by filtration. 250 mg Pd/C was added to the cyclohexane solution and the mixture was exposed to a hydrogen atmosphere using a hydrogen balloon. After stirring for 24 h, the catalyst was removed by filtration and the product was obtained as slightly yellow oil after removal of the solvent under reduced pressure.



¹H-NMR: δ [ppm] (400 MHz, CDCl_3): 3.55 (s, 9H, OCH_3), 2.68-2.64 (m, 2H, N_3CH_2), 1.46-1.25 (m, 12H, CH_2), 0.66-0.59 (m, 2H, CH_2Si).

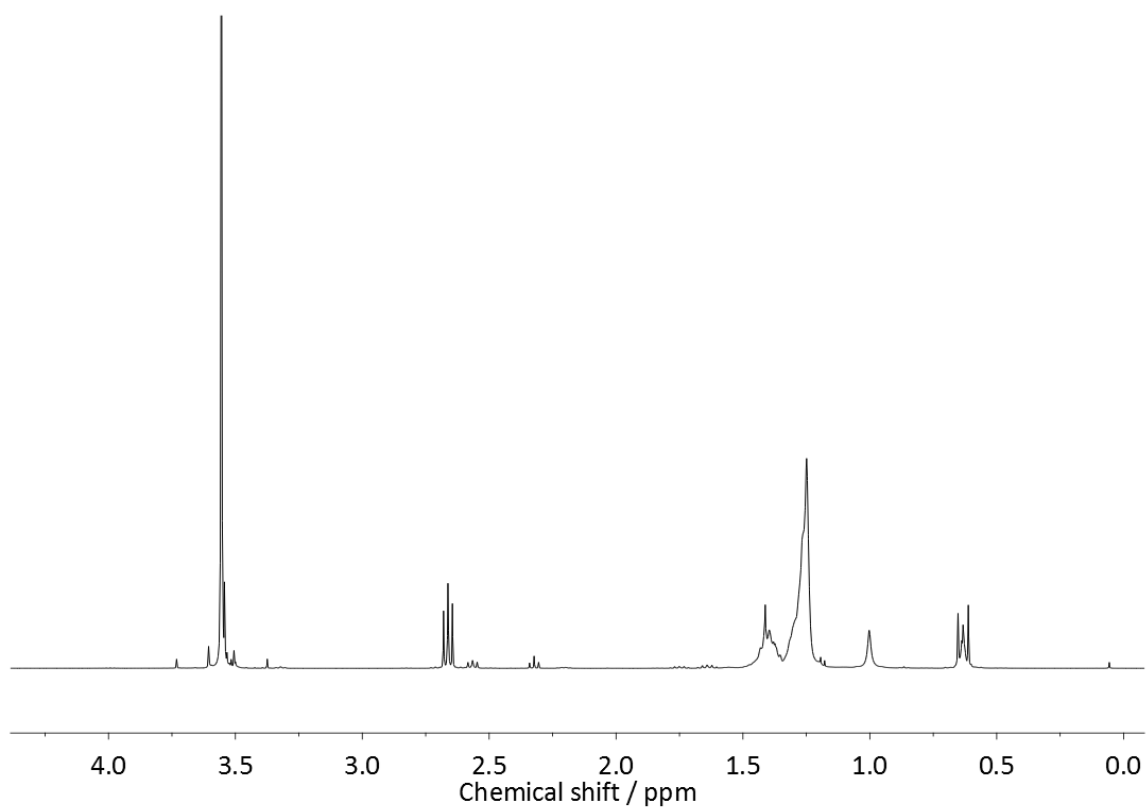
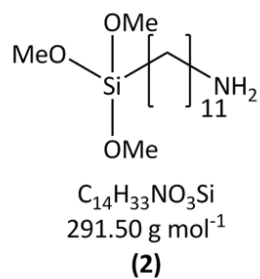


^{13}C -NMR: δ [ppm] (400 MHz, CDCl_3): 50.6 (OCH_3), 42.3 (NCH_2), 33.8 (CH_2), 33.2 (CH_2), 29.2 (CH_2), 26.9 (CH_2), 22.7 (CH_2), 9.3 (SiCH_2).

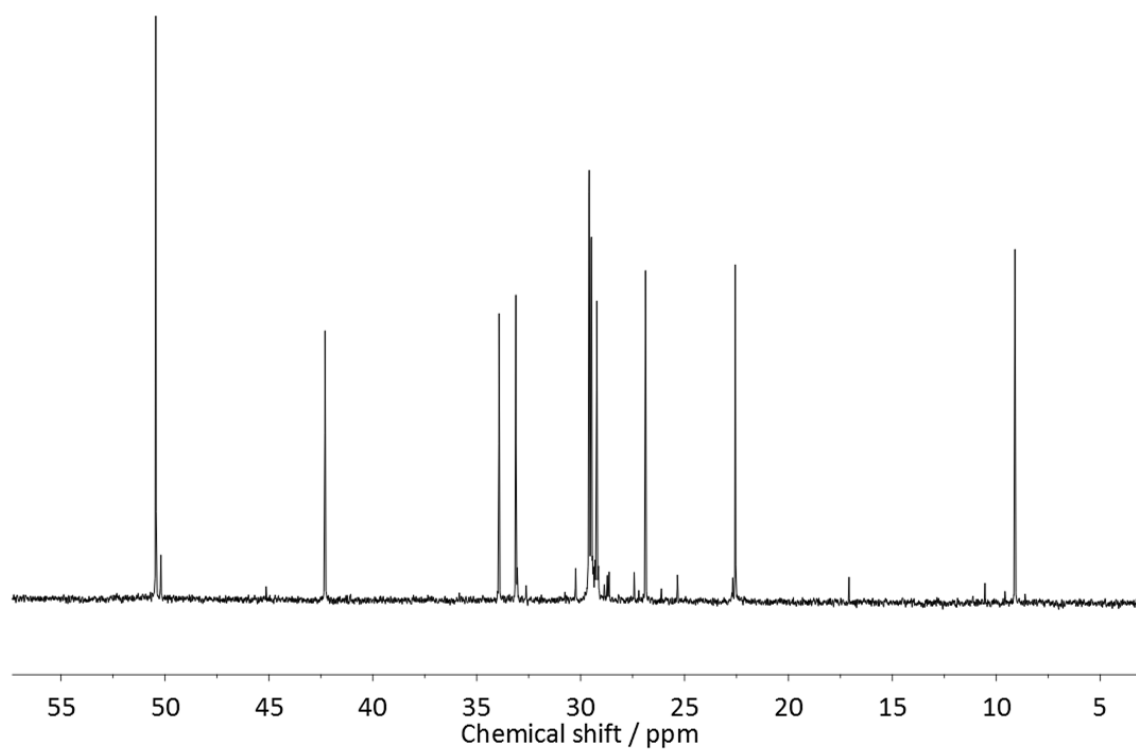


IR: NaCl (cuvette) [cm^{-1}]: = 3369, 3293, 2927, 2841, 1669, 1597, 1463, 1410, 1390, 1346, 1193, 1088, 817, 728, 407.

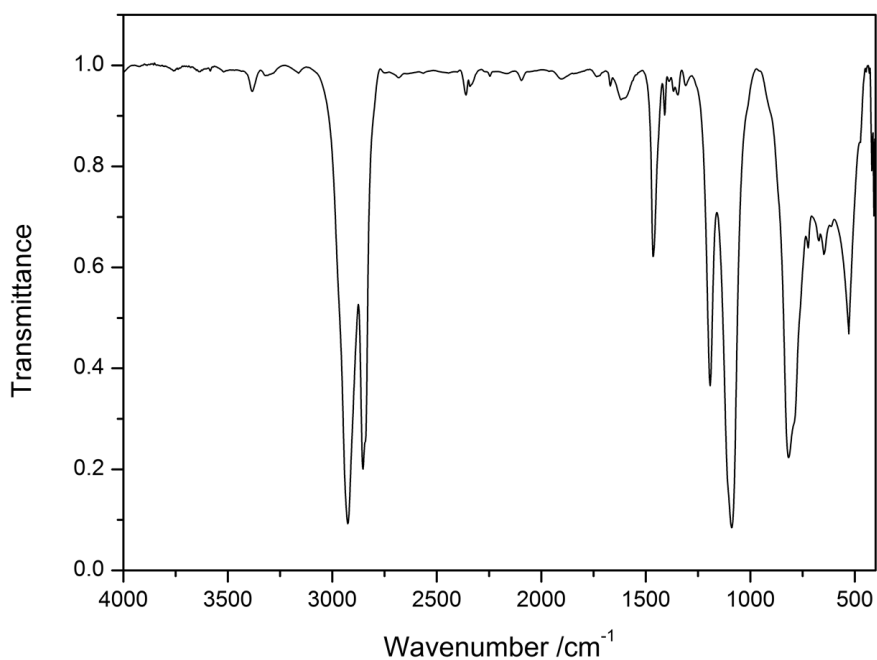
FAB-MS: 236 [$\text{M}+\text{H}$] $^+$, 204 [$\text{M}-\text{OCH}_3$]



$^1\text{H-NMR}$: δ [ppm] (400 MHz, CDCl_3): 3.53 (s, 9H, OCH_3), 2.67-2.61 (m, 2H, N_3CH_2), 1.43-1.19 (m, 18H, CH_2), 0.64-0.58 (m, 2H, CH_2Si).



$^{13}\text{C-NMR}$: δ [ppm] (400 MHz, CDCl_3): 50.6 (CH_3O), 42.4 (CH_2N), 34.1 (CH_2), 33.2 (CH_2), 29.7-29.4 (5 CH_2), 27.0 (CH_2), 22.7 (CH_2), 9.2 (CH_2Si).



IR: NaCl (cuvette) [cm^{-1}]: = 3383, 3319, 2926, 2853, 1670, 1618, 1465, 1192, 1089, 816, 723, 671, 647, 529, 408.

FAB-MS: 292 [$\text{M}+\text{H}$] $^+$, 260 [$\text{M}-\text{OCH}_3$]

Silylation of MCF with organic silanes

The functionalization of MCF was achieved by post-synthetic modification with various silanes. 200 mg MCF were heated up to 120 °C in vacuo for 3 h to remove adsorbed water. Then the silica was cooled down and redispersed in dry toluene (50 mL). After addition of the respective silane (1 mmol), the mixture was heated under reflux for 15 h. The MCF was recovered by filtration and washed with toluene, methanol, and water (each 100 mL).

Hydrolysis of MCF-suc to carboxylic acid modified MCF (MCF-CO₂H)

3-(triethoxysilyl)propyl succinic anhydride was hydrolyzed by addition of ethanol (20 mL) and water (2 mL) after heating under reflux for 1 h. The MCF-CO₂H was recovered by filtration.

Modification of MCF-NH₂ with glutardialdehyde (MCF-glu)

For the covalent immobilization, MCF-NH₂ was modified further with glutardialdehyde, 200 mg, 200 μL, 2.00 mmol) in distilled water (20 mL) by mixing 15 min at RT. The solid (MCF-glu) was recovered by centrifugation.

4.3.2.3 Synthesis and oxidation of hierarchical porous carbons**Synthesis of PMMA particles**

The PMMA particles (diameter 400 nm) were synthesized according to the literature.^[291] The PMMA monoliths were prepared by evaporation of the solvent in a petri dish over 2 weeks.

Synthesis of hierarchical porous carbons

Two precursor solutions were prepared: For the phenolic resin, phenol (3.1 g, 32.9 mmol) was melted at 40 °C. After the addition of sodium hydroxide (0.66 g, 20 wt.%), formaldehyde (5.4 g, 66.6 mmol) was added dropwise and the solution was heated up to 75 °C for 1 h. The mixture was allowed to cool to RT and neutralized with 0.6 M HCl. After evaporation of water in vacuo 50 wt.% ethanol was added. The silica precursor solution was prepared by mixing tetraethyl orthosilicate (5.0 g, 24.0 mmol)

and 0.2 M HCl (2.5 g). After combining both precursor solutions, F127 (6.3 g, 0.5 mmol) was added and the mixture was stirred until a clear solution was obtained (4 h). The PMMA monoliths were half-immersed in the precursor mixture and the immersion level was kept constant by addition of precursor. After 15 h the excess solution was wiped off the monoliths and the solvents were removed in vacuo. The monolith pieces were kept at 100 °C for thermopolymerization in a closed bottle for 24 h. The carbonization was performed at 400 °C for 3 h (1 K min⁻¹) and 900 °C for 2 h (2 K min⁻¹). The silica was removed by HF treatment for 24 h with 25 % HF. For detailed experimental procedures see ^[292].

Oxidation of hierarchical porous carbons

Oxidation of the porous carbon was achieved by immersion of the material (125 mg) in an aqueous solution of ammonium peroxodisulfate (1.7 g, 0.75 mol in 10 mL 2 M H₂SO₄) for 8 h at 40 °C. After vigorous washing with water and ethanol, the sample (Macro-CO₂H) was dried at 60 °C for 12 h.

4.3.3 IMMOBILIZATION OF G6PDH ONTO NANOPOROUS SUPPORTS

Each MCF sample (45 mg) was dispersed in HEPES buffer (4 mL, 200 mM, pH 7.4) and G6PDH solution (2.6 mL, 1.5 mg mL⁻¹ in HEPES) was added. The mixture was shaken for 24 h at 300 rpm and 25 °C. 60 mL samples were withdrawn at different times to monitor the adsorption process. The solution was separated from the silica by centrifugation (3x) and redispersed in HEPES buffer. The quantification of protein was determined in the supernatant with the BCA method.

4.3.4 BIOCHEMICAL CHARACTERIZATION

Leaching experiments

For leaching experiments, an aliquot of 100 µL of each sample was withdrawn and shaken vigorously for 24 h at 25 °C or 37 °C. The solids were recovered by centrifugation and the protein concentration in the supernatants was determined by BCA.

Activity assay

The activity of G6PDH was determined by using a variation of the protein assay (Sigma–Aldrich). The temperature was set to 37 °C and the buffer was replaced by HEPES (200 mmol, pH 7.4). 10 µL of immobilized protein (diluted to give an absorbance in a proper range (< 1.0)) was added to 2.9 mL of a mixture of NADP⁺ and G6P solution and HEPES buffer (90 µL) to start the reaction. The absorption was monitored for 5 min under continuous stirring. The activity was calculated according to Equation A1 (9.1.1).

Cycle stability

The cycle stability was accessed by taking 50 mL aliquots of the dispersions. After separation the solid was dispersed in 1.5 mL of the NADPH solution used for the activity assay and shaken for 5 min at 37 °C, subsequently separated and the absorption of the supernatant was measured to obtain the activity. Then the solid was immersed for the next cycle. To verify the leaching experiment, the activity was monitored for 1 min. No further increase in activity indicated no leaching.

Thermal and storage stability

Thermal and storage stability were determined by monitoring the activity over several days. After a defined time the activity assay was performed. Thermal stability tests were performed by incubation at 37 °C, storage stability at 4 °C. All measurements have been performed at least in triplicate.

Adsorption of NADP⁺ by MCF supports

The adsorption of NADP⁺ by MCFs was indirectly determined. 1 mg MCF was suspended in 1 mL NADP⁺ solution (500 µM in water). After incubation for 10 min the solid was removed by syringe filtration. 500 µL of the supernatant were transferred into a cuvette and 100 µL G6P solution (100 mM in water) was added. Afterwards 100 µL G6PDH solution (350 µg mL⁻¹) was added and the change in absorbance due to NADPH formation (wavelength scan 280-400 nm) was detected.

A calibration curve (Figure 4.67) for different NADP⁺ concentrations was measured according to the procedure described before.

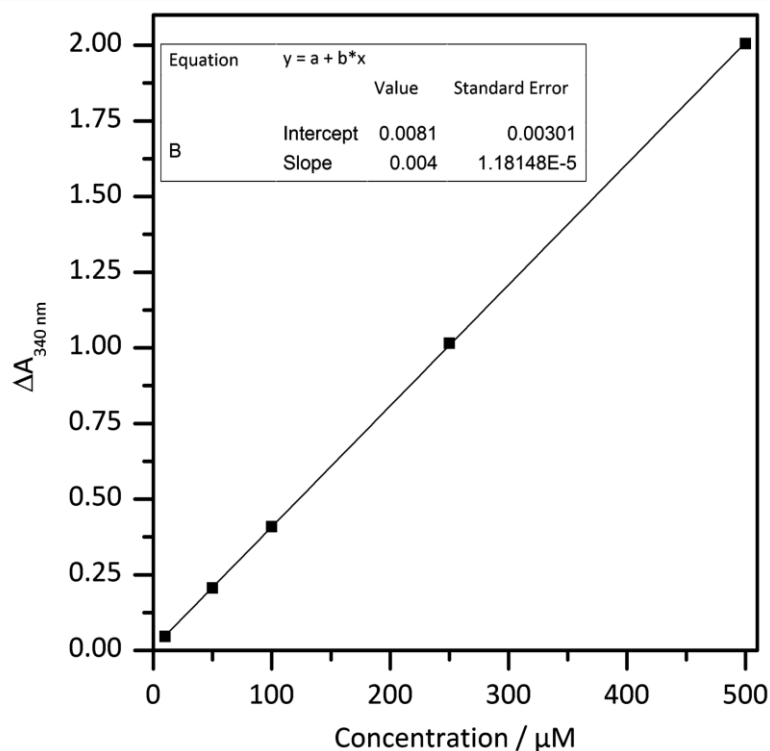


Figure 4.67: Calibration curve for various NADP^+ concentrations. Therefore NADP^+ was converted by G6PDH with addition of G6P to measure the adsorption of NADPH.

Maximum uptake capacity

The maximum uptake capacity of $\text{MCF-C}_3\text{-NH}_2$ was determined by the following procedure with a G6PDH stock solution (3.35 mg mL^{-1} in HEPES): 5 mg of silica was redispersed in G6PDH solutions with different concentrations (Table 4.28). The dispersions were shaken at 350 rpm for 24 h at $25 \text{ }^\circ\text{C}$ and then separated by centrifugation and washed with HEPES. Activity assays and concentration determination of all samples were carried out as stated above.

Table 4.28: Dilution series for the determination of the maximum uptake capacity.

HEPES buffer / μL	0	250	750	500	1.35	500
Stock / μL	1000	750	750	500	150	500
c[G6PDH] / mg mL^{-1}	3.35	2.51	1.66	0.838	0.335	0.168

Michaelis-Menten kinetics

Michaelis-Menten kinetics have been applied for G6PDH immobilized onto MCF-NH₂ as well as non-immobilized G6PDH at 37 or 25 °C. Depending on the application either a phosphate buffer (50 mM, pH 7.5) or a HEPES buffer (200 mM, pH 7.4) was used for the kinetic experiments. Inhibition with DMSO and variation of NADP⁺ and G6P has been performed. In Table 4.29 the pipette procedure with the corresponding substrate and inhibitor concentrations are shown. In all cases the initial reaction velocity was monitored by the increase of NADPH concentration during the reaction. All measurements have been performed in triplicate.

Table 4.29: Pipette scheme for Michaelis-Menten kinetics with varied G6P concentration.

Buffer / μL	2690	2490	2290	2090	1890	1690	1490	1290	1090
NADP⁺ / μL	100	100	100	100	100	100	100	100	100
G6P / μL	200	400	600	800	1000	1200	1400	1600	1800
G6PDH / μL	10	10	10	10	10	10	10	10	10
c[G6P] / mM	0.34	0.69	1.0	1.4	1.7	2.1	2.4	2.7	3.1
NADP ⁺ : 23.4 mM; G6P: 5 mM									

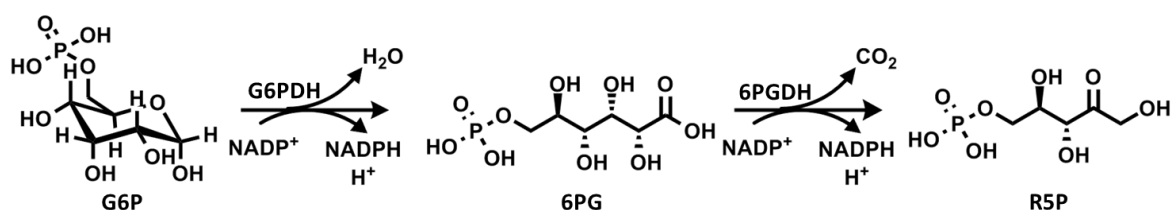
Table 4.30: Pipette scheme for Michaelis-Menten kinetics with varied NADP⁺ concentration.

Buffer / μL	2085	2080	2065	2040	1990	1940	1890	1690
Water / μL	300	300	300	300	300	300	300	300
NADP⁺ / μL	5	10	25	50	100	150	200	400
G6P / μL	600	600	600	600	600	600	600	600
G6PDH / μL	10	10	10	10	10	10	10	10
c[NADP⁺] / mM	0.02	0.04	0.1	0.2	0.4	0.6	0.8	1.6
NADP ⁺ : 12 mM; G6P: 10 mM								

Table 4.31: Pipette scheme for Michaelis-Menten kinetics with DMSO as an inhibitor and varied G6P concentration.

HEPES / μL	2530	2455	2362	2128	1750	1390	790	190
Water / μL	X	X	X	X	X	X	X	X
DMSO / μL	300-X	300-X	300-X	300-X	300-X	300-X	300-X	300-X
NADP ⁺ / μL	100	100	100	100	100	100	100	100
G6P / μL	60	135	228	462	840	1200	1800	2400
G6PDH / μL	10	10	10	10	10	10	10	10
c[G6P] / mM	0.1	0.225	0.38	0.77	1.4	2.0	3.0	4.0
NADP ⁺ : 23.4 mM; G6P: 5 mM, X = 100/ 200								

Cascade reaction



A two enzyme cascade of G6PDH and 6PGDH immobilized separately on MCF-NH₂ was established in a one pot reaction. The conversion of NADP⁺ to NADPH was measured for 2 h for each single enzyme as a reference. Two different approaches have been used for the cascade reaction:

- 1) Both enzymes have been simultaneously added to the reaction mixture.
- 2) G6PDH was used to convert G6P to 6PG until a plateau in NADPH absorption indicated complete conversion. Then 6PGDH was added.

The substrate solution for G6PDH contained 0.13 mM G6P, 0.5 mM NADP⁺ in phosphate buffer (50 mM, pH 7.5). After the addition of 30 μL of each immobilized enzyme solution (approach 1 or 2) to 3 mL substrate solution, the liberation of NADPH at 25 °C was detected at 340 nm. The substrate solution was taken as the blank.

4.4 SECTION SUMMARY AND CONCLUSION

Glucose-6-phosphate dehydrogenase from *Leuconstoc mesenteroides* was immobilized onto a variety of nanoporous materials. In order to achieve a biocatalyst with enhanced performance, in terms of uptake, activity and most important stability, the respective supports were tailored according to the properties of the enzyme. A comprehensive overview of the most important material parameters and biochemical results are shown in Table 4.32.

Table 4.32: Comprehensive summary of the main results of the immobilization of G6PDH onto nanoporous materials.

Sample	$S_{BET} / m^2 g^{-1}$	D_p / nm	$V_p / cm^3 g^{-1}$	$\rho_F^a / mmol g^{-1}$	pl	χ	Uptake / %	Activity / %	Stability ^b / %
Macro-C	518	300-350 ^c	1.5 ^c	n.d.	n.d.	n.d.	3	n.d. ^e	n.d.
Macro-CO ₂ H	388	n.d.	n.d.	n.d.	n.d.	n.d.	30	24 ^e	74
MCF	356	23/35 ^d	2.20	n.d.	2.9	n.d.	12	29 ^e	97
MCF-CO ₂ H	305	20/31	1.81	0.75	<2	n.d.	7	31 ^e	98
MCF-glu	274	22/30	1.64	1.2	7.0	n.d.	90	57 ^e	89
MCF-C ₃ -NH ₂	277	21/30	1.74	1.2	9.3	0.30	98	90 ^e /100 ^f	100
MCF-C ₇ -NH ₂	294	19/29	1.71	1.1	9.7	0.10	97	11 ^f	56
MCF-C ₁₁ -NH ₂	266	19/28	1.61	1.0	10.2	0.05	13	12 ^f	43
MCF-sNH ₂	238	18/28	1.57	1.7	9.5	n.d.	94	99 ^f	100
MCF-tNH ₂	284	20/26	1.82	1.6	9.5	n.d.	92	91 ^f	100
s-PMO	306	4-24 (14)	0.784	n.d.	10.0	0.59	81	18 ^f	58
t-PMO	517	8-14 (11)	0.926	n.d.	9.4	0.84	46	20 ^f	64
PMO-aerogel	854	12-32 (18)	>7.83b	n.d.	9.3	n.d.	94	16 ^f	45

a: Functionalization density determined for grafted MCF supports; b: 14 d, 4 °C (G6PDH: 48 %) c: Determined by mercury intrusion;

d: Pore size determined by BJH from the des/ads; e: respective to free G6PDH; f: respective to G6PDH immobilized on MCF-C₃-NH₂

n.d.: not determined/determinable

For all materials the adsorption process was monitored to gain further insight into the forces interacting between the enzyme and the support. The forces present between enzyme and material surface as well as the partitioning effect inside the pores turned out as the main influencing factors during the experiments. Materials with a variety of

surface and porosity effects have been investigated as possible supports for the immobilization of G6PDH: Hydrophobic carbons in their oxidized and non-oxidized form, periodic mesoporous organosilicas (PMOs) with different pore sizes and amine-bridges in their pore walls and most intensively investigated mesoporous siliceous foams (MCFs). The porosity of the MCF supports was roughly the same whereas the different surface characteristics (hydrophobicity and charge) were evaluated.

Besides an intensive investigation of the materials increased attention was paid to the surface and size of the enzyme. From the crystal structure the hydrodynamic diameter (> 13 nm) of the enzyme was determined as well as the nature of the surface of G6PDH which is essential for the interaction with the support. The surface of G6PDH is mainly covered with hydrophilic amino acids and is thus referred to as a hydrophilic enzyme. The high affinity of the enzyme towards the aqueous environment is partly responsible for the large hydrophilic diameter of the enzyme. Additionally, the surface of the enzyme is covered with more amino acids that are negatively charged (Asp, Glu) at neutral pH. Since all immobilization experiments have been performed at pH 7.4 the enzyme exhibited a negative net charge during the immobilization. This information derived from the crystal structure of G6PDH was used to explain the behavior of the enzyme in contact with the solid surface during and after the immobilization.

In the beginning of this chapter materials with a wide range of surface and porosity parameters have been evaluated as possible supports. The wide range of support features were scanned to evaluate which of them was beneficial for the immobilization and performance of the immobilized enzyme. Hierarchical porous carbons were synthesized with PMMA spheres as a template for the macropores and Pluronic F127 as a structure-directing agent for the mesopore formation. After the removal of the templates and a carbonization process a hierarchical carbon was obtained with macropores for the immobilization of G6PDH whereas the mesopores, too small for the enzyme, could act as diffusion paths for substrate and cofactor. Since the hierarchical carbons lacked sufficient hydrophilicity their surface was treated with ammonium peroxodisulfate as oxidizing agents. Due to the oxidation of the carbon surface and thus a creation of oxygen-containing groups the affinity towards water was increased proven by water vapor sorption.

Although, oxidation leads to a hydrophilization of the hierarchical carbons it has to be still considered as a hydrophobic support. Therefore, mesoporous silicas were chosen as a more hydrophilic counterpart to the carbon supports. At first the synthesis parameters were varied to yield a MCF with sufficiently large pores to accommodate G6PDH. Since the pore network of MCF consist of an assembly of spherical pores connected by smaller pore entrances, the focus was laid on the window size of the material. The addition of NH_4F led to sufficiently large pore windows to let G6PDH diffuse into the spherical pores of the respective MCF support. A variety of surface modifications by postsynthetic grafting with different organosilanes was performed in order to enlarge the spectrum of enzyme-support interactions. Pure MCF, MCF modified with carboxylic acid groups (MCF- CO_2H), amine-modified MCF- $\text{C}_3\text{-NH}_2$ and glutardialdehyde-modified MCF (MCF-glu) were used for immobilization of G6PDH (Figure 4.68). Most materials, except MCF-glu, were used for adsorptive immobilization. MCF-glu was used for undirected covalent immobilization by Schiff'base reaction between support aldehyde groups and lysine-residues on the surface of G6PDH.

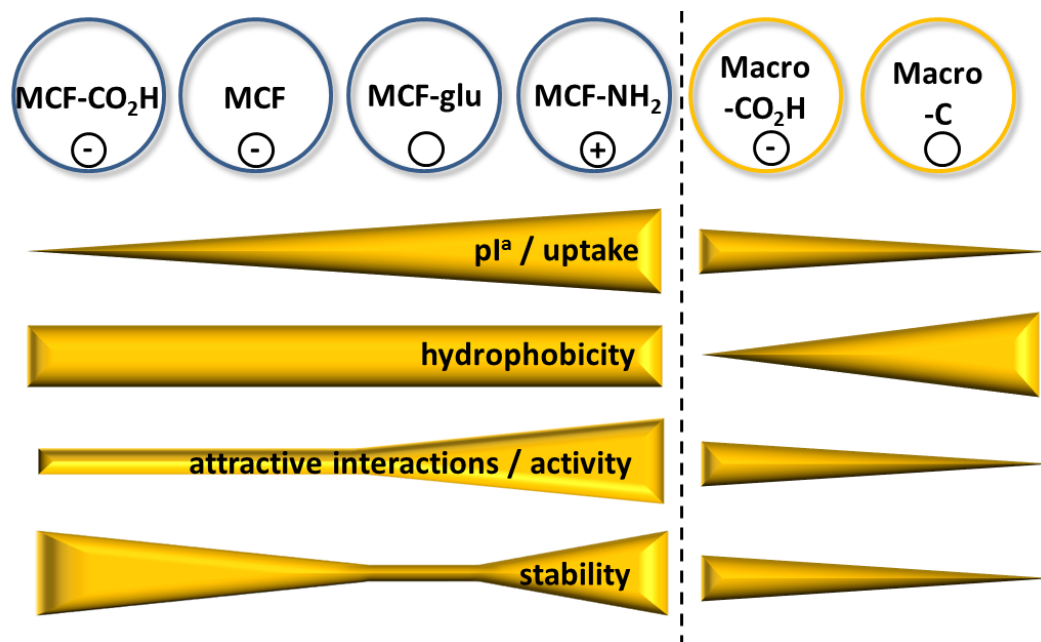


Figure 4.68: Trends observed for nanoporous materials and their behavior during the immobilization of G6PDH and their biocatalytic performance after the immobilization. (a) The isoelectric point could not be determined for carbon samples.

The uptake of enzyme from solution by the nanoporous supports was monitored in order to provide information about the affinity of the respective support towards the enzyme. Differences existed not only in the amount of enzyme taken up but also in the velocity of the uptake. Generally, a plateau in the uptake kinetics was reached very fast (< 1 h) but the uptake in amine-modified MCF was even finished after 15 min. leading to a complete uptake of the protein. This was a first hint that the amine groups led to favorable strong interactions between enzyme and support. In contrast the uptake of MCF, MCF-CO₂H and the macroporous carbons was very low. Only the covalent method (MCF-glu) approached the high uptake of MCF-C₃-NH₂. Zeta potential titrations of the MCF supports offered a reasonable explanation for this behavior. The isoelectric point of amine-functionalized MCF was the only material exhibiting a positive net charge during the immobilization whereas MCF and MCF-CO₂H were negatively charged. Thus a repulsion with the negatively charge G6PDH was obtained whereas the enzyme was attracted by the positively charged surface of MCF-C₃-NH₂. The surface of MCF-glu was almost neutral so that the creation of the covalent bond was assigned as driving force for the adsorption. The low uptake of the carbons was mainly due to the hydrophobic behavior of the material and the large pores.

The charge also strongly influenced the activity and the stability of the enzyme. The strong electrostatic attraction between the charged amine groups on the surface of MCF and the negatively charged carboxylic acid groups significantly enhanced the thermal as well as the storage stability of the enzyme. G6PDH immobilized onto MCF-C₃-NH₂ retains about 90 % of the activity whereas all other biocatalysts showed a significant drop of their relative activity compared to the free enzyme. The loss of the activity is mainly attributed to partitioning inside the pores. Partitioning is an effect that arises in the vicinity of surfaces where different conditions are developed than in solution. Inside the amine-modified pores for example a basic environment is created. Since G6PDH is more active in a basic solution this is the main factor for the activity loss of G6PDH immobilized onto negatively charged materials. Sometimes a loss of immobilized enzyme activity is caused by the orientation of the enzyme towards the support and a resulting diffusion limitation. A prediction of the enzyme orientation inside the pores according to specific amino acid areas on the surface was not possible due to a nearly homogenous distribution of the residues. Nonetheless, a maximization of contact area

was believed to occur to maximize attractive electrostatic interactions whereas a minimal contact area between enzyme surface and wall was assumed. But even in both scenarios no blocking of the active site was present.

Since all results underlined the positive influence of the strong electrostatic attraction of the charged amine surface of MCF-C₃-NH₂ and the enzyme the influence of the amine moieties was investigated in detail (Figure 4.69). Therefore amine-grafted MCFs with different carbon chain length (C3, C7, C11) were investigated. Not only the increased spacer length but also the increased hydrophobic character was assumed to have an influence on adsorption, activity and stability of G6PDH. In general, a longer spacer between wall and enzyme is generally considered as beneficial due to less constriction of the enzyme. In contrast, here it was proven that the effect of the spacer length had no positive effect on the immobilized enzyme. The increased hydrophobicity of the long carbon chain of MCF-C₁₁-NH₂ led to a lower uptake, activity as well as stability. Although, the surface is still covered with basic amine groups the attractive electrostatic interactions became less important with increasing hydrophobicity proven by water vapor sorption. The medium chain length of MCF-C₇-NH₂ however led to an almost complete uptake of G6PDH but low activity and stability of the enzyme due to less stabilizing intermolecular forces.

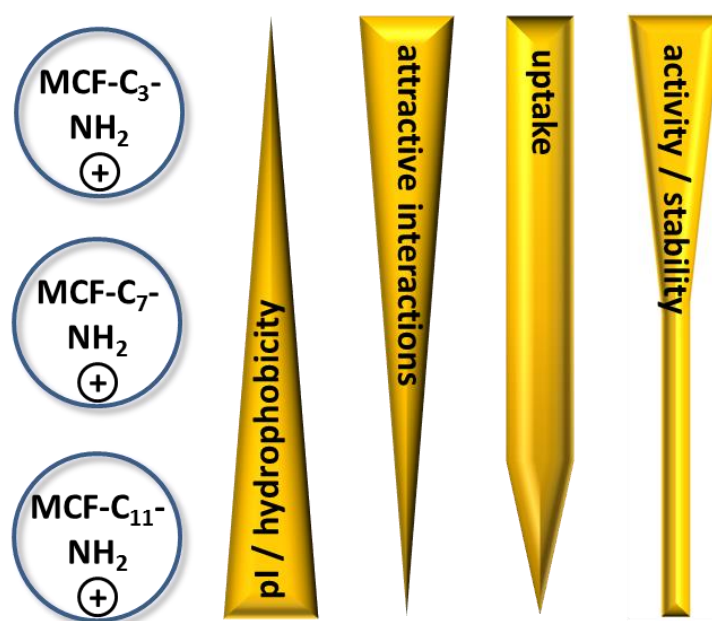


Figure 4.69: Trends observed for MCF supports with varied chain length and their behavior during the immobilization of G6PDH and their biocatalytic performance after the immobilization.

Since the dispersion of the materials in buffer became difficult with increasing chain length a complete wetting of the pore volume with buffer and thus enzyme was presumably not achieved. To diminish or reduce this influence parameter a more hydrophobic solvent, DMSO, was added to the experiments until the silica was dispersed in the buffer. All materials reached an almost complete uptake of the enzyme but the activity was drastically decreased. The addition of DMSO and thus the less polar solvent slowed down the hydrolysis of the lactone produced by G6PDH and thus an increase of the back reaction slowed down the reaction.

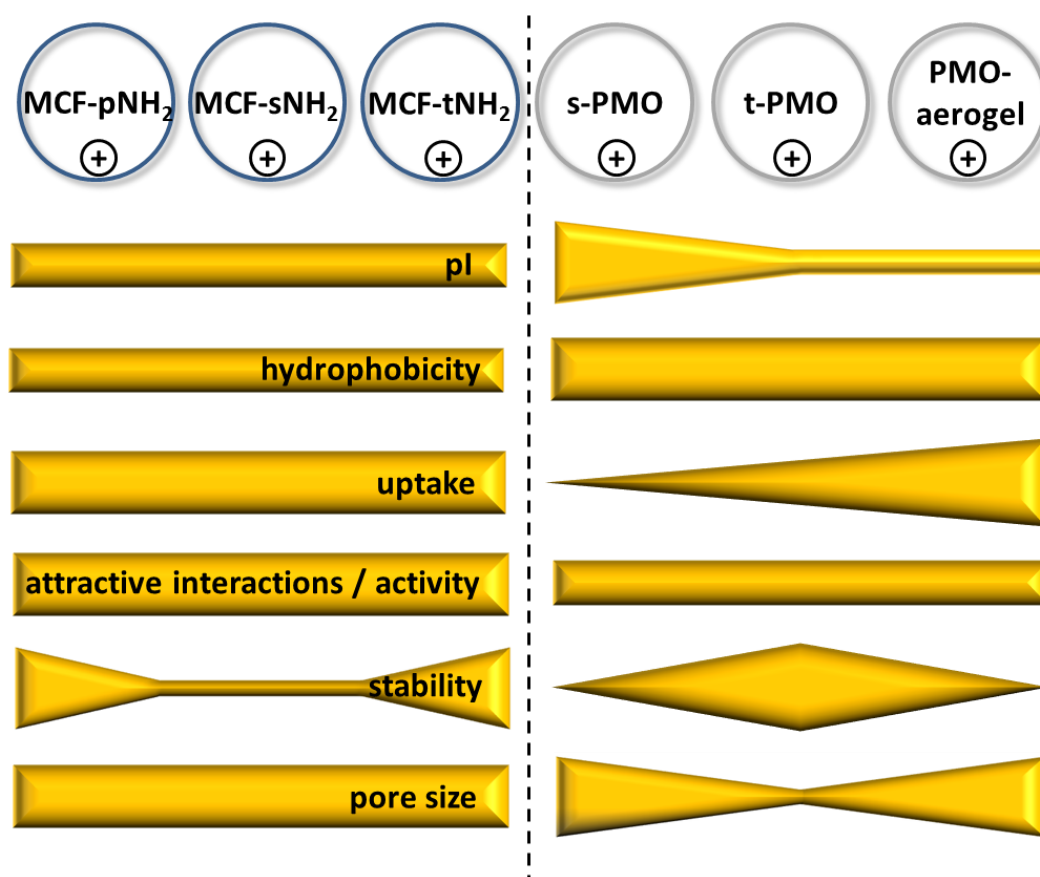


Figure 4.70: Trends observed for amine-modified MCF and PMO supports and their behavior during the immobilization of G6PDH and their biocatalytic performance after the immobilization.

Since an elongation of the spacer length did not improve the performance of the biocatalyst, other amine-modified materials have been synthesized in order to implement amines with other properties. In PMOs synthesized with secondary and tertiary amine-bridged precursors and MCF grafted with short-chain primary, secondary

and tertiary amines the site of the charged amine group modification was investigated (Figure 4.70). PMOs implement their organic functionality in the walls of the material and not extended into the pore like grafted mesoporous silicas. The high content of organics inside the network of PMOs, however, leads to a distinct hydrophobicity of the materials. The experiments with PMO and MCF supports with different amine moieties revealed no effect of the type of the amine. The MCF supports showed all similar uptake, activity and stability. The behavior of the PMOs towards the enzyme, however, was significantly changed on the respective materials. The uptake and stability of the materials was mainly influenced by the respective pore size of the material. The highest uptake was obtained for the aerogel-type PMO due to the largest pores size whereas the small pores of t-PMO led to a low uptake of G6PDH. The activity of G6PDH was similar after immobilization in PMO materials whereas the stability behaved oppositely. Large pores of PMO-aerogel led to increased leaching and thus low stability.

To conclude, MCFs with short alkyl-chain exhibited the best results in terms of uptake, activity and stability due to favorable electrostatic attraction. Negatively charged and hydrophobic materials led to a degraded performance during and after immobilization. The type of the amine (primary, secondary, tertiary) did not have an influence in the performance of the biocatalysts, neither in MCF nor in PMO supports. Thus the best performing biocatalyst MCF-C₃-NH₂ was employed in a two-enzyme sequence. Therefore, immobilized 6PGDH and G6PDH were tested in a one-pot reaction either simultaneously (1-step) or first stepwise (2-steps). The best results were obtained for the 2-step reaction that achieved a total yield of 84 %. The loss in the yield was attributed to a competitive inhibition of NADP⁺/NADPH obtained for both materials. Also for 6PGDH it was shown that the back reaction took place and minimized the reaction yield. These encouraging first results for the cascade reaction showed that it is generally possible to combine both enzymes in a one pot cascade. Further effort has to be put to optimize the reaction conditions of the cascade and implement a third enzyme for the oxidation of NADPH to NADP⁺ to close the cycle of the reaction.

5 ASSEMBLY OF AN ARTIFICIAL CELLULOSOME ON MAGNETIC INORGANIC PARTICLES¹³

5.1 INTRODUCTION

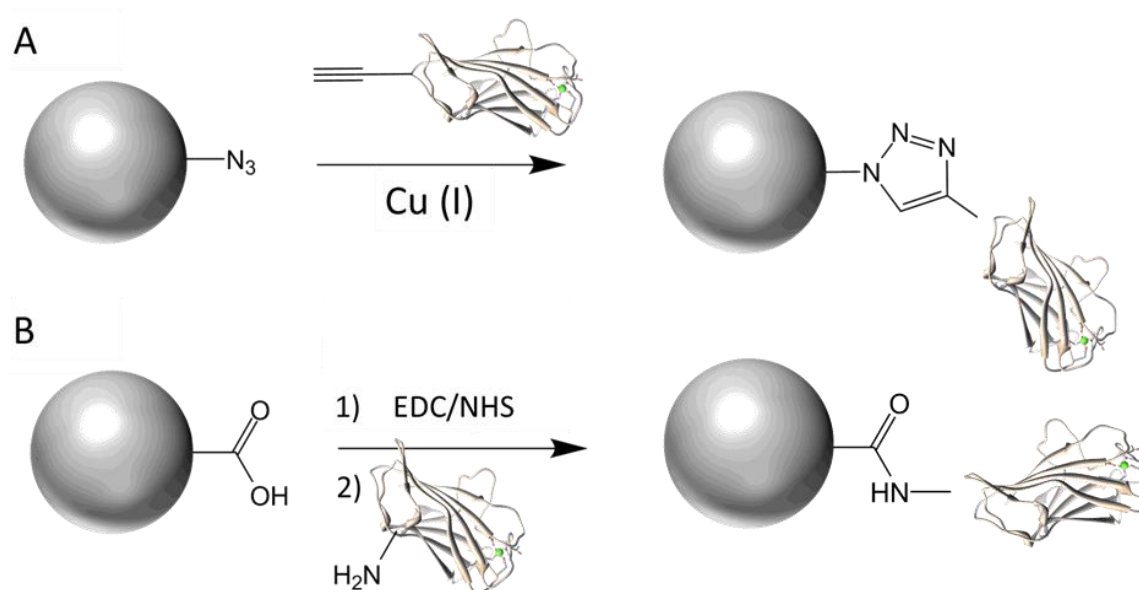
Cellulosomes are large protein complexes built on the surface of bacterial cells. These large catalytic units can easily break down plant cell walls made from cellulose, hemicellulose and lignin. Since cellulose is a highly abundant resource and does not interfere with the human crop production it is especially interesting for the use as regenerative feedstock. However, the breakdown of cellulose is difficult due to its stable crystalline structure. Cellulosomes consist of several protein units that are assembled to a highly complex system that efficiently catalyzes the degradation of cellulose. Smaller artificial cellulosomes can be assembled by combining only some of the cellulosomal parts. The most important proteins of a cellulosome complex are:

- 1) Cellulose-binding module (CBM): According to the name this part mediates the interaction between the protein and the insoluble cellulose polymer.
- 2) Cohesin and dockerin: Both units possess a very high affinity to each other and are part of the assembly to position the catalytic active units to the cellulose.
- 3) Enzymes: e.g. endo- and exoglucanases, glucohydrolases, glucosidases, cellobiohydrolases bound to dockerin units.

In this chapter an assembly of an artificial cellulosome on inorganic particles was performed as a proof of principle. The immobilization of the protein complex onto nanoparticles is currently one promising approach to guarantee easy separation and recycling of the biocatalyst from the reaction mixture as well as its stabilization. The proteins were coupled in two steps: First, CBM and cohesin (CBM-Coh) were covalently bound to the particles, prior to recombination of the cohesin-dockerin interaction in the presence of Ca^{2+} . The dockerin was already combined with the catalytic active cellulases.

¹³ This project is part of a cooperation with Prof. Dr. Andrea Rentmeister (University of Münster).

Here, two different methods have been used to covalently bind the cellulosomal proteins onto inorganic particles. The so-called click-chemistry approach, introduced by B. Sharpless in 2001, is a very popular technique, due to high yields, less contamination products and water as a possible solvent. Here, a 1,3-dipolar cycloaddition between an acetylene and an azide was used to covalently bind the CBM-Coh unit to the particle surface (Scheme 5.1A). Therefore, azide-modified particles were synthesized and reacted with alkyne-modified CBD-Coh. For simplification only the CBD unit is depicted.



Scheme 5.1: Click-chemistry approach (A) and active ester mediated covalent binding of CBM-Coh to inorganic particles.

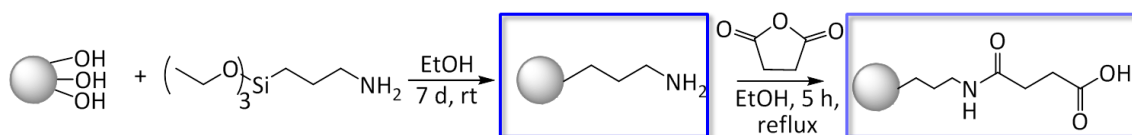
The second approach, an active ester approach (Scheme 1.1B), is a common strategy for protein conjugation. An amide bond is created between activated (N-(3-dimethylaminopropyl)-N'-ethylcarbodiimide (EDC), N-hydroxysuccinimide (NHS)) carboxylic acids and amine groups. Either the lysine groups of a protein react with the activated surface of the particles or the carboxylic acid groups of the amino acids further react with amine moieties at the particle surface.

Both approaches were performed on silica nanoparticles as a model system synthesized by a Stöber approach. In the future this concept will be transferred to synthesized magnetic $Fe_3O_4@SiO_2$ particles for an easy removal of the particles from the reaction mixture.

5.2 RESULTS AND DISCUSSION

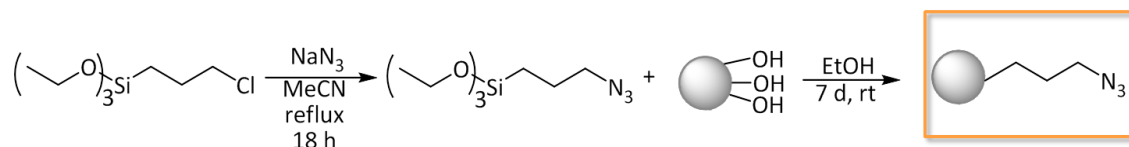
5.2.1 CHARACTERIZATION OF SILICA (STÖBER) NANOPARTICLES AS A MODEL SYSTEM

Silica nanoparticles have been prepared according to the Stöber approach with ethanol and water as solvents and ammonia as a base catalyst. In a next step the particles were postsynthetically modified with organosilanes without prior separation from the reaction mixture. Aminopropyltriethoxysilane modified particles ($\text{SiO}_2\text{-NH}_2$) were further used to obtain carboxylic acid modified particles ($\text{SiO}_2\text{-CO}_2\text{H}$) after reaction with succinic anhydride (Scheme 5.2). Both amine- and carboxylic acid modified particles can be used in the active ester approach to bind proteins.



Scheme 5.2: Amine- and carboxylic acid modification of silica nanoparticles.

Azide-functionalized silica particles ($\text{SiO}_2\text{-N}_3$) were synthesized with 3-azidopropyltriethoxysilane synthesized in a halide-exchange reaction. The direct grafting approach with azidosilane (Scheme 5.3) was preferred to a solid-state azide exchange on already halide-functionalized particles with sodium azide to minimize azide and solvent contamination during the protein coupling. Another advantage of the direct grafting is the elimination of residual halide-groups on the particle surface. The azide-functionalized particles are further used for the click-chemistry approach.



Scheme 5.3: Synthesis of 3-(azidopropyl)triethoxysilane and following preparation of azide-modified nanoparticles by grafting.

The successful functionalization and the quality of the respective silica particles was monitored with various techniques. DLS measurements (Figure 5.1, Table 5.1) are performed in order to monitor the size and polydispersity of the particles prior and after the functionalization. The DLS measurements of the functionalized particles and the respective unfunctionalized silica particles ($\text{SiO}_2\text{-1}$, $\text{SiO}_2\text{-2}$) are shown in separate colors to indicate their affiliation.

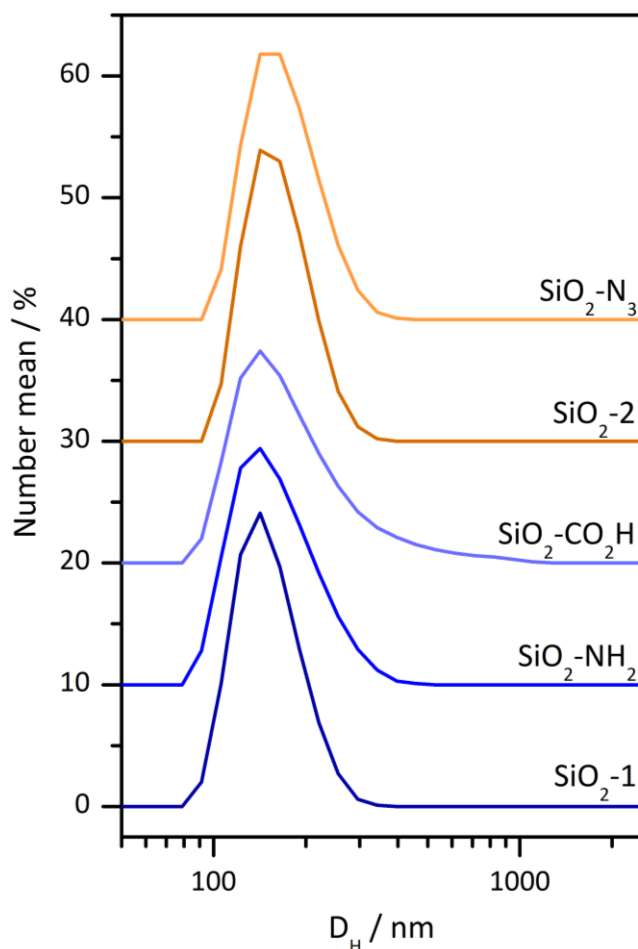


Table 5.1: Hydrodynamic diameter D_H and polydispersity index Pdl obtained by DLS.

Sample	D_H (number mean) / nm	Pdl
$\text{SiO}_2\text{-1}$	153 ± 2.2	0.015
$\text{SiO}_2\text{-NH}_2$	165 ± 4.3	0.115
$\text{SiO}_2\text{-CO}_2\text{H}$	205 ± 11	0.374
$\text{SiO}_2\text{-2}$	165 ± 1.6	0.011
$\text{SiO}_2\text{-N}_3$	171 ± 3.5	0.074

Figure 5.1: DLS measurements for silica nanoparticles. With functionalization a slightly increasing particle diameter and a broadening of the respective peaks is observed.

All particles show a monomodal size distribution. After the functionalization a broadening and a shift of the peaks to higher diameters is observed. However, the changes in the mean particle diameter are very small since the organic residues are very short (C3 carbon chain). The change in the particle diameter is also attributed to a different behavior of the particle in the solvent. Only after the carboxylic acid

modification a significant change (from 165 to 205 nm) in the particle size is observed. Prior to the modification, the particles are monodisperse whereas the peak broadening of the peak in the DLS already indicates an increase in the PDI. The SEM image (Figure 5.2) shows that spherical particles have been synthesized with a narrow particle size distribution.

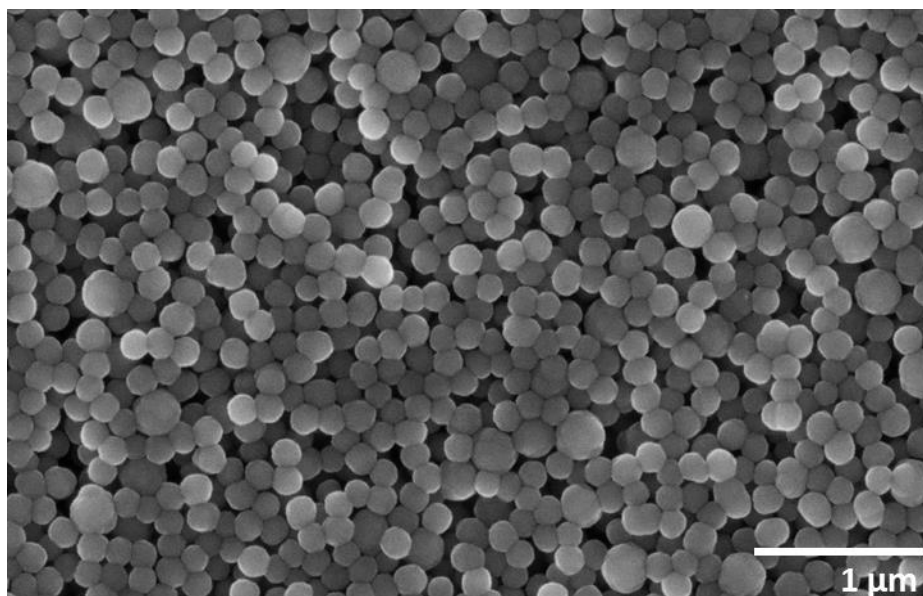


Figure 5.2: SEM image of silica nanoparticles.

Besides the morphology and the size of the particles the surface modification also affects the zeta potential of the particle surface and thus their acid-base behavior and the stability in water. The zeta potential was monitored during acid-base titration to obtain the isoelectric point of the materials (Figure 5.3, Table 5.2).

Table 5.2: Isoelectric points of silica nanoparticles.

Sample	pI
SiO ₂	3.4
SiO ₂ -NH ₂	7.9
SiO ₂ -CO ₂ H	3.8
SiO ₂ -N ₃	5.1

The isoelectric points revealed that carboxylic acid modified and unfunctionalized silica particles are mostly negatively charged whereas SiO₂-NH₂ is a basic material and

possesses a neutral net charge at pH 7.9. Since the corresponding acid to an azide is hydrazoic acid (pK_a 4.6), azides are basic compounds. The isoelectric point, however, is already reached at pH 5.1 indicating the presence of an acid-base equilibrium of the deprotonated silanols and the azide group.

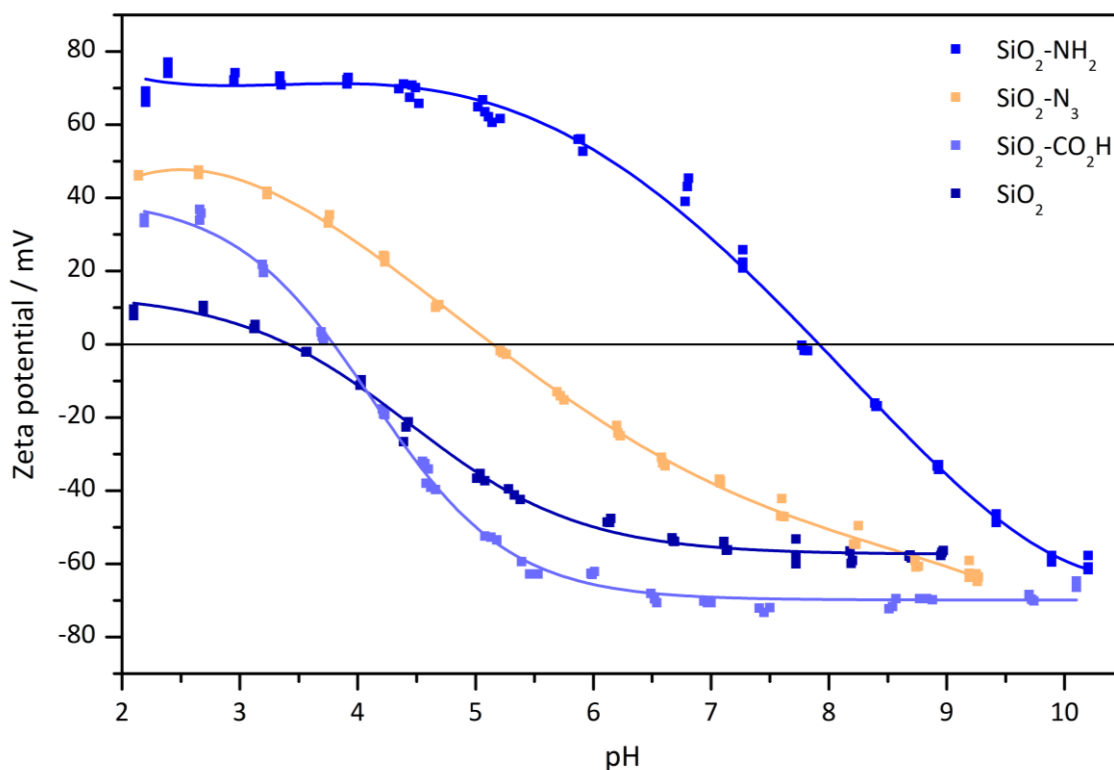


Figure 5.3: Zeta potential titrations for silica nanoparticles with solid lines as guide to the eye. At a zeta potential of zero the isoelectric point of the materials is reached.

The zeta potential is also used to interpret the stability of nanoparticles. Above a zeta potential of ± 30 mV the electrostatic repulsion between the particles is strong enough to prevent agglomeration. All particles show a high stability at wide pH ranges. Considering the use of silica nanoparticles in water at pH 7 as for many biological applications SiO₂-CO₂H has the highest zeta potential and would hence be most stable against agglomeration. SiO₂-N₃ and SiO₂ also exhibit zeta potentials higher or equal to 40 mV and are thus stable. The only positively charged material (SiO₂-NH₂) is least stable. It has to be mentioned here, that the salt of a buffer will reduce the stability of the silica particles due to compensation of the charges on the surface.

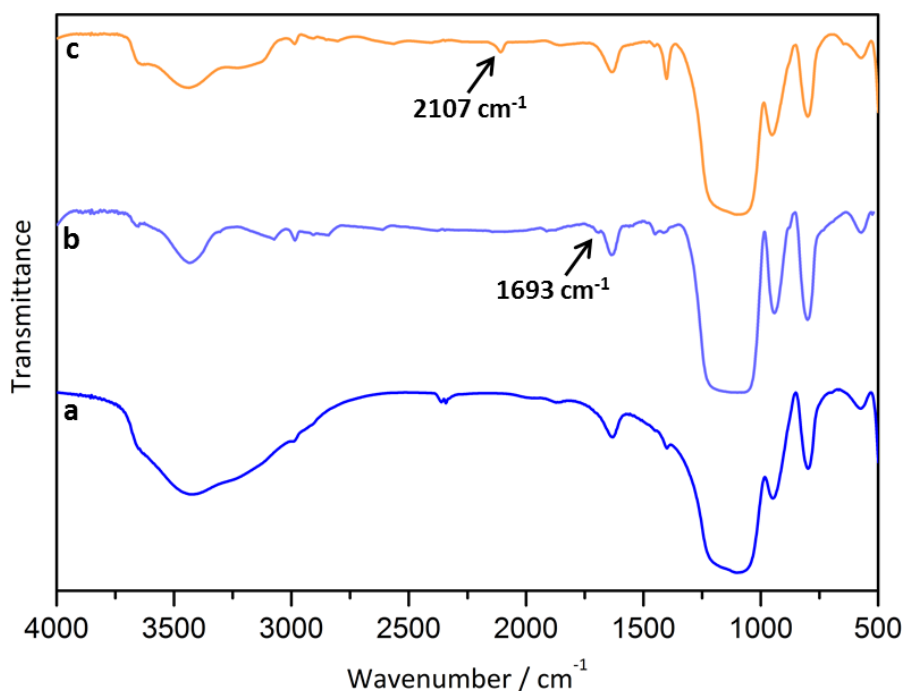


Figure 5.4: IR spectra of $\text{SiO}_2\text{-NH}_2$ (a), $\text{SiO}_2\text{-CO}_2\text{H}$ (b) and $\text{SiO}_2\text{-N}_3$ (c). The band for the azide vibration appears at 2107 cm^{-1} and the amide band of $\text{SiO}_2\text{-CO}_2\text{H}$ at 1693 cm^{-1} .

The success of the functionalization was proven by IR spectroscopy. After the conversion of the amine groups to carboxylic acid groups with succinic anhydride the presence of the amide bond was detected by a band appearing at 1693 cm^{-1} . Unfortunately, the bands of the network vibrations (see Table 4.5) mask the vibrational band for the carbonyl group of the carboxylic acid. The introduction of an azide group by postsynthetic modification of silica particles with 3-(azidopropyl)triethoxysilane was verified by the presence of the vibrational band at 2107 cm^{-1} characteristic for the azide stretching.

The presence of acidic carboxylic acid groups and basic amine groups on the particle surface was also proven by bromocresol and ninhydrin staining (see Appendix 9.1.4).

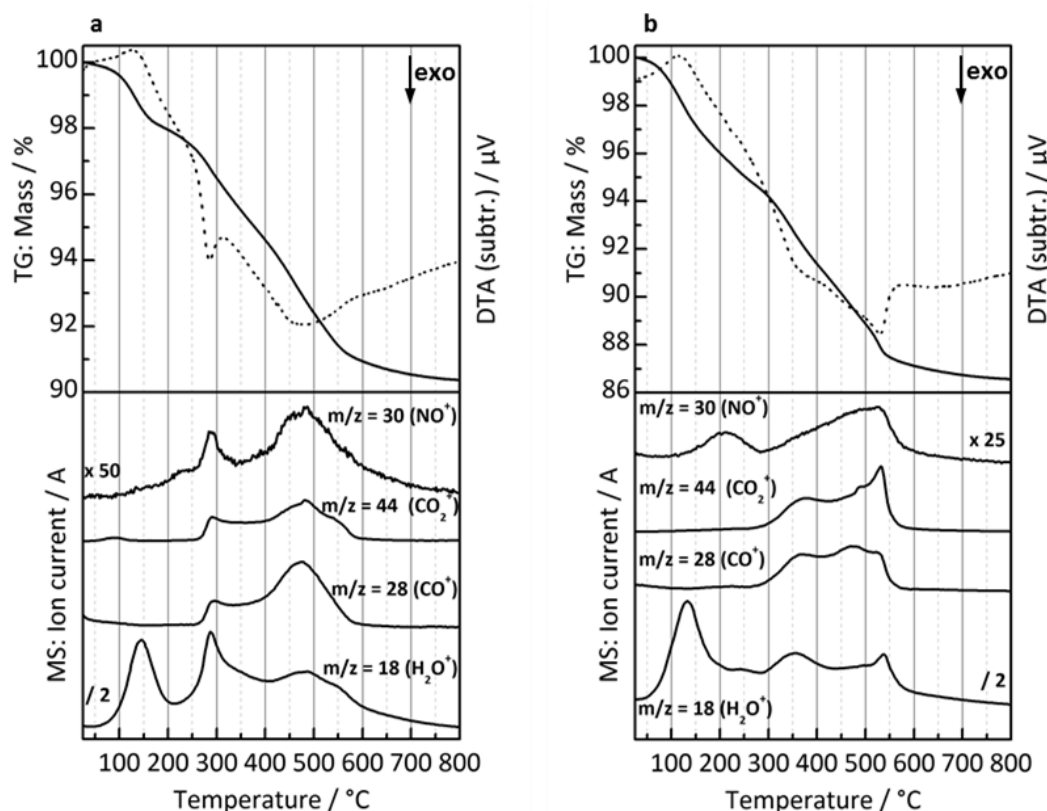


Figure 5.5: TG/DTA/MS of SiO₂-NH₂ (a) and SiO₂-CO₂H (b) performed in synthetic air. The diagram at the top shows the TG (solid line) and DTA (dotted line) curve whereas the ion currents detected by a mass spectrometer are depicted at the bottom.

The functionalization density of the silica particles was determined by TG/DTA/MS (Table 5.3, Figure 5.5) according to chapter 9.1.2 in the appendix. The combustion products, mainly CO/CO₂, NO/NO₂ and water were detected by a coupled mass spectrometer and some representative ion currents are depicted. The loss of water prior to combustion of the organic compound is due to loosely adsorbed water onto the surface of the particles. The combustion of the organic functionalization began at 200 °C for SiO₂-NH₂ and SiO₂-N₃ whereas it started at already 170 °C for SiO₂-CO₂H due to the larger organic moiety.

Table 5.3: Functionalization density and mass loss of functionalized silica particles derived by TG/DTA/MS.

Sample	Mass loss / %		$\rho_F / \text{mmol g}^{-1}$
	< 200 °C	< 600 °C	
SiO ₂ -NH ₂	2.9	7.0	1.3
SiO ₂ -CO ₂ H	3.4 ^a	9.6 (2.6) ^b	0.29
SiO ₂ -N ₃	2.6	6.3	0.77

a: mass loss up to 170 °C b: amount of succinic anhydride functionalization

The conversion of the amine-modified particles to carboxylic-acid modified particles was only achieved for 22 % (theoretical maximum: 1.3 mmol amine groups, achieved: 0.29 mmol) of the surface amines leading to residual amine groups at the surface.

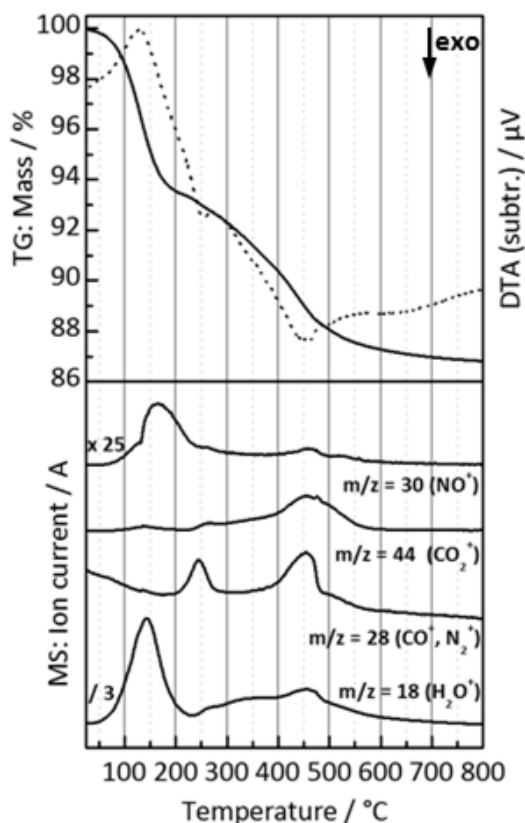


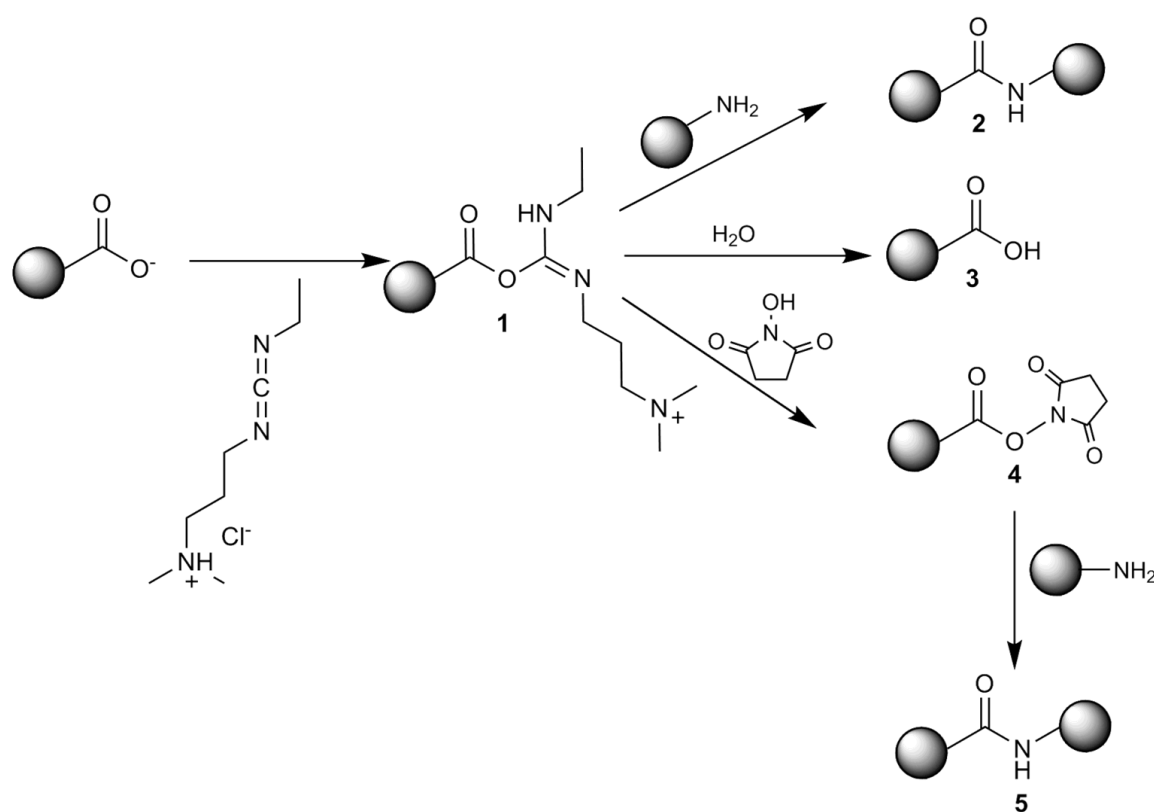
Figure 5.6: TG/DTA/MS of $\text{SiO}_2\text{-N}_3$ performed in synthetic air. The diagram at the top shows the TG (solid line) and DTA (dotted line) curve whereas the ion currents detected by a mass spectrometer are depicted at the bottom.

The thermal analysis of $\text{SiO}_2\text{-N}_3$ was not only used to calculate the functionalization density but also it proves the presence of the azide group additionally to IR spectroscopy. The mass-to-charge ratio 28 is not only characteristic for CO^+ but also for N_2^+ fragments. Usually, the ion currents for CO_2^+ and CO^+ show the same trend but here an additional peak is observed at 250 °C for the liberation of N_2 from the azide moieties.

5.2.2 ASSEMBLY OF THE CELLULOSOME ONTO SILICA NANOPARTICLES

5.2.2.1 Covalent immobilization of cohesin-CBM onto silica particles by an active ester approach

The active ester approach is a conventional method to couple biomolecules to each other, to smaller molecules or solid supports. In general solid phase conjugation of a protein to a support can be either performed with a carboxylic acid or an amine moiety on the surface of the support. The general reaction scheme is shown for an EDC/NHS mediated coupling in Scheme 5.4.



Scheme 5.4: NHS/EDC mediated bioconjugation of an amine-containing molecule to a carboxylic acid by creation of an amide bond. The activation can be either performed with EDC or a mixture of EDC and NHS or sulfo-NHS.

The carbodiimide (EDC) is generally used in its hydrochloride form due to the higher water solubility. It activates the carboxylic acid by formation of an unstable ester (1) that can be readily attacked by nucleophiles like amine-groups to yield a stable amide-bond (2). But also water acts as a nucleophile that hydrolyzes the active ester and regenerates the carboxylic acid (3). Therefore in many cases N-hydroxysuccinimide (NHS) or the

better soluble sulfo-NHS are introduced to the synthesis to yield a more stable active ester (4) that is less prone to hydrolysis but highly active towards amine-groups. Two general activation protocols exist: a 2-step and a 1-step procedure. In the 1-step procedure all coupling reagents as well as the reaction partners are mixed at once. Although this approach is more straightforward, a protein-protein conjugation or agglomeration can be observed. In a 2-step procedure the carboxylic acid support is activated prior to the addition of the coupling partner. A protein-protein conjugation is less likely in this case but a hydrolysis of the activated carboxylic acid residues can occur prior to the addition of the protein.

In this chapter the conjugation of the cohesin-CBM of a cellulosome either on carboxylic acid-modified ($\text{SiO}_2\text{-CO}_2\text{H}$) or on amine-modified ($\text{SiO}_2\text{-NH}_2$) silica particles is reported. Special attention was paid to yield a low functionalization at the interface where cohesin and dockerin will reassemble (Figure 5.7).

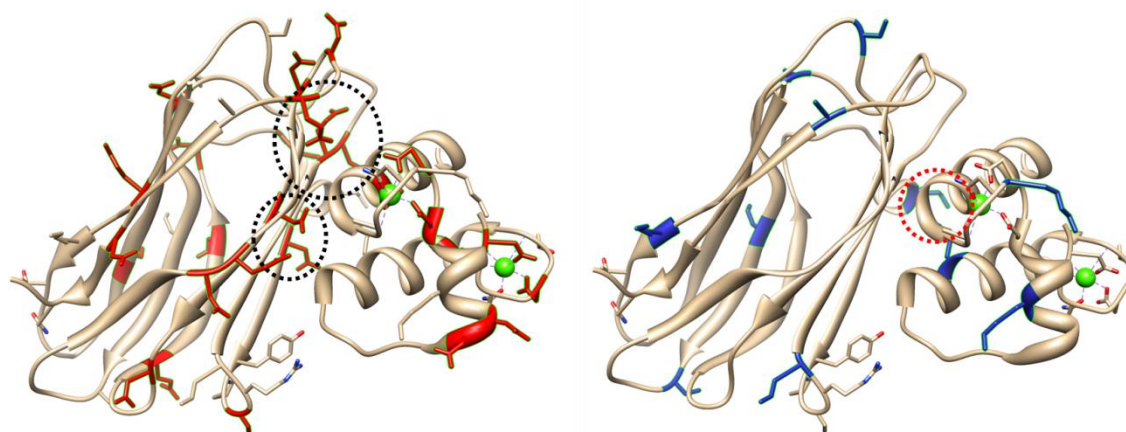


Figure 5.7: Cohesin-dockerin assembly. The amino acids that take part in the covalent binding approach should not be present at the interface of the cohesin-dockerin interaction. Thus an immobilization onto amine-modified silica-particles, which requires the carboxylic acid residues on the protein surface (left) affects the interactions of cohesin and dockerin more than the immobilization via the lysine residues (right) onto carboxylic-acid modified particles.

A covalent attachment of the cohesin to amine-modified silica particles proceeds via negatively charged amino acids (glutamate, aspartate) marked red in Figure 5.7. In this approach a disturbance of the cohesin-dockerin (coh-doc) interactions would be most likely since many amino acids of the cohesin-dockerin interface would possibly be modified. In contrast the attachment of the amine-residues (lysine, marked blue) of the

cohesin unit would be less affecting the interface of both proteins. Thus a binding of cohesin to carboxylic-acid modified particles would be preferred.

Fluorescence spectroscopy (Figure 5.8) was performed on fluorescein isothiocyanate-tagged cohesin-CBM. Although the results were not directly quantifiable the fluorescence intensity was enhanced for the coh-CBM immobilized onto $\text{SiO}_2\text{-CO}_2\text{H}$ (18363 cps) compared to $\text{SiO}_2\text{-NH}_2$ (10337 cps) about 44 %. This result indicates that the immobilization onto carboxylic acid-modified particles was more efficient.

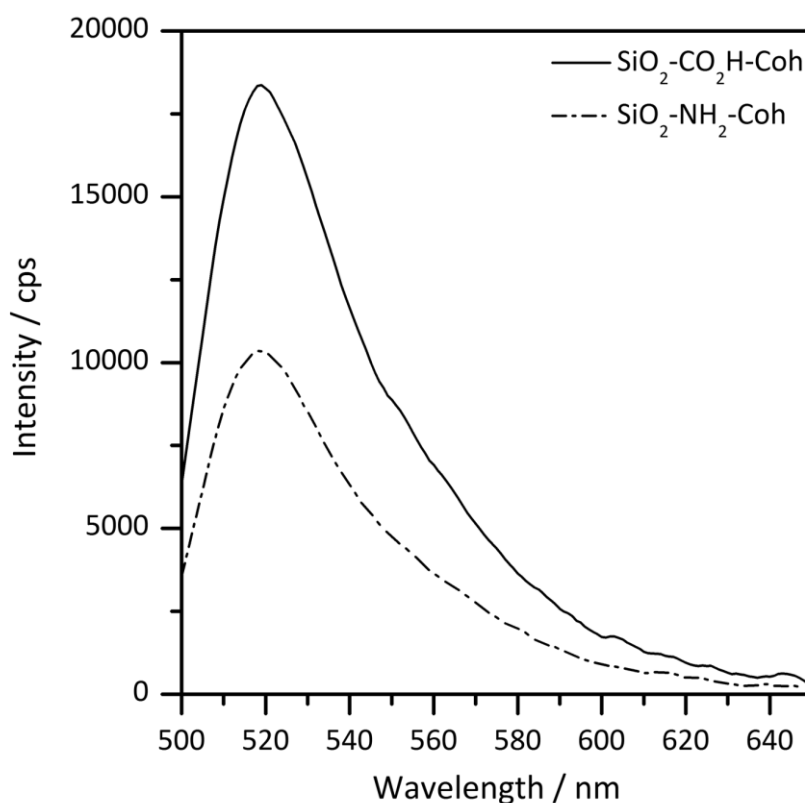


Figure 5.8: Fluorescence spectra of cohesin-CBM tagged with fluorescein isothiocyanate immobilized onto silica particles. The sample was excited at 494 nm and the emission was recorded from 500-650 nm. The curves were smoothed by 10 point adjacent averaging after subtracting the fluorescence spectra of the buffer as a blank. The maximum fluorescence emission intensity was obtained at 519 nm.

Like discussed above, a 1- or a 2-step procedure can lead to a covalent immobilization by an active ester approach. The first method that was used to covalently bind the coh-CBM unit to carboxylic acid-modified particles was a 1-step procedure with a combination of EDC-HCl and NHS. However, the detection of protein in the supernatant was not possible since NHS did strongly influence the color development of the BCA

assay.^[293,294] It was already reported, that a strong color development was observed by addition of NHS due to its reducing nature. Thus the measured concentration in the supernatant strongly exceeded the protein concentration introduced during the reaction.

To avoid the interference of NHS and the protein concentration determination a 2-step procedure was employed. In the first step the SiO₂-CO₂H particles were activated at pH 6.0 with a combination of NHS and EDC-HCl. After separation of the particles from the activation solution the particles were dispersed in a buffer at pH 7.4 prior to addition of the protein. The washing steps should ensure a removal of residual NHS whereas the buffer exchange allowed establishing the optimum pH conditions for activation and coupling reactions. No loosely attached protein was detected after the second washing step. Thus a covalent attachment of the residual protein was assumed. The protein content on the silica particles was calculated from the supernatants (580 µg mL⁻¹) and the protein content prior to the reaction (882 µg mL⁻¹). Thus 301 µg coh-CBM were attached to 19.6 mg carboxylic acid-modified silica particles, which would correspond to an amount of 15 µg (4x10⁻⁴ µmol) protein per mg silica. However, since the immobilization of the protein with an active ester approach is not site-directing, the orientation of the protein might in most cases not lead to a recombination with the dockerin-cellulase unit (doc-cel).

5.2.2.2 Covalent immobilization of cohesin-CBM onto silica particles by click-chemistry

The click-chemistry approach used here proceeds by reaction between an azide moiety on silica particles (SiO₂-N₃) and an acetylene-modified coh-CBM unit. Thus the first step is the introduction of the acetylene moiety into the protein. Therefore the lysine residues of the cohesin are chemically modified with 4-pentynoic acid (Scheme 5.5).



Scheme 5.5: 4-pentynoic acid modification of coh-CBM unit by carbodiimide activation.

Eight lysine residues (Figure 5.9) are present in the used cohesin that can be modified with 4-pentynoic acid.

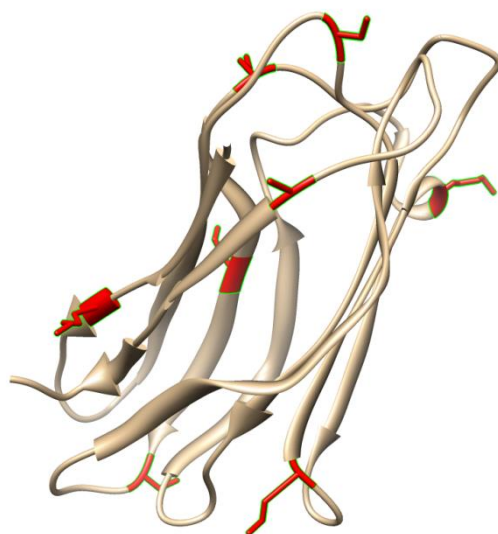


Figure 5.9: Cohesin with assigned lysine residues for modification with 4-pentynoic acid.

The protein modification was first performed according to literature.^[295] The protein was first incubated with a solution of pentynoic acid in order to allow an association of the acid groups with the lysines of the protein. In the next step the coupling reagent EDC was added and the reaction was allowed to proceed for four hours. Instead of a modification of the protein with 4-pentynoic acid a highly EDC activated protein was obtained. The m/z differences of the peaks in the respective MALDI spectrum of the protein are in the range between 151 and 157. This proves a modification with EDC ($m/z = 155$) at the carboxylic acid groups since a modification with 4-pentynoic acid would lead to a m/z difference of 80. Besides the unmodified protein ($m/z = 37721$) protein molecules with one to five activated carboxylic acid groups have been detected.

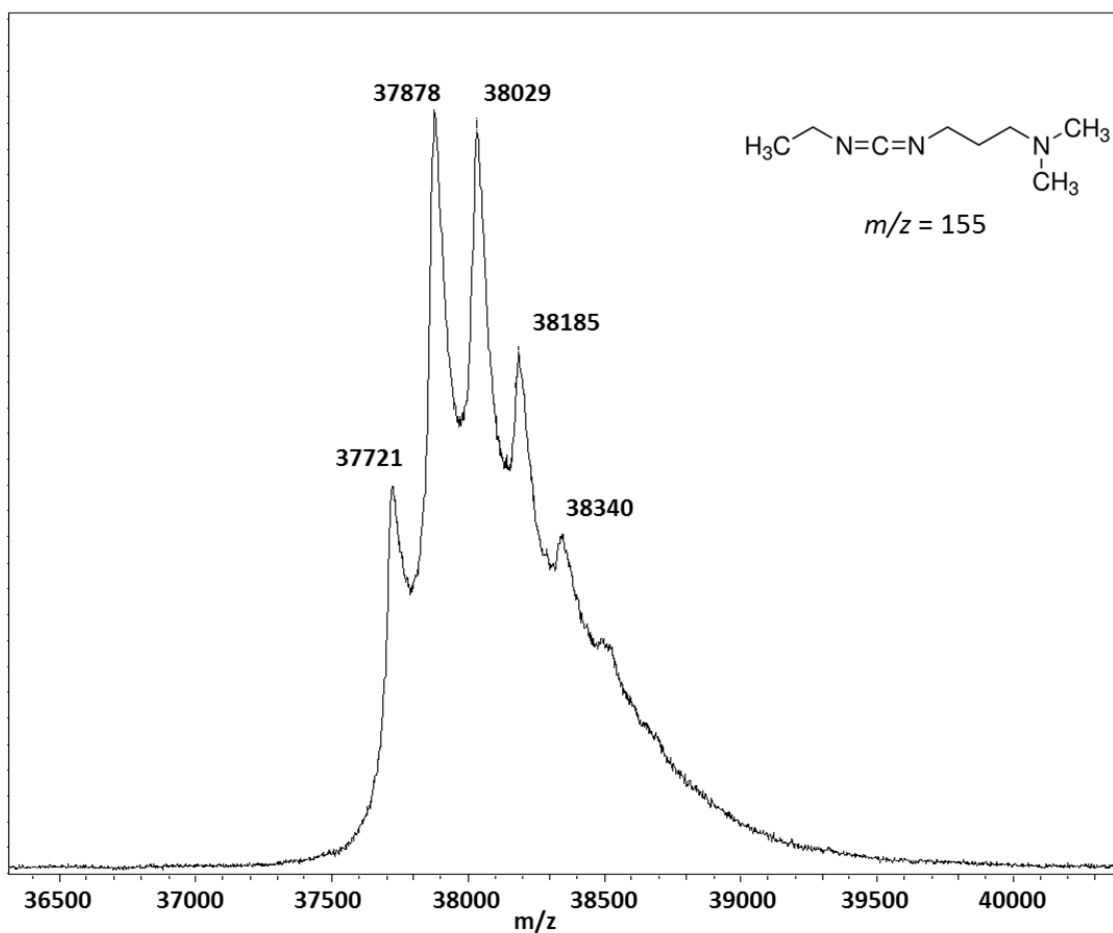


Figure 5.10: MALDI spectrum of modified coh-CBM. Instead of a modification with 4-pentynoic acid a activation of the carboxylic acid residues with EDC was observed.

Most likely the association of positively charged lysine residues with 4-pentynoic acid residues led to a shielding of the 4-pentynoic acid from the EDC activating reagent. Instead the protein was modified at the more easily accessed free glutamate and aspartate residues. Thus the next attempts tried an activation of the 4-pentynoic acid with EDC prior to the addition of the protein. To guarantee a complete reaction of the EDC an excess of the acid was used.

The comparison of the MALDI spectra of the protein prior and after the immobilization reveals a shift and a broadening of the peak. Only a shoulder indicates that unmodified protein is still left after the reaction. The m/z difference between the unmodified and the main peak of the modified protein corresponds to an EDC modification indicating that unreacted EDC was present in the reaction although an excess of the acid was used.

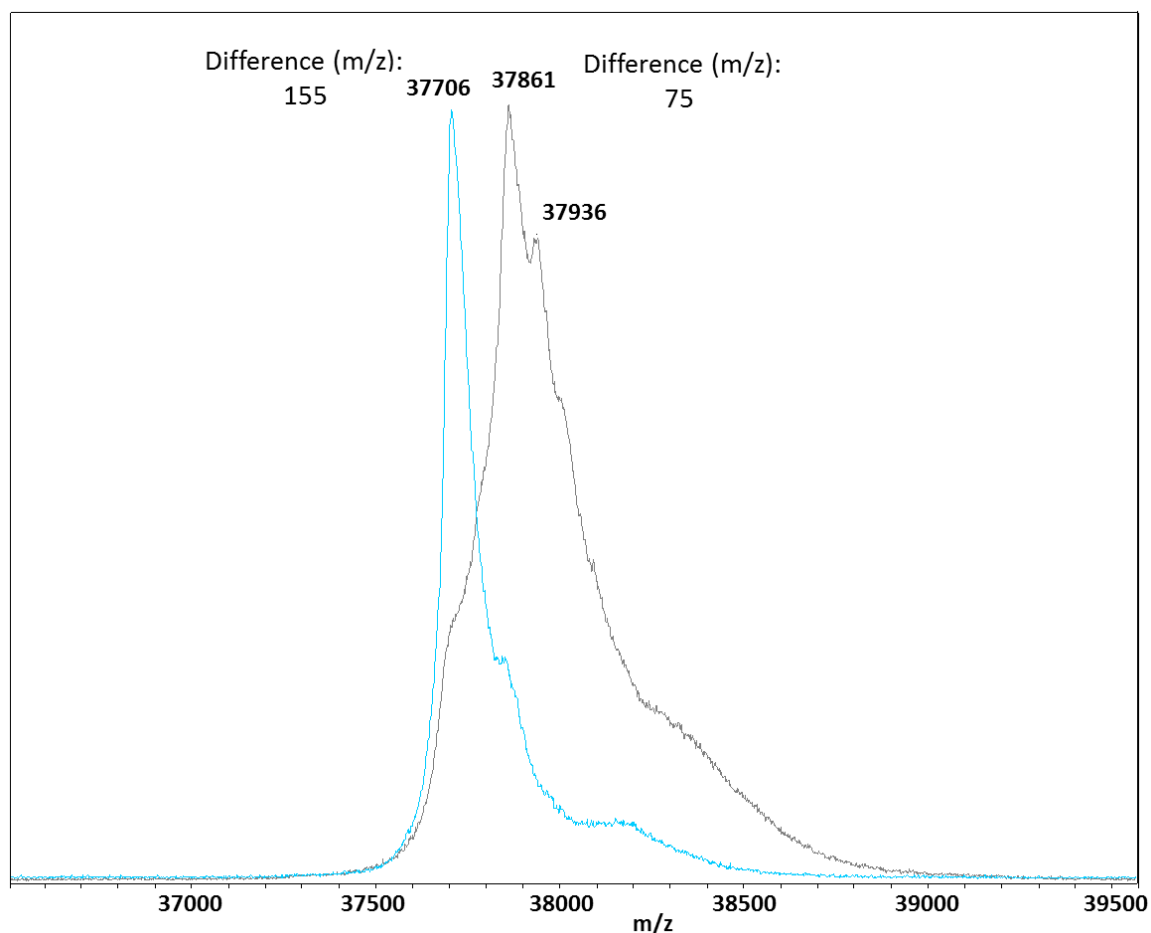


Figure 5.11: MALDI spectra for the unmodified protein (blue) and the modified protein (grey). A shift and splitting of the peak was observed.

The mass difference (m/z difference = 75) of the peak for the modified protein could possibly correspond to the modification with pentynoic acid. Small shoulders are visible that roughly correspond to an m/z difference of 80 for the 4-pentynoic acid modification. Thus the modification of the protein with 4-pentynoic acid seemed to be successful.

The obtained protein was introduced in a dipolar 1,3-cycloaddition (click-reaction) onto azide-modified silica particles ($\text{SiO}_2\text{-N}_3$). After separation and washing 383 μg protein was immobilized onto 20 mg of the silica particles. This corresponds to 19 μg (5×10^{-4} μmol) protein per mg silica which is 25 % higher than obtained for the amide approach.

5.2.2.3 Recombination of cohesin and dockerin

The recombination of the artificial cellulosome is driven by the strong interactions between cohesin and dockerin (Chapter 1.1.2). The already immobilized coh-CBM unit is hence recombined by simply bringing the doc-cellulase units in contact with each other. The presence of Ca^{2+} ions in the reaction solution assures that no defolding of the dockerin occurs since this would lead to a loss of the unique interactions between cohesin and dockerin.

As a proof of principle, the immobilized coh-CBM unit on carboxylic-acid functionalized silica nanoparticles was used in the recombination process. After the incubation of the immobilized proteins with the doc-cel unit in succinate buffer, the particles were separated from the solution. The amount of doc-cel was determined in the supernatant of the washing fractions. An amount of 86 μg in total and 4.4 μg (5.3×10^{-5} μmol) protein per mg silica particles recombined by establishing the strong coh-doc interactions. This corresponds to a yield of 13 % recombination, suggesting that 13 % of the cohesin was accessible to the dockerin unit.

It has to be mentioned, that a detection of small amounts of protein in the supernatant is always a source of errors. Thus, the obtained values are only a hint that the immobilization was successful but should not be taken as absolute values. Nonetheless, the activity of the obtained biohybrid material towards the decomposition of cellulose was tested. Therefore, LB plates with carboxymethyl cellulose (CMC) were made as substrate, since the modified cellulose is more easily decomposed by the cellulosome complex and the detection is much more sensitive. The dispersed particles were then dropped onto one of the plates and incubated at 50 °C. After the incubation period the plates were stained with Congo red and washed with brine. The areas where the cellulose was decomposed were visible as light areas. For a better visibility, the pictures are shown here in black and white.

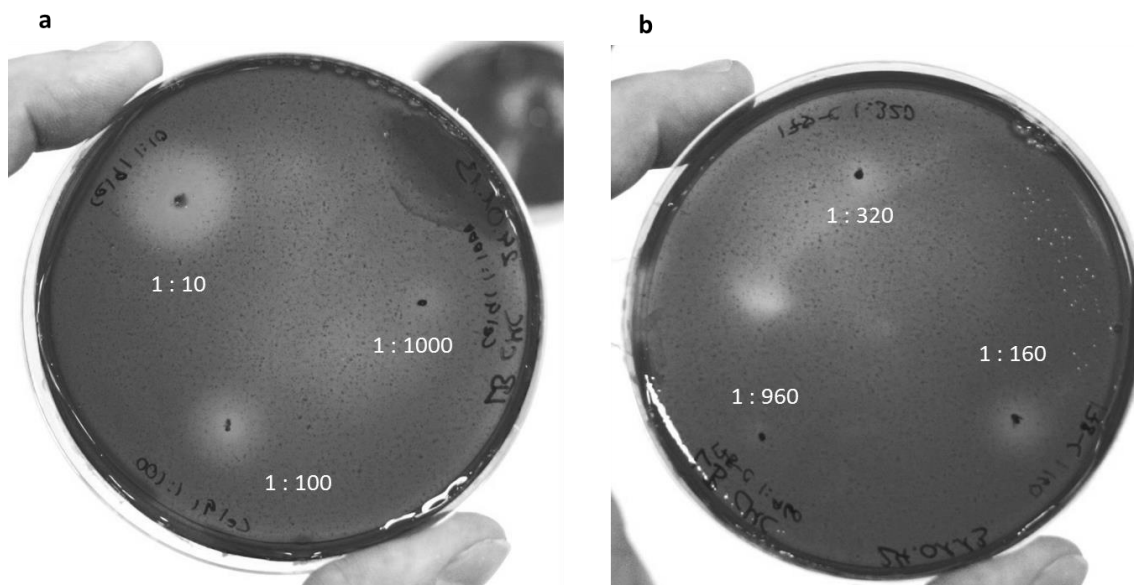


Figure 5.12: LB-CMC-plates stained with Congo red. The areas where the cellulase converted the CMC are indicated by the light spots on the plate. The black dots determine the points where the sample spots have been dropped onto and thus the center of the light areas. Three different dilutions were placed on the plates for the free doc-cel (a) and the immobilized proteins (b).

Dilutions of the free (Figure 5.12a) and immobilized cellulase (Figure 5.12b) were placed on the plates. Since the amount of cellulase immobilized on the sample could not be precisely determined the dilutions mentioned on the plates are only rough estimations. The size of the light areas can estimate the activity of the enzyme. Comparing the width of the spots for free and immobilized cellulase the width of the spots is smaller for the immobilized enzyme indicating a loss of activity due to immobilization, maybe orientation of the protein.

The experiments show that the general approach of an assembly of a cellulosome is working but the quantification of the amount of protein as well as the activity has to be further improved.

5.2.3 CHARACTERIZATION OF PURE AND COATED MAGNETITE PARTICLES AS POSSIBLE SUPPORT MATERIAL FOR THE ASSEMBLY OF A CELLULOSOME

Magnetite particles are often used as support materials for enzymes since the easy magnetic separation from the reaction mixture is a major advantage compared to other materials. However, magnetite is prone to oxidation and corrosion by acids and thus needs a protecting shell. Therefore, a popular approach is a coating with chemically robust inorganic materials. Silica, for example can be coated onto iron oxide particles by using the existing hydroxyl groups on the surface. The obtained $\text{Fe}_3\text{O}_4@\text{SiO}_2$ particles are usually more stable and easy functionalized using various organosilanes. In the next chapter the synthesis and characterization of magnetite particles is presented with a special focus on the adjustment of the silica shell thickness.

5.2.3.1 Characterization of Fe_3O_4 and $\text{Fe}_3\text{O}_4@\text{SiO}_2$ particles

The particles and coating procedure presented in this chapter were performed according to the literature.^[296] The magnetite particles were synthesized by hydrothermal treatment at 200 °C of iron (III) chloride with sodium acetate as a stabilizer and ethylene glycol as a solvent. After separation and extensive washing the nearly black magnetite particles were kept under nitrogen to prevent their oxidation. The obtained particles were then coated with a thin silica shell by according to the Stöber method with TEOS in ethanol as a solvent and ammonium hydroxide as a base catalyst.

The synthesized particles exhibit spherical shape with a rough surface that is caused by the small crystallites that are assembled to one particle. The crystallites are of a non-uniform shape and size as can be seen from TEM images (Figure 5.13). The size of the magnetite particles was not only determined from SEM but also with DLS (see chapter 5.2.3.2). The SEM images show mainly particles with diameters from 250 to 350 nm whereas the DLS measurements give a mean size of 330 nm which seems to be an overestimation. This overestimation is not only caused by the hydrodynamic behavior of the particles but also from general experimental difficulties. Since the particles are not monodisperse the fit of the correlation function is not as good as for monodisperse

system. Another problem arises due to the dark color of the sample that leads to a strong absorption of the light. Nevertheless, for the coating experiments the DLS measurements were a helpful tool to monitor the trend of the particle size.

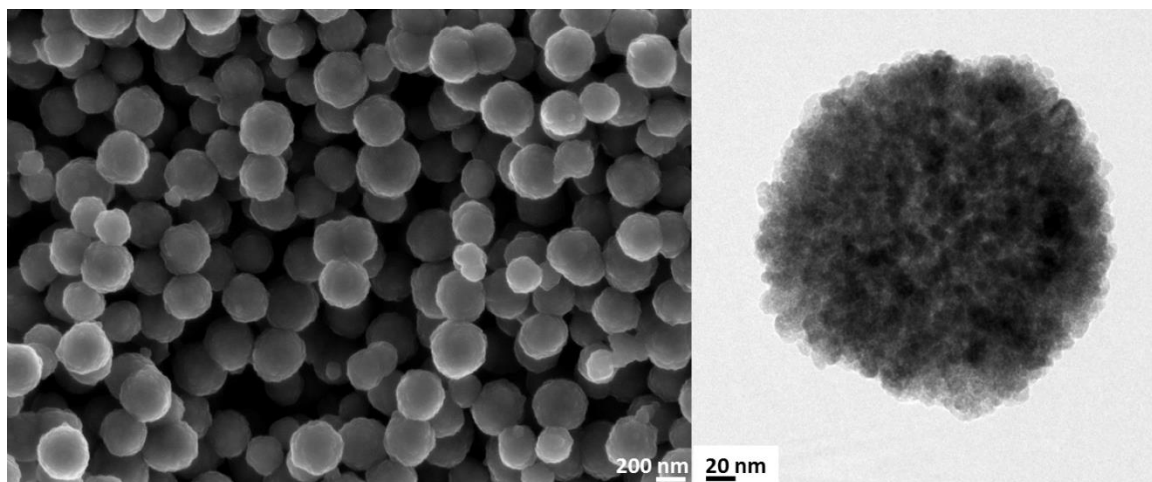


Figure 5.13: SEM and TEM images of magnetite particles.

After coating with silica, the particle surface became smoother and a thin shell (< 20 nm) became visible in the TEM images. According to the SEM and TEM images (Figure 5.14) most of the particles were still separated from each other, only a few agglomerates were present after coating.

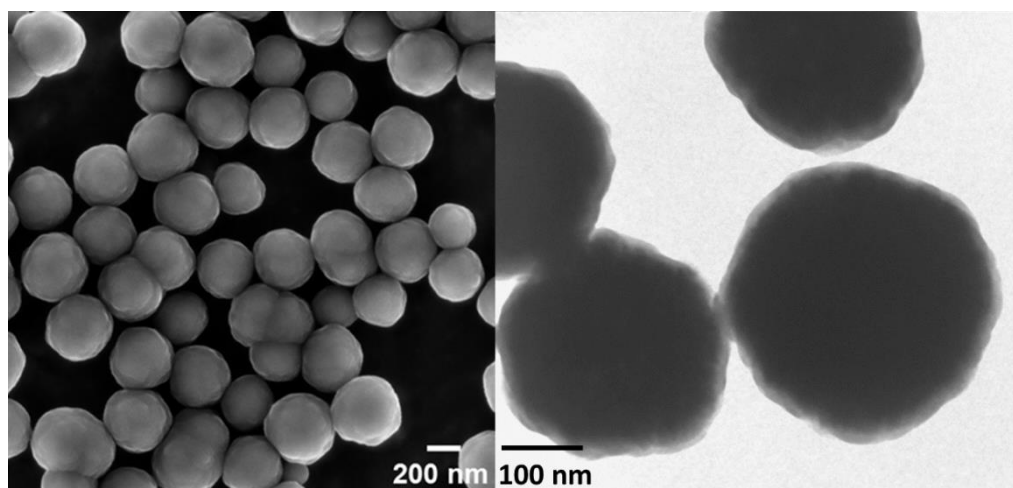


Figure 5.14: SEM and TEM images of the silica coated magnetite particles.

PXRD was performed prior and after the coating to proof whether the iron oxide was already transformed to maghemite or hematite or the magnetite phase of iron oxide was obtained. The PXRD patterns (Figure 5.15) showed broadened peaks due to the presence of the small crystallites. Comparing the obtained patterns with the reference patterns it is unlikely that a high content of maghemite was present in the samples since the less intense peaks for maghemite were not present. However, the intense peaks of both maghemite and magnetite appear at similar reflection angles and it is thus not excluded that a low amount of oxidized maghemite might be present at the surface of the particles.

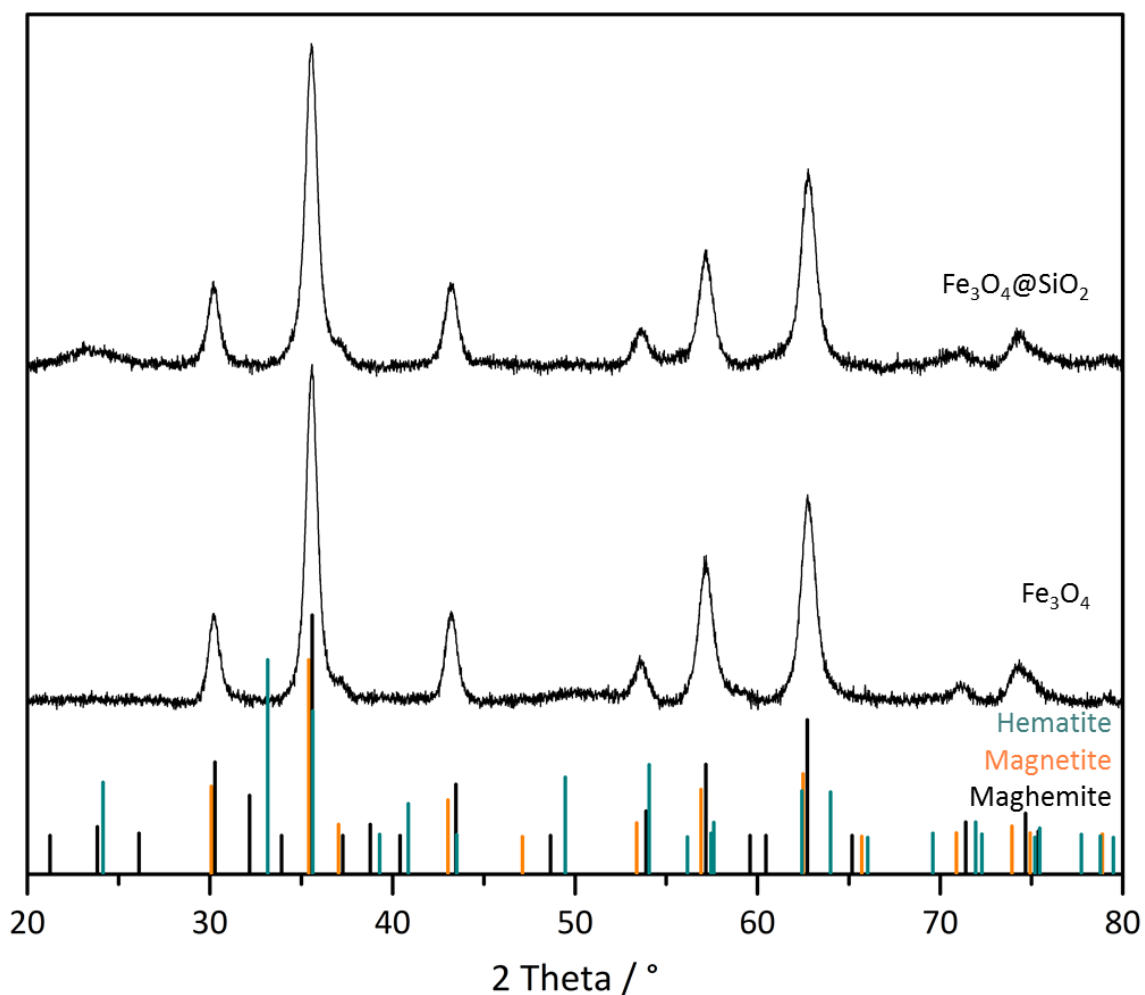


Figure 5.15: PXRD pattern of coated and pure magnetite particles with the respective reference patterns for magnetite, maghemite and hematite.

After coating of the particles with silica a broad peak appears between 20 and 25 ° due to the presence of the amorphous silica.

Since the presence of the shell was already proven by TEM, DLS and PXRD the effect of the shell on the thermal stability of the material was investigated. TG/DTA/MS measurements were performed under argon and oxygen atmosphere with coated and pure iron oxide particles. Thermal analysis of magnetite particles was extensively investigated by Egger and Feitknecht in the 60s.^[297] They found two transformations under oxygen atmosphere: First, the oxidation of magnetite to maghemite occurs at 180 °C, accompanied by an increase of the mass. Second, the thermal transformation of maghemite to hematite, the thermodynamically most stable phase of iron oxide, takes place without changes in the TG curves at 580 °C. Both events are found in the analysis of the magnetite particles under oxygen atmosphere (Figure 5.16) but additionally the combustion of organic residues is detected.

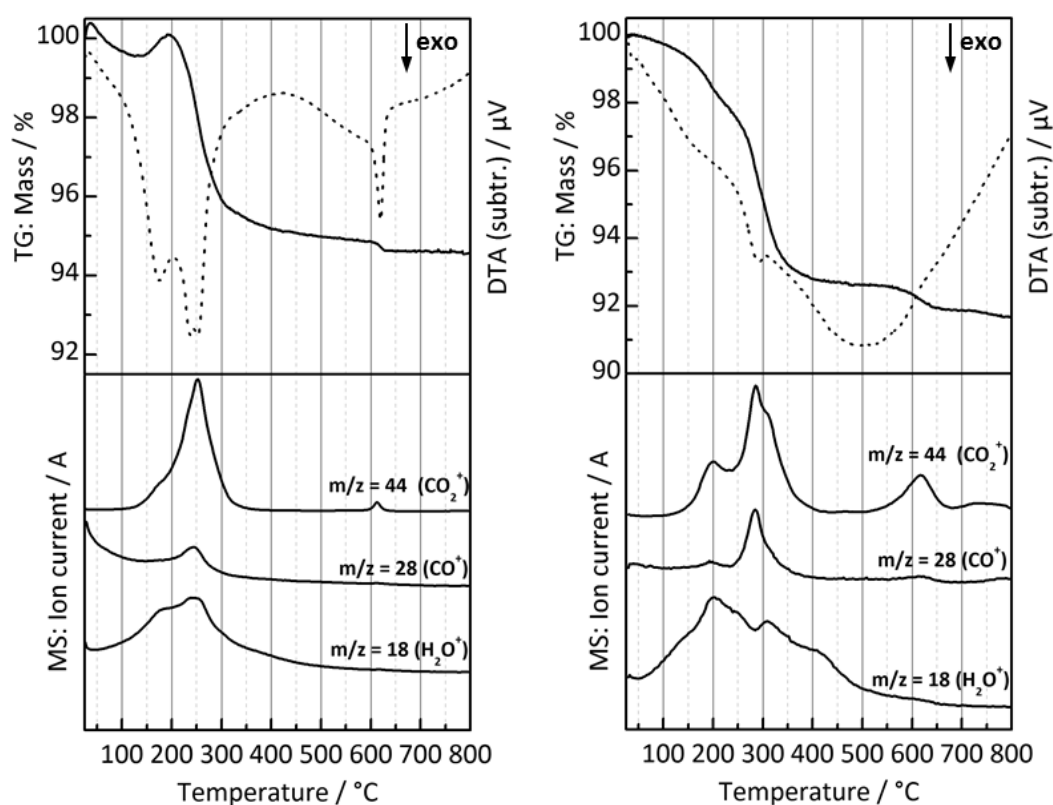


Figure 5.16: TG/DTA/MS of pure Fe_3O_4 under oxygen (left) and under argon (right) atmosphere from room temperature to 800 °C. Whereas under oxygen atmosphere clearly the oxidation of magnetite to maghemite and the thermal transformation to hematite is observed, only the combustion of residual sodium acetate is present under argon atmosphere.

The first broader exothermic step (175 °C) in the DTA can be assigned to the transformation of magnetite to maghemite and is accompanied by a mass increase due to oxidation. The second event (250 °C) that overlays partially with the first transition is the combustion of residual organics. The large amount of CO₂ compared to CO detected by mass spectrometry indicates that the organic compound is the acetate due to the liberation of large amounts CO₂. The next very sharp exothermic step (620 °C) is assigned to the thermal transformation of maghemite to hematite. However, this step should occur without any mass loss since no chemical reaction is present. A minor mass loss is detected accompanied by a detection of CO⁺ and CO₂⁺ indicating that some organics are liberated additionally in this event. Eventually, the phase transformation triggers the release of some enclosed acetate residues. The temperatures of the phase transformations match the ones observed by Eggers et al. mentioned above.

The thermal analysis conducted under argon shows no distinct transformations since no oxidation of the magnetite can occur. It also proves that only small amounts of maghemite could be present, otherwise a thermal transformation to hematite would be present at elevated temperatures. The mass loss is only attributed to the combustion of residual organic components. The total mass loss for the thermal analysis under argon is larger compared to the one under oxygen since an increase in the mass, additionally to the mass loss of the organic matter, is observed for the oxidation of the iron oxide.

Table 5.4: TG/DTA/MS results for the thermal treatment of pure and coated Fe₃O₄ particles under argon or oxygen.

Sample	Steps (DTA)		Mass change / %
	T / °C	Event	
Fe ₃ O ₄ -O ₂	175	T1	+0.51
	240	organics	-5.1
	620	T2	-0.31
Fe ₃ O ₄ -Ar	200	organics	-7.4
Fe ₃ O ₄ -SiO ₂ -O ₂	200	T1	0
	280	organics	4.8
Fe ₃ O ₄ -SiO ₂ -Ar	200	organics	-7.0

T1: phase transformation: magnetite-maghemite
 T2: phase transformation: maghemite-hematite
 Organics: combustion of residual organics

To proof the presence of the respective phases after thermal analysis PXRD (Figure 5.17) was performed. Under flowing oxygen the new peak positions clearly indicate that a completely different phase was observed. The peak positions and intensities match the ones obtained from the powder diffraction database for hematite whereas no phase change was observed for the treatment of magnetite under argon.

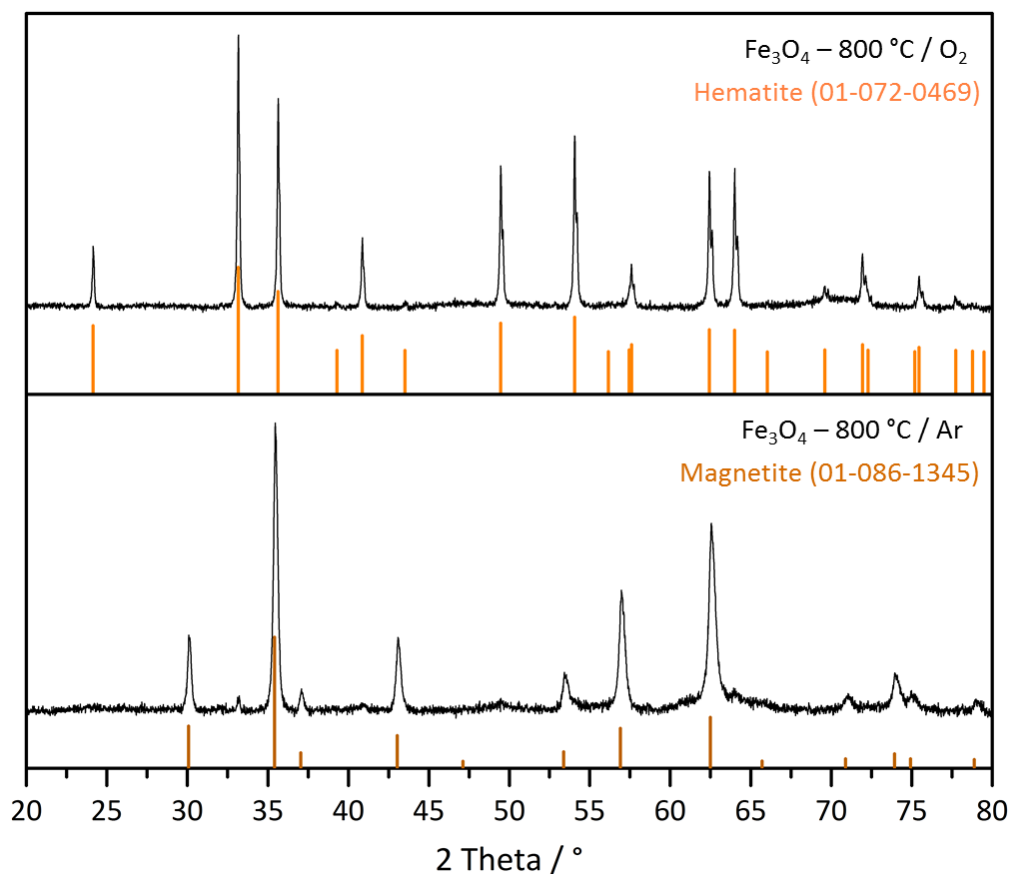


Figure 5.17: PXRD patterns for Fe_3O_4 after thermal analysis under argon and oxygen. After treatment under flowing oxygen a phase transformation to hematite was observed whereas the treatment under argon still proves the presence of magnetite.

Thermal analysis of the respective samples with silica shell (Figure 5.18) exhibit broadened signals due to the diffusion restrictions arising from the thin silica shell. The phase transformations under oxygen atmosphere cannot be clearly assigned since the transformation of magnetite to maghemite is shifted to higher temperatures. The shoulder in the DTA curve ($> 200\text{ }^\circ\text{C}$) is caused by the oxidation of the iron oxide. Since the combustion of the organics overlaps with the transformation the increase in the TG

curve observed for the pure iron oxide cannot be seen here. Only a plateau in the TG curve indicates where the transformation takes place.

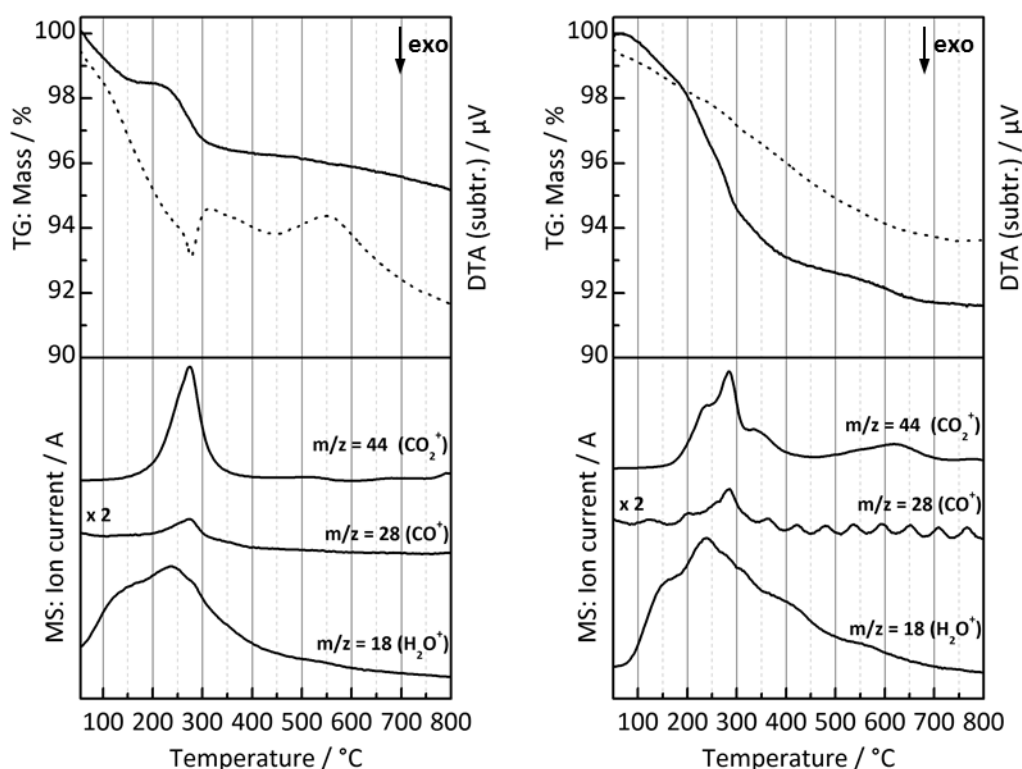


Figure 5.18: TG/DTA/MS of $\text{Fe}_3\text{O}_4@\text{SiO}_2$ under oxygen (left) and under argon (right) atmosphere from room temperature to 800 °C. Whereas under oxygen atmosphere the oxidation of magnetite to maghemite is observed, only the combustion of residual sodium acetate is present under argon atmosphere.

The second transformation is not observed as well as the release of organics at 600 °C due to the overlap of the broadened signals. Actually, the temperature of the thermal transformation should not be shifted since it is not a diffusion limited process. In contrast, the thermal treatment under argon shows the combustion at 600 °C. The release of organics and water under argon is broadened due to the reasons mentioned above.

The magnetic separation of the particles is shown in Figure 5.19. The particles can be separated easily and fast from solution.

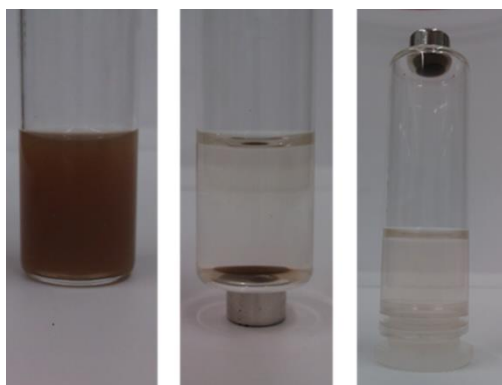


Figure 5.19: Magnetic separation of $\text{Fe}_3\text{O}_4@\text{SiO}_2$ from aqueous solution. After a magnet is placed under a vial with homogeneously dispersed magnetic particles the particles are collected after 30 s.

The saturation magnetization of the pure and coated particles was determined by magnetometry. Therefore the applied magnetic field was increased stepwise until a plateau was reached and then the applied field was decreased. The respective magnetization was obtained from the plateau of the curves.

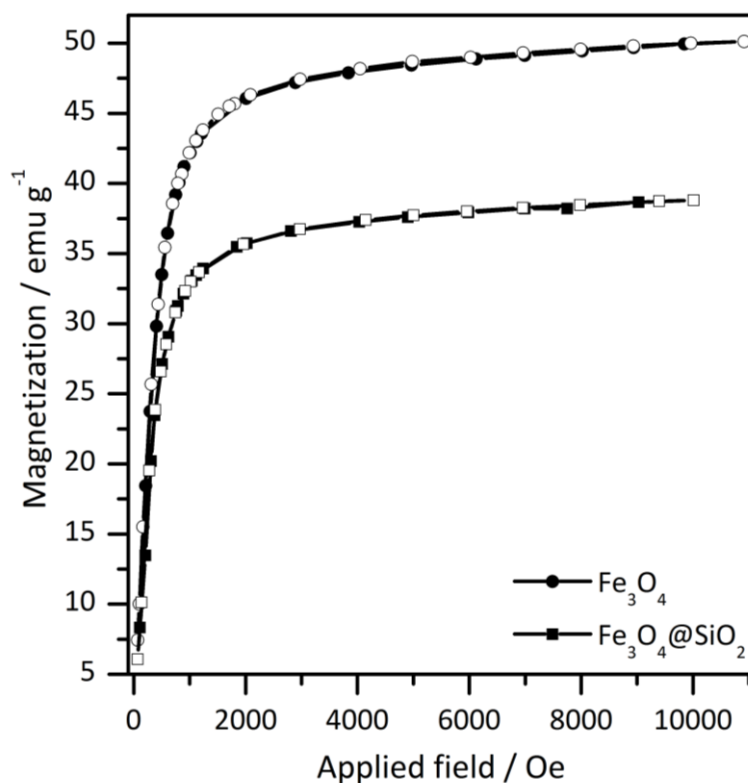


Figure 5.20: Magnetization curves (filled symbols: increasing applied field, empty symbols: decreasing applied field) of pure and coated iron oxide. The curves show no remanence indicating superparamagnetic behavior.

The pure Fe_3O_4 curves exhibited a higher saturation magnetization (50 emu g^{-1}) due to the higher content of magnetic material compared to the sample after coating (39 emu g^{-1}). The curves showed no hysteresis indicating superparamagnetic behavior. The high magnetization of the particles is responsible for the fast separation of the particles from solution.

5.2.3.2 Modification of the shell thickness

The $\text{Fe}_3\text{O}_4@ \text{SiO}_2$ particles presented in the last chapter exhibited a shell thickness smaller than 20 nm. To achieve a sufficient stabilization a thicker shell was aimed. To yield a thicker silica shell, two general ways exist:

- 1) The amount of silica precursor is increased. This method is usually either accompanied by a scale-up since a concentrated TEOS solution would lead to the formation of primary silica particles or by a reduction of the amount of core particles. Problems arising are either low particle yields or very large batches.
- 2) A stepwise addition of precursor to the reaction mixture. Therefore, the silica source is added and the reaction is run to completion prior to another addition of precursor to the reaction mixture. However, this approach is highly time-consuming since a completion of each coating takes several hours.

Two varied approaches are shown here where a compromise of applicability and perfection was aimed. Each two hours an aliquot of TEOS, of the amount used for obtaining the thin shell in the previous chapter, was added to the reaction mixture. Prior to the addition a small amount of the mixture was withdrawn to monitor the reaction progress with DLS, SEM and TEM.

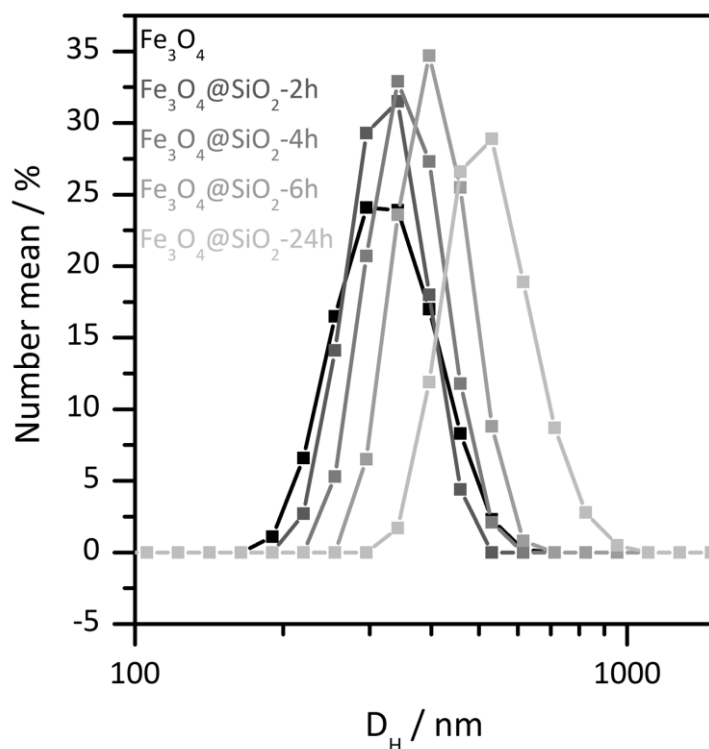


Table 5.5: Hydrodynamic diameter and polydispersity index for stepwise coating of iron oxide particles determined by DLS.

Sample	D_H (number mean) / nm	Pdl
Fe_3O_4	330 ± 4	0.283
$Fe_3O_4-SiO_2-2h$	329 ± 18	0.473
$Fe_3O_4-SiO_2-4h$	360 ± 14	0.559
$Fe_3O_4-SiO_2-6h$	400 ± 42	0.564
$Fe_3O_4-SiO_2-24h$	516 ± 37	0.436

Figure 5.21: DLS measurements of stepwise coated $Fe_3O_4@SiO_2$ particles. The brightness of the curves increases with increasing TEOS addition.

As can be seen from the data derived by DLS (Table 5.5, Figure 5.21), the particles indeed become larger with every addition of TEOS. Prior to the addition of the second aliquot after two hours the particle diameter is almost maintained indicating that the formation of the shell is not finished. After a reaction time of 24 h the particle diameter has increased from 330 to 516 nm which would correspond to a shell thickness of 93 nm. However, it has to be mentioned here, that DLS in this case is not an accurate measure, since the sample exhibits high polydispersity and the absorbance of the sample does change during the reaction. Nonetheless, the measurements show that the coating was successful.

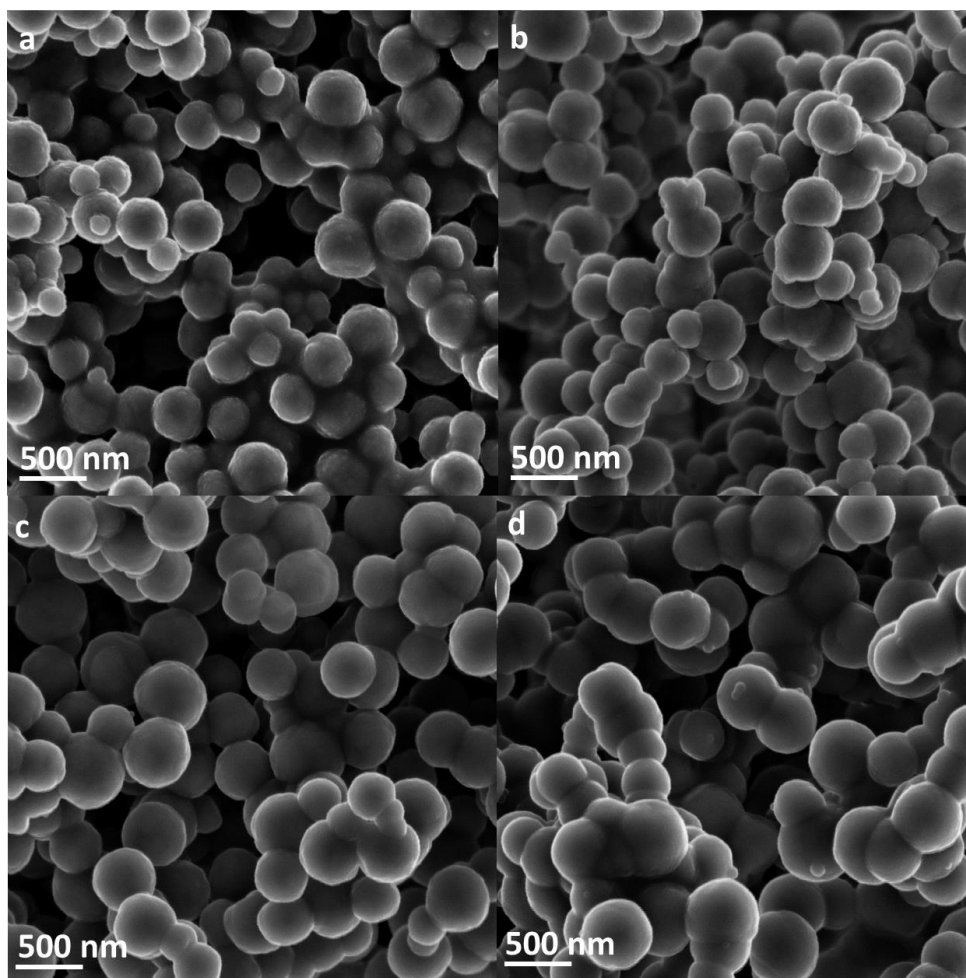


Figure 5.22: SEM images of samples withdrawn after 2 h (a), 4 h (b), 6 h (c) and 24 h (d) of the stepwise coating procedure.

The SEM images (Figure 5.22) additionally show the success of the coating process since the surface of the particles becomes smoother and the diameter seems to become larger. Additionally, the presence of smaller silica particles and agglomeration of the particles is observed. The agglomeration increases with increasing reaction time indicating that the precursor addition period of two hours was too short. Thus the amount of precursor during the reaction was too high and agglomeration and silica particle formation occurred.

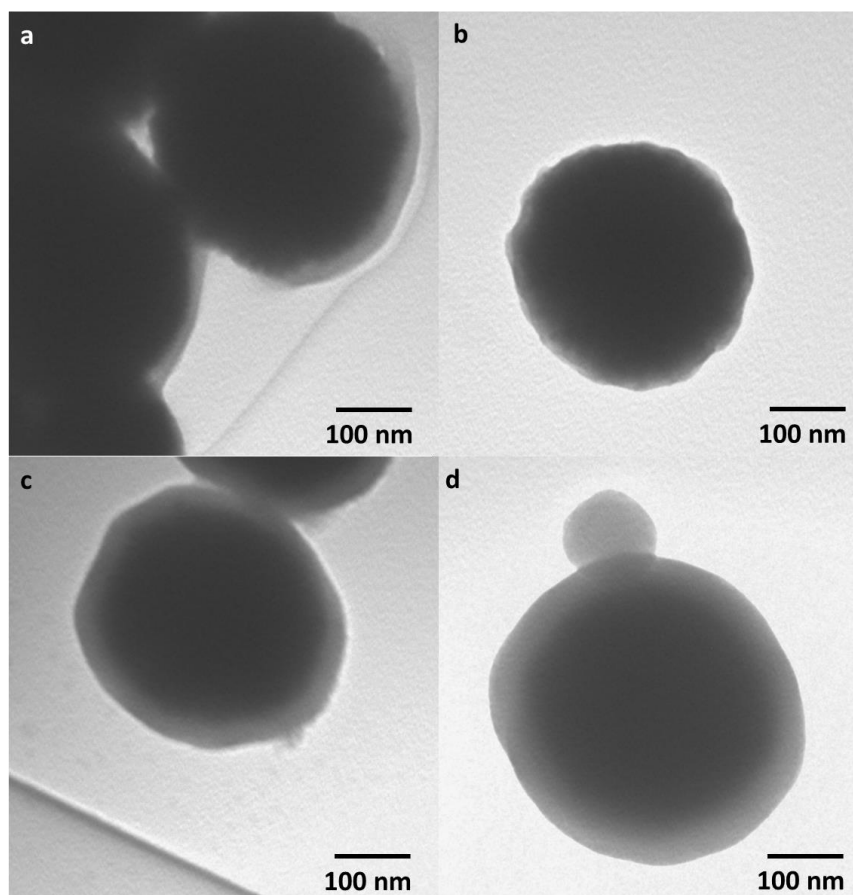


Figure 5.23: TEM images of samples withdrawn after 2 h (a), 4 h (b), 6 h (c) and 24 h (d) of the stepwise coating procedure.

From the TEM images (Figure 5.23) the growth of the silica shell with each silica aliquot is proven. After two hours only a thin (20 nm) and incomplete silica shell is observed. After four hours the thickness of the silica shell was maintained but a complete coverage of the particles was achieved. After addition of the third TEOS aliquot the shell was significantly larger (40 nm) and was increased up to 50 nm after 24 hours. As indicated in the last chapter the DLS measurements are only an indicator that the coating was successful but more than a trend cannot be derived: Since the coating does not only affect the particle diameter but also its surface chemistry and the absorbance towards the incident light, the shell thickness derived from TEM is the only reliable number. To sum up, the stepwise addition of the silica source led to a stepwise growth of the silica shell but additionally to agglomeration and formation of silica particles.

The second approach was to simply increase the amount of the silica source in one step. The results shown here compare the results obtained for the thin shell silica ($\text{Fe}_3\text{O}_4@\text{SiO}_2\text{-1}$) shown in the last chapter and magnetite particles prepared with a thicker shell ($\text{Fe}_3\text{O}_4@\text{SiO}_2\text{-2}$). The thicker coating was prepared with 6.5 equivalents of TEOS compared to the thin-shelled magnetite particle which were coated with the same amount of TEOS as the stepwise added aliquots. The DLS measurements reveal that an increased amount of TEOS indeed yielded a thicker shell. But more importantly no formation of primary silica particles was detected since the DLS showed a monomodal particle size distribution. Additionally, the polydispersity index of the samples was very good after the coating. These results already gave a hint to the high quality of the resulting coated iron oxide particles.

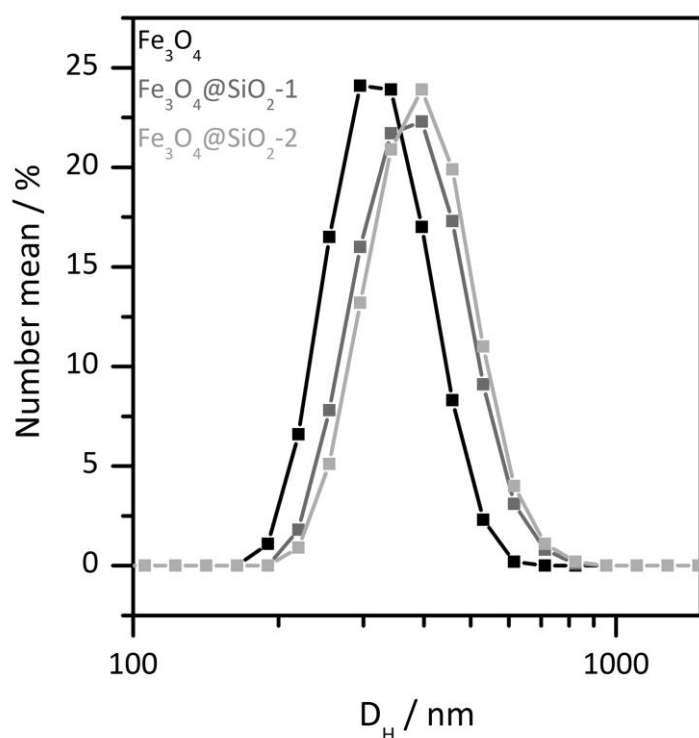


Figure 5.24: DLS measurements of coated $\text{Fe}_3\text{O}_4@\text{SiO}_2$ particles. The brightness of the curves increases with increasing amount of TEOS.

Table 5.6: Hydrodynamic diameter and polydispersity index for one step coating of iron oxide particles determined by DLS.

Sample	D_H (number mean) / nm	Pdl
Fe_3O_4	330 ± 4	0.283
$\text{Fe}_3\text{O}_4\text{-SiO}_2\text{-1}$	384 ± 5	0.149
$\text{Fe}_3\text{O}_4\text{-SiO}_2\text{-2}$	405 ± 4	0.169

These results were further proven by SEM (Figure 5.25). Most particles were present as single particles, almost no agglomerates were detected. Additionally, no small silica particles were visible in the images. The surface of the rough iron oxide particles became

smoother with increasing amount of silica source already indicating the presence of the silica shell.

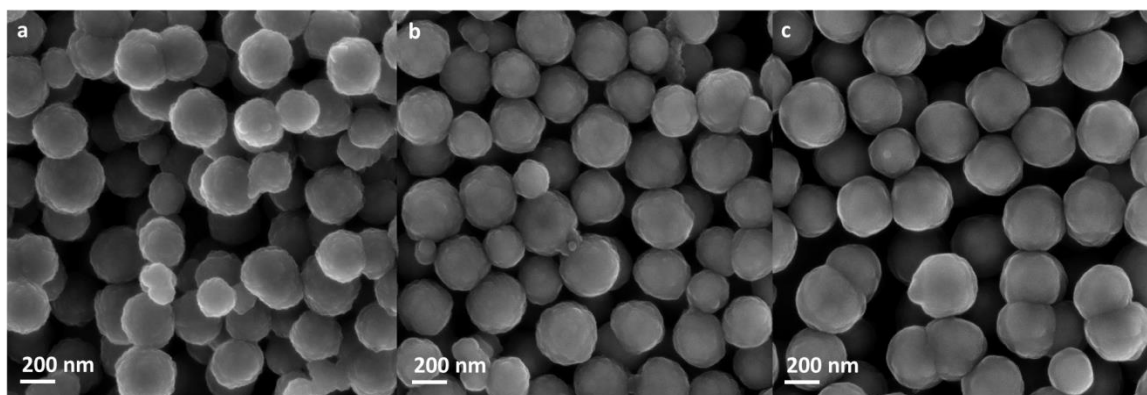


Figure 5.25: SEM images of the primary Fe_3O_4 (a), $\text{Fe}_3\text{O}_4@SiO_2-1$ (b) and $\text{Fe}_3\text{O}_4@SiO_2-2$ (c) particles.

The thickness of the silica shell is also detected by TEM. The thinner shell of the particles exhibited a thickness smaller than 20 nm whereas the thicker shell already was about 50 nm thick.

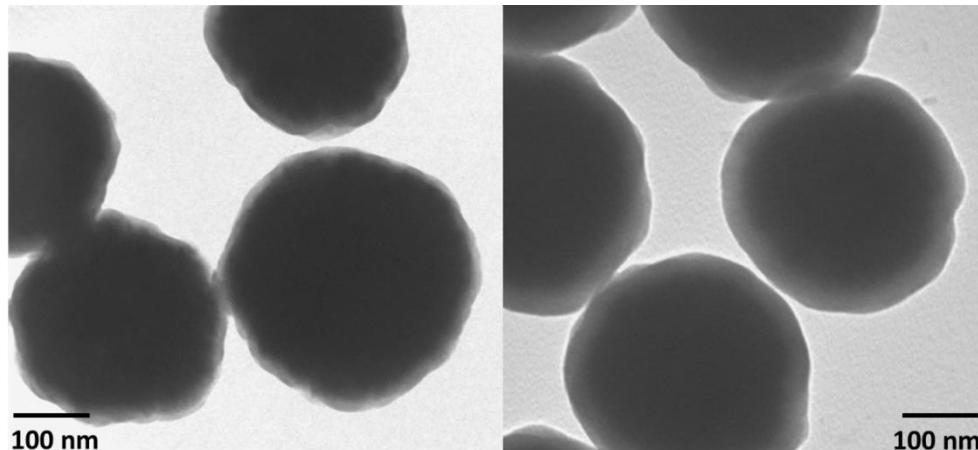


Figure 5.26: TEM images of the $\text{Fe}_3\text{O}_4@SiO_2-1$ (left) and $\text{Fe}_3\text{O}_4@SiO_2-2$ (right) particles.

To sum up, the increase of the amount of silica with constant amount of core particles and solvent led to the best coating results. No agglomeration and silica particle formation was present although the concentration of the silica source was increased. In contrast, the quality of the particles obtained by stepwise addition of the silica source was much lower. Obviously the fluctuation of the TEOS concentration led to an inhomogeneous condensation behavior due interference of the equilibrium conditions.

5.3 EXPERIMENTAL SECTION

5.3.1 CHARACTERIZATION TECHNIQUES – INSTRUMENTAL DETAILS

Instrumental details of the applied characterization techniques that changed compared to the ones listed in chapter 4.3.1 are shown here.

Powder X-ray diffraction (PXRD)

The diffraction patterns were performed with $\text{Cu}_{\text{K}\alpha}$ -radiation (1.541874 Å) in theta-theta geometry with a *MPD X'Pert Pro* from *Panalytical*. The detector was operated at a voltage of 45 kV and a current of 40 mA. Speed: 74 s/step (step size: 0.0131°).

Dynamic light scattering (DLS)

The DLS measurements were performed on a *Malvern Zetasizer Nano* equipped with a 4 mW He-Ne laser (633 nm) and a photodiode detector. All samples dispersed either in ethanol or water were treated with ultrasonication for 10 min prior to the measurement.

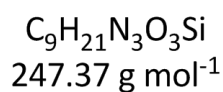
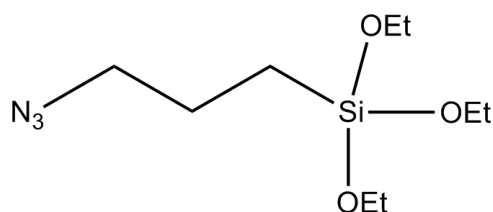
Matrix-assisted laser desorption ionization (MALDI)

MALDI-TOF-TOF was performed with a *Bruker Ultraflex Extreme* spectrometer equipped with a *smartbeam II laser*. Dihydroxy acetophenone was used as a matrix.

Thermal analysis (TG/DTA/MS)

TG/DTA/MS experiments were performed with a thermobalance *STA 449 F3 Jupiter* and a coupled *QMS 403 C Aëolos* Quadrupol mass spectrometer from *Netzsch*. All measurements were performed either under argon (gas flow: 20 mL min⁻¹) or under oxygen (gas flow: 40 mL min⁻¹). About 20 mg sample were heated in an aluminium oxide crucible with a heating rate of 10 Kmin⁻¹ from room temperature to 800 °C. The assignment of the particular combustion steps was done by analysis of the differential mass loss curve (DTG).

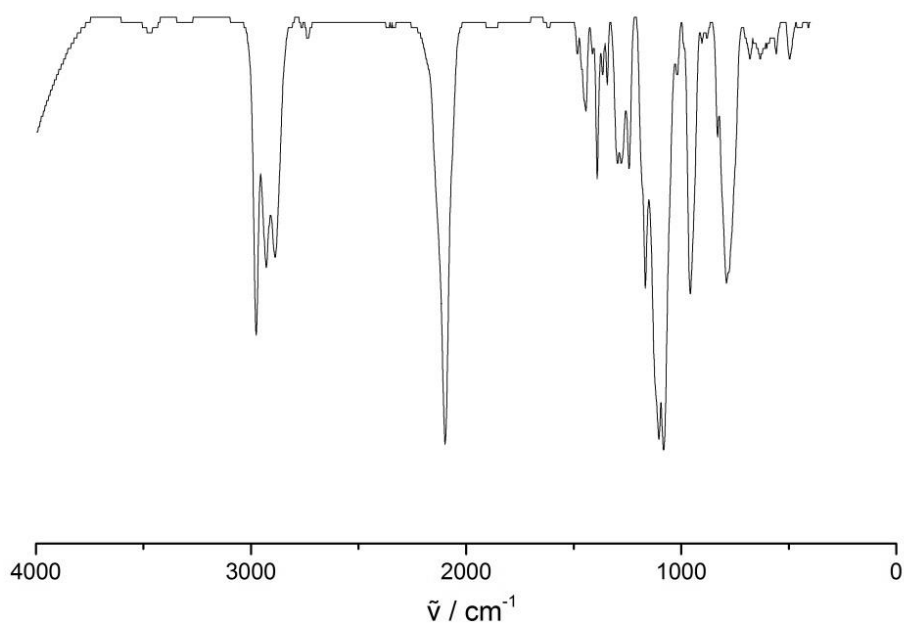
5.3.2 SYNTHESIS AND FUNCTIONALIZATION OF INORGANIC PARTICLES

Synthesis of 3-(azidopropyl)triethoxysilane

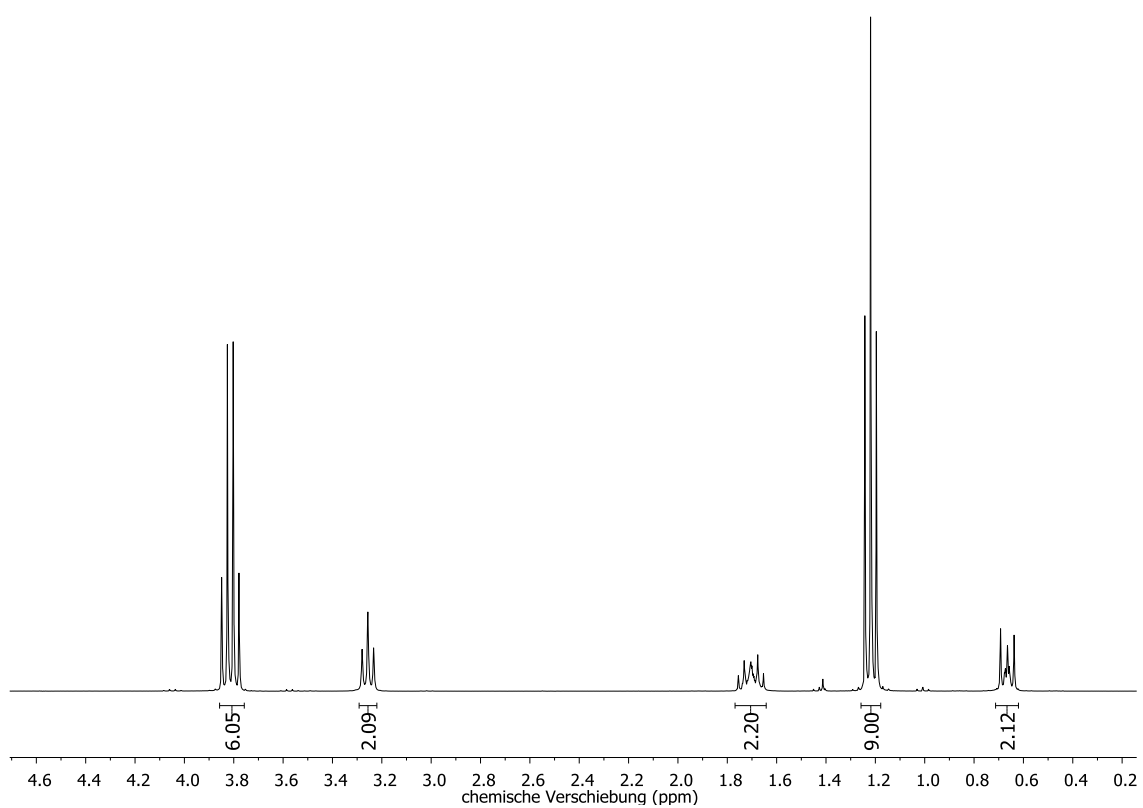
The synthesis of 3-(azidopropyl)silane was performed according to a synthesis reported in literature.^[298]

To a suspension of sodium azide (3.3 g, 50.7 mmol) and tetrabutyl ammonium bromide (1.8 g, 5.6 mmol) in 100 mL acetonitrile 3-(chloropropyl)triethoxysilane (6.0 g, 24.9 mmol) was added. The reaction mixture was heated to reflux for 18 h. The product was recovered by removal of the solvent under reduced pressure prior to separation of the inorganic salts by filtration. Therefore the residual slurry was suspended in cyclohexane and filtered. After removal of the cyclohexane the product was obtained as colorless oil.

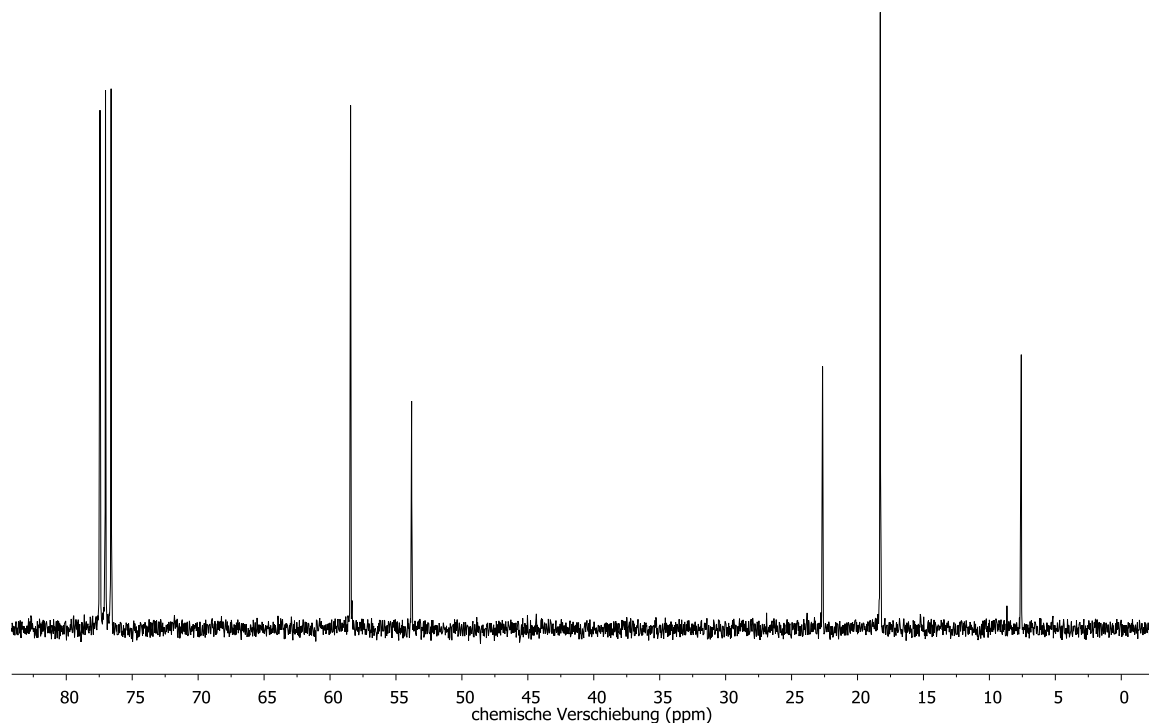
Yield: 5.5 g, 22.4 mmol, 90 %



IR: $\tilde{\nu}$ [cm^{-1}] = 2976 (ν_{as} (CH₂)), 2929 (ν_{as} (CH₂)), 2885 (ν_{as} (CH₂)), 2089 (ν_{as} (N₃)), 1105 (ν_{as} (SiO-C)), 1083 (ν_{as} (Si-O-Si)).



$^1\text{H-NMR}$ (300 MHz., rt, CDCl_3): $\delta = 3.81$ (q, 6H, $^3J=7.0$, Si-O-**CH₂**) 3.26 (t, 2H, $^3J=6.1$, -**CH₂N₃**) 1.64-1.77 (m, 2H, -SiCH₂-**CH₂**), 1.22 (t, 9H, $^3J=7.0$, Si-O-CH₂-**CH₃**), 0.61-0.71 (m, 2H, Si-**CH₂**).



$^{13}\text{C-NMR}$ (100 MHz., rt, CDCl_3): $\delta = 55.4, 53.8, 22.7, 18.2, 7.6$.

Synthesis and functionalization of silica nanoparticles (Stöber approach)^[299]

To reduce the aggregation of the silica particles, the nanoparticles were not recovered prior to functionalization.

For the synthesis of monodisperse silica particles 100 mL ethanol (abs.) and 10 mL of aqueous ammonia (25 %) were mixed. TEOS (10.5 g, 50.6 mmol) was added to the mixture dropwise within 10 min. After 20 h the respective organosilanes (9.4 mmol) were mixed with 15 mL ethanol and added to the silica nanoparticles prior to addition of 50 mL ethanol. The functionalization proceeded for 7 days at rt. The obtained organo-functionalized silica nanoparticles were separated and washed by centrifugation.

Organosilane	Weight
3-(aminopropyl)triethoxysilane	2.21 g
3-(azidopropyl)triethoxysilane	2.33 g

The carboxylic acid modified particles were prepared from 3-aminopropyl modified silica particles with succinic anhydride. Therefore 1.0 g of the silica particles were dispersed in 100 mL ethanol. Succinic acid anhydride (0.4 g, 0.4 mmol) was added and the mixture was refluxed for 5 h. The mixture was cooled to room temperature and separated and washed with ethanol by centrifugation.

Synthesis of magnetite spheres: Fe₃O₄ and Fe₃O₄@SiO₂

The synthesis of magnetite particles was performed as already described in literature.^[300]

FeCl₃·6H₂O (2.70 g, 0.01 mol) and sodium acetate (7.20 g, 0.09 mol) were dispersed in 100 mL ethylene glycol. The mixture was transferred to an autoclave and heated for 8 h at 200 °C. After the dispersion was cooled down, the particles were separated by a magnet and washed with ethanol and water (each 50 mL, 5x). The residual solvents were removed under reduced pressure for 12 h at 60 °C.

For the coating procedure 150 mg of the dried iron oxide particles were treated with dilute hydrochloric acid (0.1 M) for 10 min by ultrasonication to activate the surface. The particles were magnetically separated and washed with water and ethanol (each 50 mL) to remove residual acid. The particles were dispersed in a mixture of ethanol and water (100 g : 30 g) prior to the addition of 1.7 mL ammonium hydroxide (25 %). The mixture was mechanically stirred for 30 min prior to addition of TEOS. Different approaches were used for the addition of TEOS. For iron oxide particles with a thin shell prepared in a one-step procedure 80 µL (75 mg, 0.36 mmol) TEOS was added to the reaction mixture. For the synthesis of particles with a thicker shell 530 µL (497 mg, 2.4 mmol) TEOS were added. For the stepwise coating approach 80 µL (75 mg, 0.36 mmol) aliquots were added every 2 h (4 times) to the reaction mixture. The reaction was allowed to proceed for 24 h under mechanical stirring. The particles were separated magnetically and washed extensively with water (6x) and ethanol (3x).

5.3.3 BIOCONJUGATION AND ASSEMBLY OF CELLULOSOME COMPONENTS ONTO SILICA PARTICLES

Acetylene-functionalization of the cohesin-CBM unit

Two approaches were used for the acetylene functionalization. The first approach was a procedure reported in literature.^[295] Therefore 5 mL ($c = 1 \text{ mg mL}^{-1}$) of the protein solution in PBS buffer were mixed with 25 μL 4-pentynoic acid (0.1 M in PBS) and 15 min. incubated at 11 °C. EDC (25 μmol) was added to the solution which was shaken for another 4 h. The protein was dialyzed to remove the residual carboxylic acid.

In the second approach 4-pentynoic acid was activated with EDC prior to addition to the protein solution.

Covalent immobilization of coh-CBM onto silica particles

a) Immobilization by active ester approach

19.6 mg carboxylic acid modified particles were dispersed in 1.5 mL PBS (10 mM, pH 6.0) and activated for 30 min with a mixture of EDC/NHS (3.04 μmol /6.10 μmol). The activated particles were separated, washed with buffer once and immediately used for bioconjugation. Therefore the particles were dispersed in 1.5 mL PBS (10 mM, PBS 7.4) and 200 μL of the protein solution were added ($c = 882 \text{ }\mu\text{g mL}^{-1}$). The reaction was stopped after 4 h at rt and the particles were separated from solution and washed with 1 mL PBS (3x).

b) Immobilization by click-chemistry approach

20.0 mg azide-modified particles were dispersed in 1 mL PBS buffer (pH 7.4, 10 mM) prior to the addition of 1.6 mL acetylene-modified protein ($c = 390 \text{ }\mu\text{g mL}^{-1}$). 10 μL copper sulfate solution (1 mM with 5.7 μmol ascorbic acid) was added as a catalyst. The reaction was allowed to proceed for 20 h prior to separation of the particles by centrifugation. The particles were washed with PBS buffer (3x2 mL).

Recombination of the cohesin-dockerin interaction

The recombination of the cohesin-dockerin interaction was performed in succinate buffer (pH 6.0, 50 mM) under presence of 1 mM CaCl_2 . 19.6 mg immobilized coh-CBM

on SiO₂-CO₂H were dispersed in 1050 μ L of a doc-cel solution (595 μ g mL⁻¹) for 24 h prior to separation and washing.

Quantification

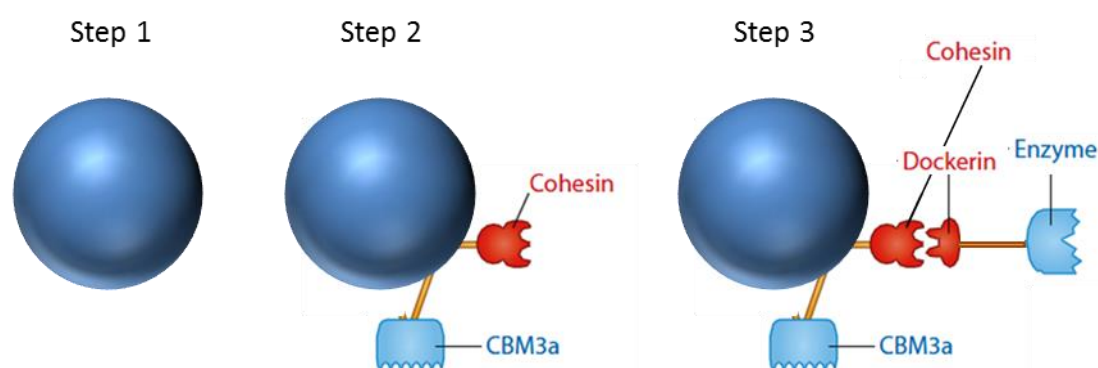
The quantification of protein was performed according to the standard BCA assay approach from Pierce.

Activity assay

The activity was performed on LB-CMC plates by dropping 1 μ L of the respective protein dilutions onto the plate. The plates were incubated at 50 °C for 2 days and stained with Congo red dye (15 min.). After staining the plates were washed with brine (1 M) to remove the residual dye.

5.4 SECTION SUMMARY AND CONCLUSION

A designer cellulosome was attached to silica particles as a model system in order to transfer the bioconjugation techniques to magnetic Fe_3O_4 particles. Different coating procedures were performed to obtain thicker silica shell on the magnetic particles. The bioconjugation of the cellulosome (Scheme 5.6) was performed in three steps: First, organosilanes modified silica particles were prepared. In a second step the cohesin-CBM unit was attached via click-chemistry or active ester approach. In the last step the catalytic active unit, consisting of dockerin and a cellulase was attached, by recombination of the cohesin-dockerin interaction.



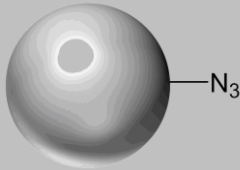
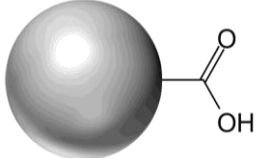
Scheme 5.6: Three steps were used to assemble a designer cellulosome onto silica nanoparticles. First, organosilanes functionalized silica nanoparticles were synthesized and in the next step covalently attached to the coh-CBM unit. In the last step the attachment of the cellulase was performed by recombination of the cohesin-dockerin interaction.

The synthesis of the silica nanoparticles was performed according to the Stöber approach. The obtained particles were directly functionalized with the respective organosilanes without prior separation. Monodisperse silica particles were obtained with diameters ranging between 150 and 200 nm. For the bioconjugation of the coh-CBM unit the silica particles were functionalized with 3-(azidopropyl)triethoxysilane whereas the active ester approach was performed with 3-(aminopropyl)triethoxysilane modified particles, that were reacted with succinic anhydride (Table 5.7).

The click-chemistry approach required an acetylene-functionalization of the coh-CBM unit that was performed by reaction of 4-pentynoic acid with the lysine residues and EDC as an activating agent. Two approaches were used here. First, a literature based approach was performed that was based on an incubation of the acid with the protein in

order to allow an association of positively charged lysine residues and the carboxylic acid residues prior to the addition of EDC. However, this approach led to an EDC activation of the enzymes carboxylic acid groups and not to a binding of the 4-pentynoic acid to the protein. In contrast, the previous activation of an excess of 4-pentynoic acid with EDC and then addition to the protein solution led most likely to a 4-pentynoic acid modification of the protein proven by MALDI. The obtained protein was conjugated in the last step to the azide-modified particles by a dipolar 1,3-cycloaddition. $19 \mu\text{g mg}^{-1}$ ($4 \times 10^{-4} \mu\text{mol mg}^{-1}$) of the coh-CBM unit was attached to the particles (Table 5.7).

Table 5.7: Bioconjugation of a designer cellulosome onto silica particles.

	Bioconjugation method	D_H / nm	pI	ρ_F / mmol g^{-1}	Protein / $\mu\text{g mg}^{-1}$	Protein / $\mu\text{mol mg}^{-1}$
	Click-chemistry approach	171±3.5	5.1	0.77	19	5×10^{-4}
	Active ester approach	205±11	3.8	0.29	15	4×10^{-4}

The conjugation of the coh-CBM unit was additionally performed with an active ester approach. Therefore, carboxylic acid modified silica particles were used as a support in a 1- or 2-step procedure. In the 1-step procedure EDC/NHS as activating agents, silica particles and the protein were added and reacted for 24 h. The quantification of the protein content was however not possible due to interferences of the reagents with the common protein quantification assays. Therefore, a 2-step procedure was used. In the first step the carboxylic acid functionalized particles were activated with EDC/NHS and then after separation reacted with the protein. $15 \mu\text{g mg}^{-1}$ ($5 \times 10^{-4} \mu\text{mol mg}^{-1}$) of the coh-CBM unit was attached to the particles (Table 5.7), 79 % compared to the click-chemistry approach.

The recombination of the cellulosome was performed on the biohybrid materials obtained from the active ester approach. The particles were incubated in a mixture with

doc-cel in the presence of Ca^{2+} in order to avoid defolding of the dockerin unit. After separation an amount of 4 μg (5.3×10^{-5} μmol) protein per mg silica particles was obtained. The first promising activity assay showed that the cel was still active on the particles. However, the good results need to be further analyzed to precisely determine the amount of attached proteins as well as the quantification of the activity of the protein complex and the comparison with the cel bound to the particles. Additionally, the concept has to be transferred to synthesized $\text{Fe}_3\text{O}_4@SiO_2$ particles.

The magnetic core shell particles were synthesized by a hydrothermal method and then coated with a silica shell of specific thickness by an approach similar to the Stöber method. Two approaches were used to increase the shell thickness in comparison to the synthesis in literature. The first approach used a stepwise addition of TEOS aliquots to maintain a low amount of silica source in the solution and thus minimize agglomeration and silica particle formation. In the second approach the amount of silica source was simply increased. Surprisingly, the second approach led to less agglomerated particles with a smooth and thick shell of silica whereas the stepwise addition led to an agglomerated sample with a high amount of small silica particles.

Table 5.8: Properties of the coated and pure magnetite particles.

	Fe_3O_4	$\text{Fe}_3\text{O}_4@SiO_2-1$	$\text{Fe}_3\text{O}_4@SiO_2-2$	$\text{Fe}_3\text{O}_4@SiO_2$ (Stepwise TEOS)
D_H / nm	330±4	384±5	405±4	516±37
Shell thickness / nm	n.d.	<20	50	50
Quality ^a	High	High	High	Low

a: amount of agglomeration, silica particle formation
n.d.: not determinable

The magnetic properties of the silica particles was investigated by magnetometry and the high saturation magnetization (39 emu g^{-1}) showed that the coated particles were an ideal support for the assembled cellulosome with regard to the degradation of cellulose due to fast and easy separation of the biocatalyst. Additionally, the higher stability of the particles after coating would be beneficial since usually higher temperatures are used in the degradation of cellulose.

6 GENERAL CONCLUSION AND OUTLOOK

The application of inorganic-biohybrids as biocatalysts in industrial approaches is one promising approach to perform environmentally friendly processes. The so-called *Green chemistry* includes the reduction or elimination of waste, the reduction of energy needed for the processes and a reduction of side-products. But enzymes can add other benefits to the catalytic processes like their high selectivity, activity and mild reaction conditions. To balance the optimum performance with an easy handling of the biocatalyst their attachment to a solid carrier is often required. The immobilization of the enzymes facilitates their recovery and enhances their stability.

In the last decade the use of immobilized enzymes in biocatalysis was not only influenced from advances made in biotechnology but also in materials science. Two approaches were applied here to yield stable and easy separable biocatalysts that can be used for applications in *Green chemistry*.

Nanoporous materials were used as carrier materials for glucose-6-phosphate dehydrogenase (G6PDH) to yield a stable biocatalyst. G6PDH is a co-factor regenerating enzyme that will be beneficial for the operation of enzyme cascades. A two-enzyme cascade was used to proof the general applicability of this enzyme for applications in cascades. To yield a highly stable and active biocatalyst the porosity and surface characteristics of the nanoporous materials were intensively studied in order to find a material perfectly tailored according to the enzymes' needs. The size of the pores was a major criterion for the selection of the materials since the enzymes hydrodynamic diameter was supposed to be larger than 13 nm. Various carbon and silica based materials were used as possible support materials. The group of silica materials was divided into periodic mesoporous organosilicas (PMOs) and mesostructured siliceous foams (MCFs).

At first a screening of MCFs and carbon materials with different properties was performed in order to locate possible carrier materials for the adsorption of G6PDH. The carbon materials exhibited macropores (> 300 nm) that were supposed to host the enzyme without any diffusion limitations during catalysis. Unfortunately, the high

hydrophobicity of the carbons led to a low amount of immobilization at pH 7.4 and high leaching of the hydrophilic enzyme as well as poor biocatalytic performance. MCF was grafted with different organic moieties in order to provide different surface charges. The coulomb interactions were found to be the major driving force of the immobilization. Thus negatively charged materials showed low uptake of enzyme due to electrostatic repulsion with the enzyme (pI 4.6) whereas G6PDH immobilized on positively charged 3-aminopropyl-modified MCF exhibited excellent affinity towards the material. Not only the uptake performance was superior to all other used materials but also retention of 90 % of the activity and a high stabilization due to the confinement in the pores was obtained.

Due to the promising results amine-modified porous materials were studied in more detail. The chain length of the amine-containing spacer was increased in order to study the effect of increasing hydrophobicity and mobility of the enzyme. The best results were still obtained for the support modified with the short-chain (C3) whereas the increasing hydrophobicity of C7 and C11 chain length showed poor biocatalytic performance. One reason of the low performance was the low dispersibility of the hydrophobic materials in buffer. Thus DMSO was added to the mixture and indeed a high uptake of enzyme was observed due to the wetting of the material on the external and internal surface. Unfortunately, the enzyme was inhibited by DMSO and the activity dropped significantly.

Secondary and tertiary amine-bridged PMOs were applied as supports in order to use materials with a high content of organic groups as well as to investigate if the position of the organic moiety has an influence on the affinity towards the enzyme. As a comparison MCF materials modified with short-chain primary, secondary and tertiary amines were chosen as supports. Due to similar surface characteristics the uptake and biocatalytic performance of the PMO materials was mainly determined by their differences in their pore size. The PMO synthesized with the tertiary amine precursor exhibited the highest stability since its pores were the smallest and therefore the confinement effect was enhanced. The uptake of enzyme from solution was highest for the aerogel-type PMO since the large pores induced no diffusion limitations. Since no differences in porosity were observed for the MCF materials with primary, secondary and tertiary amines, the biocatalytic performance was not affected. All MCF materials

exhibited high uptake, activity and stability. The results showed that the immobilization inside the porous network of the materials was highly beneficial for the biocatalytic performance. Additionally it was proven that the tailoring of porous materials according to the enzyme is a highly useful technique in biocatalysis.

The most promising biocatalyst (G6PDH on MCF-C₃-NH₂) was combined with immobilized 6PGDH in a two-enzyme sequence for the conversion of glucose-6-phosphate to ribulose-5-phosphate. The general applicability of the biocatalyst in enzyme cascades was proven with these experiments. In the future the construction of enzyme cascades with G6PDH and other enzymes would be one main scope of application for this optimized biocatalyst. Even more likely would be an application with the focus of energy generation or fuel synthesis. For example, a coupling of the two-enzyme sequence with a hydrogenase that produces hydrogen would be a possibility.

The assembly of a designer cellulosome onto inorganic particles built the second part of this dissertation. Cellulosomes are protein complexes that efficiently degrade cellulose into glucose moieties which can be used as educt for biofuels or basis chemicals for chemical industry. The immobilization of the cellulosome was performed in three steps: First, silica particles were synthesized and functionalized with organosilanes. The silica particles were used as a model system to optimize the coupling chemistry and will be replaced by silica coated iron oxide particles. Second, the cohesin-CBM unit of the cellulosome was covalently bound to the particles. Two approaches were used here: The click-chemistry approach between azide-functionalized particles and acetylene-functionalized proteins required a modification of the lysines with 4-pentynoic acid prior to the immobilization. The modification was performed by activation of the 4-pentynoic acid with EDC. The modified protein was then bound covalently onto azide-modified silica particles by 1,3-dipolar cycloaddition catalyzed by Cu(I). The second approach was an active ester approach onto carboxylic acid modified particles. A two-step procedure was performed that consisted of an activation of the particles by EDC/NHS prior to the covalent attachment of the protein. The click-chemistry approach led to the highest obtained yields of 19 $\mu\text{g mg}^{-1}$ ($4 \times 10^{-4} \mu\text{mol mg}^{-1}$). The catalytic active cellulase was attached by the highly specific recombination of the cohesin-dockerin domains. The first activity tests showed that the combined

immobilized cellulosome was still active towards the degradation of carboxymethyl cellulose but the quantification of the activity as well as the comparison with immobilized cellulase without cohesin and CBM have still to be done.

For the transfer of the coupling chemistry onto magnetic particles, the coating of magnetite particles was optimized. It was proven that an addition of the TEOS at one time leads to particles of higher quality than the addition in small aliquots. The obtained particles would be optimum supports for the application of immobilized cellulosomes in cellulose degradation. The first results obtained for the assembly and application of a cellulosome were very promising and thus have to be transferred to the application in a mixture with crystalline cellulose.

All in all, the application of biohybrid materials in Green chemistry was achieved by careful tuning of the support characteristics and thus efficient immobilization. In the future the focus of the research will be laid more on the design of complex catalytic processes and the need to construct them not only environmentally but also economically feasible. Here it is important to address major criteria for industrial use that are: costs, flow and diffusion of reaction mixtures as well as mechanical stability of the materials since most of the materials will be used in complex reactor systems. The reduction of the process costs may be achieved in the future when porous materials are used simultaneously as purification device for the proteins that are immobilized since the use of highly purified enzymes is very expensive. Despite all difficulties the use of immobilized enzymes will be one of the key issues in industrial synthesis in the next decades.

7 ZUSAMMENFASSUNG

Die Anwendung von anorganischen Biohybridmaterialien als Katalysatoren in industriellen Anwendungen stellt eine vielversprechende Methode zur Entwicklung von ökologisch nachhaltigen Prozessen dar. Diese sogenannte *Grüne Chemie* wird in der Regel aus einer Vielfalt an wichtigen Prozessen gebildet, z.B. der Reduktion von chemischen Abfällen sowie Nebenprodukten. Ein weiterer Kernpunkt ist die Reduktion von Energie, die den Prozessen zugeführt werden muss. Hierbei leisten Enzyme, die in der Regel bei milden Reaktionsbedingungen arbeiten, einen wichtigen Beitrag. Aber auch ihre hohe katalytische Effizienz ist ein weiterer großer Vorteil der Biokatalysatoren. Diesen Vorteilen stehen jedoch auch einige Nachteile gegenüber wie z.B. die problematische Abtrennung von Enzymen aus Reaktionsgemischen oder ihre geringe Stabilität bei bestimmten Reaktionsbedingungen (z.B. hohe Temperatur). Die Immobilisierung der Enzyme kann hier entgegenwirken und einen entscheidenden Beitrag zur effizienten industriellen Nutzung von Enzymen in der Biokatalyse leisten.

Einhergehend mit der Weiterentwicklung der Enzyme für biokatalytische Anwendungen wurde im letzten Jahrzehnt viel an den jeweiligen Trägermaterialien geforscht. Ziel dieser Arbeit war es Materialien entsprechend der Eigenschaften der Enzyme zu gestalten und somit eine effiziente Stabilisierung und biokatalytische Leistung zu erzielen. Hierbei wurden zwei verschiedene Themenbereiche bearbeitet.

Im ersten Teil der Dissertation wurden nanoporöse Materialien als Träger für Glucose-6-phosphat Dehydrogenase (G6PDH) verwendet um einen stabilen Biokatalysator für den Einsatz als Cofaktorregenerator in Enzymkaskaden zu erhalten. Hierbei wurden verschiedene nanoporöse Trägermaterialien auf Basis von Kohlenstoff und Silica eingesetzt. Die Oberfläche der Trägermaterialien sowie deren Porosität wurden den Eigenschaften des Enzyms entsprechend modifiziert und ihre Eigenschaften intensiv untersucht. Einer der Kernpunkte beim Beginn der Immobilisierungsversuche war der große hydrodynamische Durchmesser (> 13 nm) des Enzyms, der die Auswahl der porösen Träger bestimmte.

Anfangs wurde eine grobe Einschränkung der möglichen Trägermaterialien durchgeführt bei der hierarchische Kohlenstoffe sowie mesostrukturierte Silicaschäume mit unterschiedlicher organischer Funktionalisierung verwendet wurden. Die Makroporen der Kohlenstoffträger (> 300 nm) wurden als Wirtstruktur für G6PDH verwendet unter der Annahme, dass die Diffusion durch die großen Poren nicht gehindert wird. Leider führte die Hydrophobizität der Kohlenstoffe zu niedriger Aufnahme an Enzym sowohl als auch zu schlechter biokatalytischer Leistung. Die MCF Materialien wurden postsynthetisch mit unterschiedlichen Organosilanen funktionalisiert um eine Vielfalt an Wechselwirkungen mit dem Enzym zu erzielen. Bei der Adsorption der Enzyme wurde festgestellt, dass Coulomb-Kräfte die Triebkraft der Immobilisierung darstellten. Bei negativ geladenen Trägern wurden daher beim pH Wert der Immobilisierung (pH 7.4) durch die Abstoßung mit dem überwiegend negativ geladenen Enzym (pI 4.6) niedrige Aufnahmekapazitäten erhalten, wohingegen positiv geladenes 3-Aminopropyl-funktionalisierte MCF das gesamte Protein aus der Lösung aufnahm. Aber nicht nur die Aufnahme des Enzyms aus der Lösung war überdurchschnittlich hoch, sondern auch der Aktivitätserhalt (90 %) sowie die Stabilität waren den anderen Biokatalysatoren weit überlegen.

Auf Grund der aussichtsreichen Resultate der Experimente wurde der Fokus auf die Immobilisierung der G6PDH im Folgenden auf Amin-funktionalisierte Materialien gerichtet. Hierfür wurden MCF Trägermaterialien mit Aminosilanen unterschiedlicher Kettenlänge (C3, C7, C11) modifiziert und in der Immobilisierung eingesetzt. Es wurde festgestellt, dass die zunehmende Kettenlänge eine starke Hydrophobizität der Materialien herbeiführte, die zu einer Reduktion der Aufnahme, der Stabilität und Aktivität führte. Die Zugabe von DMSO zur Erhöhung der Hydrophobizität des Puffers führt zwar zur besseren Benetzung des Materials und somit zu Erhöhung der Proteinaufnahme, jedoch auch zur Inhibierung des Enzyms.

Des Weiteren wurden periodische mesoporöse Organosilica (PMO) als mögliche Träger untersucht. Da sich bei diesen Materialien die organische Gruppe, in diesem Fall sekundäre und tertiäre amin-verbrückte Silane, in der Wand des Materials befinden und nicht in die Poren hineinragen, wurden die Unterschiede zu MCFs, die mit primären, sekundären und tertiären kurzkettigen Aminosilanen (C3) funktionalisiert waren, als Träger getestet. Auf Grund der Ähnlichkeit der Oberflächen der PMOs stellte sich

heraus, dass Unterschiede in der biokatalytische Performance sowie der Proteinaufnahme nur mit der Porengröße der PMOs korrelierte. Das PMO mit der geringsten Porengröße, in diesem Fall synthetisiert auf der Basis eines tertiären aminverbrückten Präkursoren, wies die höchste Enzymstabilität auf, da das Protein durch die enge Umschließung der Poren stabilisiert wurde. Im Gegensatz hierzu wurde von einem Aerogel-PMO die höchste Menge an Enzym aufgenommen, da die großen Poren eine ungehinderte Diffusion in das Material erlaubten. Da die jeweiligen MCF Referenzmaterialien keine Unterschiede in ihren Porengrößen aufwiesen, konnten keine signifikanten Unterschiede in ihrer Aktivität, Proteinaufnahme sowie Stabilität nachgewiesen werden.

G6PDH adsorbiert auf 3-Aminopropyl-modifiziertem MCF stellte sich in den vorhergehenden Experimenten als bestes Trägermaterial für die Immobilisierung von G6PDH heraus und wurde daher für die Erstellung einer zwei-Enzym Sequenz mit immobilisierter 6-Phosphogluconat Dehydrogenase verwendet. In dieser Sequenz wurde erfolgreich Glucose-6-phosphat zu Ribulose-5-phosphat unter Umsetzung von NADP^+ zu NADPH umgewandelt.

Die Resultate dieser Testreihen belegen eindeutig die Stabilisierung des eingesetzten Enzyms und somit auch den Einsatz maßgeschneiderter Materialien als Träger für die Biokatalyse. Der Einsatz in einer zwei-Enzym Sequenz unterstreicht die mögliche Anwendung des Enzyms im Hinblick auf die Cofaktor-Regeneration in Enzymkaskaden.

Der zweite Teil dieser Arbeit beschäftigte sich mit dem Aufbau eines Designer-Cellulosoms auf anorganischen sphärischen Partikeln. Cellulosome sind Proteinkomplexe, die in der Natur effizient Cellulose zu Glukose zerlegen und somit für die Synthese von Biokraftstoffen sowie die Synthese von Basischemikalien in der Zukunft von Bedeutung sind.

Der Aufbau des Cellulosoms aus seinen Komponenten wurde in drei Schritten durchgeführt: Zuerst wurden Silicapartikel nach der Stöbermethode synthetisiert und mit Organosilanen funktionalisiert. Die Silicapartikel fungierten in diesem Fall als Modellsystem um die Kupplungsreaktionen zu optimieren und in Zukunft auf mit Silica beschichtete Magnetitpartikel zu übertragen. Der zweite Schritt befasste sich mit der kovalenten Anbindung der Cohesin und CBM Einheiten des Cellulosoms. Hierbei wurden

zwei verschiedene Kupplungsreaktionen angewandt: Ein Click-Chemie Ansatz, der sich mit der Anbindung von Acetylen-funktionalisierten Proteinen an azidfunktionalisierte Silicapartikel beschäftigte. Diese Methode erforderte die Modifizierung der Cohesin-CBM Einheit mit 4-Pentinsäure an den jeweiligen Lysinen der Proteine. Die Aktivierung der 4-Pentinsäure erfolgte mit EDC vor der Anbindung an das Protein. Das modifizierte Protein wurde anschließend über eine 1,3-dipolare Cycloaddition unter Cu(I)-Katalyse an die Silicapartikel gebunden. Die zweite konventionelle Biokonjugationsmethode, die Aktivestersynthese, ermöglichte die direkte Anbindung des Proteins ohne vorherige Modifizierung. Hierfür wurden in einer 2-stufigen Syntheseroute zuerst Carbonsäure-modifizierte Partikel mit EDC/NHS aktiviert und im nächsten Schritt mit den Proteinen umgesetzt. Der Click-Chemie Ansatz erzielte in der Anbindung der Cohesin-CBM Einheit höhere Kupplungsausbeuten mit $19 \mu\text{g mg}^{-1}$ ($4 \times 10^{-4} \mu\text{mol g}^{-1}$). Im letzten Schritt wurde die katalytische Einheit (Cellulase) mit Hilfe der spezifischen Cohesin-Dockerin Wechselwirkung angebonden. Die ersten Aktivitätstests des erhaltenen immobilisierten Cellulosoms zeigten, dass der erhaltene Biokatalysator die Zersetzung von Carboxymethylcellulose erfolgreich durchführte. Jedoch muss die Quantifizierung der Aktivität sowohl als auch ein Vergleich mit immobilisierter Cellulase ohne Cohesin und CBM Einheit noch erfolgen.

Für den zukünftigen Transfer der Kupplungsprozesse auf Silica beschichtete Magnetitpartikel wurden die Bedingungen für die Beschichtung optimiert. Die einmalige Zugabe von TEOS stellt sich in den Versuchen als bessere Methode heraus im Vergleich zur Zugabe von mehreren Aliquots TEOS. Die mit der ersten Methode erhaltenen Partikel wiesen wenig Agglomeration und keine Bildung von kleinen Silicapartikeln auf, stattdessen wurden spherische Partikel mit einer geschlossenen Schicht (ca. 50 nm) aus Silica erhalten. Da die ersten Resultate des auf Silicapartikeln zusammengesetzten Cellulosoms sehr vielversprechend waren, sollten sie in Zukunft auf magnetischen Partikeln zur Zersetzung von kristalliner Cellulose angewendet werden.

Zusammenfassend wurden in dieser Dissertation zwei Anwendungsgebiete für Biohybride in der Katalyse erfolgreich durchgeführt. Außerdem wurde die Immobilisierung von Enzymen auf Trägermaterialien als vielversprechender Ansatz in der Biokatalyse bestätigt.

8 BIBLIOGRAPHY

- [1] L. Cao, *Curr. Opin. Chem. Biol.* **2005**, *9*, 217–226.
- [2] F. J. Díaz, K. J. Balkus Jr, *J. Mol. Catal. B* **1996**, *2*, 115–126.
- [3] S. Hudson, J. Cooney, E. Magner, *Angew. Chem. Int. Ed.* **2008**, *47*, 8582–8594.
- [4] S. Laurent, D. Forge, M. Port, A. Roch, C. Robic, L. Vander Elst, R. N. Muller, *Chem. Rev.* **2008**, *108*, 2064–2110.
- [5] C. G. C. M. Netto, H. E. Toma, L. H. Andrade, *J. Mol. Catal. B* **2013**, *85-86*, 71–92.
- [6] W. Wu, Q. He, C. Jiang, *Nanoscale Res. Lett.* **2008**, *3*, 397–415.
- [7] D. I. Fried, F. J. Brieler, M. Fröba, *ChemCatChem* **2013**, *5*, 862–884.
- [8] E. Fischer, *Ber. Dtsch. Chem. Ges.* **1894**, *27*, 2985.
- [9] E. C. Webb, *Enzyme Nomenclature*, Academic Press, San Diego, **1992**.
- [10] S. Tanvir, J. Pantigny, P. Boulnois, S. Pulvin, *J. Membr. Sci.* **2009**, *329*, 85–90.
- [11] S. A. Meeuwissen, A. Rioz-Martínez, G. de Gonzalo, M. W. Fraaije, V. Gotor, J. C. M. van Hest, *J. Mater. Chem.* **2011**, *21*, 18923–18926.
- [12] R. Wichmann, D. Vasic-Racki, *Adv. Biochem. Engin./Biotechnol.* **2005**, *92*, 225–260.
- [13] R. G. Kemp, I. A. Rose, *J. Biol. Chem.* **1964**, *239*, 2998–3006.
- [14] P. Rowland, A. K. Basak, S. Gover, H. R. Levy, M. J. Adams, *Structure* **1994**, *2*, 1073–1087.
- [15] M. S. Cosgrove, C. Naylor, S. Paludan, M. J. Adams, H. R. Levy, *Biochem.* **1998**, *2960*, 2759–2767.
- [16] M. S. Cosgrove, S. N. Loh, J.-H. Ha, H. R. Levy, *Biochemi.* **2002**, *41*, 6939–6945.
- [17] C. Olive, M. E. Geroch, H. R. Levy, *J. Biol. Chem.* **1971**, *246*, 2047–2054.
- [18] W. H. Schwarz, *Appl. Microbiol.. Biotechnol.* **2001**, *56*, 634–649.
- [19] E. M. Rubin, *Nature* **2008**, *454*, 841–815.
- [20] E. a Bayer, H. Chanzy, R. Lamed, Y. Shoham, *Curr. Opin. Struct. Biol.* **1998**, *8*, 548–557.
- [21] E. a Bayer, J.-P. Belaich, Y. Shoham, R. Lamed, *Annu. Rev. Microbiol.* **2004**, *58*, 521–54.
- [22] E. M. Rubin, *Nature* **2008**, *454*, 841–815.
- [23] R. H. Doi, A. Kosugi, *Nat. Rev. Microbiol.* **2004**, *2*, 541–551.

- [24] S. W. Stahl, M. A. Nash, D. B. Fried, M. Slutzki, Y. Barak, E. A. Bayer, H. E. Gaub, *PNAS* **2012**, *109*, 20431–20436.
- [25] E. A. Bayer, J.-P. Belaich, Y. Shoham, R. Lamed, *Annu. Rev. Biochem.* **2004**, *58*, 521–554.
- [26] J. Tormo, R. Lamed, A. J. Chirino, E. Morag, E. A. Bayer, Y. Shoham, T. A. Steitz, *EMBO J.* **1996**, *15*, 5739–5751.
- [27] C. M. G. A. Fontes, H. J. Gilbert, *Annu. Rev. Biochem.* **2010**, *79*, 655–681.
- [28] A. L. Carvalho, F. M. V Dias, J. a M. Prates, T. Nagy, H. J. Gilbert, G. J. Davies, L. M. A. Ferreira, M. J. Romão, C. M. G. A. Fontes, *PNAS* **2003**, *100*, 13809–13814.
- [29] U. T. Bornscheuer, *Angew. Chem. Int. Ed.* **2003**, *42*, 3336–3337.
- [30] C. Garcia-Galan, Á. Berenguer-Murcia, R. Fernandez-Lafuente, R. C. Rodrigues, *Adv. Synth. Catal.* **2011**, *353*, 2885–2904.
- [31] U. Hanefeld, L. Gardossi, E. Magner, *Chem. Soc. Rev.* **2009**, *38*, 453–468.
- [32] C. Mateo, J. M. Palomo, G. Fernandez-Lorente, J. M. Guisan, R. Fernandez-Lafuente, *Enzym. Microb. Technol.* **2007**, *40*, 1451–1463.
- [33] R. Fernandez-Lafuente, *Enzym. Microb. Technol.* **2009**, *45*, 405–418.
- [34] K. C. Dee, D. A. Puleo, R. Bizios, *An Introduction To Tissue-Biomaterial Interactions*, John Wiley & Sons, Inc., New York, USA, **2002**.
- [35] P. Wang, S. Dai, S. D. Waezsada, A. Y. Tsao, B. H. Davison, *Biotech. Bioeng.* **2001**, *74*, 249–55.
- [36] C.-H. Lee, T.-S. Lin, C.-Y. Mou, *Nano Today* **2009**, *4*, 165–179.
- [37] M. Hartmann, D. Jung, *J. Mater. Chem.* **2010**, *20*, 844–857.
- [38] R. C. Rodrigues, Á. Berenguer-Murcia, R. Fernandez-Lafuente, *Adv. Synth. Catal.* **2011**, *353*, 2216–2238.
- [39] Y. Wan, D. Zhao, *Chem. Rev.* **2007**, *107*, 2821–2860.
- [40] C. T. Kresge, M. E. Leonowicz, W. J. Roth, J. C. Vartuli, J. S. Beck, *Nature* **1992**, *359*, 710–712.
- [41] J. S. Beck, J. C. Vartuli, W. J. Roth, M. E. Leonowicz, C. T. Kresge, K. D. Schmitt, C. T. W. Chu, D. H. Olson, E. W. Sheppard, *J. Am. Chem. Soc.* **1992**, *114*, 10834–10843.
- [42] D. Zhao, J. Feng, H. Qisheng, N. Melosh, G. H. Fredrickson, B. F. Chmelka, G. D. Stucky, *Science (80-)* **1998**, *279*, 548–552.
- [43] P. Schmidt-Winkel, W. W. Lukens, D. Zhao, P. Yang, B. F. Chmelka, G. D. Stucky, *J. Am. Chem. Soc.* **1999**, *121*, 254–255.
- [44] F. Kleitz, S. H. Choi, R. Ryoo, *Chem. Commun.* **2003**, 2136–2137.
- [45] C. Yu, Y. Yu, D. Zhao, *Chem. Commun.* **2000**, 575–576.

- [46] J. Fan, C. Yu, F. Gao, J. Lei, B. Tian, L. Wang, Q. Luo, B. Tu, W. Zhou, D. Zhao, *Angew. Chem. Int. Ed.* **2003**, *42*, 3146–3150.
- [47] F. Hoffmann, M. Cornelius, J. Morell, M. Fröba, *Angew. Chem. Int. Ed.* **2006**, *45*, 3216–3251.
- [48] C. Liang, Z. Li, S. Dai, *Angew. Chem. Int. Ed.* **2008**, *47*, 3696–3717.
- [49] S. Jun, S. H. Joo, R. Ryoo, M. Kruk, M. Jaroniec, Z. Liu, T. Ohsuna, O. Terasaki, *J. Am. Chem. Soc.* **2000**, *122*, 10712–10713.
- [50] A. Vinu, M. Miyahara, V. Sivamurugan, T. Mori, K. Ariga, *J. Mater. Chem.* **2005**, *15*, 5122–5127.
- [51] Y. Meng, D. Gu, F. Zhang, Y. Shi, L. Cheng, D. Feng, Z. Wu, Z. Chen, Y. Wan, A. Stein, et al., *Chem. Mater.* **2006**, *18*, 4447–4464.
- [52] Y. Oda, K. Fukuyama, K. Nishikawa, S. Namba, H. Yoshitake, T. Tatsumi, *Chem. Mater.* **2004**, *16*, 3860–3866.
- [53] A. Stein, *Microporous Mesoporous Mater.* **2001**, *44-45*, 227–239.
- [54] F. Schüth, *Angew. Chem. Int. Ed.* **2003**, *42*, 3604–3622.
- [55] G. S. Attard, J. C. Glyde, C. G. Göltner, *Nature* **1995**, *378*, 366–368.
- [56] A. Monnier, F. Schüth, Q. Huo, D. Kumar, D. Margolese, R. S. Maxwell, G. D. Stucky, M. Krishnamurty, P. M. Petroff, A. Firouzi, et al., *Science (80-.)*. **1993**, *261*, 1299–1303.
- [57] M. A. Carreon, V. V. Guliants, *Eur. J. Inorg. Chem.* **2005**, *2005*, 27–43.
- [58] Y. Ren, Z. Ma, P. G. Bruce, *Chem. Soc. Rev.* **2012**, *41*, 4909–4927.
- [59] J. Lee, J. Kim, T. Hyeon, *Adv. Mater.* **2006**, *18*, 2073–2094.
- [60] P. Zhang, Z. Wu, N. Xiao, L. Ren, X. Meng, C. Wang, F. Li, Z. Li, F.-S. Xiao, *Langmuir* **2009**, *25*, 13169–13175.
- [61] P. Schmidt-Winkel, C. J. Glinka, G. D. Stucky, *Langmuir* **2000**, *16*, 356–361.
- [62] J. S. Lettow, Y. J. Han, P. Schmidt-Winkel, P. Yang, D. Zhao, G. D. Stucky, J. Y. Ying, *Langmuir* **2000**, *16*, 8291–8295.
- [63] P. Schmidt-Winkel, W. W. Lukens, P. Yang, D. I. Margolese, J. S. Lettow, J. Y. Ying, G. D. Stucky, *Chem. Mater.* **2000**, *12*, 686–696.
- [64] K.-J. Liu, J. L. Parsons, *Macromolecules* **1969**, *2*, 529–533.
- [65] S. L. Nolan, R. J. Phillips, P. M. Cotts, S. R. Dungan, *J. Colloid Interface Sci.* **1997**, *191*, 291–302.
- [66] J. C. Brinker, *Sol-Gel Science*, Academic Press, San Diego, **1990**.
- [67] E. Serra, Á. Mayoral, Y. Sakamoto, R. M. Blanco, I. Díaz, *Microporous Mesoporous Mater.* **2008**, *114*, 201–213.

- [68] S. Inagaki, S. Guan, T. Ohsuna, O. Terasaki, *Nature* **2002**, *416*, 304–307.
- [69] J. Liu, C. Li, Q. Yang, J. Yang, C. Li, *Langmuir* **2007**, *23*, 7255–7262.
- [70] A. Katiyar, S. Yadav, P. G. Smirniotis, N. G. Pinto, *J. Chromatogr., A* **2006**, *1122*, 13–20.
- [71] J. Sun, H. Zhang, R. Tian, D. Ma, X. Bao, D. S. Su, H. Zou, *Chem. Commun.* **2006**, *1*, 1322–1324.
- [72] W. Shan, B. Wang, Y. Zhang, Y. Tang, *Chem. Commun.* **2005**, 1877–1879.
- [73] S.-Y. Chen, Y.-T. Chen, J.-J. Lee, S. Cheng, *J. Mater. Chem.* **2011**, *21*, 5693–5703.
- [74] G. Zhou, Y. Chen, S. Yang, *Microporous Mesoporous Mater.* **2009**, *119*, 223–229.
- [75] E. Weber, D. Sirim, T. Schreiber, B. Thomas, J. Pleiss, M. Hunger, R. Gläser, V. B. Urlacher, *J. Mol. Catal. B* **2010**, *64*, 29–37.
- [76] T. Noji, C. Kamidaki, K. Kawakami, J.-R. Shen, T. Kajino, Y. Fukushima, T. Sekitoh, S. Itoh, *Langmuir* **2011**, *27*, 705–713.
- [77] A. Takimoto, T. Shiomi, K. Ino, T. Tsunoda, A. Kawai, F. Mizukami, *Microporous Mesoporous Mater.* **2008**, *116*, 601–606.
- [78] A. Vinu, N. Gokulakrishnan, V. V Balasubramanian, S. Alam, M. P. Kapoor, K. Ariga, T. Mori, *Chem. Eur. J.* **2008**, *14*, 11529–11538.
- [79] S. Águila, R. Vazquez-Duhalt, C. Covarrubias, G. Pecchi, J. B. Alderete, *J. Mol. Catal. B* **2011**, *70*, 81–87.
- [80] J. Aburto, M. Ayala, I. Bustos-Jaimes, C. Montiel, E. Terrés, J. M. Domínguez, E. Torres, *Microporous Mesoporous Mater.* **2005**, *83*, 193–200.
- [81] H. Takahashi, B. Li, T. Sasaki, C. Miyazaki, T. Kajino, S. Inagaki, *Chem. Mater.* **2000**, *12*, 3301–3305.
- [82] Y.-J. Han, J. T. Watson, G. D. Stucky, A. Butler, *J. Mol. Catal. B* **2002**, *17*, 1–8.
- [83] L. Washmon-Kriel, V. L. Jimenez, K. J. Balkus Jr, *J. Mol. Catal. B* **2000**, *10*, 453–469.
- [84] C. Bernal, L. Sierra, M. Mesa, *ChemCatChem* **2011**, *3*, 1948–1954.
- [85] W. Guo, H. Bi, L. Qiao, J. Wan, K. Qian, H. H. Girault, B. Liu, *Mol. BioSyst.* **2011**, *7*, 2890–2898.
- [86] Z. Sun, Y. Deng, J. Wei, D. Gu, B. Tu, D. Zhao, *Chem. Mater.* **2011**, *23*, 2176–2184.
- [87] J. Zhao, Y. Wang, G. Luo, S. Zhu, *Bioresour. Technol.* **2011**, *102*, 529–535.
- [88] D. B. Gornowich, G. J. Blanchard, *J. Phys. Chem. B* **2012**, *116*, 12165–12171.
- [89] L.-C. Sang, A. Vinu, M.-O. Coppens, *Langmuir* **2011**, *27*, 13828–13837.
- [90] S. Budi Hartono, S. Z. Qiao, J. Liu, K. Jack, B. P. Ladewig, Z. Hao, G. Q. Lu, *J. Phys. Chem. B* **2010**, *114*, 8353–8362.

- [91] S. Budi Hartono, S. Z. Qiao, K. Jack, B. P. Ladewig, Z. Hao, G. Q. M. Lu, *Langmuir* **2009**, *25*, 6413–6424.
- [92] K. Szymanska, J. Bryjak, J. Mrowiec-Bialon, A. B. Jsrzebski, *Microporous Mesoporous Mater.* **2007**, *99*, 167–175.
- [93] M. Shakeri, K. Kawakami, *Microporous Mesoporous Mater.* **2009**, *118*, 115–120.
- [94] E. Serra, E. Díez, I. Díaz, R. M. Blanco, *Microporous Mesoporous Mater.* **2010**, *132*, 487–493.
- [95] P. H. Pandya, R. V. Jasra, B. L. Newalkar, P. N. Bhatt, *Microporous Mesoporous Mater.* **2005**, *77*, 67–77.
- [96] J. Kim, R. J. Desch, S. W. Thiel, V. V. Guliants, N. G. Pinto, *J. Chromatogr., A* **2011**, *1218*, 7796–7803.
- [97] J. Kim, R. J. Desch, S. W. Thiel, V. V. Guliants, N. G. Pinto, *Microporous Mesoporous Mater.* **2012**, *149*, 60–68.
- [98] H. Essa, E. Magner, J. Cooney, B. K. Hodnett, *J. Mol. Catal. B* **2007**, *49*, 61–68.
- [99] D. I. Fried, K. Tropp, M. Fröba, *ChemCatChem* **2013**, *5*, 931–938.
- [100] S. E. Baker, A. M. Sawvel, J. Fan, Q. Shi, N. Strandwitz, G. D. Stucky, *Langmuir* **2008**, *24*, 14254–14260.
- [101] D. Jung, M. Paradiso, D. Wallacher, A. Brandt, M. Hartmann, *ChemSusChem* **2009**, *2*, 161–164.
- [102] Q. Jin, G. Jia, Y. Zhang, Q. Yang, C. Li, *Langmuir* **2011**, *27*, 12016–12024.
- [103] J. Lee, J. Kim, J. Kim, H. Jia, M. Il Kim, J. H. Kwak, S. Jin, A. Dohnalkova, H. G. Park, H. N. Chang, et al., *Small* **2005**, *1*, 744–753.
- [104] P. A. Russo, M. M. L. Ribeiro Carrott, P. A. M. Mourão, P. J. M. Carrott, *Colloids Surf., A* **2011**, *386*, 25–35.
- [105] Y. Zhang, L. Zhao, J. Li, H. Zhang, L. Zheng, S. Cao, C. Li, *Biochem. Biophys. Res. Commun.* **2008**, *372*, 650–655.
- [106] H. Zhou, Y. Qu, Y. Bu, X. Li, C. Kong, Q. Ma, Q. Zhang, X. Zhang, J. Zhou, *Chempluschem* **2012**, *77*, 293–300.
- [107] J. Deere, E. Magner, J. G. Wall, B. K. Hodnett, *J. Phys. Chem. B* **2002**, *106*, 7340–7347.
- [108] H. Essa, E. Magner, J. Cooney, B. K. Hodnett, *J. Mol. Catal. B* **2007**, *49*, 61–68.
- [109] L. Giussani, E. Fois, E. Gianotti, G. Tabacchi, A. Gamba, S. Coluccia, *ChemPhysChem* **2010**, *11*, 1757–1762.
- [110] C. Lei, T. A. Soares, Y. Shin, J. Liu, E. J. Ackerman, *Nanotechnology* **2008**, *19*, 125102–125111.
- [111] L. Zhu, K. Wang, T. Lu, W. Xing, J. Li, X. Yang, *J. Mol. Catal. B* **2008**, *55*, 93–98.
- [112] B. E. Feller, J. T. Kellis, L. G. Cascão-Pereira, C. R. Robertson, C. W. Frank, *Langmuir* **2011**, *27*, 250–263.

- [113] S. Hudson, E. Magner, J. Cooney, B. K. Hodnett, *J. Phys. Chem. B* **2005**, *109*, 19496–19506.
- [114] M. Vinoba, M. Bhagiyalakshmi, S. K. Jeong, Y. I. Yoon, S. C. Nam, *J. Phys. Chem. B* **2011**, *115*, 20209–20216.
- [115] R. H.-Y. Chang, J. Jang, K. C.-W. Wu, *Green Chem.* **2011**, *13*, 2844–2850.
- [116] A. Galarneau, M. Mureseanu, S. Atger, G. Renard, F. Fajula, *New J. Chem.* **2006**, *30*, 562–571.
- [117] T. Itoh, R. Ishii, S. Matsuura, J. Mizuguchi, S. Hamakawa, T. Hanaoka, T. Tsunoda, F. Mizukami, *Colloids Surf. B* **2010**, *75*, 478–482.
- [118] S. Hudson, E. Magner, J. Cooney, B. K. Hodnett, *J. Phys. Chem. B* **2005**, *109*, 19496–19506.
- [119] B. Nohair, P. thi H. Thao, V. T. H. Nguyen, P. Q. Tien, D. T. Phuong, L. G. Hy, S. Kaliaguine, *J. Phys. Chem. B* **2012**, *116*, 10904–10912.
- [120] K. Qian, W. Gu, P. Yuan, F. Liu, Y. Wang, M. Monteiro, C. Yu, *Small* **2011**, *8*, 231–236.
- [121] S. Hudson, J. Cooney, B. K. Hodnett, E. Magner, *Chem. Mater.* **2007**, *19*, 2049–2055.
- [122] S. Z. Qiao, H. Djojoputro, Q. Hu, G. Q. Lu, *Prog. Solid State Chem.* **2006**, *34*, 249–256.
- [123] S. Z. Qiao, C. Z. Yu, W. Xing, Q. H. Hu, H. Djojoputro, G. Q. Lu, *Chem. Mater.* **2005**, *17*, 6172–6176.
- [124] Z. Zhou, A. Inayat, W. Schwieger, M. Hartmann, *Microporous Mesoporous Mater.* **2012**, *154*, 133–141.
- [125] T. Asefa, M. J. MacLachlan, N. Coombs, G. A. Ozin, *Nature* **1999**, *402*, 867–871.
- [126] B. J. Melde, B. T. Holland, C. F. Blanford, A. Stein, *Chem. Mater.* **1999**, *11*, 3302–3308.
- [127] S. Inagaki, S. Guan, Y. Fukushima, T. Ohsuna, O. Terasaki, *J. Am. Chem. Soc.* **1999**, *121*, 9611–9614.
- [128] W. Na, Q. Wei, J.-N. Lan, Z.-R. Nie, H. Sun, Q.-Y. Li, *Microporous Mesoporous Mater.* **2010**, *134*, 72–78.
- [129] C. Li, J. Liu, X. Shi, J. Yang, Q. Yang, *J. Phys. Chem. B* **2007**, *111*, 10948–10954.
- [130] M. M. Wan, L. Gao, Z. Chen, Y. K. Wang, Y. Wang, J. H. Zhu, *Microporous Mesoporous Mater.* **2012**, *155*, 24–33.
- [131] T. J. Pisklak, M. Macías, D. H. Coutinho, R. S. Huang, K. J. Balkus, *Top. Catal.* **2006**, *38*, 269–278.
- [132] J. Gan, J. Zhu, G. Yan, Y. Liu, P. Yang, B. Liu, *Anal. Chem.* **2012**, *84*, 5809–5815.
- [133] X. Wang, D. Lu, R. Austin, A. Agarwal, L. J. Mueller, Z. Liu, J. Wu, P. Feng, *Langmuir* **2007**, *23*, 5735–5739.
- [134] M. S. Bhattacharyya, P. Hiwale, M. Piras, L. Medda, D. Steri, M. Piludu, A. Salis, M. Monduzzi, *J. Phys. Chem. B* **2010**, *114*, 19928–19934.
- [135] E. Serra, E. Díez, I. Díaz, R. M. Blanco, *Microporous Mesoporous Mater.* **2010**, *132*, 487–493.

- [136] M. Park, S. S. Park, M. Selvaraj, D. Zhao, C. Ha, *Microporous Mesoporous Mater.* **2009**, *124*, 76–83.
- [137] Z. Zhou, R. N. K. Taylor, S. Kullmann, H. Bao, M. Hartmann, *Adv. Mater.* **2011**, *23*, 2627–2632.
- [138] O. Muth, C. Schellbach, M. Fröba, *Chem. Commun.* **2001**, 2032–2033.
- [139] L. Zhu, X. Liu, T. Chen, Z. Xu, W. Yan, H. Zhang, *Appl. Surf. Sci.* **2012**, *258*, 7126–7134.
- [140] J. Wan, K. Qian, J. Zhang, F. Liu, Y. Wang, P. Yang, B. Liu, C. Yu, *Langmuir* **2010**, *26*, 7444–7450.
- [141] P. Wang, L. Zhao, R. Wu, H. Zhong, H. Zou, J. Yang, Q. Yang, *J. Phys. Chem. B* **2009**, *113*, 1359–1366.
- [142] S. El Hankari, B. Motos-Pérez, P. Hesemann, A. Bouhaouss, J. J. E. Moreau, *Chem. Commun.* **2011**, *47*, 6704–6706.
- [143] K. Wang, H. Yang, L. Zhu, Z. Ma, S. Xing, Q. Lv, J. Liao, C. Liu, W. Xing, *Electrochim. Acta* **2009**, *54*, 4626–4630.
- [144] S. Pei, S. Qu, Y. Zhang, *Sensors* **2010**, *10*, 1279–1290.
- [145] X. Lu, Y. Xiao, Z. Lei, J. Chen, *Biosens. Bioelectron.* **2009**, *25*, 244–247.
- [146] M. Quirós, A. B. García, M. A. Montes-Morán, *Carbon N. Y.* **2011**, *49*, 406–415.
- [147] M. Sevilla, P. Valle-Vigón, P. Tartaj, A. B. Fuertes, *Carbon N. Y.* **2009**, *47*, 2519–2527.
- [148] L.-C. Sang, A. Vinu, M.-O. Coppens, *Langmuir* **2011**, *27*, 13828–37.
- [149] J. Yu, J. Tu, F. Zhao, B. Zeng, *J. Solid State Chem.* **2010**, *14*, 1595–1600.
- [150] L. J. Kennedy, P. K. Selvi, A. Padmanabhan, K. N. Hema, G. Sekaran, *Chemosphere* **2007**, *69*, 262–270.
- [151] R. Gadiou, E. a dos Santos, M. Vijayaraj, K. Anselme, J. Dentzer, G. a Soares, C. Vix-Guterl, *Colloids Surf., B* **2009**, *73*, 168–174.
- [152] M. Il Kim, Y. Ye, B. Y. Won, S. Shin, J. Lee, H. G. Park, *Adv. Funct. Mater.* **2011**, *21*, 2868–2875.
- [153] G. Yushin, E. N. Hoffman, M. W. Barsoum, Y. Gogotsi, C. a Howell, S. R. Sandeman, G. J. Phillips, A. W. Lloyd, S. V. Mikhalovsky, *Biomater.* **2006**, *27*, 5755–5762.
- [154] S. Wu, H. Ju, Y. Liu, *Adv. Funct. Mater.* **2007**, *17*, 585–592.
- [155] D. Lee, J. Lee, J. Kim, J. Kim, H. Bin Na, B. Kim, C.-H. Shin, J. H. Kwak, A. Dohnalkova, J. W. Grate, et al., *Adv. Mater.* **2005**, *17*, 2828–2833.
- [156] Y. Piao, D. Lee, J. Kim, J. Kim, T. Hyeon, H.-S. Kim, *Analyst* **2009**, *134*, 926–932.
- [157] K. Y. Kwon, J. Youn, J. H. Kim, Y. Park, C. Jeon, B. C. Kim, Y. Kwon, X. Zhao, P. Wang, B. I. Sang, et al., *Biosens. Bioelectron.* **2010**, *26*, 655–660.
- [158] A. Vinu, M. Miyahara, K. Ariga, *J. Phys. Chem. B* **2005**, *109*, 6436–6441.

- [159] A. Vinu, C. Streb, V. Murugesan, M. Hartmann, *J. Phys. Chem. B* **2003**, *107*, 8297–8299.
- [160] A. Vinu, M. Miyahara, T. Mori, K. Ariga, *J. Porous Mater.* **2006**, *13*, 379–383.
- [161] A. Vinu, K. Z. Hossian, P. Srinivasu, M. Miyahara, S. Anandan, N. Gokulakrishnan, T. Mori, K. Ariga, V. V. Balasubramanian, *J. Mater. Chem.* **2007**, *17*, 1819–1825.
- [162] H. Qin, P. Gao, F. Wang, L. Zhao, J. Zhu, A. Wang, T. Zhang, R. A. Wu, H. Zou, *Angew. Chem. Int. Ed.* **2011**, *50*, 1–5.
- [163] M. Vijayaraj, R. Gadiou, K. Anselme, C. Ghimbeu, C. Vix-Guterl, H. Orikasa, T. Kyotani, S. Ittisanronnachai, *Adv. Funct. Mater.* **2010**, *20*, 2489–2499.
- [164] A.-H. Lu, E. L. Salabas, F. Schüth, *Angew. Chem. Int. Ed.* **2007**, *46*, 1222–1244.
- [165] S. Laurent, D. Forge, M. Port, A. Roch, C. Robic, L. Vander Elst, R. N. Muller, *Chem. Rev.* **2008**, *108*, 2064–2110.
- [166] W. Wu, Q. He, C. Jiang, *Nanoscale Res. Lett.* **2008**, *3*, 397–415.
- [167] R. M. Cornell, U. Schwertmann, *The Iron Oxides - Structure, Properties, Reactions, Occurrences and Uses*, Wiley-VCH, Weinheim, **2003**.
- [168] A. S. Teja, P.-Y. Koh, *Prog. Cryst. Growth Charact. Mater.* **2009**, *55*, 22–45.
- [169] L. H. Andrade, L. P. Rebelo, C. G. C. M. Netto, H. E. Toma, *J. Mol. Catal. B* **2010**, *66*, 55–62.
- [170] A. S. Demir, F. N. Talpur, S. Betül Sopacı, G.-W. Kohring, A. Celik, *J. Biotechnol.* **2011**, *152*, 176–183.
- [171] M. J. Khan, Q. Husain, A. Azam, *Biotechnol. Bioprocess Eng.* **2012**, *17*, 377–384.
- [172] M. Tudorache, A. Nae, S. Coman, V. I. Parvulescu, *RSC Adv.* **2013**, *3*, 4052–4058.
- [173] W. Xie, N. Ma, *Biomass Bioenergy* **2010**, *34*, 890–896.
- [174] W. Xie, N. Ma, *Energy Fuels* **2009**, *23*, 1347–1353.
- [175] M. Il Kim, Y. Ye, B. Y. Won, S. Shin, J. Lee, H. G. Park, *Adv. Funct. Mater.* **2011**, *21*, 2868–2875.
- [176] J. Kim, J. Lee, H. Bin Na, B. C. Kim, J. K. Youn, J. H. Kwak, K. Moon, E. Lee, J. Kim, J. Park, et al., *Small* **2005**, *1*, 1203–1207.
- [177] J. Lee, D. Lee, E. Oh, J. Kim, Y.-P. Kim, S. Jin, H.-S. Kim, Y. Hwang, J. H. Kwak, J.-G. Park, et al., *Angew. Chem. Int. Ed.* **2005**, *44*, 7427–7432.
- [178] J. Lee, H. Bin Na, B. C. Kim, J. H. Lee, B. Lee, J. H. Kwak, Y. Hwang, J.-G. Park, M. B. Gu, J. Kim, et al., *J. Mater. Chem.* **2009**, *19*, 7864–7870.
- [179] S. S. Lee, S. N. Riduan, N. Erathodiyil, J. Lim, J. L. Cheong, J. Cha, Y. Han, J. Y. Ying, *Chem. Eur. J.* **2012**, *18*, 7394–7403.
- [180] Y. Liu, Z. Zeng, G. Zeng, L. Tang, Y. Pang, Z. Li, C. Liu, X. Lei, M. Wu, P. Ren, et al., *Bioresour. Technol.* **2012**, *115*, 21–26.

- [181] R. Konwarh, D. Kalita, C. Mahanta, M. Mandal, N. Karak, *Appl. Microbiol. Biotechnol.* **2010**, *87*, 1983–1992.
- [182] S. Y. Lee, S. Lee, I. H. Kho, J. H. Lee, J. H. Kim, J. H. Chang, *Chem. Commun.* **2011**, *47*, 9989–9991.
- [183] M. Sureshkumar, C.-K. Lee, *Carbohydr. Polym.* **2011**, *84*, 775–780.
- [184] M. Vinoba, M. Bhagiyalakshmi, S. K. Jeong, S. C. Nam, Y. Yoon, *Chem. Eur. J.* **2012**, *18*, 12028–12034.
- [185] T. Valdés-Solís, A. F. Rebolledo, M. Sevilla, P. Valle-Vigón, O. Bomati-Miguel, A. B. Fuertes, P. Tartaj, *Chem. Mater.* **2009**, *21*, 1806–1814.
- [186] S. Wang, P. Su, J. Huang, J. Wu, Y. Yang, *J. Mater. Chem. B* **2013**, *1*, 1749–1754.
- [187] F. Wang, C. Guo, L. Yang, C.-Z. Liu, *Bioresour. Technol.* **2010**, *101*, 8931–8935.
- [188] E. Woo, K. M. Ponvel, I.-S. Ahn, C.-H. Lee, *J. Mater. Chem.* **2010**, *20*, 1511–1515.
- [189] Y. Zhu, S. Kaskel, J. Shi, T. Wage, K.-H. van Pée, *Chem. Mater.* **2007**, *19*, 6408–6413.
- [190] Y. Zhuo, P.-X. Yuan, R. Yuan, Y.-Q. Chai, C.-L. Hong, *Biomater.* **2009**, *30*, 2284–2290.
- [191] L. Zhang, S. Qiao, Y. Jin, H. Yang, S. Budi Hartono, F. Stahr, Z. Yan, X. Wang, Z. Hao, G. Q. Lu, *Adv. Funct. Mater.* **2008**, *18*, 3203–3212.
- [192] J. Lee, J. Kim, J. Kim, H. Jia, M. Il Kim, J. H. Kwak, S. Jin, A. Dohnalkova, H. G. Park, H. N. Chang, et al., *Small* **2005**, *1*, 744–753.
- [193] M. Kalantari, M. Kazemeini, F. Tabandeh, A. Arpanaei, *J. Mater. Chem.* **2012**, *22*, 8385–8393.
- [194] M. Sevilla, P. Valle-Vigón, P. Tartaj, A. B. Fuertes, *Carbon N. Y.* **2009**, *47*, 2519–2527.
- [195] R. A. Sheldon, *Chem. Commun.* **2008**, 3352–3365.
- [196] Y.-H. P. Zhang, L. R. Lynd, *Biotech. Bioeng.* **2004**, *88*, 797–824.
- [197] R. Rinaldi, F. Schüth, *Energy Environ. Sci.* **2009**, *2*, 610–626.
- [198] S.-H. Jun, J. Lee, B. C. Kim, J. E. Lee, J. Joo, H. Park, J. H. Lee, S.-M. Lee, D. Lee, S. Kim, et al., *Chem. Mater.* **2012**, *24*, 924–929.
- [199] A. L. Machsun, M. Gozan, M. Nasikin, S. Setyahadi, Y. J. Yoo, *Biotechnol. Bioprocess Eng.* **2011**, *15*, 911–916.
- [200] A. Salis, D. Meloni, S. Ligas, M. F. Casula, M. Monduzzi, V. Solinas, E. Dumitriu, *Langmuir* **2005**, *21*, 5511–5516.
- [201] G. Banerjee, J. S. Scott-Craig, J. D. Walton, *BioEnergy Res.* **2010**, *3*, 82–92.
- [202] M. J. Khan, Q. Husain, A. Azam, *Biotechnol. Bioprocess Eng.* **2012**, *17*, 377–384.
- [203] A. K. Mukherjee, T. S. Kumar, S. K. Rai, J. K. Roy, *Biotechnol. Bioprocess Eng.* **2011**, *15*, 984–992.

- [204] K. Yang, N.-S. Xu, W. W. Su, *J. Biotechnol.* **2010**, *148*, 119–127.
- [205] M. Vinoba, M. Bhagiyalakshmi, S. K. Jeong, Y. I. Yoon, S. C. Nam, *J. Mol. Catal. B* **2012**, *75*, 60–67.
- [206] Y. Yu, B. Chen, W. Qi, X. Li, Y. Shin, C. Lei, J. Liu, *Microporous Mesoporous Mater.* **2012**, *153*, 166–170.
- [207] L. Fernando Bautista, G. Morales, R. Sanz, *Bioresour. Technol.* **2010**, *101*, 8541–8548.
- [208] A. Salis, M. Pisano, M. Monduzzi, V. Solinas, E. Sanjust, *J. Mol. Catal. B* **2009**, *58*, 175–180.
- [209] H. Zhang, E. Xun, J. Wang, G. Chen, T. Cheng, Z. Wang, T. Ji, L. Wang, *Int. J. Mol. Sci.* **2012**, *13*, 5998–6008.
- [210] E. T. Hwang, B. Lee, M. Zhang, S.-H. Jun, J. Shim, J. Lee, J. Kim, M. B. Gu, *Green Chem.* **2012**, *14*, 1884–1887.
- [211] Y. Zhang, J. Li, D. Han, H. Zhang, P. Liu, C. Li, *Biochem. Biophys. Res. Commun.* **2008**, *365*, 609–613.
- [212] D. Jung, C. Streb, M. Hartmann, *Microporous Mesoporous Mater.* **2008**, *113*, 523–529.
- [213] P. Mäki-Arvela, S. Sahin, N. Kumar, T. Heikkilä, V.-P. Lehto, T. Salmi, D. Y. Murzin, *J. Mol. Catal. A* **2008**, *285*, 132–141.
- [214] L. T. Phuoc, P. Laveille, F. Chamouleau, G. Renard, J. Drone, B. Coq, F. Fajula, A. Galarneau, *Dalt. Trans.* **2010**, *39*, 8511–8520.
- [215] M. Eguílaz, R. Villalonga, P. Yáñez-Sedeño, J. M. Pingarrón, *Anal. Chem.* **2011**, *83*, 7807–7814.
- [216] Q. Dong, L.-M. Ouyang, H.-L. Yu, J.-H. Xu, *Carbohydr. Res.* **2010**, *345*, 1622–1626.
- [217] U. Kragl, W. Kruse, W. Hummel, C. Wandrey, *Biotech. Bioeng.* **1996**, *52*, 309–319.
- [218] K. Goldberg, A. Krueger, T. Meinhardt, W. Kroutil, B. Mautner, A. Liese, *Tetrahedron: Asymmetry* **2008**, *19*, 1171–1173.
- [219] J. Rocha-Martín, B. D. Las Rivas, R. Muñoz, J. M. Guisán, F. López-Gallego, *ChemCatChem* **2012**, *4*, 1279–1288.
- [220] A. Galarneau, G. Renard, M. Mureseanu, A. Tournette, C. Biolley, M. Choi, R. Ryoo, F. Di Renzo, F. Fajula, *Microporous and Mesoporous Mater.* **2007**, *104*, 103–114.
- [221] M. Vittorini, E. Dumitriu, G. Barletta, F. Secundo, *Bioprocess Biosys. Eng.* **2011**, *34*, 247–251.
- [222] K. S. W. Sing, D. H. Everett, R. A. W. Haul, L. Moscou, R. A. Pierotti, J. Rouquerol, T. Siemieniowska, *Pure App* **1985**, *57*, 603–619.
- [223] S. Brunauer, P. H. Emmett, E. Teller, *J. Am. Chem. Soc.* **1938**, *60*, 309–319.
- [224] E. P. Barrett, L. G. Joyner, P. P. Halenda, *J. Am. Chem. Soc.* **1951**, *73*, 373–380.
- [225] P. I. Ravikovitch, A. V Neimark, *Langmuir* **2006**, *22*, 11171–11179.

- [226] C. Lastoskie, K. E. Gubbins, N. Quirke, *J. Phys Chem.* **1993**, *97*, 4786–4796.
- [227] E.-P. Ng, S. Mintova, *Microporous Mesoporous Mater.* **2008**, *114*, 1–26.
- [228] M. Thommes, C. Morlay, R. Ahmad, J. P. Joly, *Adsorption* **2011**, *17*, 653–661.
- [229] M. W. Anderson, J. Klinowski, *J. Chem. Soc. Faraday Trans.* **1986**, *82*, 1449.
- [230] A. Giaya, R. W. Thompson, R. Denkwicz Jr, *Microporous Mesoporous Mater.* **2000**, *40*, 205–218.
- [231] D. . Olson, W. . Haag, W. . Borghard, *Microporous Mesoporous Mater.* **2000**, *35-36*, 435–446.
- [232] J. Stelzer, M. Paulus, M. Hunger, J. Weitkamp, *Microporous Mesoporous Mater.* **1998**, *22*, 1–8.
- [233] M. Thommes, S. Mitchell, J. Pérez-Ramírez, *J. Phys. Chem. C* **2012**, *116*, 18816–18823.
- [234] E.-P. Ng, S. Mintova, *Microporous Mesoporous Mater.* **2008**, *114*, 1–26.
- [235] A. Cauvel, D. Brunel, F. Di Renzo, E. Garrone, B. Fubini, *Langmuir* **1997**, *13*, 2773–2778.
- [236] K. Kaneko, Y. Hanzawa, T. Iiyama, T. Kanda, T. Suzuki, *Adsorption* **1999**, *13*, 7–13.
- [237] T. Ohba, H. Kanoh, K. Kaneko, *J. Phys. Chem. B* **2004**, *108*, 14964–14969.
- [238] M. Thommes, J. Morell, K. Cychosz, M. Fröba, *Langmuir* **2013**, DOI 10.1021/la402832b.
- [239] K. Kaneko, Y. Hanzawa, T. Iiyama, T. Kanda, T. Suzuki, *Adsorption* **1999**, *13*, 7–13.
- [240] T. Ohba, H. Kanoh, K. Kaneko, *J. Phys. Chem. B* **2004**, *108*, 14964–14969.
- [241] S. Lowell, J. E. Shields, M. A. Thomas, M. Thommes, *Characterization of Porous Solids and Powders: Surface Area, Pore Size and Density*, Springer, Dordrecht, **2006**.
- [242] H. Giesche, *Parti. Part. Syst. Charact.* **2006**, *23*, 9–19.
- [243] M. Thommes, R. Skudas, K. K. Unger, D. Lubda, *J. Chromatogr., A* **2008**, *1191*, 57–66.
- [244] J. Rouquerol, G. V. Baron, R. Denoyel, H. Giesche, J. Groen, P. Klobes, P. Levitz, A. V. Neimark, S. Rigby, R. Skudas, et al., *Microporous Mesoporous Mater.* **2012**, *154*, 2–6.
- [245] J. Rouquerol, G. Baron, R. Denoyel, H. Giesche, J. Groen, P. Klobes, P. Levitz, A. V. Neimark, S. Rigby, R. Skudas, et al., *Pure Appl. Chem.* **2012**, *84*, 107–136.
- [246] E. W. Washburn, *Phys. Rev.* **1921**, *17*, 273–283.
- [247] H. L. Ritter, L. C. Drake, *Ind. Eng. Chem., Anal. Ed.* **1945**, *17*, 782–786.
- [248] S. Lowell, J. . Shields, *J. Colloid Interface Sci.* **1981**, *80*, 192–196.
- [249] B. J. Berne, R. Pecora, *Dynamic Light Scattering*, Dover Publications Inc., New York, **2000**.
- [250] A. Einstein, *Ann. Phys.* **2005**, *14*, 182–193.

- [251] M. Kosmulski, **2009**.
- [252] H.-J. Butt, K. Graf, M. Kappl, *Physics and Chemistry of Interfaces*, Wiley-VCH, Weinheim, **2006**.
- [253] "www.zeta-meter.com," **2013**.
- [254] D. C. Henry, *Proc. Roy. Soc.* **1931**, *133*, 106–129.
- [255] D. C. Henry, *Trans. Faraday Soc.* **1948**, *44*, 1021–1026.
- [256] A. Liese, K. Seelbach, C. Wandrey, *Industrial Biotransformations*, Wiley-VCH, Weinheim, **2006**.
- [257] R. Wichmann, D. Vasic-Racki, *Adv. Biochem. Engin./Biotechnol.* **2005**, *92*, 225–260.
- [258] U. Kragl, W. Kruse, W. Hummel, C. Wandrey, *Biotech. Bioeng.* **1996**, *52*, 309–19.
- [259] W. Hummel, M. R. Kula, *Eur. J. Biochem.* **1989**, *184*, 1–13.
- [260] A. Vinu, K. Z. Hossian, P. Srinivasu, M. Miyahara, S. Anandan, N. Gokulakrishnan, T. Mori, K. Ariga, V. V. Balasubramanian, *J. Mater. Chem.* **2007**, *17*, 1819–1825.
- [261] M. Joubert, C. Delaite, E. Bourgeat-Lami, P. Dumas, *Macromol. Rapid Commun.* **2005**, *26*, 602–607.
- [262] H. Günzler, H.-U. Gremlich, *IR Spectroscopy*, Wiley-VCH, Weinheim, Germany, **2002**.
- [263] X.-Y. Yang, Y. Li, A. Lemaire, J.-G. Yu, B.-L. Su, *Pure Appl. Chem.* **2009**, *81*, 2265–2307.
- [264] Z. Sun, Y. Deng, J. Wei, D. Gu, B. Tu, D. Zhao, *Chem. Mater.* **2011**, *23*, 2176–2184.
- [265] H. P. Boehm, *Carbon N. Y.* **2002**, *40*, 145–149.
- [266] M. F. Cardosi, *Methods Biotechnol.* **1997**, *1*, 217–222.
- [267] S. Kohl, A. Drochner, H. Vogel, *Catal. Today* **2010**, *150*, 67–70.
- [268] C. Olive, H. R. Levy, *J. Biol. Chem.* **1971**, *246*, 2043–2046.
- [269] D. Jung, C. Streb, M. Hartmann, *Int. J. Mol. Sci.* **2010**, *11*, 762–778.
- [270] A. Schlossbauer, D. Schaffert, J. Kecht, E. Wagner, T. Bein, *J. Am. Chem. Soc.* **2008**, *130*, 12558–12559.
- [271] H. Zhou, K. A. Dill, *Biochem.* **2001**, *40*, 11289–11293.
- [272] R. B. Bhatia, C. J. Brinker, A. K. Gupta, A. K. Singh, *Chem. Mater.* **2000**, *12*, 2434–2441.
- [273] S. A. Yamanaka, B. Dunn, J. S. Valentine, J. I. Zink, *J. Am. Chem. Soc.* **1995**, *117*, 9095–9096.
- [274] S. Y. Shimizu, H. M. Lenhoff, *J. Solid-Phase Biochem.* **1979**, *4*, 75–94.
- [275] H. K. Hall, *J. Am. Chem. Soc.* **1957**, *79*, 5441–5444.
- [276] J. C. Hicks, R. Dabestani, A. C. Buchanan, C. W. Jones, *Chem. Mater.* **2006**, *18*, 5022–5032.

- [277] M. W. McKittrick, C. W. Jones, *Chem. Mater.* **2003**, *15*, 1132–1139.
- [278] A. Walcarius, M. Etienne, B. Lebeau, *Chem. Mater.* **2003**, *15*, 2161–2173.
- [279] D. Brühwiler, *Nanoscale* **2010**, *2*, 887–892.
- [280] P. Somasundaran, T. W. Healy, D. W. Fuerstenau, *J. Phys. Chem.* **1964**, *68*, 3562–3566.
- [281] T. Deschner, Y. Liang, R. Anwender, *J. Phys. Chem. C* **2010**, *114*, 22603–22609.
- [282] R. E. Viola, *Arch. Biochem. Biophys.* **1984**, *228*, 415–424.
- [283] M. A. Firestone, M. L. Shank, S. G. Sligar, P. W. Bohn, *J. Am. Chem. Soc.* **1996**, *118*, 9033–9041.
- [284] M. Kotorman, L. M. Simon, B. Szajani, *Enzym. Microb Technol* **1994**, *16*, 974–978.
- [285] J.-R. Simons, Surface Interaction of Glucose-6-Phosphate Dehydrogenase: Reversible and Site-Specific Immobilization, Technical University of Hamburg Harburg, **2013**.
- [286] J. Huheey, E. Keiter, R. Keiter, *Anorganische Chemie*, Walter De Gruyter, Berlin, **1995**.
- [287] C. Wong, G. M. Whitesides, *J. Am. Chem. Soc.* **1981**, *103*, 4890–4899.
- [288] F. M. Veronese, E. Boccù, A. Fontana, C. A. Benassi, E. Scoffone, *Biochim. Biophys. Acta, Enz.* **1974**, *334*, 31–44.
- [289] S. Hanau, K. Montin, C. Cervellati, M. Magnani, F. Dallochio, *J. Biol. Chem.* **2010**, *285*, 21366–21371.
- [290] B. P. Pichon, M. Wong Chi Man, C. Bied, J. J. E. Moreau, *J. Organomet. Chem.* **2006**, *691*, 1126–1130.
- [291] R. C. Schroden, M. Al-Daous, S. Sokolov, B. J. Melde, J. C. Lytle, A. Stein, M. C. Carbajo, J. T. Fernandez, E. E. Rodriguez, *J. Mater. Chem.* **2002**, *12*, 3261–3267.
- [292] Z. Wang, A. Stein, *Chem. Mater.* **2008**, *20*, 1029–1040.
- [293] S. K. Vashist, C. K. Dixit, *Biochem. Biophys. Res. Commun.* **2011**, *411*, 455–457.
- [294] S. K. Vashist, B. Zhang, D. Zheng, K. Al-Rubeaan, J. H. T. Luong, F.-S. Sheu, *Analyt. Biochem.* **2011**, *417*, 156–158.
- [295] A. Gole, C. J. Murphy, *Langmuir* **2008**, *24*, 266–272.
- [296] Y. Deng, D. Qi, C. Deng, X. Zhang, D. Zhao, *J. Am. Chem. Soc.* **2008**, *130*, 28–29.
- [297] K. Egger, W. Feitknecht, *Helv. Chim. Acta* **1962**, *45*, 2042–2057.
- [298] M. Kar, P. S. Vijayakumar, B. L. V Prasad, S. Sen Gupta, *Langmuir* **2010**, *26*, 5772–5781.
- [299] W. Stöber, A. Fink, E. Bohn, *J. Colloid Interface Sci.* **1968**, *26*, 62–69.
- [300] X. Xu, C. Deng, M. Gao, W. Yu, P. Yang, X. Zhang, *Adv. Mater.* **2006**, *18*, 3289–3293.

- [301] D. I. Fried, F. J. Brieler, M. Fröba, *ChemCatChem* **2013**, *5*, 862–884.
- [302] E. F. Pettersen, T. D. Goddard, C. C. Huang, G. S. Couch, D. M. Greenblatt, E. C. Meng, T. E. Ferrin, *J. Comput. Chem.* **2004**, *25*, 1605–1612.

9 APPENDIX

9.1 SUPPLEMENTARY INFORMATION FOR CHAPTER 4

9.1.1 CALCULATION OF ACTIVITY FOR G6PDH

$$\text{Activity(Units/mL)} = \frac{A_{340\text{nm}}/\text{min}(\text{Sample}) - A_{340\text{nm}}/\text{min}(\text{Blank}) V_1 \cdot df}{\varepsilon \cdot V_2} \quad (\text{A1})$$

$A_{340\text{nm}}$ = Absorbance at 340 nm

ε = Extinction coefficient

V_1 = Total volume

V_2 = sample volume

df = dilution factor

9.1.2 CALCULATION OF THE FUNCTIONALIZATION DENSITY FOR MCF SAMPLES

$$\frac{m(\text{functionalization per g material})}{M(\text{organic residue})} = \delta_F \quad (\text{A2})$$

$$\delta_F \cdot (100 - \text{mass loss}(\%)) = \delta_F \quad (\text{A3})$$

9.1.3 CHANGE OF PH DURING GENERATION OF NADPH

The conversion of NADP^+ is coupled to a generation of protons. The pH change (Table S1) was monitored to proof that there is no influence of the pH on the performance of the biocatalysts during the activity measurements.

Table S1: Change of pH during the conversion of NADP⁺ to NADPH.

t / min	pH
1	7.27
5	7.26
10	7.26
12	7.27
20	7.26
30	7.25

9.1.4 BROMOCRESOL GREEN STAINING

The bromocresol staining was performed by using two drops of a bromocresol green solution (0.04% in ethanol). This solution was dropped on the specific MCF support on a filter paper. Depending on the acidity of the surface functional groups the acidic materials were colored yellow and the basic and neutral materials blue.

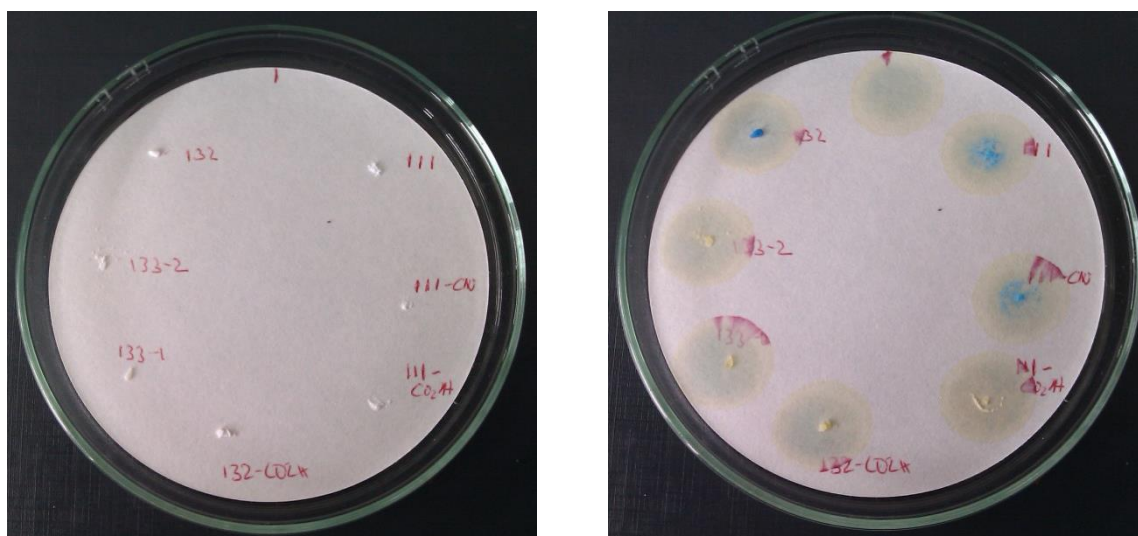


Figure S1: Bromocresol green staining of MCF supports. The yellow spots indicate carboxyl-modified MCF materials. Number 132 is MCF-NH₂ and number 111 pure MCF.

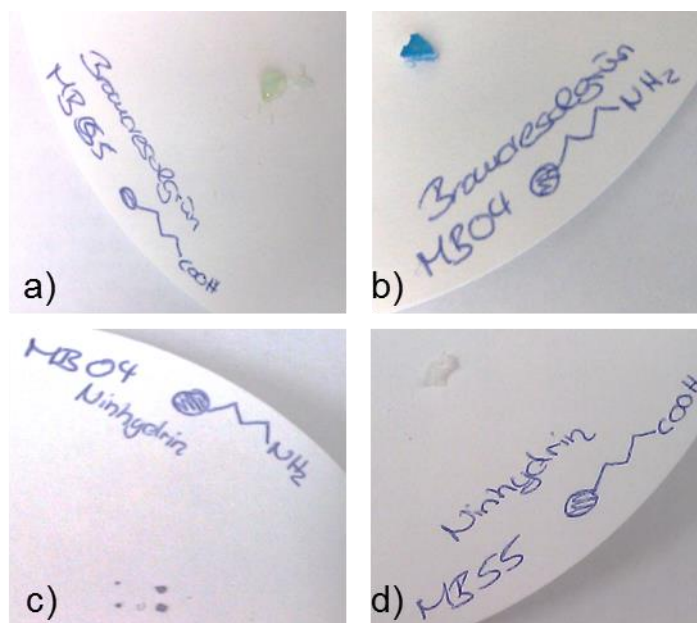


Figure S2: Bromocresol green and ninhydrin staining of functionalized silica nanoparticles. The yellow spots indicate carboxylic acid-modified silica nanoparticles by changing to bromokresol green stain to a yellow color whereas ninhydrin colors basic amine groups purple.

9.1.5 MICHAELIS-MENTEN KINETICS

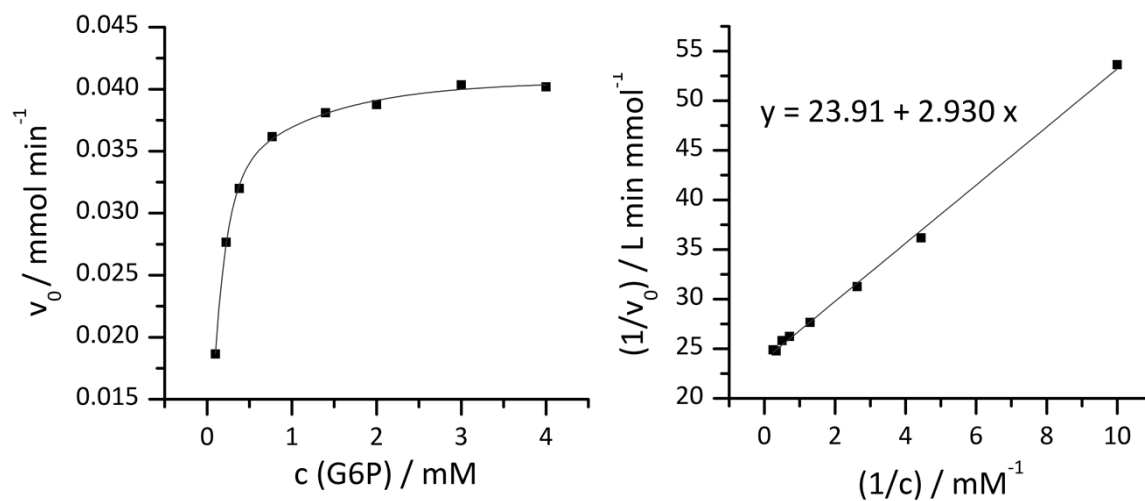


Figure S3: Michaelis-Menten and Lineweaver Burk plot of free G6PDH with varied G6P concentration at 37 °C.

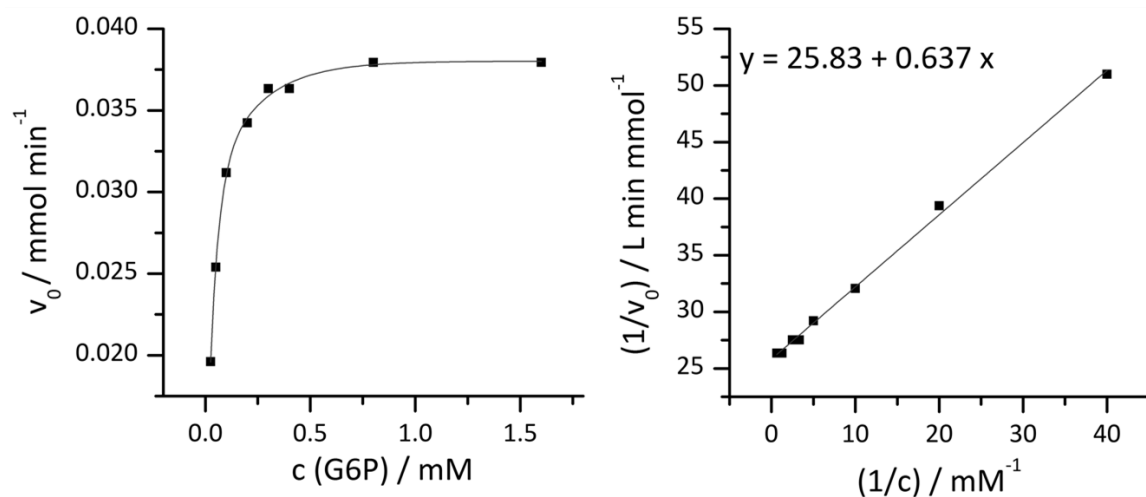


Figure S4: Michaelis-Menten and Lineweaver Burk plot of free G6PDH with varied NADP concentration at 37 °C.

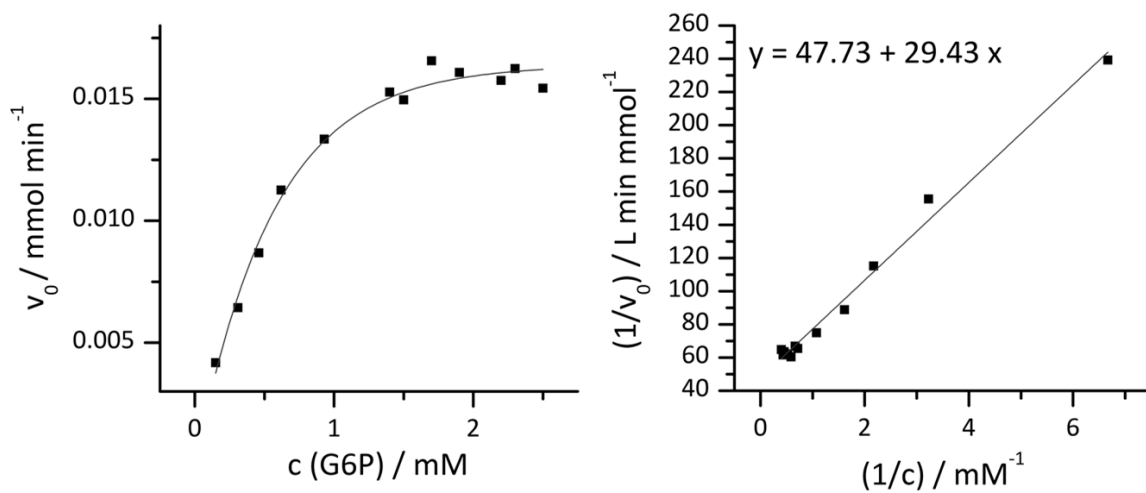


Figure S5: Michaelis-Menten and Lineweaver Burk plot of immobilized G6PDH with varied G6P concentration at 37 °C.

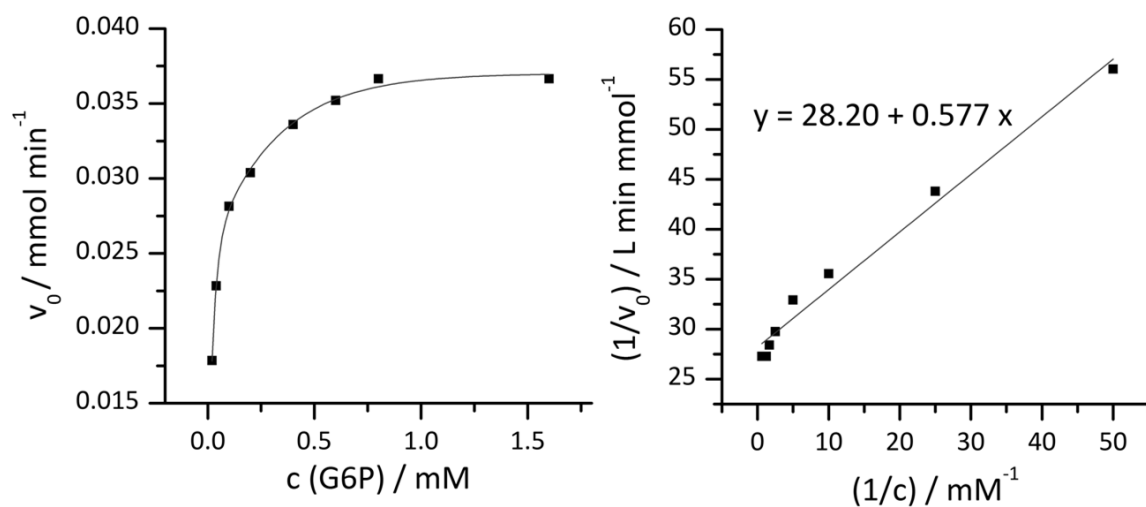


Figure S6: Michaelis-Menten and Lineweaver Burk plot of immobilized G6PDH with varied NADP concentration at 37 °C.

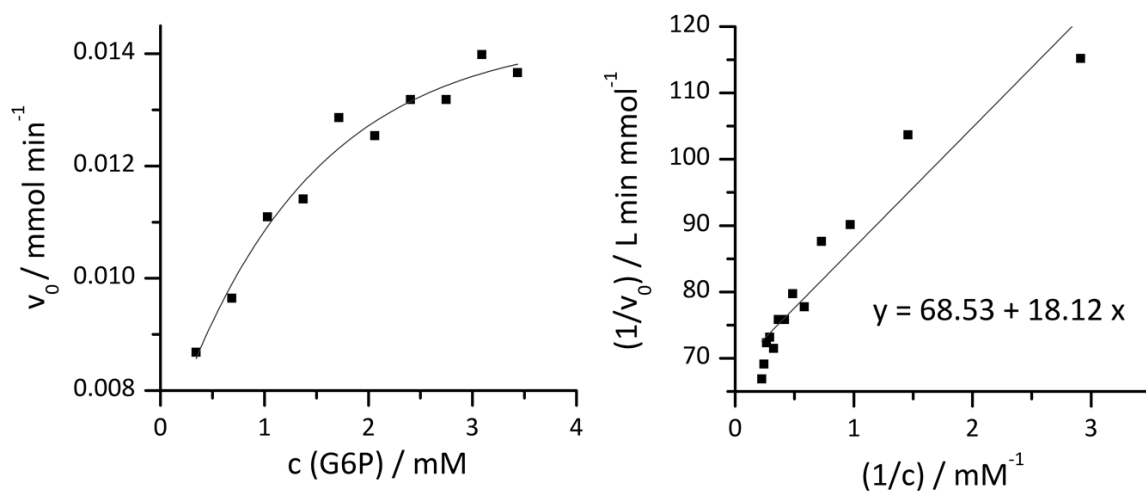


Figure S7: Michaelis-Menten and Lineweaver Burk plot of immobilized G6PDH with varied G6P concentration at 25 °C.

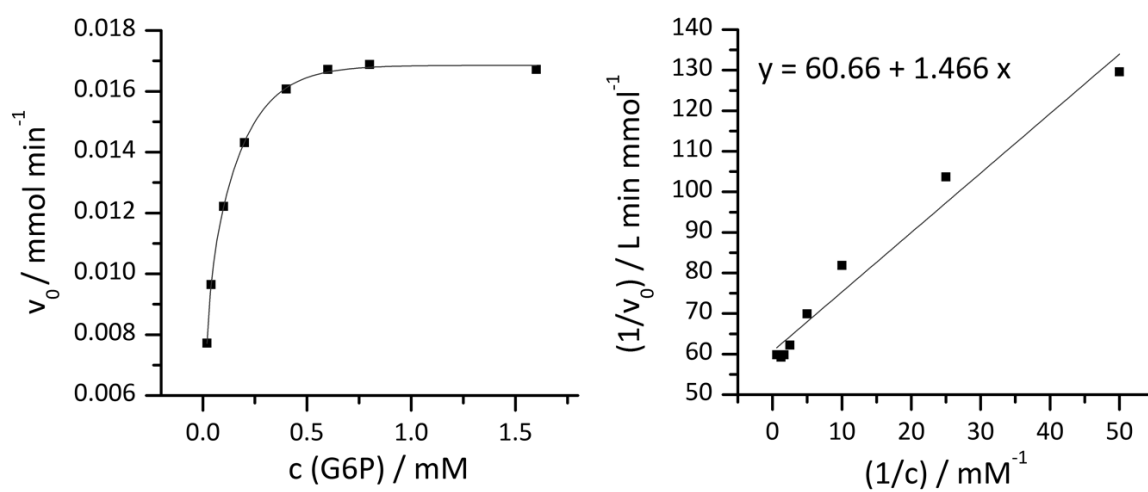


Figure S8: Michaelis-Menten and Lineweaver Burk plot of immobilized G6PDH with varied NADP concentration at 25 °C.

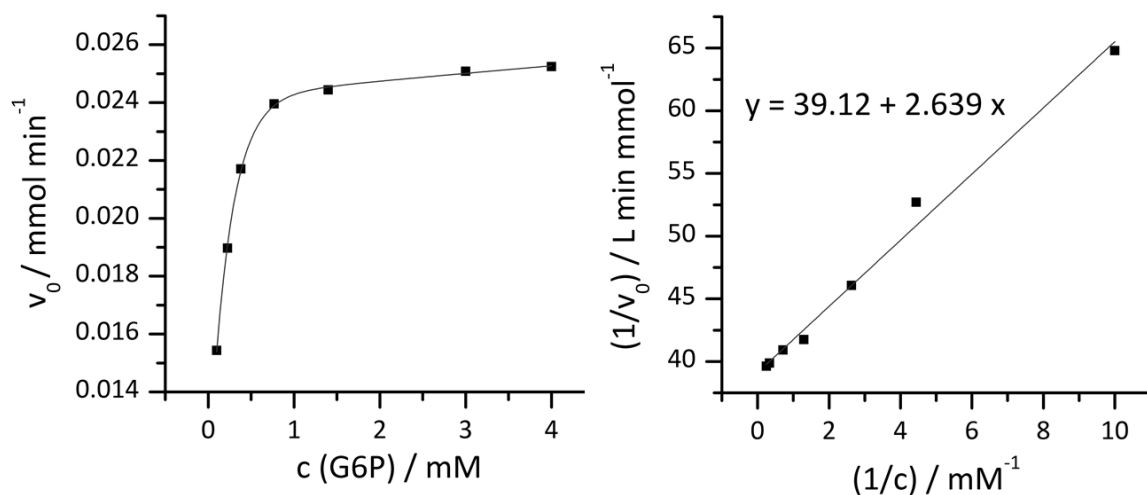


Figure S9: Michaelis-Menten and Lineweaver Burk plot of immobilized G6PDH with varied G6P concentration at 37 °C and 1/15 DMSO.

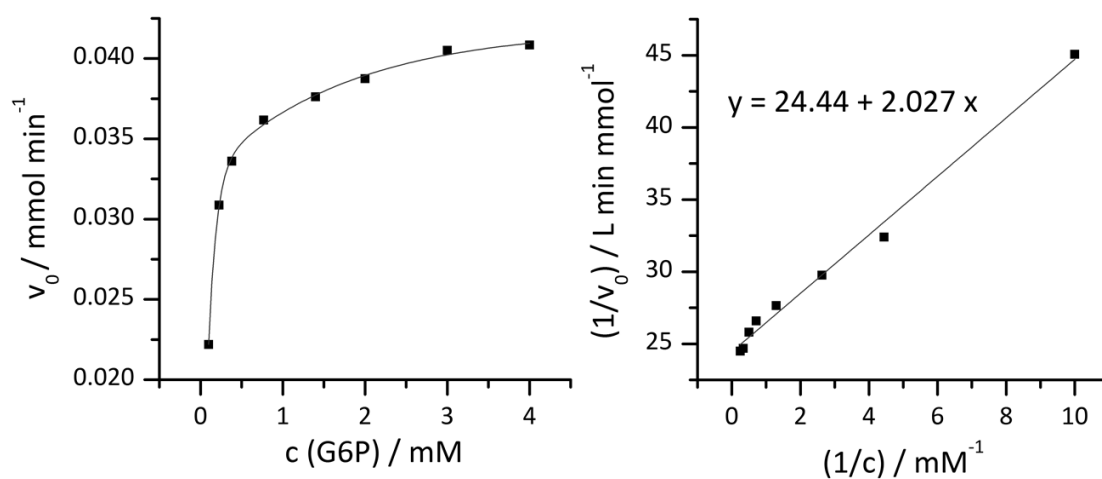


Figure S10: Michaelis-Menten and Lineweaver Burk plot of immobilized G6PDH with varied G6P concentration at 37 °C and 1/30 DMSO.

9.1.6 ARGON PHYSISORPTION ISOTHERMS

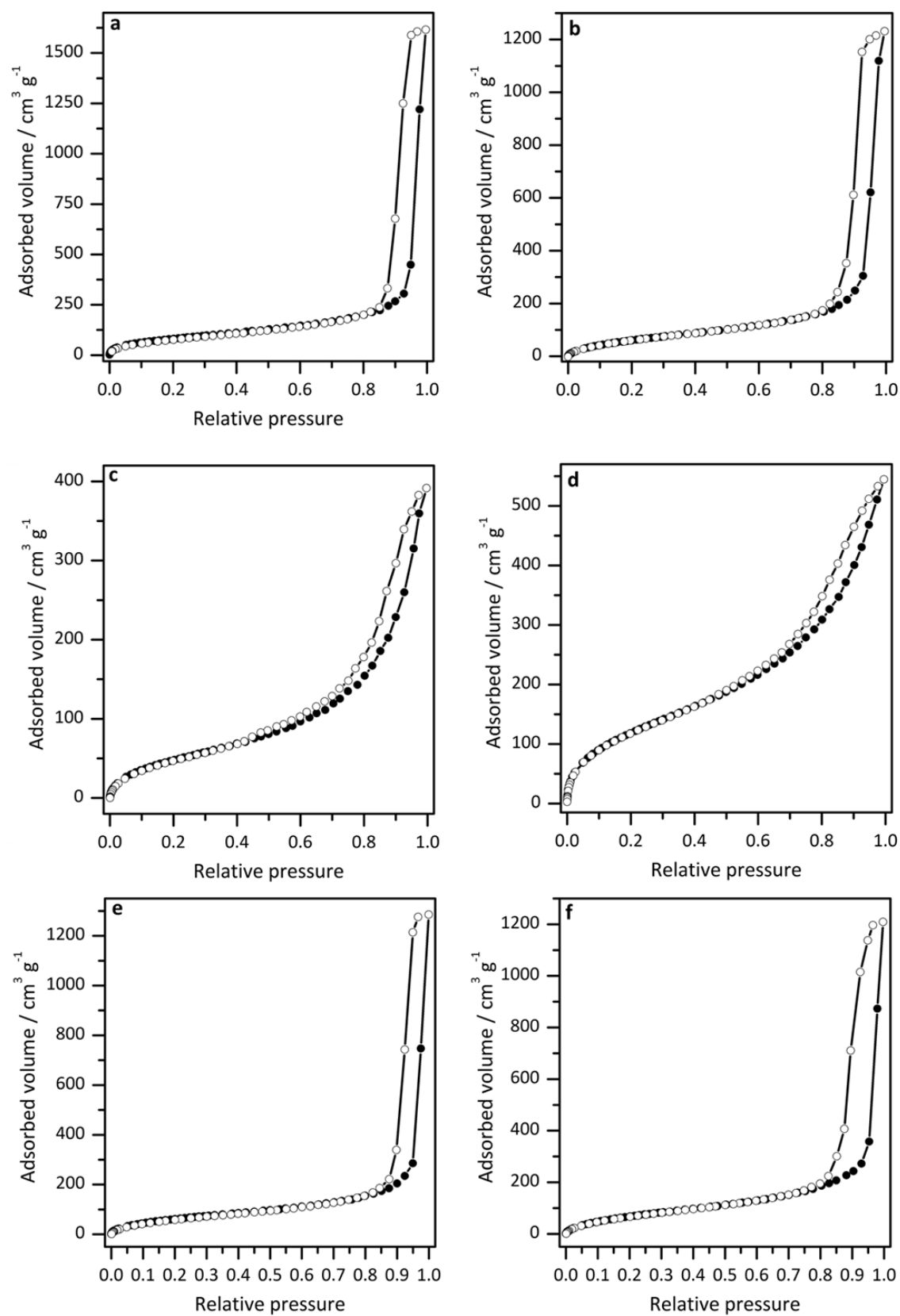


Figure S11: Argon physisorption isotherms at 87 K of pure MCF (a), MCF-C₁₁-NH₂ (b), s-PMO (c), t-PMO (d), MCF-C₃-NH₂ (e) and MCF-C₇-NH₂ (f).

9.1.7 CELLULASE ACTIVITY ASSAY

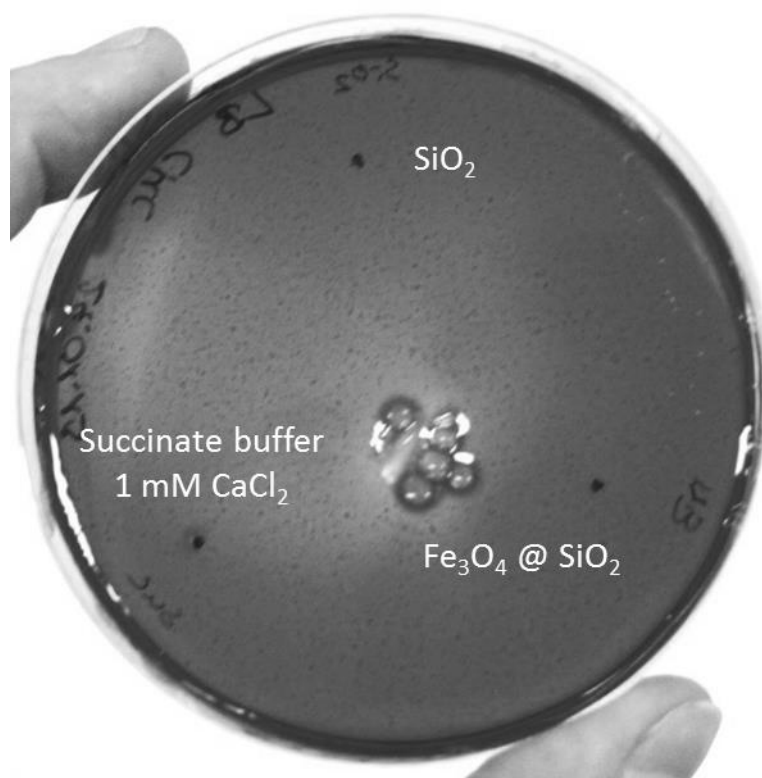


Figure S12: Negative control for the cellulase activity assay.









9.2 CHEMICALS CATEGORIZED ACCORDING TO GHS

	Gefahren- piktogramme	H – Sätze	P - Sätze
1-Ethyl-3-(3-dimethyl-aminopropyl)carbodiimid-hydrochlorid	05, 07 Achtung	315, 319, 335	261, 280, 305 + 351 + 338
(11-Bromundecyl)trimethoxysilan	05, 07 Gefahr	314, 315, 319, 335	261, 305 + 351 + 338
3-(Aminopropyl)triethoxysilan	05, 07 Gefahr	302, 314	280, 305 + 351 + 338, 310
3-(Chloropropyl)triethoxysilan	02, 05 Achtung	226, 315, 319	305 + 351 + 338
(3-Cyanopropyl)triethoxysilan	07 Achtung	315, 319, 335	261, 305 + 351 + 338
(3-Mercaptopropyl)triethoxysilan	07 Achtung	315, 319, 335	261, 305 + 351 + 338
3-(Triethoxysilylpropyl)bernsteinsäureanhydrid	07 Achtung	315, 319, 335	261, 305 + 351 + 338
4-Pentinsäure	05 Gefahr	314	280, 305 + 351 + 338
(7-Bromheptyl)trimethoxysilan	05, 07 Gefahr	314, 315, 319, 335	261, 305 + 351 + 338
7-Acetoxy-4-(bromomethyl)coumarin	05 Gefahr	314	280, 305 + 351 + 338, 310
Aceton	02, 07 Gefahr	225, 319, 336	210, 261, 305 + 351 + 338
Acetonitril	02, 07	225, 302 + 312 + 332, 319	210, 305+351+338, 403+235
Ammoniaklösung (25 %)	05, 07, 09 Gefahr	290, 314, 335, 400	273, 280, 301 + 330 + 331, 304 + 340, 305 + 351 + 338, 309 + 310
Ammoniumfluorid	06 Gefahr	301, 311, 331	280, 309 + 310, 302 + 352, 304 + 340
Bernsteinsäure, Dinatriumsalz	07 Gefahr	319	305 + 351 + 338
Bernsteinsäureanhydrid	07 Gefahr	302, 319, 335	305 + 351 + 338

Calciumchlorid	07 Achtung	319	305 + 351 + 338
Cyclohexan	02, 05, 07, 08, 09 Gefahr	225, 304, 315, 336, 410	210, 240, 273, 301 + 310, 331, 403 + 235
Diammoniumperoxodisulfat	03, 07, 08 Gefahr	272, 302, 315, 319, 335, 334, 317	280, 305 + 351 + 338 , 302 + 352, 304 + 341, 342 + 311
Dikaliumperoxodisulfat	03, 07, 08 Gefahr	272, 302, 315, 319, 335, 334, 317	280, 305 + 351 + 338 , 302 + 352, 304 + 341, 342 + 311
Eisen(III)chlorid-Hexahydrat	05, 07 Gefahr	290, 302, 315, 318	280, 305 + 351 + 338
Ethanol	02 Gefahr	225	210, 233, 240, 403 + 235
Ethylenglycol	07 Achtung	307	
Fluorescein-5-isothiocyanat	08 Gefahr	334	261, 342 + 311
Glutardialdehyd (25 %)	05, 07, 08, 09 Gefahr	302 + 332, 314, 317, 334, 335, 400	261, 273, 280, 305 + 351 + 338, 310
Glycidylpropyltrimethoxysilan	05, 07 Gefahr	314, 315, 319, 335	261, 305 + 351 + 338
Hexadecyltrimethylammonium bromide (CTAB)	05, 07, 09 Gefahr	302, 315, 318, 335, 410	261, 273, 280, 305 + 351 + 338, 501
Salzsäure (32 %)	05, 07 Gefahr	314, 335, 290	234, 260, 305 + 351 + 338, 303 + 361 + 353, 304 + 340, 309 + 311
Kupfersulfat-Pentahydrat	07, 09 Achtung	302, 315, 319, 410	273, 305 + 351 + 338, 501
Mesitylen	02, 07, 09 Achtung	226, 335, 411	210, 243, 280, 261, 273, 391
Methylmethacrylat	02, 07 Gefahr	225, 335, 315, 317	210, 262, 280, 301 + 310, 315
N,N'-Dimethylformamid ¹ (DMF)	05, 07, 08 Gefahr	360D, 226, 332, 312, 319	261, 280, 305 + 351 + 338

Natriumazid	06, 09 Gefahr	300, 410	264, 273, 301 + 310, 501
Phenol ²	05, 06, 08 Gefahr	331, 301, 311, 314, 341, 373	280, 302 + 352, 301 + 330 + 331, 309, 310, 305 + 351+ 338
Tetrabutylammoniumbromid	07 Achtung	315, 319, 335	261, 305+351+338
Tetraethylorthosilicat (TEOS)	02, 07 Achtung	226, 319, 332, 335	216, 305 + 351 + 338
Tetramethylorthosilicat (TMOS)	02, 07 Achtung	226, 319, 332, 335	216, 305 + 351 + 338
Toluol ¹	02, 08, 07 Gefahr	225, 304, 315, 336, 361d, 373	210, 280, 302 + 352, 403+235
Wasserstoff (g)	02, 04 Gefahr	210, 220, 280	377, 381

GHS-Gefahrenpiktogramme:

GHS 02 	GHS 03 	GHS 04 	GHS 05 	GHS 06 	GHS 07 
GHS 08 	GHS 09 				

¹KMR-Kategorie 2

²KMR-Kategorie 1B

Gefahrenhinweise (H-Sätze)

H200-Reihe: Physikalische Gefahren	
H220	Extrem entzündbares Gas.
H225	Flüssigkeit und Dampf leicht entzündbar.
H226	Flüssigkeit und Dampf entzündbar.
H280	Enthält Gas unter Druck; kann bei Erwärmung explodieren.
H290	Kann gegenüber Metallen korrosiv sein.

H300-Reihe: Gesundheitsgefahren	
H300	Lebensgefahr bei Verschlucken.
H301	Giftig bei Verschlucken.

H302	Gesundheitsschädlich bei Verschlucken.
H304	Kann bei Verschlucken und Eindringen in die Atemwege tödlich sein.
H311	Giftig bei Hautkontakt.
H312	Gesundheitsschädlich bei Hautkontakt.
H314	Verursacht schwere Verätzungen der Haut und schwere Augenschäden.
H315	Verursacht Hautreizungen.
H317	Kann allergische Hautreaktionen verursachen.
H318	Verursacht schwere Augenschäden.
H319	Verursacht schwere Augenreizung.
H331	Giftig bei Einatmen.
H332	Gesundheitsschädlich bei Einatmen.
H334	Kann bei Einatmen Allergie, asthmaartige Symptome oder Atembeschwerden verursachen.
H335	Kann die Atemwege reizen.
H336	Kann Schläfrigkeit und Benommenheit verursachen.
H341	Kann vermutlich genetische Defekte verursachen (Expositionsweg angeben, sofern schlüssig belegt ist, dass diese Gefahr bei keinem anderen Expositionsweg besteht).
H360 D	Kann das Kind im Mutterleib schädigen.
H361 d	Kann vermutlich das Kind im Mutterleib schädigen.
H373	Kann die Organe schädigen (alle betroffenen Organe nennen, sofern bekannt) bei längerer oder wiederholter Exposition (Expositionsweg angeben, wenn schlüssig belegt ist, dass diese Gefahr bei keinem anderen Expositionsweg besteht).

H400-Reihe: Umweltgefahren

H400	Sehr giftig für Wasserorganismen.
H410	Sehr giftig für Wasserorganismen mit langfristiger Wirkung.
H411	Giftig für Wasserorganismen, mit langfristiger Wirkung.

Sicherheitshinweise(P-Sätze)**P 200-Reihe: Prävention**

P210	Von Hitze / Funken / offener Flamme / heißen Oberflächen fernhalten nicht rauchen.
P211	Nicht gegen offene Flamme oder andere Zündquelle sprühen.
P233	Behälter dicht verschlossen halten.
P234	Nur im Originalbehälter aufbewahren.
P240	Behälter und zu befüllende Anlage erden.
P243	Maßnahmen gegen elektrostatische Aufladungen treffen.
P264	Nach Gebrauch ... gründlich waschen.
P273	Freisetzung in die Umwelt vermeiden.
P280	Schutzhandschuhe / Schutzkleidung / Augenschutz / Gesichtsschutz tragen.

P 300-Reihe: Reaktion

P309	BEI EXPOSITION ODER UNWOHLSEIN:
P310	Sofort GIFTINFORMATIONSZENTRUM oder Arzt anrufen.
P315	Sofort ärztlichen Rat einholen / ärztliche Hilfe hinzuziehen.
P331	KEIN Erbrechen herbeiführen.
P377	Brand von ausströmendem Gas: Nicht löschen, bis Undichtigkeit gefahrlos beseitigt werden kann.
P381	Alle Zündquellen entfernen, wenn gefahrlos möglich.
P391	Verschüttete Mengen aufnehmen.
P301 + P310	BEI VERSCHLUCKEN: Sofort GIFTINFORMATIONSZENTRUM oder Arzt anrufen.

P301 + P330 + P331	BEI VERSCHLUCKEN: Mund ausspülen. KEIN Erbrechen herbeiführen.
P302 + P352	BEI KONTAKT MIT DER HAUT: Mit viel Wasser und Seife waschen.
P303 + P361 + P353	BEI KONTAKT MIT DER HAUT (oder dem Haar): Alle verschmutzten, getränkten Kleidungsstücke sofort ausziehen. Haut mit Wasser abwaschen/duschen.
P304 + P340	BEI EINATMEN: An die frische Luft bringen und in einer Position ruhigstellen, die das Atmen erleichtert.
P304 + P341	BEI EINATMEN: Bei Atembeschwerden an die frische Luft bringen und in einer Position ruhigstellen, die das Atmen erleichtert.
P305 + P351 + P338	BEI KONTAKT MIT DEN AUGEN: Einige Minuten lang behutsam mit Wasser spülen. Vorhandene Kontaktlinsen nach Möglichkeit entfernen. Weiter spülen.
P309 + P311	BEI EXPOSITION ODER UNWOHLSEIN: GIFTINFORMATIONSZENTRUM oder Arzt anrufen.
P342 + P311	Bei Symptomen der Atemwege: GIFTINFORMATIONSZENTRUM oder Arzt anrufen.

P 400-Reihe: Aufbewahrung	
----------------------------------	--

P403 + P235	Kühl an einem gut belüfteten Ort aufbewahren.
-------------	---

DOROTHEE IRMGARD FRIED
SEERING 36, 23845 ITZSTEDT • 0177-2436520 • 04535-463
FRIED@CHEMIE.UNI-HAMBURG.DE

CURRICULUM VITAE

PERSÖNLICHE INFORMATIONEN

Geboren am 16. November 1984 in Bad Kreuznach

Familienstand: ledig

Staatsangehörigkeit: deutsch

SCHULBILDUNG

1991 – 1995 Grundschule, Ringschule, Bad Kreuznach

1995 – 2004 Lina-Hilger-Gymnasium, Bad Kreuznach

03/2004 Abitur

STUDIUM

10/2004 – 06/2009 Studium der Chemie an der *Ludwig-Maximilians Universität*,
München

10/2006 Diplomvorprüfung in Chemie

10/2008 Diplomprüfung in Chemie

12/2008 – 06/2009 Diplomarbeit "*Click-Chemistry in Mesoporous Silica Hosts*" in der
Arbeitsgruppe von Prof. Dr. T. Bein am *Institut für Physikalische
Chemie, Department Chemie und Biochemie der Ludwig-
Maximilians Universität*, München

01/2010-01/2014 Promotion zum Dr. rer. nat. in Chemie am *Institut für Anorganische
und Angewandte Chemie der Universität Hamburg* im Arbeitskreis
von Prof. Dr. M. Fröba

BERUFSERFAHRUNG UND PRAKTIKA

05-07/2004	Praktikum bei <i>Dr. Graner & Partner GmbH</i> , Labor für Analytische und Pharmazeutische Chemie, München
03-04/2009	Tutor im Praktikum Anorganische Chemie für Biologen
04-07/2009	Tutor zur Vorlesung Physikalische Chemie I
07-08/2009	Wissenschaftliche Hilfskraft in der Arbeitsgruppe von Prof. Dr. T. Bein, <i>Ludwig-Maximilians Universität</i> , München
09-12/2009	Forschungsaufenthalt in <i>den Sandia National Labs/University of New Mexico in Albuquerque, USA</i> , zum Thema „ <i>Aerosol Deposition Printing of Horseradish Peroxidase</i> “
Seit 01/2010	Wissenschaftlicher Mitarbeiter in der Arbeitsgruppe von Prof. Dr. M. Fröba, Universität Hamburg

SONSTIGE QUALIFIKATIONEN

seit 2010	Verantwortlicher für die Betreuung der Dynamischen Lichtstreuung, Physisorption und Quecksilberporosimetrie
seit 2010	Fachliche Betreuung von Diplomanden und Studenten im Master- sowie Bachelorstudium in der Anorganischen Chemie

AUSZEICHNUNGEN

	„ <i>Best poster award winner</i> “
Mai 2013	International Mesostructured Materials Symposium (IMMS) 2013 , Awaji Islands, Hyogo, Japan

10 PUBLICATIONS AND PRESENTATIONS

PUBLICATIONS

DOROTHEE I. FRIED, FELIX J. BRIELER, MICHAEL FRÖBA

Designing inorganic porous materials for enzyme adsorption and applications in biocatalysis

ChemCatChem **2013**, *5*, 931-938.

DOROTHEE I. FRIED, KRISTIN TROPP, MICHAEL FRÖBA

On the Way to Cofactor Regeneration in Nanopores: Tailoring Porous Materials for Glucose-6-phosphate dehydrogenase Immobilization

ChemCatChem **2013**, *5*, 862-884.

DOROTHEE I. FRIED, AXEL SCHLOSSBAUER, THOMAS BEIN

Immobilizing glycopyranose on mesoporous silica via “click-chemistry” for borate adsorption

Microporous Mesoporous Mater. **2012**, *147*, 5-9.

DOROTHEE I. FRIED, ALESJA IVANOVA, VESNA MÜLLER, JIRI RATHOUSKY, BERND M. SMARSLY, DINA FATTAKHOVA-ROHLFING

A facile synthesis of mesoporous crystalline tin oxide films involving a base-triggered formation of sol-gel building blocks

Nanoscale **2011**, *3*, 1234-1239.

ORAL PRESENTATIONS

DOROTHEE I. FRIED, KRISTIN TROPP, MICHAEL FRÖBA

Tuning porous materials for large-size protein immobilization

24. Deutsche Zeolith-Tagung **2012**, Magdeburg

DOROTHEE I. FRIED, KRISTIN TROPP, MICHAEL FRÖBA

On the way to cofactor regeneration in nanopores: Tailoring porous materials for Glucose-6-phosphate dehydrogenase immobilization

International Mesostructured Materials Symposium (IMMS) **2013**, Awaji Islands, Japan

“Best poster award winner”

POSTER PRESENTATIONS

DOROTHEE I. FRIED, KRISTIN TROPP, MICHAEL FRÖBA

On the way to cofactor regeneration in nanopores: Tailoring porous materials for Glucose-6-phosphate dehydrogenase immobilization

International Mesostructured Materials Symposium (IMMS) **2013**, Awaji Islands, Japan

DOROTHEE I. FRIED, ANDREA RENTMEISTER, MICHAEL FRÖBA

Artificial cellulosomes on magnetic core-shell particles

24. Deutsche Zeolith-Tagung **2013**, Hamburg

DOROTHEE I. FRIED, KRISTIN TROPP, MICHAEL FRÖBA

Tuning porous materials for large-size protein immobilization

International workshop on new and synthetic bioproduction systems **2012**, Hamburg

DOROTHEE I. FRIED, KRISTIN TROPP, MICHAEL FRÖBA

Tuning porous materials for large-size protein immobilization

Characterization of porous materials (CPM-6) **2012**, Delray Beach, Florida, USA

DOROTHEE I. FRIED, MICHAEL FRÖBA

Covalent immobilization of glucose-6-phosphate dehydrogenase on a mesoporous silica support

23. Deutsche Zeolith-Tagung **2011**, Erlangen

DOROTHEE I. FRIED, AXEL SCHLOSSBAUER, THOMAS BEIN

Biofunctionalization of mesoporous silica hosts by click chemistry

22. Deutsche Zeolith-Tagung **2010**, München

